Direct Jet Reconstruction in Proton–Proton and Copper–Copper Collisions at $\sqrt{s_{NN}} = 200$ GeV

Yue Shi Lai

Submitted in partial fulfillment of the

requirements for the degree

of Doctor of Philosophy

in the Graduate School of Arts and Sciences

Columbia University

2012

Abstract

Direct Jet Reconstruction in Proton–Proton and Copper–Copper Collisions at $\sqrt{s_{NN}} = 200$ GeV

Yue Shi Lai

Collision of heavy nuclei at the Relativistic Heavy Ion Collider (RHIC) recreates the state of high temperature quark–gluon plasma that existed shortly after the Big Bang. Measurement using single particle spectra and two-particle correlation shows that this medium is largely opaque to the transit of a high energy quark or gluon. Reconstructing the kinematics of these quarks and gluons can provide additional constraints for the property of their interaction with the medium. While the direct reconstruction of quantum chromodynamics jets, the final state showers of quarks and gluons, has become an indispensable tool at hadron and electron accelerator experiments, the application of this technique to heavy ion collisions at the RHIC energy has been considered a hard problem. The relatively low yield of high transverse momentum jets would have to be detected within a large, fluctuating background that can give rise to a false jet signal. At the RHIC PHENIX experiment, jet reconstruction also has to cope with the limited aperture of the central arm spectrometers. To overcome both problems, which can distort the jet signal in the traditional reconstruction algorithms, this thesis develops an algorithm that reconstructs the jets as maxima of the Gaussian filtered event transverse momentum distribution. The Gaussian angular weighting causes the algorithm to become more sensitive to the jet core versus the jet periphery. It is then combined with a fake jet rejection discriminant to remove the background fluctuation from the jet signal. This algorithm is used to obtain the first jet measurement in heavy ion environment at PHENIX, using data from the 2004/2005 RHIC run. The result includes the proton–proton inclusive jet spectrum, the proton–proton fragmentation function, the copper–copper jet nuclear modification factor, the copper–copper jet central-to-peripheral modification factor, and the copper–copper dijet azimuthal correlation. The measured copper–copper jet nuclear modification factor shows that there is a significant initial state effect to the jet suppression. The observation of no broadening in the copper–copper dijet azimuthal correlation indicates that the traditional energy loss picture via multiple soft scattering may not be applicable to the quark–gluon plasma.

Table of Contents

List of Figures

List of Tables

Acknowledgments

I would like to thank my adviser, Brian Cole, for suggesting one of the most exciting topics in the field to work on. I am deeply indebted to him, both for his guidance and the patience to endure all the set-backs, along the long and winding path towards this complex and highly visible measurement. I am also obliged for the encouragement and insight Bill Zajc was always able to provide.

It was a pleasure and intellectually stimulating working with my fellow graduate students, Mickey Chiu, Tatia Engelmore, Justin Franz, Janette Hanks, Jiamin Jin (金佳敏), Eric Vazquez, and Chun Zhang (张纯). And as the saying *nanos gigantium humeris insidentes* goes, this thesis is written while standing on the shoulders of my numerous PHENIX co-collaborators and the Collider–Accelerator Department of the Brookhaven National Laboratory.

This thesis also would not have been possible without the longstanding support and encouragement by my parents Jingjuan (静娟) and Xiaowei (晓威). I am also grateful for many people, who, during my childhood, fostered my scientific curiosity and engineering knowledge, most notably Roland Zielke and Gerhard Schultz.

Finally, I would like to acknowledge funding by the German National Academic Foundation (*Studienstiftung des deutschen Volkes*) and the German–American Fulbright Commission during my undergraduate *Diplomstudium* in Bielefeld and the first years as a graduate student in New York. This work was supported by the U.S. Department of Energy, Office of Science under grant DE-FG02-86ER40281.

Dedicated to my parents

Common Abbreviations

AdS/CFT	Anti de Sitter/conformal field theory
AGS	lternating Gradient Synchrotron
ASIC	Application-specific integrated circuit
ATLAS	A Toroidal LHC ApparatuS
ATP	Assembly Trigger Processor
BBC	Beam–beam counter
BNL	Brookhaven National Laboratory
CERN	European Organization for Nuclear Research[1]
CERNLIB	CERN Program Library
CGS	Centimeter–gram–second
CMB	Cosmic microwave background
CODATA	Committee on Data for Science and Technology
CPU	Central processing unit
DAQ	Data acquisition
DC	Drift chamber
DCM	Data Collection Module
DIS	Deep inelastic scattering
DST	Data summary tape
EMCal	Electromagnetic calorimeter
ERT	EMCal/RICH trigger
EvB	Event Builder
FEM	Front End Module

[1] historically: *Conseil Européen pour la Recherche Nucléaire* (European Council for Nuclear Research)

FIR	Finite impulse response (filter)
FNAL	Fermi National Accelerator Laboratory (Fermilab)
FODO	Focusing quadrupole–drift space–defocusing quadrupole–drift space
GEANT	GEometry ANd Tracking
GL1	Global Level-1 (trigger)
GSVD	Generalized (quotient) SVD
HEP	High energy physics
HERWIG	Hadron Emission Reactions With Interfering Gluons
HIJING	Heavy Ion Jet INteraction Generator/he yi jing (核易经)
IEEE	Institute of Electrical and Electronics Engineers
IIR	Infinite impulse response (filter)
IR	Infrared
	Interaction region (experiment)
IRC	Infrared/collinear
ISR	Intersecting Storage Ring
LAPACK	Linear Algebra PACKage
ΛCDM	Cosmological constant–cold dark matter
LHC	Large Hadron Collider
LINAC	Linear accelerator
LL1	Local Level-1 (trigger)
LO	Leading order
LP	Linear programming
MB	Minimum bias
MIP	Minimum ionizing particle
MWPC	Multiwire proportional chamber
NLO	Next-to-leading order
OPPIS	Optically pumped polarized ion source
PC	Pad chamber
PbGl	Pb (lead) glass
PbSc	Pb (lead) scintillator

PHENIX	Pioneering High-Energy Nuclear Interaction eXperiment
PISA	PHENIX Integrated Simulation Application
PMT	Photomultiplier tube
PQCD	Perturbative QCD
PRDF	PHENIX Raw Data Format
PRNG	Pseudorandom number generator
PSS	Phase space splicing
QCD	Quantum chromodynamics
QED	Quantum electrodynamics
QGP	Quark–gluon plasma
RICH	Ring imaging Cherenkov detector
RHIC	Relativistic Heavy Ion Collider
SEB	Sub Event Buffer
SM	Standard Model
SIMD	Single instruction, multiple data
SISCone	Seedless/infrared safe cone (algorithm)
SPS	Super Proton Synchrotron
SSE	Streaming SIMD Extension
SUSY	Supersymmetry
SVD	Singular value decomposition
TOF	Time of flight
UV	Ultraviolet
WCM	Wall current monitor
ZDC	Zero degree calorimeter

Mathematical Notation

&	Bitwise and
|	Bitwise or
$\|\mathbf{x}\|_{\mathbf{A}}$	$= \sqrt{\mathbf{x}^T \mathbf{A}^{-1} \mathbf{x}}$, the Mahalanobis distance
$\lfloor x \rfloor$	The floor function of x, the greatest integer $\leq x$
$^{(n)}$	n-th iteration
$\wedge$	Logical and
$\vee$	Logical or
$\mathbf{A}^{\dagger}_{\mathrm{MP}}$	The Moore–Penrose pseudoinverse of $\mathbf{A}$ (from the singular value decomposition)
$\mathbf{A}^{\dagger}_{\mathbf{B}}$	The B-weighted pseudoinverse of $\mathbf{A}$ (from the generalized singular value decomposition)
$(n_M \ldots n_1 n_0 . n_{-1} \ldots n_{-N})_b$	$\equiv \sum_{k=-N}^{M} n_k b^k$, the radix-$b$ number representation
α_s	The quantum chromodynamics coupling constant
cpe	clock per element
β	$= v/c$, velocity (in natural units)
	β function (renormalization)
β^*	Betatron amplitude function
$\mathrm{Cov}(x)$	Covariance
d	Number of dimensions
	Distance
$D(z), D(x, Q^2)$	Fragmentation function
$\mathrm{diag}(\mathbf{x})$	Diagonal matrix
ds	Line element
ϵ	Efficiency (experimental)

ε	Emittance (accelerator physics)
ϵ_A	Achievable machine accuracy
ϵ_M	Machine precision
η	Pseudorapidity
	Infinitesimal (dimensional renormalization)
$f(x, Q^2)$	Parton distribution function
f_{ch}	Charged fraction
$h(\ldots)$	The impulse response
$H(\ldots)$	The complex transfer function
i	$\equiv \sqrt{-1}$, the imaginary unit
$\mathbf{j}_T$	The transverse (to jet axis) momentum vector
K	$= \int \mathbf{B} \times d\mathbf{l}$, the effective field integral
$\mathscr{L}$	Lagrangian (quantum chromodynamics)
	Luminosity (accelerator physics)
$=$ min!	Minimize
$\mathscr{M}$	Invariant matrix element
$\overline{\text{MS}}$	Modified minimal subtraction scheme
N_c	Number of color charges
p	The (four) momentum
$P(x)$	Probability
$P(x\|y)$	Conditional probability
p_T	$\equiv \sqrt{p_x^2 + p_y^2}$, the transverse momentum
ϕ	Azimuth
ϕ^*	$\equiv \phi - 2\pi\lfloor(\phi + \pi)/(2\pi)\rfloor$, the angular range reduced azimuth
$\Delta\phi$	$\equiv (\phi_2 - \phi_1)^*$, the (angular range reduced) pair azimuthal opening angle
Ψ	Reaction plane
R_{AA}	The nuclear modification factor, ratio between heavy ion and $p+p$ cross sections
R_{CP}	The central to peripheral collision modification factor
s	$= (p_1 + p_2)^2 = (p_3 + p_4)^2$, the square of the center-of-mass energy
S	$= \int \mathscr{L} dt$, the action

σ	Cross section
	Standard deviation
$\mathrm{SU}(n)$	Special unitary group of degree n
T	Temperature
$\mathbf{A}^T$	Transpose of matrix $\mathbf{A}$
$T_k(x)$	Chebyshev polynomial of the first kind
ulp	unit in the last place
$\mathrm{Var}(x)$	Variance
z	$\equiv p_\parallel / p^{\mathrm{jet}}$, the longitudinal momentum fraction (kinematics)
	Complex argument of the Z-transform (digital filter)

Chapter 1

Introduction

The strong interaction, which governs the structure of nucleons, describes quarks as bound particles in virtually all conditions on Earth, while only in highly energetic conditions – e.g. scattering of nucleons, or heated to sufficiently high temperature – they would emerge as particles no longer bound inside the nucleons. From the Big Bang cosmology, it is expected that the nucleons as we know them today, froze out of such a hot "soup" of freely roaming quarks and gluons (other unstable hadrons, such as mesons, would also freeze out, but decay eventually), until no outward charge of the strong interaction – "color" – remains. Since this soup is theoretically the strong interaction equivalent of an electromagnetic plasma (the "electron–photon plasma"), it was coined as the quark–gluon plasma (QGP, a term introduced by E. V. Shuryak [14]).

Using collision of nuclei to recreate this phase of matter has been proposed as far back as the Berkeley Bevalac [15]. The Relativistic Heavy Ion Collider (RHIC) is the first accelerator systematically designed to produce such a state and study its properties. This was made possible by an accelerator that can collide independent beam types and directly compare the baseline, "cold" nucleus on nucleus collisions, with the "hot" nucleus–nucleus collisions, where the emergence of the QGP is expected.

For the very same reason that hadrons would freeze out from QGP when the universe cools, the so produced, naked quarks and gluons would "hadronize" by converting the excess energy into a spray of particles, which carries roughly the momentum of the originating quark or gluon. In collisions of protons and electrons, when in one of the rare occasions, the quarks and gluons in the colliding nucleons scatter energetically, this process becomes quite evident as a collimated spray of particles, coined a "jet" (S. D. Drell, J. D. Levy, and T.-m. Yan [16]). While in the collisions of protons and electrons, the jet is cleanly observable, the large number of interaction involved in the collision of nuclei typically produces 200 particles per unit spherical angle. Simply by Poisson fluctuation, the detection is more or less a game of luck, unless more sophisticated techniques are applied to clear the vision.

Several of the techniques developed to work around this problem is to detect the jet statistically. This has

been applied successfully to RHIC in the form of single particle yield [17] and two particle correlation [18]. These observations have been as signature of jet quenching. The later paper summarizes the predominant view regarding jet reconstruction at RHIC:

> "The traditional identification of jets through hadronic calorimetry and cluster algorithms is problematic in Au Au collisions at RHIC, since low-energy jets ($<$ 10–20 GeV) are overwhelmed by other produced particles in the underlying event and high-energy jets are p relatively rare at $\sqrt{s_{NN}} = 200$ GeV. Instead, we study hard-scattered single partons and parton pairs through angular correlations of high-p_T hadron pairs."

The obstacle that prevented full jet measurement for nearly a decade at RHIC is the low jet yield with a comparably high background that fluctuate significantly. Naïve application of jet algorithm to heavy ion collisions in fact predates RHIC and should be well-known to anyone with memory dating back to the Fermilab E557 Collaboration. When RHIC was designed, people (still remembering the impact of the hard-to-remove fluctuation, as opposed to the energy offset from the underlying event, which is not the main issue) looked at the Poisson fluctuation of central $\sqrt{s_{NN}} = 200$ GeV Au + Au collisions and (still) saw the hopelessness to extract jets reliably. While I will partially contradict this conclusion, by showing that there are phase spaces where it is feasible, the conclusion remains correct that a naïve application of jet algorithm to RHIC will cause problems even with $\sqrt{s_{NN}} = 200$ GeV and light ions.

This thesis is therefore most likely the first that studies the jet quenching in heavy ion colliders using jet reconstruction – and with advent of LHC, and the tools now established for RHIC herein, there will be many to come.

Chapter 2

Quark–Gluon Plasma

This thesis is mostly concerned with both the isolated and bulk property of quarks and gluons, which, to our present understanding (and collider energy reach), are both fundamental and point-like constituents of matter.

The discovery of quarks and gluons as the composition of baryons by M. Gell-Mann and K. Nishijima follows a long historical succession that started as schools of atomism in Ancient Greece [19] and India [20], and includes their spread to medieval Europe to Central Asia [21]. The chemical composition of matter and the existence of atoms was discovered in the 18th and 19th century Europe by A. Lavoisier [22], J. Dalton [23], and D. Mendeleev [24]. With the rise of modern physics, e^-, p, and n as subatomic particles were discovered by J. J. Thomson [25], E. Rutherford [26], and J. Chadwick [27] in 1897, 1919, and 1932, respectively.

Property of hadrons at high temperature has been studied even before discovery of the flavor quantum numbers. The discovery of large number of hadronic resonances led R. Hagedorn to develop the statistical bootstrap model (SBM). Under the assumption of "infinitly composed particles", the asymptotic hadronic state density becomes [28]

$$dn(m) \sim \frac{A}{m^{5/2}} \exp\left(\frac{m}{T_H}\right) dm, \quad A \text{ constant} \tag{2.1}$$

Calculating the partition function by

$$\langle \epsilon \rangle \approx A \left(\frac{T}{2\pi}\right)^{3/2} \frac{T_H T}{T_H - T} \exp\left(-m_0\right) \ln Z(V, T) \tag{2.2}$$

gives as corollary of SBM the divergence of the partition function at the finite Hagedorn temperature T_H, i.e. approaching T_H would require increasing energy to produce hadronic resonances, leading to infinite energy at T_H, which therefore would be the upper bound of any equilibrium temperature. Using spectra from $\sqrt{s} =$ 12.5–30 GeV $p+p$ collisions, Hagedorn obtained $T_H \approx 160$ MeV. This gives the first hint that for hadronic matter, something nontrivial may occur when heated to this temperature.

In following, I will review the basic theoretical ingredients that provides (or are hopeful candidates for) predictions in jet production and jet interaction with the QGP.

2.1 QCD

QCD is a theory of quantized Yang–Mills field described by the Lagrangian

$$\mathscr{L}_{\mathrm{QCD}} = -\frac{1}{4}\sum_a F^a_{\mu\nu}F^{a\mu\nu} + \sum_f \bar{q}_a \left[i\gamma_\mu D^\mu - m_f\right]_{ab} q_b, \tag{2.3}$$

consisting of the Klein-Gordon Lagrangian for the field tensor of the spin-1 gluons

$$F^a_{\mu\nu}(x) = \partial_\mu A^a_\nu(x) - \partial_\nu A^a_\mu(x) + g_s f^{abc} A^b_\mu(x) A^c_\nu(x), \tag{2.4}$$

and the Dirac Lagrangian for the spin-$\frac{1}{2}$, non-Abelian quark field q_f. The structure constant f^{abc} arises from the fundamental representation of the SU(N_c) group

$$[t^a, t^b] = if^{abc}t^c, \tag{2.5}$$

while the covariant derivative is defined as

$$(D_\mu)_{ab} = \partial_\mu \delta_{ab} + ig_s A^a_\mu(x) t^a, \tag{2.6}$$

and the QCD coupling is

$$\alpha_s = \frac{g_s^2}{4\pi} \tag{2.7}$$

Symmetry with respect to the color charges of the quark and gluon fields give rise to the SU(N_c) group in QCD. Up to the fourth order for QCD, the following invariants can be derived (which we will encounter later)

$$\begin{gathered} T_F = \frac{1}{2} \qquad N_A = N_c^2 - 1 \qquad C_A = N_c \qquad C_F = \frac{N_c^2 - 1}{2N_c} \\ \frac{d_A^{abcd} d_A^{abcd}}{N_A} = \frac{N_c^2(N_c^2 + 36)}{24} \qquad \frac{d_F^{abcd} d_A^{abcd}}{N_A} = \frac{N_c(N_c^2 + 6)}{48} \\ \frac{d_F^{abcd} d_F^{abcd}}{N_A} = \frac{N_c^4 - 6N_c + 18}{96N_c^2} \end{gathered} \tag{2.8}$$

For small coupling, Feynman rules can be derived by varying $\mathscr{L}_{\mathrm{QCD}}$ in momentum space. The quark propagator is obtained by setting $\partial^\alpha = -ip^\alpha$, while the gluon propagator requires the selection of a gauge.

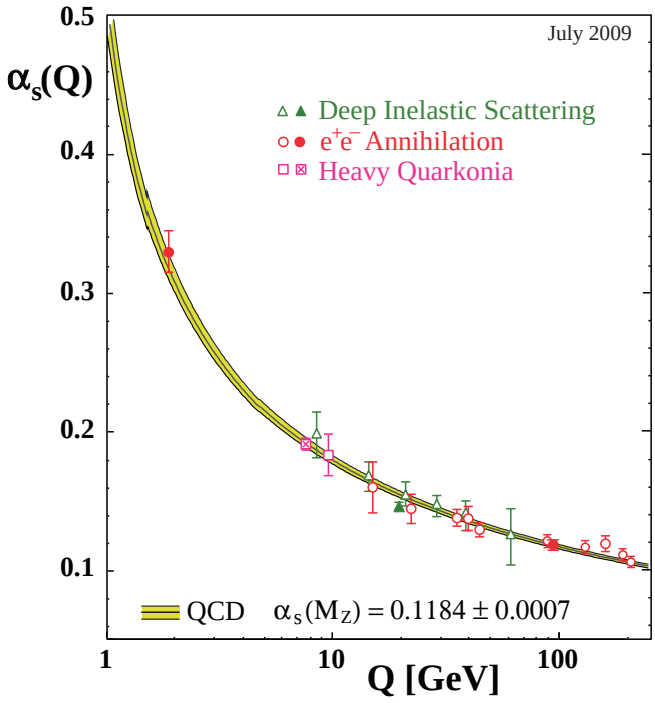

Figure 2.1: The running QCD coupling constant $\alpha_s(Q^2)$ fitted to the experimental values as function of momentum transfer Q, and with the fitted value $\alpha_s(M_Z)$ at the Z^0 mass shown. From [1].

Feynman rules arises for quark–gluon scattering, and due to the self-interaction with non-Abelian fields, both three and four vertices gluon interaction. Unlike quantum electrodynamics (QED), these additional gluon interactions can propagate non-physical degrees of freedom, and therefore the additional (gauge dependent) rule corresponding to the Fadeev–Popov ghost interacting with the gluon field has to be observed.

2.1.1 Asymptotic Freedom

Like in any quantized, interacting field, loop contribution gives a Q^2-dependent renormalization to the propagator. The coupling of a perturbative field theory follows the renormalization group equation

$$Q^2 \frac{\partial \alpha}{\partial Q^2} = \beta(\alpha) = -\sum_{k=0}^{\infty} \beta_k \left(\frac{\alpha}{4\pi}\right)^{k+2} \tag{2.9}$$

where β_k is the $(k+1)$-loop contribution to the β function. Due to exact cancellations, β_0, β_1 are renormalization scheme independent, while the higher loop orders are not.

In QED, the one and two-loop contribution to the β function for n fermions at the one-loop order

$$\beta^{\mathrm{QED}}(\alpha) = \frac{4}{3}\left(\frac{\alpha}{4\pi}\right)^2 + 4n\left(\frac{\alpha}{4\pi}\right)^3 + O(\alpha^4) \tag{2.10}$$

are all negative (by convention of (2.9)), which is a consequence of the charge screening: At high $\sqrt{Q^2}$, more of the bare charge is probed, thus the increasing coupling strength. The QCD analogue of the Gauss's and Faraday's law can be obtained by summing over the spatial components of the covariant derivative (and disregarding for a moment the SU(N_c) structure):

$$\begin{aligned} \nabla \cdot \mathbf{E} + ig_s(\mathbf{A} \cdot \mathbf{E} - \mathbf{E} \cdot \mathbf{A}) &= \frac{q}{\epsilon_0} \\ \nabla \cdot \mathbf{B} + ig_s(\mathbf{A} \cdot \mathbf{B} - \mathbf{B} \cdot \mathbf{A}) &= 0 \end{aligned} \tag{2.11}$$

where the extra commutator term to the color field $\mathbf{A}$ results from the requirement of gauge covariance [29]. The additional term from a point color charge to a radial divergence in (2.11) suggests that the point charge will lead to a nonradial charge separation and screening, which is very unlike QED. Gerard 't Hooft was the first to provide heuristic argument for a $\beta_0 > 0$ and thus a negative slope. D. Gross, F. Wilczek, and D. Politzer, and obtained

$$\beta_0 = \frac{11}{3} C_A - \frac{4}{3} T_F n_f, \tag{2.12}$$

with n_f being the number of quark flavors, and the gluon loop therefore providing the negative slope of the β function, which results in the asymptotic freedom of QCD. The QCD beta function up to the fourth loop in $\overline{\text{MS}}$ has been evaluated by W. E. Caswell, D. R. T. Jones, E. Egorian, and O. V. Tarasov (two-loop) [30], O. V. Tarasov, A. A. Vladimirov, A. Y. Zharkov, S. A. Larin, and J. A. M. Vermaseren (three-loop) [31], and T. van Ritbergen, J. A. M. Vermaseren, and S. A. Larin (four-loop) [32]

$$\beta_1 = \frac{34}{3} C_A^2 - 4 C_F T_F n_f - \frac{20}{3} C_A T_F n_f \tag{2.13}$$

$$\begin{aligned} \beta_2 = {} & \frac{2857}{54} C_A^3 + 2 C_F^2 T_F n_f - \frac{205}{9} C_F C_A T_F n_f - \frac{1415}{27} C_A^2 T_F n_f + \frac{44}{9} C_F T_F^2 n_f^2 \\ & + \frac{158}{27} C_A T_F^2 n_f^2 \end{aligned} \tag{2.14}$$

$$\begin{aligned}\beta_3 = &\left[\frac{150653}{486} - \frac{44}{9}\zeta(3)\right] C_A^4 + \left[-\frac{39143}{81} + \frac{136}{3}\zeta(3)\right] C_A^3 T_F n_f \\ &+ \left[\frac{7073}{243} - \frac{656}{9}\zeta(3)\right] C_A^2 C_F T_F n_f + \left[-\frac{4204}{27} + \frac{352}{9}\zeta(3)\right] C_A C_F^2 T_F n_f \\ &+ 46 C_F^3 T_F n_f + \left[\frac{7930}{81} + \frac{224}{9}\zeta(3)\right] C_A^2 T_F^2 n_f^2 + \left[\frac{1352}{27} - \frac{704}{9}\zeta(3)\right] C_F^2 T_F^2 n_f^2 \\ &+ \left[\frac{17152}{243} + \frac{448}{9}\zeta(3)\right] C_A C_F T_F^2 n_f^2 + \frac{424}{243} C_A T_F^3 n_f^3 + \frac{1232}{243} C_F T_F^3 n_f^3 \\ &+ \left[-\frac{80}{9} + \frac{704}{3}\zeta(3)\right] \frac{d_A^{abcd} d_A^{abcd}}{N_A} + \left[\frac{512}{9} - \frac{1664}{3}\zeta(3)\right] \frac{d_F^{abcd} d_A^{abcd}}{N_A} n_f \\ &+ \left[-\frac{704}{9} + \frac{512}{3}\zeta(3)\right] \frac{d_F^{abcd} d_F^{abcd}}{N_A} n_f^2, \end{aligned} \tag{2.15}$$

with $\zeta(3) = 1.20206\ldots$ being the Riemann ζ function (which comes from momentum integration and appears in intermediate diagrams at lower loop order – and even for the QED β function – but they usually cancel out until higher loop orders). Evaluation of β_3 involves approximately 50 000 diagrams (which, with no interference terms, is still quite manageable compared e.g. to scattering processes to the four-loop order).

Figure 2.1 shows a current fit of the running QCD coupling constant $\alpha_s(Q^2)$ against the experimental values as function of momentum transfer Q.

2.1.2 Lattice QCD

Lattice gauge theory is the formulation of $d = 4$ quantum field theory as a Euclidean theory on discrete space time

$$S_{\mathrm{QCD}} \mapsto i S_{\mathrm{QCD}}^{(\mathrm{eucl})} = S_G^{(\mathrm{eucl})} + S_F^{(\mathrm{eucl})} \tag{2.16}$$

The space time discretization is performed by the substitution

$$\begin{aligned} x_\mu &\mapsto a n_\nu \\ \int d^D x &\mapsto a^D \sum_n \\ \Box &\mapsto \frac{1}{a^2} \hat{\Box} \\ D &\mapsto \prod_n d. \end{aligned} \tag{2.17}$$

where a is the lattice spacing.

The next step now is to obtain the lattice QCD action, where the quantized theory is given as the partition

function

$$Z = \int [dU][d\bar{q}\, dq] \exp[-S_G(U) - S_F(\bar{q}, q, U)] \tag{2.18}$$

The evaluation of the partition function by analytical integration is not feasible. However, using Monte Carlo integration and massively parallel processing, it is possible to evaluate Z for small time/spatial grids on the order of $N_t \sim N_s \sim 10$. The

QCD calculation using the lattice is however very costly in both (increasing) size and (decreasing) lattice spacing. Generally, the computational cost behaves as

$$\text{cost} \sim \left(\frac{L}{a}\right)^4 \frac{1}{m_\pi a^2}. \tag{2.19}$$

2.1.2.1 Gauge Actions

Starting with the Wilson line

$$U_\mu(n) \equiv U_{n,n+\mu} = \exp[igaA_\mu(n)] = U^\dagger_{-\mu}(n + \hat{\mu}) \tag{2.20}$$

the "plaquette operator" constructs the most trivial, local gauge invariant operator as

$$U_{\mu\nu}(n) = U_\mu(n) U_\nu(n + \hat{\mu}) U^\dagger_\mu(n + \hat{\mu} + \hat{\nu}) U^\dagger_\nu(n). \tag{2.21}$$

It follows that

$$U_{\mu\nu}(n) = \exp[iga^2 \mathcal{E}_{\mu\nu}(n)] \tag{2.22}$$

where

$$\mathcal{E}_{\mu\nu}(n) = \sum_{a=1}^{N_c^2-1} \frac{\lambda^a}{2} F^a_{\mu\nu} \tag{2.23}$$

denotes the gluon field strength tensor representation in the SU(N_c) algebra. Evaluating the discrete derivative (while keeping track the noncommutative part) gives

$$\mathcal{E}_{\mu\nu}(n) = \frac{1}{a}\{[\mathcal{A}_\nu(n + \hat{\mu}) - \mathcal{A}_\nu(n)] - [\mathcal{A}_\mu(n + \hat{\nu}) - \mathcal{A}_\mu(n)] + ig[\mathcal{A}_\mu, \mathcal{A}_\nu]\} \tag{2.24}$$

Comparing against the gluon action while keeping track of the color factors and the trace gives

$$\lim_{a\to 0} \frac{2N_c}{g^2} \sum_n \sum_{\mu<\nu} \left\{1 - \frac{1}{2N_c} \text{Tr}[U_{\mu\nu}(n) + U^\dagger_{\mu\nu}(n)]\right\} = \frac{a^4}{2} \text{Tr} \sum_{n,\mu,\nu} \mathcal{E}_{\mu\nu}(n) \mathcal{E}_{\mu\nu}(n) \tag{2.25}$$

where the summation over (n, μ, ν) with $\mu < \nu$ is the distinct plaquettes, and therefore the Wilson gauge action is

$$S_G^{\text{SU}(N_c)}[U] = \frac{2N_c}{g^2} \sum_{\text{plaquette}} \left\{1 - \frac{1}{2N_c} \text{Tr}[U_{\mu\nu}(n) + U^\dagger_{\mu\nu}(n)]\right\} \tag{2.26}$$

2.1.2.2 Fermion Actions

Naive discretization the continuum fermion action on the lattice results in the effect of fermion doubling. Wilson fermion action avoids the doubling by introducing a second derivative, chiral symmetry breaking term

$$S_F^{(\mathrm{W})} = S_F - \frac{r}{2}\sum_n \underset{\sim}{\bar{q}}(n)(a^2\Box)\underset{\sim}{q}(n) \tag{2.27}$$

where r is the Wilson parameter. For the fermion fields, we need additionally the following substitution that preserve proper integral measure:

$$\begin{aligned} m &\mapsto \frac{1}{a}m \\ q_\alpha(x) &\mapsto \frac{1}{a^{3/2}}q_\alpha(na) \\ \partial_\mu q_\alpha(x) &\mapsto \frac{1}{a^{5/2}}\partial_\mu q_\alpha(na). \end{aligned} \tag{2.28}$$

The Wilson fermion action

$$\begin{aligned} S_F^{(\mathrm{W})} = {} & (m+4r)\sum_n \underset{\sim}{\bar{q}}(n)\underset{\sim}{q}(n) \\ & -\frac{1}{2}\sum_{n,\mu}[\underset{\sim}{\bar{q}}(n)(r-\gamma_\mu)\underset{\sim}{U}_\mu(n)\underset{\sim}{q}(n+\hat{\mu}) + \underset{\sim}{\bar{q}}(n+\hat{\mu})(r+\gamma_\mu)\underset{\sim}{U}_\mu^\dagger(n)\underset{\sim}{q}(n)] \end{aligned} \tag{2.29}$$

Another widely used alternative is the formulation of the Kogut–Susskind staggered fermion action. This method also removes the fermion doubling via the breaking of chiral symmetry. To obtain the staggered fermion action, a local change of variable is performed, such that on each site, only one field component can be selected and kept.

2.1.2.3 Finite Temperature

Renormalization group on the lattice gives the necessary relation to relate the temperature with the coupling as

$$T \approx \frac{\Lambda_{\mathrm{LAT}}}{N_t}\exp\left[\frac{1}{2\beta_0 g^2(a)}\right] \tag{2.30}$$

where Λ_{LAT} is a scale set by experimental comparison, and β_0 is the one-loop β function. Pressure on the lattice can the be obtained via the pressure

$$P = \frac{T}{V}\ln Z \tag{2.31}$$

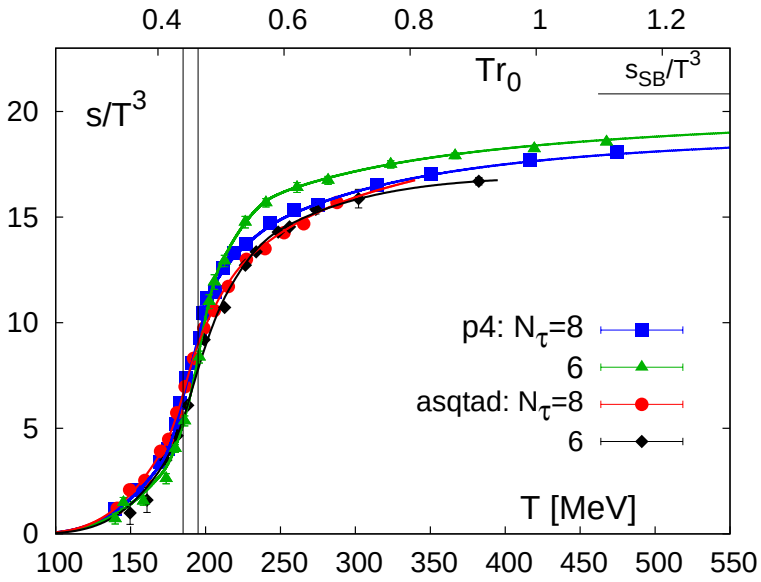

Figure 2.2: Entropy density s divided by the third power of the temperature T as function of T for QCD using lattice calculation and different staggered fermion actions and temporal extents N_τ. The transition temperature region 185 MeV $< T <$ 195 MeV is shown using the two vertical lines, and entropy density in the Stefan–Boltzmann limit s_{SB} is indicated to the right. From [2].

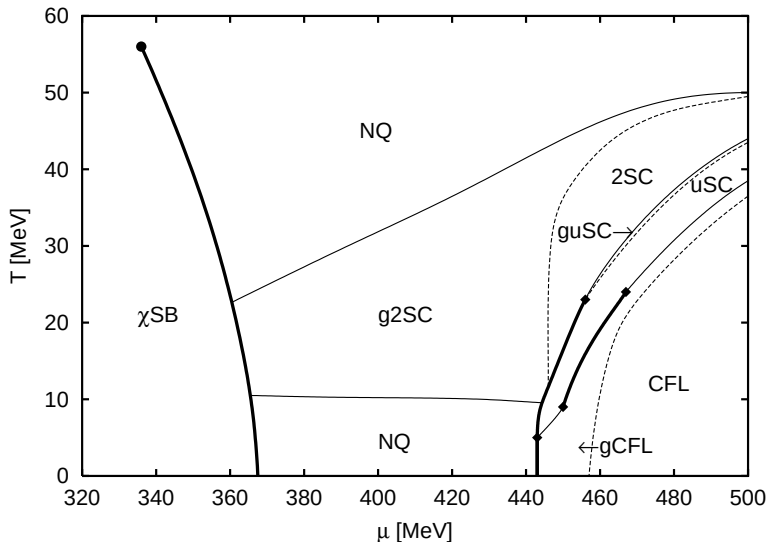

Figure 2.3: The temperature T vs. baryon chemical potential μ phase diagram of three-flavor quark matter using the Nambu–Jona–Lasinio model, from [3]. The phases are: χSB – chiral symmetry breaking, NQ – normal quark, 2SC – two-flavor color-superconducting, uSC – up-quark super-conducting, CFL – color-flavor locked, g2SC – gapless 2SC, guSC – gapless uSC, gCFL – gapless CFL.

and once there, the energy density ε as the crucial indicator of deconfinement is obtained via the entropy

$$\begin{aligned} s &= \frac{\partial P}{\partial T} \\ \varepsilon + P &= sT \end{aligned} \tag{2.32}$$

Figure 2.2 shows a lattice QCD calculation of the entropy density s as function of temperature T, together with the entropy density in the Stefan–Boltzmann limit s_{SB} and the transition temperature region $185\,\mathrm{MeV} < T < 195$ MeV.

2.1.3 The QCD Phase Diagram

Lattice calculation at $\mu_B = 0$ firmly establishes a phase cross over at $T_c \approx 170$ MeV for the $N_f = 3$ and finite quark masses.

Finite baryon chemical potential μ_B in lattice QCD calculation causes imaginary contribution to appear in the fermion actions. This inhibits a direct calculation, and one has to resort to (costly) indirect techniques such as Taylor series expansion or analytic continuation.

The next interesting object in terms of increasing μ_B on the QCD phase diagram is the critical point, which however proved difficult to locate. Lattice results vary from $\mu_B = 200$–700 MeV, while up to $\mu_B = 1.4$ GeV have been obtained by Model-based calculation e.g. using the Nambu–Jona–Lasinio (NJL) model [3].

Figure 2.3 shows the temperature T vs. baryon chemical potential μ phase diagram of three-flavor quark matter using the Nambu–Jona–Lasinio model.

Further along the direction of increasing μ_B, the chiral symmetry broken matter hits a phase boundary at small T. Recent lattice QCD calculation provides a rough estimate for the a phase boundary at $\mu_B \approx 300\,\mathrm{MeV}$.

Due to the difficulty in lattice calculation at high μ_B, little of the $\mu_B > 400$ GeV structure of QCD phase diagram is known. However, the formation of color Cooper pairs resulting in a color-flavor-locked (CFL) phase at very high μ_B, and intermediate phases between the boundary of the χSB and CFL has been predicted using weak coupling QCD, Dyson–Schwinger equation, and the NJL model.

The large μ_B region of the QCD phase diagram is mostly relevant to the study of compact objects, where neutron stars can have core that is a color superconductor, and (depending on the actual location of the phase boundary) possibly QGP can occur shortly after a supernova, when the neutron star is still hot. Quark stars as purely quark matter stellar objects have also been proposed by Itoh 1970 and Witten 1984. Galactic objects such as RX J1856.5–3754 [33], 3C 58 [34], and XTE J1739–285 [35] have been conjectured to be quark stars, although the reliability of the measurement and the underlying model assumptions have been questioned.

But since my measurement is quite far from the large μ_B region, I will not explore the formalisms associated with this QCD phase region further.

2.2 QGP in the Early Universe

The current body of cosmological observational is well explained by the ΛCDM model, which derives its name from its description of the content of the universe using the cosmological constant (Λ) and the cold dark matter (CDM), in addition to baryonic (or "ordinary") matter. Among the six free parameters of ΛCDM are the physical baryon density $100\Omega_b h^2 \approx 2.3$, the physical CDM density $\Omega_c h^2 \approx 0.11$, the cosmological constant $\Omega_\Lambda \approx 0.73$, with the contribution of the cosmological constant and CDM to the geometry of the universe therefore far exceeding that of the ordinary matter ($h = H_0/(100\,\mathrm{km\,s^{-1}\,Mpc^{-1}})$ is the scaled value of the Hubble constant H_0). Metric expansion of space results in the early universe to undergo a phase where $T > T_c$, from which the baryon content in today's universe is formed. The point of time relative to the present universe can be dated by fitting the six ΛCDM parameters against the observational data of the cosmic microwave background (CMB), the baryon acoustic oscillation (BAO), and the Hubble constant H_0. Maximum-likelihood fit using these data dates the quark epoch to be $\tau_0 = 13.76 \pm 0.11\ \mathrm{Gyr} = 4.342 \pm 0.035 \times 10^{17}$ s before present [36]. The one other strong evidence for ΛCDM model is the Big Bang nucleosynthesis (BBN), which is not used to extract cosmological parameters (due to the uncertainty of nuclear reaction cross sections), but for light elements, still reproduces well the observed stellar composition.

Witten proposed early on the possibility of detecting the signature of the cosmological quark phase, if the hadronization is a first order phase transition [37]. Today, it is known from lattice QCD calculation that for $\mu_q = 0$, the SM hadronization occurs via a phase cross over. However, beyond SM scenarios has been proposed where particle properties in the early universe causes $\mu_q > 0$ and thus a first order phase transition can occur. Three large categories of signature has been proposed:

- Relic objects, e.g. strangelets, magnetic fields, black holes
- Density perturbations, e.g. in the cold dark matter
- Primordial gravitational waves

Today, no corresponding relict objects, or have density perturbation been observed. Calculations show that a phase cross over generally results in insufficient perturbation to generate any relic objects or observable

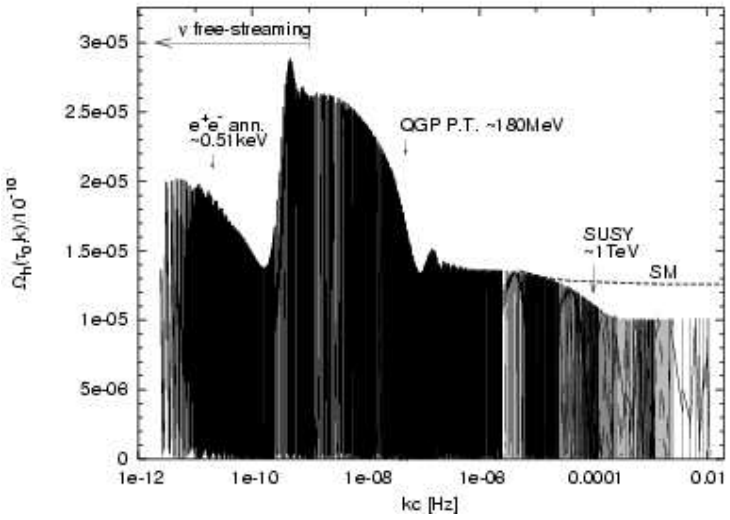

Figure 2.4: The scaled relative spectral density $\Omega_h(\tau_0, k)/10^{-10}$ of the primordal gravitational wave as function of the comoving wave number k (or in the observed frequency at present, $\nu = kc/2\pi$). Arrows indicate the feature in the spectrum due to the electron annihilation, QGP phase transition, and the breaking of supersymmetry (SUSY), where the standard model (SM) spectrum envelope is marked using dashed line. The arrow to the left indicates the envelope when the free-streaming neutrino, that decouples from the photons at $T \approx 2$ MeV, is ignored. From [4].

density fluctuations. Alternatively, constraints for the hadronization can be derived based on the fact that no relic objects or cold dark matter fluctuations have been observed.

Since the hadronization occurred before the recombination, any direct signature of the QGP in early universe lies beyond the surface of last scattering at $T \approx 0.3$ eV, and is therefore inaccessible to electromagnetic detection. This leaves the primordial gravitational wave to be the other signature carried by a long range force. Red shift of the primordial gravitational wave to today would give a detectable signature of the QGP at $\nu \approx 10^{-7}$ s^{-1}. Precise calculations gives the necessary sensitivity for the relative spectral energy density to be $\Omega_h < 10^{-15}$ [4], where the Ω_h is the Fourier transform of the $0, 0$ component of the energy–stress tensor of the gravitational field divided by the critical density of the universe. The necessary sensitivity paired with the extremely low frequency is unfortunately out of the reach with the vibrational background in today's terrestrial interferometers, but satellite-based interferometers have been proposed with a sufficient sensitivity for detection.

Figure 2.4 shows the relative spectral density $\Omega_h(\tau_0, k)$ of the primordal gravitational wave as function of the comoving wave number k, along with the position of the features in the spectrum due to the electron

annihilation, QGP phase transition, and the breaking of supersymmetry (SUSY).

2.3 Jets in Perturbative QCD

The asymptotic freedom of a theory such as QCD allows the short distance interaction in high energy collision to be factorized from the binding structure of hadrons. Two body scattering of quarks and gluons at the center of mass (CM) energy $\sqrt{\hat{s}}$ samples a relative momentum fraction of $x = \hat{s}/s$ of the total scattering CM energy $\sqrt{s}$.

Early deep inelastic scattering (DIS) experiments show that modulo a kinematic factor, the proton structure dependent part of the cross section is a function of mostly x, which is the Bjorken scaling. The (largely) kinematic independence of the proton structure justifies the parton model, where the gluons and valence quark density in momentum space is largely a function of x only. This allows a set of parton distribution functions (PDF) to be derived that empirically describes the nonperturbative structure of hadrons.

However, due to the collinear splitting of quarks and gluons, the PDF has a slow evolution with respect to the momentum transfer Q^2, which is denoted as the scaling violation. This is similar to the QED resummation of logarithmic electron mass enhancement, and can be described using a set of evolution equation derived by Dokshitzer, Gribov, Lipatov, Altarelli, Parisi, and collectively called the DGLAP equation [38].

2.3.1 Leading Order Jet Production

The scattering cross section of the individual parton subprocesses in leading order (LO) is related to the invariant matrix elements $\mathcal{M}$ by isolating the momentum conserving δ function

$$\frac{E_3\, E_4\, d^6\hat{\sigma}}{d^3p_3\, d^3p_4} = \frac{1}{2\hat{s}^2}\frac{1}{16\pi^2}\overline{\sum}|\mathcal{M}|^2\delta^4(p_1 + p_2 - p_3 - p_4). \tag{2.33}$$

The flavor and color averaged square of QCD matrix elements of the relevant subprocesses have been calculated as [39]:

$$q_jq_k \to q_jq_k,\ q_j\bar{q}_k \to q_j\bar{q}_k\ (j \neq k): \quad \overline{\sum}|\mathcal{M}|^2 = \frac{4}{9}\frac{\hat{s}^2 + \hat{u}^2}{\hat{t}^2} \tag{2.34}$$

$$q_j\bar{q}_j \to q_k\bar{q}_k\ (j \neq k): \quad \overline{\sum}|\mathcal{M}|^2 = \frac{4}{9}\frac{\hat{t}^2 + \hat{u}^2}{\hat{s}^2} \tag{2.35}$$

$$q_jq_j \to q_jq_j: \quad \overline{\sum}|\mathcal{M}|^2 = \frac{4}{9}\left(\frac{\hat{s}^2 + \hat{u}^2}{\hat{t}^2} + \frac{\hat{s}^2 + \hat{t}^2}{\hat{u}^2}\right) - \frac{8}{27}\frac{\hat{s}^2}{\hat{u}\hat{t}} \tag{2.36}$$

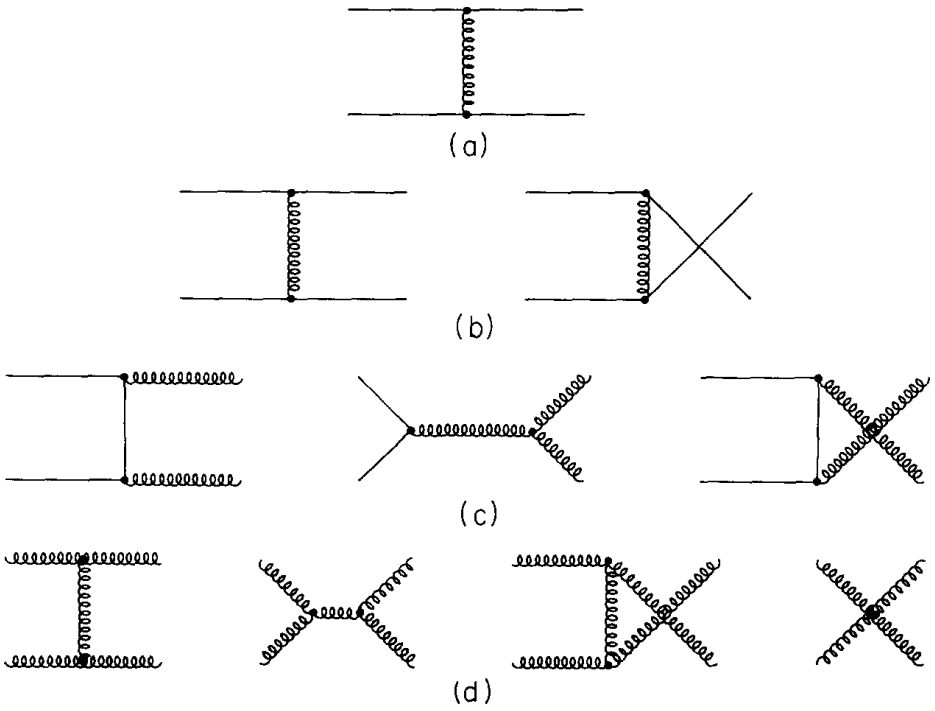

Figure 2.5: Leading order, $O(\alpha_s^2)$ QCD scattering Feynman diagrams, from [5].

$$q_j\bar{q}_j \to q_j\bar{q}_j: \qquad \overline{\sum}|\mathcal{M}|^2 = \frac{4}{9}\left(\frac{\hat{u}^2+\hat{s}^2}{\hat{t}^2}+\frac{\hat{u}^2+\hat{t}^2}{\hat{s}^2}\right)-\frac{8}{27}\frac{\hat{u}^2}{\hat{s}\hat{t}} \tag{2.37}$$

$$q\bar{q} \to gg: \qquad \overline{\sum}|\mathcal{M}|^2 = \frac{32}{27}\frac{\hat{u}^2+\hat{t}^2}{\hat{u}\hat{t}}-\frac{8}{3}\frac{\hat{u}^2+\hat{t}^2}{\hat{s}^2} \tag{2.38}$$

$$gg \to q\bar{q}: \qquad \overline{\sum}|\mathcal{M}|^2 = \frac{1}{6}\frac{\hat{u}^2+\hat{t}^2}{\hat{u}\hat{t}}-\frac{3}{8}\frac{\hat{u}^2+\hat{t}^2}{\hat{s}^2} \tag{2.39}$$

$$qg \to qg: \qquad \overline{\sum}|\mathcal{M}|^2 = \frac{\hat{u}^2+\hat{s}^2}{\hat{t}^2}-\frac{4}{9}\frac{\hat{u}^2+\hat{s}^2}{\hat{u}\hat{s}} \tag{2.40}$$

$$gg \to gg: \qquad \overline{\sum}|\mathcal{M}|^2 = \frac{9}{2}\left(3-\frac{\hat{u}\hat{t}}{\hat{s}^2}-\frac{\hat{u}\hat{s}}{\hat{t}^2}-\frac{\hat{s}\hat{t}}{\hat{u}^2}\right) \tag{2.41}$$

For $p+p$ scattering, the matrix elements have to be convolved with the PDFs to

$$\frac{d^3\sigma}{dy_3\,dy_4\,dp_T^2} = \frac{1}{16\pi^2}\sum_{i,j,k,l=q,\bar{q},g}\frac{f_i(x_1,\mu^2)}{x_1}\frac{f_j(x_2,\mu^2)}{x_2}\overline{\sum}|\mathcal{M}(ij\to kl)|^2\frac{1}{1+\delta_{kl}} \tag{2.42}$$

In the simple form of zero mass quarks, the inclusive jet cross section is the the integration

$$\begin{aligned}\frac{Ed^3\sigma}{d^3p} = \frac{1}{s}\frac{1}{16\pi^2}\sum_{i,j,k,l=q,\bar{q},g}\int_0^1\frac{dx_1}{x_1}\int_0^1\frac{dx_2}{x_2}f_i(x_1,\mu^2)f_j(x_2,\mu^2)\times \\ \times\overline{\sum}|\mathcal{M}(ij\to kl)|^2\frac{1}{1+\delta_{kl}}\delta(\hat{s}+\hat{t}+\hat{u})\end{aligned} \tag{2.43}$$

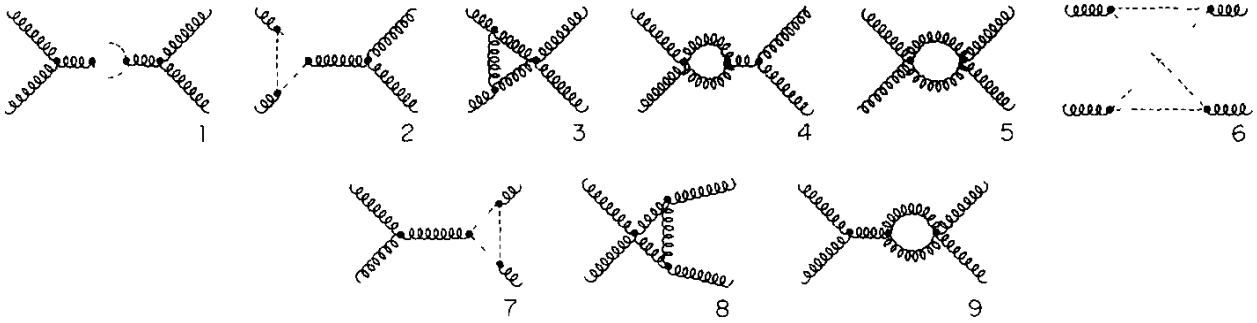

Figure 2.6: Diagrams of the $O(\alpha_s^3)$ virtual corrections to the $gg \to gg$ scattering. From [5].

Figure 2.5 shows the LO Feynman diagrams that contribute to the QCD $2 \to 2$ hard scattering.

2.3.2 Next-To-Leading Order Jet Production

The next-to-leading order (NLO) calculation of jet production includes parton–parton subprocesses to the order $O(\alpha_s^3)$. Key difference to the leading-order calculation arises from the divergences in the loop-integrals, the phase space integration, and practical issues from the computational complexity.

The NLO cross section

$$d\hat{\sigma}_{ij}^{\mathrm{NLO}} = d\hat{\sigma}_{ij}^{\mathrm{virt}} + d\hat{\sigma}_{ij}^{\mathrm{real}} \tag{2.44}$$

consists of $d\hat{\sigma}_{ij}^{\mathrm{virt}}$ being the $O(\alpha_s^3)$ one loop virtual corrections to the tree level diagrams for the Born amplitude, and $d\hat{\sigma}_{ij}^{\mathrm{real}}$ as the real $n = 2$ plus one parton emission on top of the Born amplitude. For the virtual contributions, the $O(\alpha_s^3)$ cross section arises from interference terms of one LO diagram with one NLO diagram. As an example, figure 2.6 shows the diagrams of the virtual correction to the $gg \to gg$ scattering, and figure ... lists the $O(\alpha_s^3)$ interference topologies. The NLO $2 \to 2$ and $2 \to 3$ matrix elements are usually too extensive to perform purely manually, and typically computer algebra systems are being used. And since their algebraic results are also too unwieldy to be reproduced in their entirety here, and readers are referred to ....

As illustration, figures 2.6 and 2.7 show the $gg \to gg$ part of the NLO Feynman diagrams and interference terms to the amplitudes, that contribute to the virtual correction of the QCD $2 \to 2$ hard scattering.

The two sets of NLO matrix elements by themselves diverge in $d = 4$ dimensions. Individual virtual correction diagrams contain ultraviolet (UV), infrared (IR) and collinear divergences. The existence of UV divergences is intrinsic to the short distance behavior of the field theory and can be absorbed by subtraction

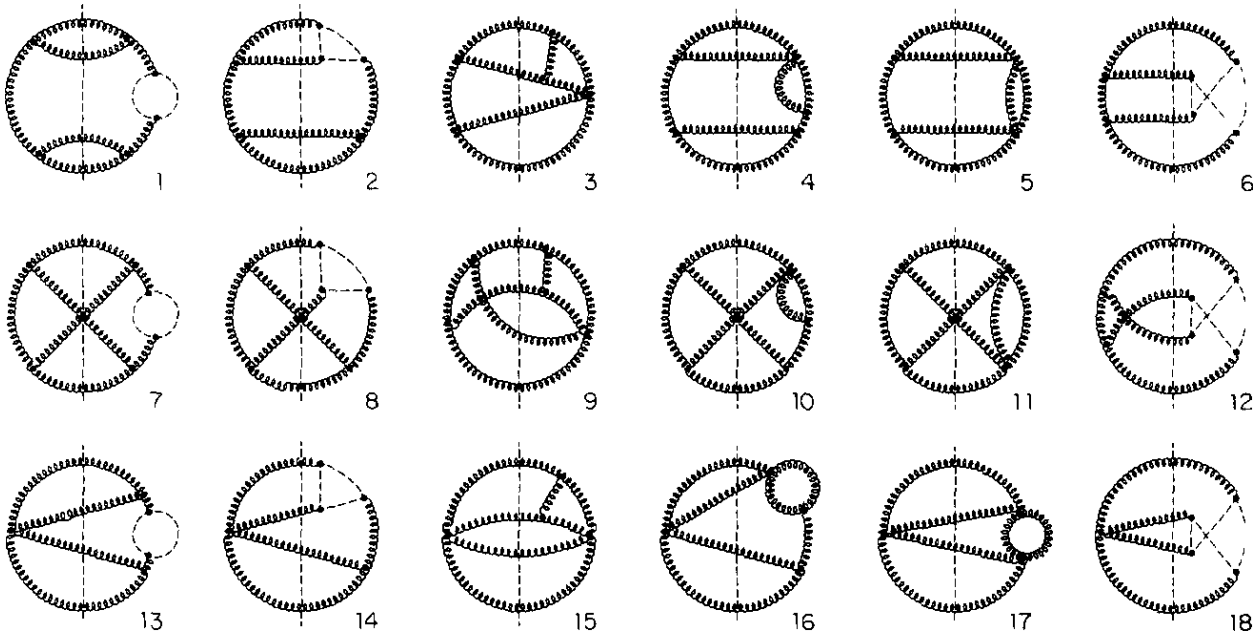

Figure 2.7: Independent topologies for the $gg \to gg$ virtual correction amplitudes. From [5].

using the given renormalization scheme. (Disregard for a moment the initial state IR divergence) the IR and collinear divergences in the virtual correction cancel with their $n+1$ diagram counterparts that arises during the $(n+1)$-body phase space integration (the Kinoshita–Lee–Nauenberg theorem [40]). The existence of these phase space divergences can be illustrated by e.g. examining the interference topology for the off-shell decay part $g^* \to q\bar{q}g$ of the NLO jet production diagrams. Figure 2.8 shows this interference term. The two quark propagators give rise to the factor

$$\begin{aligned} \frac{1}{(p_1+p_3)^2}\frac{1}{(p_2+p_3)^2} &= \frac{1}{s^4}\frac{1}{(1-x_1)(1-x_2)} \\ &= \frac{1}{s^4}\frac{1}{x_3}\left(\frac{1}{1-x_1}+\frac{1}{1-x_2}\right) \end{aligned} \tag{2.45}$$

The limits $x_1 \to 1$ or $x_2 \to 1$ represent the collinear divergences, while $x_3 \to 0$ is the IR divergence. Only remaining now is the initial state IR divergence, which is absorbed into the PDF ("mass factorization") [41].

When performing the phase space integration analytically, these divergence can be dimensionally regularized by going into $d = 4 - 2\epsilon$ dimensions, and the single or double poles/logarithms cancel for physical quantities. But generally, for $N \geq 3$ final states, the analytical phase space integration is algebraically difficult, and a Monte Carlo integration is therefore often preferred. And for jet production calculations, this approach further allows the final state to be defined using jet reconstruction algorithms. For Monte Carlo phase space

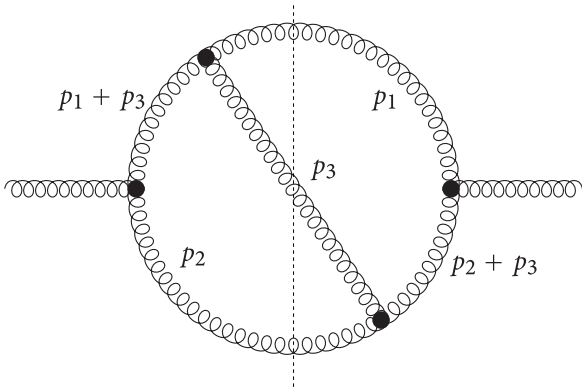

Figure 2.8: An interfering diagram of the 3-body $g^* \to q\bar{q}g$ decay with the two three-body divergence propagators $(p_1 + p_3)^{-1}$ and $(p_2 + p_3)^{-1}$.

integration, two main methods have been developed. The phase space slicing (PSS) [42] splits the divergent integral into small region around IR and collinear poles that can be approximated analytically, and will contain dimensional poles in ϵ and logarithms in the cutoffs δ_s, δ_c. The remaining regions are integrated numerically, which will give a finite but cutoff dependent result. Using a 1-dimensional example,

$$I = \int_0^1 dx\, x^{\epsilon-1} f(x) \tag{2.46}$$

for $\delta \ll 1$ can be approximated by

$$\begin{aligned} I &\approx f(0) \int_0^\delta dx\, x^{\epsilon-1} + \int_\delta^1 dx\, x^{\epsilon-1} f(x) \\ &= \frac{f(0)}{\epsilon} + f(0) \log \delta + \int_\delta^1 \frac{dx}{x} f(x). \end{aligned} \tag{2.47}$$

Therefore, for sufficiently small δ_s, δ_c, this approximation "converges" to the actual, finite part plus any divergences, while the divergences are confined in the analytically integrated region and cancel. The Catani–Seymour subtraction method [43] schematically introduces a cancellation term

$$d\hat{\sigma}_{ij}^{\text{sub}} = \sum_{\text{dipole}} d\hat{\sigma}_{ij}^{\text{LO}} \otimes dV_{ij,k} \tag{2.48}$$

such that $d\hat{\sigma}_{ij}^{\text{sub}}$ is one parton phase space integrable, with the splitting function $V_{ij,k}$ embodying the contribution of introducing an additional leg k into the diagram. Catani and Seymour derived a set of process-independent expression for $V_{ij,k}$. Then, (2.44) phase space integrated becomes (modulo the initial state divergence)

$$\hat{\sigma}_{ij}^{\text{NLO}} = \int_{S^{n+1}} \left(d\hat{\sigma}_{ij}^{\text{virt}} - d\hat{\sigma}_{ij}^{\text{sub}} \right)_{\epsilon \to 0} + \int_{S^n} \left(d\hat{\sigma}_{ij}^{\text{real}} + \int_{S^1} d\hat{\sigma}_{ij}^{\text{sub}} \right)_{\epsilon \to 0} \tag{2.49}$$

and both integrals are finite, and therefore can be directly evaluated using Monte Carlo techniques. The NLO event generator JETRAD is an example of Monte Carlo integration using PSS, while JETRAD++ implements the Catani–Seymour subtraction method.

The absorption of the initial state divergence into the PDF is done by the defining the scale independent PDF (e.g. [43; 44])

$$\tilde{f}(a,x;\epsilon,\mu_F^2) = \sum_b \int \frac{dz}{z} f(b,x/z)\left[\delta_{ab}\delta(1-z) - \frac{(4\pi\mu^2/\mu_F^2)^\epsilon}{\epsilon\Gamma(1-\epsilon)}\frac{\alpha_s}{2\pi}P_{a/b}^{(1)}(z) + K_{a/b}(z) + O(\alpha_s^2)\right] \quad (2.50)$$

which is essentially the DGLAP evolution, only with an additional $(4\pi\mu^2/\mu_F^2)^\epsilon/\Gamma(1-\epsilon)$ phase space factor to allow it to absorb the $d-2$ angular integration of the additional emission. The finite correction term $K_{a/b}(z)$ is renormalization scheme dependent, and for the $\overline{\text{MS}}$ scheme, $K_{a/b}(z) = 0$. The resulting NLO cross section is finite, but depends on the factorization scale. Therefore, for the validity of NLO results, the sensitivity to the factorization scale must be checked. Typically, the residual factorization scale dependence due to is determined by a scan of cross section at $\mu_F = \frac{1}{2}\max p_T^{\text{jet}}$, $\mu_F = \max p_T^{\text{jet}}$, and $\mu_F = 2\max p_T^{\text{jet}}$, and quoted as the systematic uncertainty of the NLO calculation.

2.3.3 Units

After momentum integration in the (particle physics) natural unit system with $\hbar = c = 1$ and GeV, the obtained cross section is expressed in GeV^{-2}. To obtain a cross section in the SI derived barn, this has to be multiplied by the additional factor $\hbar^2c^2/(\text{GeV b})$, which is numerically the inverse of the the Josephson constant $K_\text{J} = 2e/h$ modulo exact constants, and is presently also best constrained by measurements using the Josephson effect [45]. CODATA 2010 [46] global fit results in the equivalent values

$$\begin{aligned} K_\text{J} &= 483\,597.870 \pm 0.011\ \text{GHz V}^{-1} \\ \hbar c &= 197.326\,971\,8 \pm 0.000\,004\,4\ \text{MeV fm}, \end{aligned} \quad (2.51)$$

which gives

$$\hbar^2c^2 = 389\,379.338 \pm 0.017\ \text{GeV}^2\,\text{nb}. \quad (2.52)$$

2.4 Jet Fragmentation

Quenched lattice QCD calculation shows that unlike QED, the $q\bar{q}$ binding potential changes from approximately Coulomb into being proportional to the separation. While the quenched QCD does not contain

dynamic light quarks to act to produce screening effects, full QCD calculation on the lattice indeed show that the $q\bar{q}$ potential in fact does not increase indefinitely, but rather quickly level off beyond 1 fm separation [47].

In the discussion of jet production we have seen that the QCD production cross section factorizes into schematically the convolution

$$\sigma_{p+p\to\text{jets}} = f_{\text{parton}/p}(x, Q^2) \otimes \sigma_{\text{parton}}(Q^2) \tag{2.53}$$

QCD factorization also separates the nonperturbative, long distance interaction in forming the hadrons, and the hadronic cross section becomes

$$\sigma_{p+p\to h+X} = f_{\text{parton}/p}(x, Q^2) \otimes \sigma_{\text{parton}}(Q^2) \otimes D_{h/\text{parton}}(z, Q^2) \tag{2.54}$$

with $D(z, Q^2)$ being the fragmentation function.

Similar as the parton distribution function $f(x, Q^2)$, the fragmentation function exhibits scaling violation due to parton splitting, and therefore also evolves according to the DGLAP equation. Since $D(x, Q^2)$ cannot be derived from perturbation theory and has to be measured at a specific scale, and is typically parametrized in the form

$$D(x, Q_0^2) = Nx^{\alpha}(1-x)^{\beta}\left(1 + \frac{\gamma}{x}\right) \tag{2.55}$$

2.4.1 Lund string model

The Lund string model is an model of fragmentation based on the observation that in the absence of dynamic quarks and screening effects, the far field $q\bar{q}$ binding potential is approximately proportional to the separation. While this observation and motivation of the Lund model was originally due to meson mass spectra, this behavior can be made today rigorously using quenched QCD calculations on the lattice.

As q and $\bar{q}$ move apart, the potential energy in the string increases, and break with the production of a pair $\bar{q}'$ and q', where the mechanism of the string breaking motivated by a tunneling process. Each of the created quarks therefore having a Gaussian m_T spectrum, which also causes a suppressed heavy quark production. The split bound with the original string now become $q\bar{q}'$ and $q'\bar{q}$. In the Lund string model, strings can additionally have gluon "kinks", i.e. a configuration $qg\ldots g\bar{q}$, with the gluons ultimately split into diquarks. Baryon production can be either modeled by splitting by diquarks $q\bar{q} \to qq'q'' + \bar{q}''\bar{q}'\bar{q}$, or the popcorn model, where virtual color fluctuation appear on the string $q\bar{q} \to qq'\bar{q}'\bar{q}$, and a later string breaking creates two three-quark configurations. Depending whether the string breaking continues until only on-shell hadrons are left, with these hadron being a string strip with two quarks at each end.

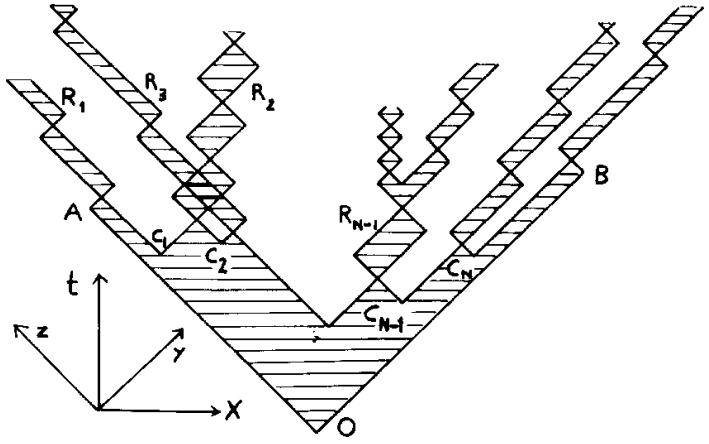

Figure 2.9: Diagram of string fragmentation, where the "repetition of strips" indicate string dynamics, and C_i and R_i are the first generation cuts and resonances. From [6].

The fragmentation function modeled by the Lund model is itself controlled by the scaling function

$$f_{\alpha\beta}(z, m_{h,\perp}^2)dz = N_{\alpha\beta}\frac{dz}{z}z^{a_\alpha}\left(\frac{1-z}{z}\right)^{a_\beta}\exp\left(-\frac{bm_{h,\perp}^2}{z}\right) \tag{2.56}$$

which describes the probability to find a hadron containing the original quark. The transverse mass term in the Gaussian broadening term is $m_\perp^2 = m^2 + p_\perp^2$. The index α, β potentially allows a differing quark vs. diquark scaling, although it is not needed to describe the present data. Since the normalization N is fixed by the exponent a via the normalization $\int_0^1 dz\, f_{\alpha\beta}(z, m_{h,\perp}^2) = 1$, this leaves only the a (PARJ(41) in PYTHIA/JETSET), b (PARJ(42)) as the free parameters of the Lund model. Phenomenologically, there is no need to select flavor dependent scaling. Fits to ALEPH, L3, and OPAL data show that $a \approx 0.11$–0.50, and $b \approx 0.34$–0.9 GeV^{-2}, while $a = 0.30$, $b = 0.58$ GeV^{-2} is the PYTHIA/JETSET default.

Figure 2.9 shows a diagram of string fragmentation.

2.4.2 Cluster fragmentation

The cluster fragmentation is a method of forcibly splitting the parton via QCD branching, and iteratively perform cluster fissions. While the intermediate color connections can be regarded as group theoretic strings, there is no string dynamics in the cluster fragmentation. Notably, the event generator HERWIG (Hadron Emission Reactions With Interfering Gluons) implements the cluster fragmentation scheme.

Free parameters in the cluster fragmentation are the effective gluon mass during hadronization M_g (variable RMASS(13) in HERWIG), and the maximum cluster mass parameter $M_{\max}$ (CLMAX). And additional pa-

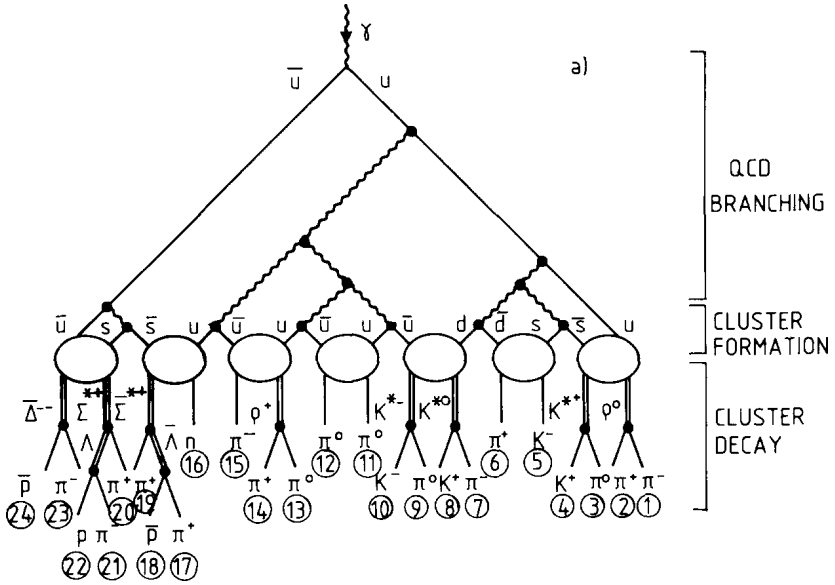

Figure 2.10: Diagram of cluster fragmentation, showing the temporal evolution from the formation of color singlet clusters and decay to resonances. From [7].

rameter CLPOW $= 2$ has effect on the ratio of heavy to light quarks, and is mostly left unchanged in tunes.

The string fission of clusters is controlled by the mass scale M_f, with clusters having a mass

$$M_C > M_f^{\text{CLPOW}} = M_{\text{max}}^{\text{CLPOW}} + (m_1 + m_2)^{\text{CLPOW}} \tag{2.57}$$

split into either $u\bar{u}$, $d\bar{d}$, $s\bar{s}$. The masses m_1, m_2 are that of the original quarks. ALEPH, L3, and OPAL fits show that $M_g \approx 0.65$–0.83, and $M_{\text{max}} \approx 3.00$–$3.78\,\text{GeV}^{-2}$. At the end of cluster fragmentation, clusters have the quark content of the form $q_1\bar{q}_2$. A nondynamic quark/antiquark flavor pair $q_3\bar{q}_3$ or diquark pair $d_3\bar{d}_3$ is chosen at random to decay the cluster via two-meson or baryon/antibaryon decay.

Figure 2.10 shows a diagram of the temporal sequence of cluster fragmentation.

2.5 Jet Phenomenology

Particle production with a p_T spectrum deviating from a thermal shape was first observed at the CERN Intersecting Storage Ring (ISR) at $\sqrt{s} = 63\,\text{GeV}$. The first experiment that attempted to reconstruct jet using a clustering algorithm was the British–French–Scandinavian Collaboration at the Split Field Magnet (SFM). Two methods were developed, Since jet production at such a low $\sqrt{s}$ is exceedingly rare, direct measurement of jets at the ISR proved to be difficult until calorimetric triggering capabilities on jets was developed.

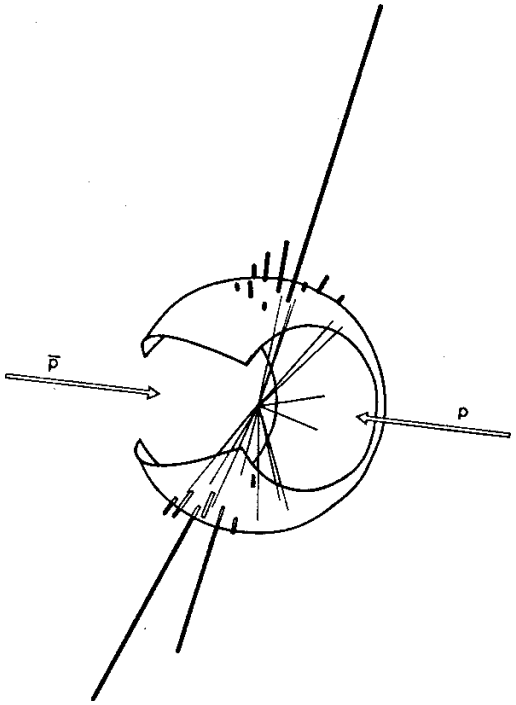

Figure 2.11: Event display of a dijet with 57 and 60 GeV taken by the UA2 experiment, from [8].

The Axial Field Spectrometer (AFS) triggered on high E_T clusters in the event using two limited acceptance ("floor" and "roof") U–Cu hadronic calorimeter (where the fission compensation in U results in a nearly equal response to electromagnetic energy). The tower energy is used directly as the "jet energy", and no clustering has been attempted [48]. The CERN–Columbia–Oxford–Rockefeller Collaboration (CCOR) triggers using a Pb glass electromagnetic calorimeter [49]. In the early 1980s, the opinion regarding the existence of jets in high energy collisions remained widely skeptical. Both the Aachen–Berlin–CERN–Cracow–London–Vienna–Warsaw Collaboration (ABCCLVW) [50] using the Big European Bubble Chamber (BEBC) and the Bari–Krakow–Liverpool–Max Planck Institute Munich–Nijmegen Collaboration using a [51] showed little jet-like structure.

While the previous attempts to see a jet signal has been mostly statistical, the increased energy at SPS allowed the UA1 and UA2 experiment to make the clear observation of jet structure in single events, in addition to the measurement of jet cross section and jet fragmentation functions. Scattering at TeV scale by the Tevatron further enhanced the access to jet signal, in term of integrated luminosity and the enhanced yield that comes with the collision energy. This produced a large body of precision jet measurement as tests for QCD.

Figure 2.11 shows a dijet event with a 57 and a 60 GeV by the UA2 experiment.

2.6 Perturbative Energy Loss

The perturbative model of parton energy loss is based on the processes of gluon scattering with the medium. "Radiative" energy loss describes inelastic scattering with static scattering centers, as opposed to "collisional" energy loss with elastic scatterings.

2.6.1 BDMPS-Z

In the 1950s, high energy electron–nucleus scattering revealed that coherent multiple scattering causes destructive interference and therefore suppresses the bremsstrahlung, which is also knwon as the Landau–Pomeranchuk–Megdal (LPM) effect. M. Gyulassy and X.-n. Wang were the first to derive the non-Abelian equivalent of the LPM effect [52]. Radiative energy loss is enforced by introducing static scattering scenters that are screened by one gluon exchange. In the original Gyulassy–Wang model, quarks emit gluon only once and subsequently do not further interact with the medium.

The Baier–Dokshitzer–Mueller–Peigne–Schiff–Zakharov (BDMPS-Z) model [53] provides an full tretment of the multiple soft scattering by considering the quark rescattering contribution.

The medium is considered as thick, as the mean free path $\lambda_g \gg \mu^{-1}$, with μ being the screening mass. In the static medium approximation, the gluon radiation cross section corresponds to a harmonic oscillator. The rescattering as Brownian motion is described by the path integral

$$\mathcal{H} = \int \mathcal{D}\mathbf{r} \exp\left\{ i \int d\xi \left[\frac{i\omega}{2}\dot{\mathbf{r}} - \frac{1}{2} n(\xi)\sigma(\mathbf{r}) \right] \right\} \tag{2.58}$$

where $n(\xi)$ is the density of rescattering centers and $\sigma(\mathbf{r})$, and in dipole approximation

$$n(\xi)\sigma(\mathbf{r}) = \frac{1}{2}\hat{q}(\xi)\mathbf{r}^2, \tag{2.59}$$

and $\hat{q} = \mu^2/\lambda_g$ is the transport coefficient. Since the coherence length is $L > \sqrt{2\omega\lambda_g/\mu^2}$, $\omega < \frac{1}{2}\hat{q}L$.

Evaluating the BDMPS-Z energy loss in the leading log approximation gives

$$-\frac{dE}{dz} = \frac{\alpha_s C_R}{8}\frac{\mu}{\lambda_g}L^2 \log\left(\frac{L}{\lambda_g}\right) \tag{2.60}$$

Comparison of BDMPS-Z energy loss with the RHIC neutral hadron suppression data consistently produce a large transport coefficient in the range of $\hat{q} \approx 5$–15 GeV^2/fm.

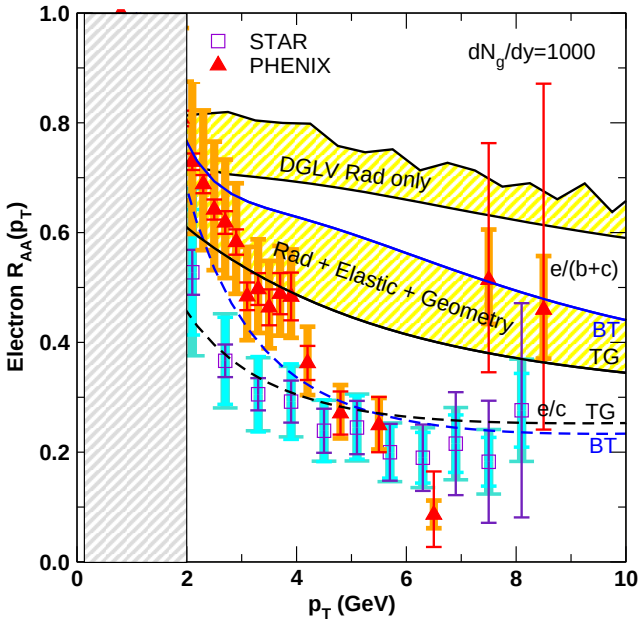

Figure 2.12: The RHIC nonphotonic electron nuclear modification factor compared to the energy loss predicted by the Wicks–Horowitz–Djordjevic–Gyulassy model, from [9].

2.6.2 GLV

Unlike BDMPS-Z and multiple soft scattering, the Gyulassy–Lévai–Vitev (GLV) models [54] describes the QGP using N color screened Yukawa potentials, that are separated in the sense $\lambda_g \gg \mu^{-1}$.

The opacity expansion then can be realized via two reaction operators: Operator $\hat{D}$ is for one gluon exchange with color and momentum exchange, plus a non-interacting gluon emission. $\hat{V}$ is for a virtual double exchange that leaves the parton color and momentum intact. The double Born terms are needed for the purpose of unitarity.

To the first order in opacity, the medium induced energy loss in the leading log approximation is

$$-\frac{dE^{(1)}}{dz} = \frac{\alpha_s C_R}{N(E)}\frac{\mu}{\lambda_g}L^2 \log\left(\frac{E}{\lambda_g}\right) \tag{2.61}$$

Here, $N(\infty) = 4$ if there are no kinematic constraints, but $N(E) = 10.1$ is given for $E = 50$ GeV jets. Numerical evaluation of $\frac{dE^{(2)}}{dz}$ shows that the series converges rapidly except for high opacity of $L/\lambda_g > 4$ and at the SPS energy. This kinematic constraint is also found to suppress the dE/dz compared to BDMPS-Z for RHIC and SPS energies.

The originally massless GLV opacity expansion was extended to describe heavy quark energy loss by

M. Djordjevic (DGLV) [55], where the effect of having a finite mass is found to cause a frequency shift. The Wicks–Horowitz–Djordjevic–Gyulassy (WHDG) energy loss [9] further extends the radiative DGLV calculation by the elastic energy loss from E. Braaten, M. H. Thoma, and M. Gyulassy [56]. This is then combined with the path length dependence due to geometry fluctuation to describe the RHIC data on the suppression of nonphotonic electrons.

Figure 2.12 shows a comparison of the RHIC nonphotonic electron nuclear modification factor to the WHDG energy loss calculation.

There are a few other PQCD based formalisms to calculate the parton–medium interaction. The finite temperature field theory approach by P. Arnold, G. Moore, and L. Yaffe (AMY) uses hard thermal loops (HTL) to model both the jet propagation and medium feedback. The main caveat of AMY is however, that the medium is weakly coupled. Also, flavor changing inside the medium is not modelled. The higher twist (HT) approach resums power corrections to the leading twist cross section, and derives a medium-modified fragmentation function for the leading hadron, from which single particle suppression can be obtained. There is no medium backscattering or flavor changing. Unfortunately, the setup is at a poor position to serve a predictor for partonic/jet energy loss, or that of the nonleading particles.

A crucial test of the consistency among PQCD approaches is the medium property extraction. For GLV, the range obtained is $\hat{q} \approx 3\ \mathrm{GeV}^2/\mathrm{fm}$, which is in reasonable proximity of the $\hat{q} \approx 2\ \mathrm{GeV}^2/\mathrm{fm}$ with the HT and $\hat{q} \approx 4\,\mathrm{GeV}^2/\mathrm{fm}$ with the AMY formalism. However, these three formalism stand in stark contrast to the result from BDMPS-Z.

2.7 AdS/CFT Energy Loss

Unlike $d = 4$ field theory, the elementary perturbative object in the string theory are open and closed strings. These are world sheet that can be parametrized as $X^\mu(\sigma, \tau)$, with σ and τ being the spatial and temporal variables of parametrization, which are not physical. When quantizing bosonic strings, the Faddeev–Popov ghosts give rise to a central charge $c = -26$. In order to preserve the conformal symmetry $c = 0$ must hold. This can be established by introducing d scalar fields, therefore making $d = 26$ the critical dimension. However, bosonic strings suffer from the existence of tachyon, which cannot be fixed by the choice of d.

The existence of the tachyon in string theory is fixed by the introduction of supersymmetry (SUSY). In the traditional SM representation of fields, internal degrees of freedom cause quantized fields to commute

or anticommute according to the spin-statistics theorem. These two algebras can be combined into a Lie superalgebra by Z_2-grading [57]. The fermionic degrees of freedom can be introduced either as world-sheet (Ramond–Neveu–Schwarz formalism [58]) or space-time supersymmetry (Green–Schwarz [59] and the pure spinor [60] formalisms), which are equivalent. For the supersymmetric or super strings, there are additional 11 superconformal ghosts, bringing down the central charge to $c = -15$. Existence of the supersymmetric degrees of freedom means that physical fields contribute as $\frac{3}{2}d$, resulting in a critical dimension of $d = 10$.

From closed strings states, 35 states of $d = 10$ gravitons, 28 Kalb–Ramond (a tensorial generalization of the Maxwell field), and one dilaton (a scalar field lacking a QFT analog, which controls the coupling) are universal to any string theory. Choice of symmetric and antisymmetric boundary conditions for the fermionic degrees of freedom splits the each of the left/right moving direction of modes into the Ramond (R, symmetric) and Neveu–Schwarz (NS, antisymmetric) sectors.

Open strings must satisfy either the Neumann (N) or Dirichlet (D) boundary condition (but they can be mixed, i.e. with the two endpoints, strings can satisfy either of the NN, ND, DN, and DD boundary conditions). The imposed p degrees of freedom of a Dirichlet boundary condition can be thought as moving along a Dp brane. Since Dp branes can emit closed string by converting the brane-bound open strings to freely moving, closed strings, the Dp brane can be considered as a nonperturbative object that can interact with strings.

Five types of $d = 10$ consistent supersymmetric string theories are known: type I (unoriented), type IIA/B (left-moving/right-moving open superstrings), and the $E_8 \times E_8$ and SO(32) heterotic (left-moving bosonic, right-moving supersymmetric). Heterotic string theories do not have open strings and therefore no Dp branes at all. Type II string theories are produced by combining left/right moving modes with while requiring the existence of the R–NS type (otherwise, the type 0 is obtained, which contains a tachyon). Type IIA and IIB are distinguished by the sign choice in one of the motion direction, e.g. the right-moving (NS+, R±) and (R+, R±) (choosing this to the left moving modes gives the reflected IIA′, IIB′, which are physically the same), while IIB in that case corresponds to the choice of identical Ramond sectors. This has implications of R–R bosons and therefore stable Dp branes. Type IIA permits stable D0 and D2 branes, while type IIB D7, D1, and D3 branes. The unoriented type I string theory is obtained by orientifolding IIB, and only D1, D5, D9 branes are stable.

2.7.1 The AdS/CFT Conjecture

The AdS/CFT correspondence is an example of the holographic principle that appears in the supergravity. The dynamics of the string theory on the asymptotically AdS space times a manifold is equivalent to the CFT on the conformal boundary, which is given by the vanishing Weyl tensor. In the case of $\mathrm{AdS}_5 \times S^5$, the type IIB string theory is equivalent to the dynamics of the D3 branes on the boundary, which forms $\mathcal{N} = 4$ super Yang–Mills (SYM) theory of stacked D3 branes.

The $\mathcal{N} = 4$ SYM field is the supersymmetric $\mathrm{SU}(N_c)$ gauge theory, with $\mathcal{N}$ counting the four spinor supercharges, which is also the maximally possible supersymmetry without including supergravity. The $\mathcal{N} = 4$ SYM contains as gauge multiplets: a gauge field A_μ (the gluon), four left Weyl fermion fields $\lambda^1_\alpha, \ldots, \lambda^4_\alpha$ (the gluinos), and six scalar fields $X^1, \ldots, X^6$. Poincaré and scale invariance combines into a $\mathrm{SO}(2,4) \sim \mathrm{SU}(2,2)$ group, which again is combined with the $\mathcal{N} = 4$ Poincaré supersymmetry into the superconformal group $\mathrm{SU}(2,2 \mid 4)$.

Despite a lack of rigorous proof, the AdS/CFT correspondence can be tested by a comparison of the symmetries. In that case, the isometry in $\mathrm{AdS}_5 \times S^5$ turns out to be also of the superconformal group $\mathrm{SU}(2,2 \mid 4)$.

The AdS black hole metric in the light cone coordinates $(r, x^\pm, x_2, x_3)$ and in the Minkowski coordinates (r, t, x_1, x_2, x_3) is

$$\begin{aligned} ds^2 &= -\left[\frac{r^2}{R^2} + h(r)\right] dx^+ dx^- + \frac{1}{2}\left[\frac{r^2}{R^2} - h(r)\right][(dx^+)^2 + (dx^-)^2] + \frac{r^2}{R^2}(dx_2^2 + dx_3^2) \\ &\quad + \frac{1}{h(r)} dr^2 \\ &= -h(r)dt^2 + \frac{r^2}{R^2}(dx_1^2 + dx_2^2 + dx_3^2) + \frac{1}{h(r)} dr^2 \end{aligned} \tag{2.62}$$

where

$$h(r) \equiv \frac{r^2}{R^2}\left(1 - \frac{r_H^4}{r^4}\right) \tag{2.63}$$

and R is the curvature of the AdS space, which is related to the 't Hooft coupling

$$\sqrt{\lambda} = \frac{R^2}{\alpha'} \tag{2.64}$$

with $T_0 \equiv (2\pi\alpha')^{-1}$ being the string tension. The radius r_H is related to the both the Hawking temperature of the black hole and the temperature of the d-dimensional SYM via

$$T_H = \frac{r_H d}{4\pi R} \tag{2.65}$$

Two independent, AdS/CFT-based methods to calculate jet quenching phenomenology have emerged. Herzog *et al.* use a open string with one endpoint describing a heavy quark to evaluate the full medium interaction, represented by the AdS black brane [61]. Liu *et al.* invoke a $k_\perp$ broadening analogy to describe the radiative part of the energy loss [62].

2.7.2 Wilson Loop Approach

The approach by H. Liu, K. Rajagopal, and U.A. Wiedemann calculates the radiative energy loss via a timelike Wilson loop. The Wilson loop corresponds to the propagation of a $q\bar{q}$ system on the AdS_5 boundary, and its screening by the black hole background. Using the simple setup of a D3 brane at the conformal boundary, no attempts in mimicking the QCD N_c and n_f is attempted, and the goal is to find a $\hat{q}$ that is hopefully universal among strongly interacting theories.

In the high energy limit $\omega \to 0$, the Wilson loop corresponds to the exponentiating the BDMPS-Z rescattering (2.58) along the scattering length $\Delta z = L^-/\sqrt{2}$, and the becomes

$$\langle W^A(\mathscr{C}_{\text{light-like}})\rangle = \exp\left[\frac{1}{4\sqrt{2}}\hat{q}L^- L^2\right] \tag{2.66}$$

which provide a Wilson loop based definition of the transport coefficient $\hat{q}$.

The next step is to obtain a equation of motion for the extremal world sheet that describes the $q\bar{q}$ system.

$$y' = \frac{1}{q}\sqrt{(y^4-1)(y^4-y_c)}, \quad y_c^4 \equiv \cosh^2\eta + q^2 \tag{2.67}$$

where q is a constant of integration. The nontrivial solution corresponds to a string that starts on the D3 brane, descends, and touches the AdS black hole event horizon, and returns to the D3 brane. Inserting this into the action and compare with the Wilson loop gives

$$\hat{q}_{\text{SYM}} = \frac{\pi^2}{a}\sqrt{\lambda}T^3 = \frac{\pi^{3/2}\Gamma(3/4)}{\Gamma(5/4)}\sqrt{\lambda}T^3 \approx 26.69\sqrt{\alpha_{\text{SYM}}N_c}T^3 \tag{2.68}$$

Inserting a realistic condition, such as with $N_c = 3$, $\alpha_s = 0.5$, and $T = 300$MeV, gives a $\hat{q}_{\text{SYM}} \approx 4.5\text{GeV}^2/\text{fm}$, which is between the $\hat{q}$ from the group of GLV, AMY and HT formalisms, and that of BDMPS-Z.

The crucial, and experimentally (given a suitable detector) accessible prediction from the AdS/CFT energy loss is a strongly different suppression behavior than PQCD with respect to light versus heavy quark flavors. The heavy versus light quark jet suppression therefore can be regarded as an indicator for the PQCD versus strongly coupled jet suppression in heavy ion collisions. The sensitivity is particularly pronounced at the LHC energies, but is still accessible at RHIC. However, due to the lack of vertex detector, this prediction unfortunately could not be explored in this thesis.

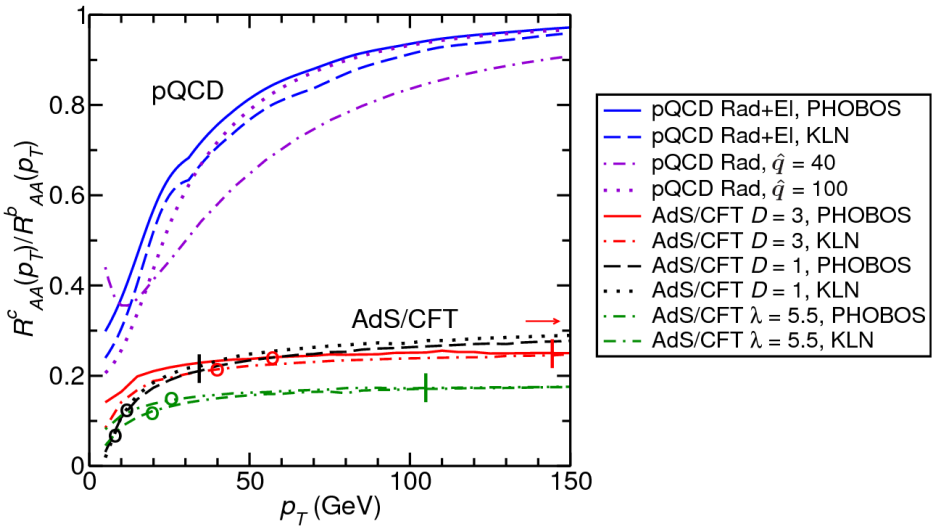

Figure 2.13: Charm quark to bottom quark nuclear modification factor double ration for the LHC comparing the Wicks–Horowitz–Djordjevic–Gyulassy and AdS/CFT string drag energy loss. From [10].

2.7.3 String Drag Approach

The string drag approach describes the full energy loss using a D3/D7 brane intersection, where the M D7 branes are introduced as flavor probes. Quarks are modeled as string that connects the AdS black hole with a D7 brane.

The string motion solves to

$$x(r,t) = x_0 + vF(r) + vt \tag{2.69}$$

where $F(r)$ parametrizes the curved string that is being dragged behind the moving quark

$$F(r) = \frac{1}{2r_H}\left[\frac{\pi}{2} - \tan^{-1}\left(\frac{r}{r_H}\right) - \cot^{-1}\left(\frac{r}{r_H}\right)\right] \tag{2.70}$$

In the large mass limit $m \gg \Delta m(T)$, where

$$\Delta m(T) = \frac{1}{2}\sqrt{\lambda}T \tag{2.71}$$

is the thermal rest mass shift of the quark, the result is a surprisingly, mass independent energy loss

$$-\frac{dE}{dx} = -\frac{1}{v}\frac{dE}{dt} = \pi T \Delta m(T)\frac{v}{\sqrt{1-v^2}} \tag{2.72}$$

and

$$\frac{d}{dt}\langle p_T^2\rangle = 4\pi\Delta m(T)T^2. \tag{2.73}$$

which implies a mass dependent relationship between the energy loss and transverse broadening, as opposed to the case with BDMPS-Z or AdS/CFT-Wilson loop.

Figure 2.13 shows the difference between the WHDG AdS/CFT string drag energy loss, when comparing the c quark to b quark nuclear modification factor double ration for the LHC.

Chapter 3

Jet Measurement in Fixed-Target and Collider Experiments

3.1 "Traditional" Jet Reconstruction Algorithms

We will discuss in more detail a algorithmic definition of the collinear and infrared safety test when the Gaussian filter algorithm is introduced.

3.1.1 Sphericity and Thrust

The very early idea to reconstruct jets were all based on the examination of the event quadruple moment [63], i.e.

$$Q^{\alpha\beta} = \sum_{k=1}^{N} p_k^{\alpha} p_k^{\beta} \tag{3.1}$$

(Counihan) or as the traceless tensor

$$T^{\alpha\beta} = \frac{1}{2} \sum_{k=1}^{N} \left(3 p_k^{\alpha} p_k^{\beta} - \delta^{\alpha\beta} p_k^2 \right) \tag{3.2}$$

(Bjorken and Brodsky) as a measure of jet presence. Diagonalizing $T^{\alpha\beta}$, $\alpha, \beta = 1 \ldots, 3$ yields three eigenvalues $\lambda_1 \geq \lambda_2 \geq \lambda_3$, where in modern notation, λ_3 specifies the jet angular spread $\sum j_T^2$. At the Stanford Positron Electron Accelerating Ring (SPEAR), the derived quantity sphericity was defined as

$$S = \frac{3\lambda_3}{\lambda_1 + \lambda_2 + \lambda_3} \tag{3.3}$$

with the value approaches $S \approx 0$ for jet-like events, and $S = 1$ for fully isotropic events. In principle, the eigenvector associated with λ_3 points to the direction of the dijet. The danger is however, that this biases towards coplanar dijet.

The British–French–Scandinavian Collaboration at the CERN ISR adapted this technique into the "principal axis method". It minimizes the "in-cone" sphericity sum plus the "out-of-cone" energy square

$$x^2 = \sum_{j_{T,k}<p_{T,k}\wedge z_k>0} j_{T,k}^2 + \sum_{j_{T,k}\geq p_{T,k}\vee z_k\leq 0} p_{T,k}^2. \tag{3.4}$$

While the pursuit of this method was quickly abandoned, together with the first application of Gaussian smearing to jet finding, the usage of in-cone transverse momentum balancing appears in the algorithm that was devised next.

Another early event shape variable that involves maximization is the thrust variable [64] which in the original, half-sphere definition involves the spherical maximization of

$$d(\hat{\mathbf{r}}) = \frac{\sum_k (\mathbf{p}_k \cdot \hat{\mathbf{r}})\, \theta(\mathbf{p}_k \cdot \hat{\mathbf{r}})}{\sum_k |\mathbf{p}_k|} \tag{3.5}$$

with respect to the orientation of the unit vector $\hat{\mathbf{r}}$, where θ is the step function.

3.1.2 Cone Algorithm

The iterative cone algorithm was introduced to hadronic collider by the Snowmass accord [65]. However, unbeknownst to the high energy/nuclear physics community then, the iterative cone algorithm without the split/merge step was already used as nonparametric density estimator in pattern recognition for over a decade, and is alternatively known as the mean-shift iteration. To the pattern recognition literature, a equivalence between the mean shift and convolution is also known [66]. Therefore, two equivalent definition of the (non-split/merge) iterative cone algorithm can be obtained.

Figure 3.1 shows an example of mean-shift iteration used in the pattern recognition.

The "classical" cone definition starts with $(\eta_J^{(0)}, \phi_J^{(0)})$ of a jet axis guess, which can be the direction of a high-p_T seed particle. Then, the fixed point iteration over k

$$\begin{aligned} \eta_J^{(k+1)} &= \frac{\sum_{\Delta R_{ij}<R} p_{T,i}\eta_i}{\sum_{\Delta R_{ij}^{(k)}<R} p_{T,i}} \\ \phi_J^{(k+1)} &= \frac{\sum_{\Delta R_{ij}<R} p_{T,i}\phi_i}{\sum_{\Delta R_{ij}^{(k)}<R} p_{T,i}} \end{aligned} \tag{3.6}$$

with the radial distance measure between the i-th final state particle and cone jet axis J at the k-th iteration is defined as

$$(\Delta R_{iJ}^{(k)})^2 = (\eta_i - \eta_J^{(k)})^2 + (\phi_i - \phi_J^{(k)})^2 \tag{3.7}$$

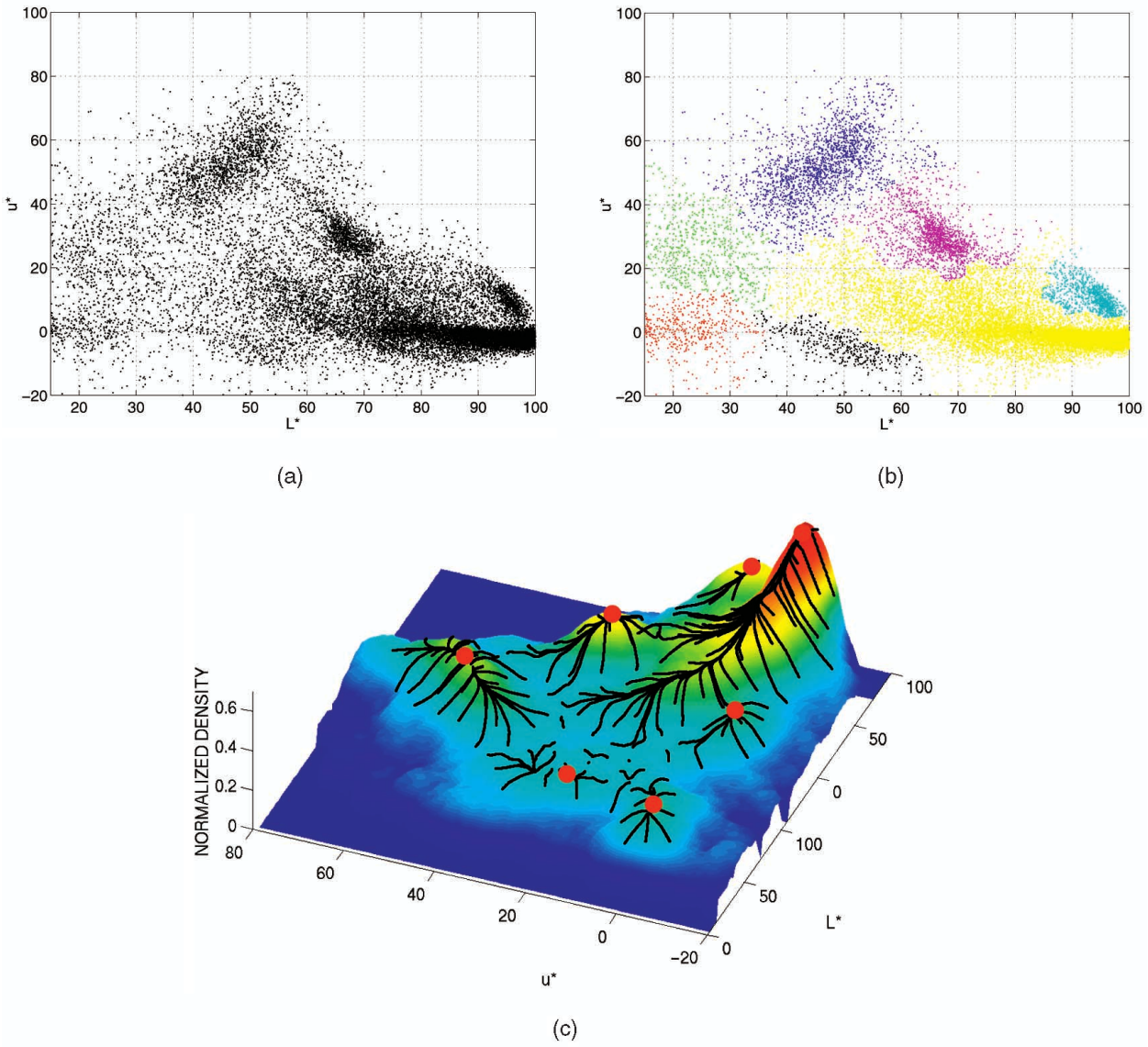

Figure 3.1: Example of mean-shift iteration in pattern recognition: Image segmentation in the (L^*, u^*) color space, from [11]

and R is the radial cutoff of the cone algorithm. The iteration terminates with reaching of the fixed point

$$\begin{aligned} \eta_J^{(k+1)} &= \eta_J^{(k)} \\ \phi_J^{(k+1)} &= \phi_J^{(k)} \end{aligned} \tag{3.8}$$

Rewriting the above fix point condition as weighted sample mean

$$\begin{aligned} \eta_J^{(k+1)} - \eta_J^{(k)} &= \frac{\sum_i p_{T,i}(\eta_i - \eta_J^{(k)})\theta[R^2 - (\eta_i - \eta_J^{(k)})^2 - (\phi_i - \phi_J^{(k)})^2]}{\sum_i p_{T,i}\theta[R^2 - (\eta_i - \eta_J^{(k)})^2 - (\phi_i - \phi_J^{(k)})^2]} = 0 \\ \phi_J^{(k+1)} - \phi_J^{(k)} &= \frac{\sum_i p_{T,i}(\phi_i - \phi_J^{(k)})\theta[R^2 - (\eta_i - \eta_J^{(k)})^2 - (\phi_i - \phi_J^{(k)})^2]}{\sum_i p_{T,i}\theta[R^2 - (\eta_i - \eta_J^{(k)})^2 - (\phi_i - \phi_J^{(k)})^2]} = 0 \end{aligned} \tag{3.9}$$

where the integral bound is now expressed as the step function weighting

$$k(r) = \theta(R^2 - r^2) \tag{3.10}$$

This notation with an explicit step function lays the groundwork for the "nonclassical" discussion of the cone algorithm below.

We can convert the 2D equation to an differential form by noting that (given that $k(r)$ satisfies the necessary integrability conditions)

$$h(r) = C\int_r^\infty dr'\, r' k(r') = -C\int_0^r dr'\, r' k(r') \tag{3.11}$$

which translates to the differential relation

$$\nabla h(r) = h'(r)\nabla r(\mathbf{r}) = k(r)\,\mathbf{r} \tag{3.12}$$

For the cone algorithm, the differential form of the fixed point condition is therefore

$$\nabla\left[\sum_i p_{T,i}\, h(\eta_i - \eta_J^{(k)}, \phi_i - \phi_J^{(k)})\right] = 0 \tag{3.13}$$

where h, with the proper radial cutoff in the integration observed, and dropping unnecessary constants (for the condition of a vanishing gradient, neither a multiplicative nor a constant offset matters), is the Epanechnikov kernel [67]

$$h(r) = \max(0, R^2 - r^2). \tag{3.14}$$

In a later chapter, I will show that this correspondence can be used to derived different algorithms that generalizes the cone algorithm while retaining some of its useful traits.

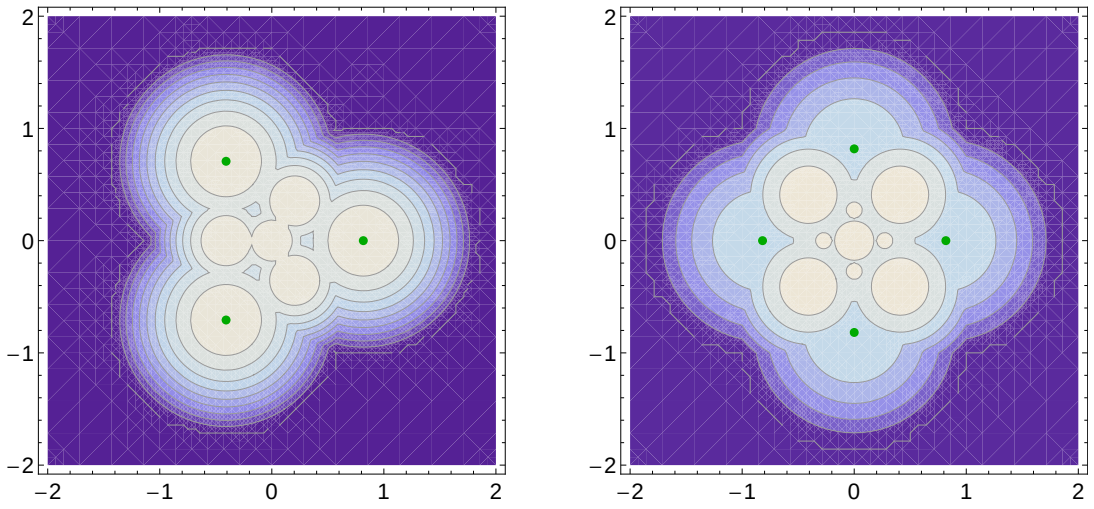

Figure 3.2: Examples of $N = 3$ and $N = 4$ configuration with 7 and 9 stable cone axes, respectively, which are stationary points in the convolution by Epanechnikov kernel. Particle positions are shown as green dots.

Figure 3.2 shows examples of $N = 3$ and $N = 4$ configuration with 7 and 9 stable cone axes, respectively, which are stationary points in the convolution by Epanechnikov kernel.

The procedure of introducing a p_T threshold during the seeding, while "weeding out" undesirable stable axes, results in a final state particle p_T dependent phase space cutoff, that is a collinear and infrared unsafe slicing of the two-body/three-body final state at the NLO level of jet cross section, since the cross section would depend on the fragmentation property. Defining the cone algorithm as convolution with the Epanechnikov kernel makes it much clearer why the cone algorithm is traditionally seeded and an unseeded definition is highly problematic at high multiplicity environment such as the heavy ion collision: Convolution with the Epanechnikov kernel is potentially maximum-creating, and therefore, in a suitably event configuration, there can be more stable cones than final state particles! Therefore, finding the stable cones without seeding is not sufficient to obtain a practical, seeded cone-like definition.

The seedless/infrared safe cone (SISCone) version of the cone algorithm alleviates the problem of the high density of stable axes by introducing a split/merge procedure that is infrared and collinearly safe.

For a longitudinally isotropic underlying event with (ideally) infinitely dense final state particles, like a mid-rapidity heavy ion collision, the characteristic, effective cone radius is not R, but to the first order already $(R + R_1)$, with R_1 being the distance of the first order cone merge, which for a flat background, is given by

the inversion of the equation

$$\frac{4}{\pi}\int_{R_1/2}^{1} dx\,\sqrt{1-x^2} = 2\cos^{-1}\left(\frac{R_1}{2}\right) - \frac{R_1}{2}\sqrt{4-R_1^2} = \text{overlap threshold} \tag{3.15}$$

which numerically evaluates to $R_1 \approx 0.81R$ for an overlap threshold 0.5 and $R_1 \approx 0.40R$ for the overlap threshold 0.75, which are nonnegligible contribution over the zeroth order R. In practice, however, higher order merge distances $R_n, n \geq 2$ do not necessarily drop in magnitude, and applying SISCone to events generated e.g. by the HIJING event generator exhibits the behavior of merging the background into strips of multiple units of rapidity.

3.1.3 Iterative Recombination

The generalized form of the Catani–Dokshitzer–Ellis–Soper $k_\perp$ algorithm starts with $p_{T,i}$, denoted protojet in the $k_\perp$ terminology, and successively combines based on the distance measure

$$d(i,j) \equiv \min(p_{T,i}^k, p_{T,j}^k)\frac{\sqrt{(\eta_i-\eta_j)^2+(\phi_i-\phi_j)^2}}{D} \tag{3.16}$$

and a "beam-distance" is defined by

$$d(i,\text{beam}) \equiv p_{T,i}^k. \tag{3.17}$$

Note that $d(i,j)$ is a true distance function/metric, such that the algorithm e.g. can be redefined by $d^2(i,j)$ instead. At each step, if there exists a $j \neq i$ with $d(i,j) < d(i,\text{beam})$, a longitudinal (i,j) protojet combining is performed by removing the protojet i, j and add the new protojet

$$\begin{aligned} p_{T,i+j} &= p_{T,i} + p_{T,j} \\ \eta_{T,i+j} &= \frac{p_{T,i}\eta_i + p_{T,j}\eta_j}{p_{T,i+j}} \\ \phi_{T,i+j} &= \frac{p_{T,i}\phi_i + p_{T,j}\phi_j}{p_{T,i+j}} \end{aligned} \tag{3.18}$$

And if for all $j \neq i$, $d(i,j) > d(i,\text{beam})$, the i-th protojet is removed from the list as a final, fully reconstructed jet.

For the ordinary $k_\perp$, $k = 1$, and the clustering follows a sequence of increasing transverse momentum order for QCD splitting, thus "$k_\perp$". Setting $k = 0$ gives the Cambridge–Aachen algorithm, and $k = -1$ is the anti-$k_\perp$ algorithm. The term "anti-$k_\perp$" is in fact a misnomer, since modifying k does not make it cluster in the opposite direction of a $k_\perp$ ordering.

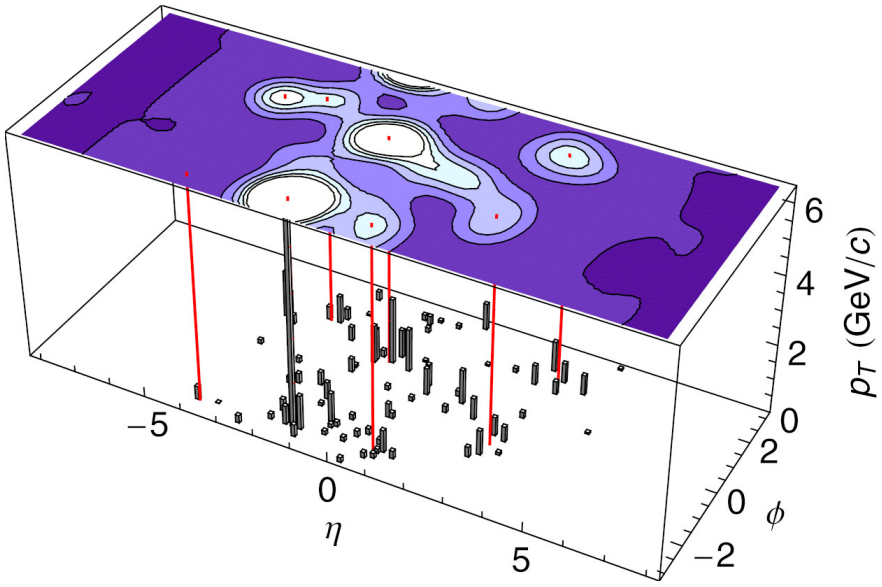

Figure 3.3: Event display of $p+p$ event from PYTHIA with the Gaussian filter jet reconstruction. From bottom to top, the event display consists of: Lego plot of the deposited energy by final state particles, red lines are the reconstructed jet axes, contour plot at the top indicates the filter output, where the maxima coincide with the reconstructed jet axes.

Anti-$k_\perp$ has been frequently compared to the cone algorithm. However, the coverage area is the crucial difference here. An unseeded cone algorithm will inevitably have both split and merge decision in order to avoid many mostly overlapping cone directions. We showed above that higher order cone merges have nonnegligible contribution to the effective cone radius. Anti-$k_\perp$ however, has the opposite behavior. Iterative recombination with a protojet center dominated distance cutoff has the effect of a coverage oscillating with each recombination step. (Note that the behavior is different than the infrared safety, as infrared safety is an asymptotic behavior at the presence of infinitely low momentum particles.) Therefore, the characteristic radius is in the range of D and D minus the average particle separation, i.e. it may decide to kick one particle out of the "cone". This behavior is in addition to the lack of merging. Therefore, the behavior of anti-$k_\perp$ diverges from the cone algorithm with either increasing wider jet fragmentation or an increasing magnitude of the underlying event.

3.2 Gaussian filter

3.2.1 Filter Definition

Figure 3.3 shows an event display of $p+p$ event from PYTHIA with the Gaussian filter jet reconstruction, where a Lego plot of the final state particle energy deposit is overlaid with the filter output contour plot, and the maxima as the reconstructed jet axes.

For a filter-based jet reconstruction, and including heavy ion events, we define the event p_T density to be

$$p_T(\eta,\phi) = \sum_{i\in\text{fragment}} p_{T,i}\delta(\eta-\eta_i)\delta(\phi-\phi_i), \tag{3.19}$$

For the Gaussian filter, the filter kernel is set to be

$$h_{\sigma_{\text{fil}}}(\eta,\phi) = \exp\left[-(\eta^2+\phi^{*2})/(2\sigma_{\text{fil}}^2)\right], \tag{3.20}$$

with $\phi^* \equiv \phi - 2\pi\lfloor(\phi+\pi)/(2\pi)\rfloor$ being the angular range reduced ϕ (see also section A.3.2 how to implement it). The set of jets J as the three-tuple (p_T,η,ϕ) is then given by the local maximization

$$J = \{\,(p_T,\eta,\phi) \mid p_T = \tilde{p}_T(\eta,\phi) \text{ a local maximum}\,\}, \tag{3.21}$$

in which the (η,ϕ)-convolved p_T density is

$$\tilde{p}_T(\eta,\phi) = \iint_{\mathbb{R}\times S^1} d\eta' d\phi' p_T(\eta',\phi')h(\eta-\eta',\phi-\phi'). \tag{3.22}$$

For heavy ion events, underlying event has a finite and sizable contribution to the jet p_T. We can take advantage of the linearity of the convolution, and define the background corrected p_T density as the expectation value

$$p_T^{\text{bg}}(\eta,\phi) = \langle p_T(\eta,\phi)\rangle_{\text{nonjet}}, \tag{3.23}$$

where the averaging is understood to exclude real jet production (i.e. in situation with large true jet yield, the regions with jets have to be excluded. Then, (3.19) can be redefined as

$$p_T(\eta,\phi) = \sum_{i\in\text{fragment}} p_{T,i}\delta(\eta-\eta_i)\delta(\phi-\phi_i) - p_T^{\text{bg}}(\eta,\phi), \tag{3.24}$$

and $p_T^{\text{bg}}(\eta,\phi) \equiv 0$ can be thought if there are no underlying event. Due to the linearity of the convolution, the contribution from the underlying event can be precomputed as

$$\tilde{p}_T^{\text{bg}}(\eta,\phi) = \iint_{\mathbb{R}\times S^1} d\eta' d\phi' p_T^{\text{bg}}(\eta',\phi')h(\eta-\eta',\phi-\phi'). \tag{3.25}$$

There are a few direct properties to the Gaussian filter that becomes evident:

1. There is no immediate need for split/merge. Since convolution with the Gaussian kernel do not create maxima, there is no merging step necessary to remove higher order stable axes, as with the cone algorithm.

2. From a purely mathematical point of view, the filter kernel h is a test function, which regulates the δ distribution from the point-like final states, and makes a diffuse background the same objects as the final state particles, therefore facilitates a direct subtraction of the event background.

3. The algorithm has a fixed geometry, which makes the subtraction of underlying event easy. A dynamic geometry algorithm (which includes cone algorithm with split/merge) has an event-by-event and jet-by-jet fluctuating underlying event area, which either means either some integration algorithm has to provide the amount of the underlying event dynamically, or it is estimated event-by-event (which can make the problem cyclic/self reinforcing). This is in principle achievable with other jet algorithms, but the jet definition has to be changed to make it fixed-geometry.

In practical realization, the reconstruction of an event is divided into the following two steps, which will be explained in detail in the following sections:

1. Obtain an discrete convolution of the event p_T using a digital filter implementation of the filter.

2. Subtract the discretized $\tilde{p}_T^{\mathrm{bg}}(\hat{\eta}, \hat{\phi})$, which can be precomputed and stored.

3. Find the maxima and stationary points $(\hat{\eta}, \hat{\phi})$ from $\tilde{p}_T(\hat{\eta}, \hat{\phi})$.

4. Refine upon the discretized jet position using continuous optimization algorithm to obtain the true jet position.

3.2.1.1 Infinite Impulse Response Realization

1. Obtain an rectangular histogram as a discretized approximation to the p_T density. The continuous (η, ϕ) is replaced by the discretization $(\hat{\eta}, \hat{\phi})$ with

$$\begin{aligned} \hat{\eta} &= \left\lfloor (\eta - \eta_{\min}) \frac{N_\eta}{\Delta\eta} \right\rfloor \frac{\Delta\eta}{N_\eta} + \eta_{\min} \\ \hat{\phi} &= \left\lfloor (\phi - \phi_{\min}) \frac{N_\phi}{\Delta\phi} \right\rfloor \frac{\Delta\phi}{N_\phi} + \phi_{\min} \end{aligned} \tag{3.26}$$

where N_η is the number of discrete pseudorapidity bins and Δ_η the pseudorapidity range, and analogously for the azimuth ϕ. The finite bin size introduces a constant renormalization to the otherwise infinities in the distribution.

2. Filter the histogram using a discrete realization of the filter. This can be implemented using either in (η, ϕ) domain using a finite impulse response (FIR) or an infinite impulse response (IIR) realization, or in the Fourier domain.

The discrete Z-transform (e.g. [68]) is defined via the Laurent series

$$F(z) = \sum_{n=-\infty}^{\infty} f(nT)\, z^{-n} \tag{3.27}$$

For brevity, I will used $f_n \equiv f(nT)$ as shorthand for the discrete sequence. Infinite impulse response (IIR) digital filters are recurrent filters, which in the frequency space, have a transfer function $H(z)$ being a rational function of $z = e^{i\omega}$. From the discrete time realization

$$y_n = \sum_{k=1}^{N} b_k x_{n-k} - \sum_{k=1}^{N} a_k y_{n-k} \tag{3.28}$$

we obtain after the separation of variables

$$y_n + \sum_{k=1}^{N} a_k y_{n-k} = \sum_{k=0}^{N} b_k x_{n-k}. \tag{3.29}$$

Z-transform both side gives

$$z^n \left(1 + \sum_{k=1}^{N} a_k z^{-k}\right) Y(z) = z^n \left(\sum_{k=0}^{N} b_k z^{-k}\right) X(k) \tag{3.30}$$

or for the transfer function

$$H(z) \equiv \frac{Y(z)}{X(z)} = \frac{\sum_{k=0}^{N} b_k z^{-k}}{1 + \sum_{k=1}^{N} a_k z^{-k}} \tag{3.31}$$

The fact that only negative exponents appear causes this filter structure to be causal, i.e. only time-retarded input is used to produce the filter output.

IIR approximation to a Gaussian convolution have been provided as a pole-zero, parallel filter by R. Deriche [69], and as an all-pole, cascade filter by van Vliet, Young and Verbeek [70], for which I will provide an improved fourth order approximation. Since jet reconstruction operates on the input offline (in the signal processing sense, i.e. the entire input is known), the all-pole cascade realization eliminates the otherwise

undesirable phase delay of an IIR filter is eliminated by a zero delay filter structure (e.g. [71])

$$H(z) = H^+(z)\,H^-(z), \quad H^-(z) \equiv H^+(z^{-1}) \tag{3.32}$$

where the causal part of the filter is $H^+(z)$ and noncausal (or anticausal) part $H^-(z)$, which is essentially $H^+(z)$ with the spatial filter direction reversed. For the fourth order filter realization, the structure is

$$\begin{aligned} H^+(z) &= \frac{b_0}{1 + a_1 z^{-1} + a_2 z^{-2} + a_3 z^{-3} + a_4 z^{-4}} \\ H^-(z) &= \frac{b_0}{1 + a_1 z^{1} + a_2 z^{2} + a_3 z^{3} + a_4 z^{4}}. \end{aligned} \tag{3.33}$$

D. Hale noted that the parallel implementation is computationally advantageous, and the van Vliet, Young and Verbeek approximation can be converted to a parallel structure by partial fraction expansion [72]. Hale also noted that for the discrete $\hat{\sigma} > 8$ (with $\hat{\sigma} = \sigma N_\eta/\Delta\eta$ for the pseudorapidity and similarly for the azimuth), the difference between the Deriche and van Vliet approximation are negligible, while the Deriche filter scales poorly with increasing $\hat{\sigma}$, which explains our choice. It should however be pointed out that the continuous optimization we apply after the discrete filter will mask any approximation at this scale. In fact, we started out using the suboptimal approximation provided by van Vliet, Young and Verbeek and subsequently improved our approximation.

The structure of a polynomial is numerically more accurately described by its roots. Expressed in roots, appendix B.1 derives the complex location $d_{1,3}$ of the poles, by minimizing $|H(e^{i\omega}) - \exp(-2\omega^2)|$, as

$$\begin{aligned} d_1 &= 1.047\,190 + 1.276\,950\,i \\ d_3 &= 1.664\,977 + 0.472\,724\,i, \end{aligned} \tag{3.34}$$

or expressed in polynomial coefficients

$$\begin{aligned} a_1 &= -5.424\,333 \\ a_2 &= 12.697\,011 \\ a_3 &= -15.355\,431 \\ a_4 &= 8.169\,664 \\ b_0 &= 1.086\,911 \end{aligned} \tag{3.35}$$

where b_0 is simply a normalization to ensure $H(z = 1) = 1$.

While a rigorous introduction to the scaling theorem with the discrete Z-transform (that relates the Z-transform of the sequence $h(nT)$ to $h(T)$) would be a bit distracting to the discussion here, examining the

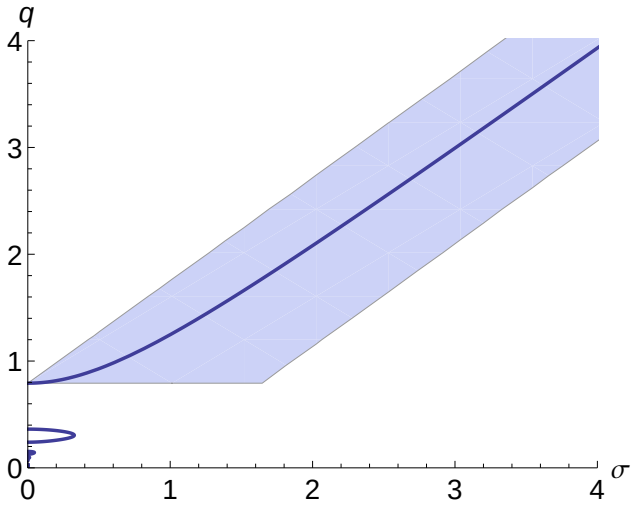

Figure 3.4: Scaling factor q of the IIR Gaussian filter approximation as function of the standard deviation σ (with only the non-linear, small q region depicted). Shaded region is the suggested bound for root finding. Multiple roots exist for $\sigma < 0.3264$.

definition (3.27) strongly suggest that, should $f(nT)$ be the discrete sampling of a continuous function, the Z-transform would scale according a parameter change. An arbitrary σ therefore would be achieved by the scaling of the poles via $d_k \mapsto d_k^{1/q}$, $q \in \mathbb{R}_+$. Since such a scaling with respect to a discrete and sequence is not exact, we would examine the effect on the actual variance of the impulse response and parametrize any residual effect. Transforming the definition of the variance into Fourier space gives

$$\operatorname{Var} h = \sum_{n=-\infty}^{\infty} n^2 h(nT) = \operatorname{Re} \sum_k \frac{2 d_k^{\sigma_0/q}}{(d_k^{\sigma_0/q} - 1)^2} \tag{3.36}$$

where $\sigma_0 = 2$ is width used in the initial approximation. As opposed to previous publications, we use the bracketing equation solver by G. Alefeld, F. A. Potra, and Y.-x. Shi [73] to invert the relation and obtain the value of q. By investigating the small q plus asymptotic behavior, obtained a suitable (and ensure that the slopes are representable by IEEE 754 single precision) bound

$$\max(0.792\,552\,02, 0.962\,887\,64\,\sigma - 0.823\,265\,93) \leq q \leq 0.962\,887\,70\,\sigma + 0.823\,099\,19 \tag{3.37}$$

The lower bound is relaxed to center the root, which may avoid difficulties from root finding if the root is too close to the edge.

Figure 3.4 shows the scaling factor q of the IIR Gaussian filter approximation as function of the standard

deviation σ (with only the non-linear, small q region depicted), together with the shaded region corresponding to the inequalities in (3.37).

Since the IIR approximation calculates a linear convolution in both η, ϕ, the azimuthal wrap-around in ϕ is approximated by extending the star the convolution by π to 2π (i.e. depending on the causal direction of the filter, from -3π--2π to π, or from $-\pi$ to 2π–3π).

There is a slight detail when implementing the filter either using linear or circular convolution (or use linear convolution to mimic circular convolution, as detailed above). Circularly convolve the event with a Gaussian distribution also filters away noncyclic frequency component, and the actual azimuthal function being convolved with is therefore the Jacobi theta function ϑ_3 ([74], section 16.27.3, p. 576)

$$h(\eta, \phi) = \frac{|\sigma|}{\sqrt{2\pi}} e^{-\eta^2/(2\sigma^2)} \vartheta_3\left(\frac{\phi}{2}, e^{-\sigma^2/2}\right). \tag{3.38}$$

For practical sizes of σ, the effect is negligible and corrected during the continuous optimization.

3.2.1.2 Approximation of the Background Distribution

The basic constraint imposed by the continuous maximum finding to the parametrization of the filter convolved background $\tilde{p}_T^{\text{bg}}$ is that it is a second order differentiable function. Two obvious choices exist for the parametrization

- Polynomial over the entire (η, ϕ) range, which has the advantage of compact coefficients. However, the Runge phenomenon of the directly calculable, least square, L_2 approximation causes the pointwise approximation error (i.e. if the jet happens to be on a "unlucky" (η, ϕ) position) to be unbounded, while the minimax approximation that provides a bounded, pointwise approximation requires iterative algorithms to calculate.

- B-splines with order ≥ 3, which has the advantage that the Runge phenomenon is easier to constrain by noniterative algorithms, but requires a large set of coefficients to be carried around (in fact, computing optimal, minimum number of nodes B-splines is even less trivial than using minimax polynomials).

In this implementation, we chose the polynomial approximation, while calculating its coefficients using an arbitrary dimensional (convex) extension to the Remez algorithm [75] by G. A. Watson [76].

The Remez–Watson algorithm calculates the linear approximation of a target function $f(\mathbf{x})$, where the residual function is

$$r(\boldsymbol{\alpha}, \mathbf{x}) = \sum_{j=1}^{n} \alpha_j \varphi_j(\mathbf{x}) - f(\mathbf{x}) \tag{3.39}$$

and its maximum norm $\|r(\boldsymbol{\alpha}, \mathbf{x})\|_\infty$ is minimized, with $\boldsymbol{\alpha}$ being the resulting coefficients, and $\boldsymbol{\varphi}$ are the basis functions. This is accomplished by the iteration:

1. Initialize using the r points $\mathbf{x}_1, \ldots, \mathbf{x}_r$, and with $a_{jl} = \varphi_l(\mathbf{x}_j)$, $f_j = f(\mathbf{x}_j)$ the coefficient matrix and right-hand-side vector

$$\mathbf{C}^{(1)} = \begin{pmatrix} \mathbf{A} & \mathbf{1}_{1\times r} \\ -\mathbf{A} & \mathbf{1}_{1\times r} \end{pmatrix} \qquad \mathbf{c}^{(1)} = \begin{pmatrix} \mathbf{f} \\ -\mathbf{f} \end{pmatrix} \tag{3.40}$$

2. Solve the linear programming (LP) subproblem

$$\begin{aligned} &\text{minimize} \quad h \\ &\text{subject to} \quad \mathbf{C}^{(k)} \begin{pmatrix} \boldsymbol{\alpha} \\ h \end{pmatrix} \geq \mathbf{c}^{(k)} \end{aligned} \tag{3.41}$$

3. Search for points where the maximum norm $\|r(\boldsymbol{\alpha}, \mathbf{x})\|_\infty$, and consider points that are not already in $\mathbf{C}^{(k)}$ and $\mathbf{c}^{(k)}$. If no additional points can be found, terminate.

4. Otherwise, using the set of new extrema $\mathbf{x}_s, \ldots, \mathbf{x}_{s+t-1}$ and, evaluate the new sets of $\mathbf{A}'$ and $\mathbf{f}'$ rows, with with $a'_{jl} = \varphi_l(\mathbf{x}_{s+j-1})$, $f_j = f(\mathbf{x}_{s+j-1})$, analogously to step 1. Update the LP subproblem by extending the rows:

$$\mathbf{C}^{(k+1)} = \left(\begin{array}{cc} \multicolumn{2}{c}{\mathbf{C}^{(k)}} \\ \hline \mathbf{A}' & \mathbf{1}_{1\times r} \\ -\mathbf{A}' & \mathbf{1}_{1\times r} \end{array}\right) \qquad \mathbf{c}^{(k+1)} = \left(\begin{array}{c} \mathbf{c}^{(k)} \\ \hline \mathbf{f}' \\ -\mathbf{f}' \end{array}\right). \tag{3.42}$$

   Go to step 2.

The implementation of the algorithm above (or any best uniform optimization algorithm) requires local optimization to determine the position of the point that contributes to the L_∞ norm. Note that for a 2D problem, it is not sufficient to just implement the $N = 2$-dimensional, unconstrained local optimization, since with best uniform approximation, the boundary surface is usually populated with extrema. For the problem here, the boundary and associated constraints are purely axial, therefore an unconstrained, limited

storage Broyden–Fletcher–Goldfarb–Shanno (BFGS) algorithm [77] is used first. Depending on the initial location of the optimization (which may be on the boundary surface), the appropriate constraints are applied by converting the problem into an 1D or (the trivial) 0D one, and then use unconstrained optimization on the remaining dimensions.

The target function is determined by the convolution of the measured detector response. To calculate the target function, a finite impulse response (FIR) filter implementation of the filter is used. FIR filters are essentially special cases of an IIR filter with no recursive component, and setting a_k in (3.31) shows that FIR filters can be simply realized by linear convolution. The filter is realized as circular convolution in the Fourier space. Since the resulting convolution is already circular, nothing has to be done in the azimuthal axis. The effect of using circular instead of linear convolution in the pseudorapidity is mitigated by extending the pseudorapidity range to be much larger than the detector's pseudorapidity coverage. And because piecewise Newton interpolation do not necessarily have continuous derivatives at the nodes, algorithm FD in [78], section 8.6.2.2, pp. 343–344, is used to obtain the numerical gradient instead of the analytic one. And since the target function is largely "smooth" (in the sense that the trust region of a local quadratic approximation is far larger than the point-to-point distance), applying a continuous maximization with the numerical gradient remains efficient.

Further acceleration of the problem can be achieved by noting that the problem is really one that is defined on discrete (η, ϕ) points, since the target function is approximated by FIR. However, any practical resolution in (η, ϕ) would result in $N_{\eta,\phi} \approx 10^4$ grid points and becomes computationally unpractical to solve by a brute force N-D LP. The usage of the continuous Remez–Watson algorithm here provides an efficient mean to reduce N to $\approx 10^3$, where the linear programming can be solved even with the simplex algorithm. In case here of a target function that is really only defined on a grid, I found that the convergence of the Remez–Watson can be accelerated by round the extrema in each step to the grid position.

Because this thesis only considers two type of detectors:

- Ideal detectors with only an (kinematic) η dependence of the background and no ϕ dependence (e.g. resulting from acceptance inperfection)
- The PHENIX detector with a large gap at $\phi = -\pi/2$

we only encounter cases where no ϕ parametrization or a parametrization that is discontinuous at $\phi = -\pi/2$ is possible and efficient. In the latter case, we use a tensor Chebyshev polynomial in (η, ϕ). A full 2π-azimuth

detector with acceptance inperfection would need to extend this approach to tensor Chebyshev–Fourier polynomials (i.e., in η and ϕ).

For practical purpose, we found that an initial set of grid points for the LP of $k(N+1)$, with N being the approximation order and $k = 2 \ldots 3$ to be sufficient for the PHENIX acceptance. Except for the (unlikely) scenario of a even more severe detector nonuniformity, there is little need go beyond this value.

3.2.1.3 Discrete Maximum Finding

The discrete location of the local maxima are found using comparisons against the nine neighboring pixels. Infrequently, events may possess a maximum that lies exactly between two pixels. In lieu of a more elaborate test, whether a contiguous group of equally valued pixels is bounded by values that are smaller, we simply add points where adjacent pixels have equal values to the list of potential "maxima". Continuous maximum finding (described next) is used to weed out stationary points that are not true local maxima (i.e. minima or saddle points), since these initial values will either

- converge into a continuous minimum or saddle point, and terminate
- diverge and terminate by hitting the pseudorapidity boundary
- converge into another maximum and filtered out by the "ghost cut"

3.2.1.4 Continuous Optimization

Once the discrete, approximate position of a maximum or stationary point is found, the continuously defined jet direction is determined by using standard multidimensional optimization algorithms.

While in the purely additive situation of $p+p$, the generate distributions are relatively simple Gaussian mixture distributions that can be easily accomplished by Newton iterations, doing so when a background distribution is subtracted and repeating this reliably over multiple billion events requires a more robust approach. The biased Wolfe trust region algorithm [79] (pp. 30–31, algorithm 2.2.4) is used. The biased Wolfe trust region iterates on $k < k_{\max}$, and for each step k:

1. Obtain $\mathbf{s}^{(k)} \equiv (\Delta\eta^{(k)}, \Delta\phi^{(k)})$ as the k-th solution of the trust-region subproblem within the "radius" $\|N^{(k)}\mathbf{s}^{(k)}\| \leq \delta^{(k)}$. This is described by the quadratic programming (QP) problem

$$\begin{aligned} &\text{minimize} && Q^{(k)}(\mathbf{s}^{(k)}) \\ &\text{subject to} && \|N^{(k)}\mathbf{s}^{(k)}\| \leq \delta^{(k)} \end{aligned} \tag{3.43}$$

where

$$Q^{(k)}(\mathbf{s}^{(k)}) \equiv (\mathbf{g}^{(k)})^T \mathbf{s}^{(k)} + (\mathbf{s}^{(k)})^T \mathbf{B}^{(k)} \mathbf{s}^{(k)} \tag{3.44}$$

where $\mathbf{g}^{(k)}$ and $\mathbf{B}^{(k)}$ are the local estimate of the gradient and the Hessian of $\tilde{p}_T(\eta, \phi)$. The actual shape of the trust region depends on the choice of norm, and the L_∞ norm is used for simplicity. Since in our situation, (η, ϕ) are properly scaled, $N^{(k)} \equiv \mathbf{1}$.

2. Determine the Armijo rule discriminant for the trust region update

$$\rho^{(k)} = \frac{\tilde{p}_T(\eta^{(k)} + \Delta\eta^{(k)}, \phi^{(k)} + \Delta\phi^{(k)}) - \tilde{p}_T(\eta^{(k)}, \phi^{(k)})}{Q^{(k)}(\Delta\eta^{(k)}, \Delta\phi^{(k)})} \tag{3.45}$$

3. Perform an exact line search for a step size $\alpha^{(k)}$ using the algorithm by Moré and Thuente [80], such that the step size satisfies the Wolfe conditions, consisting of the Armijo rule

$$\tilde{p}_T(\eta^{(k)} + \Delta\eta^{(k)}, \phi^{(k)} + \Delta\phi^{(k)}) - \tilde{p}_T(\eta^{(k)}, \phi^{(k)}) < c_1 Q^{(k)}(\alpha^{(k)}\eta^{(k)}, \alpha^{(k)}\phi^{(k)}) \tag{3.46}$$

and the curvature condition

$$\nabla \tilde{p}_T(\eta^{(k)} + \Delta\eta^{(k)}, \phi^{(k)} + \Delta\phi^{(k)}) \leq c_2 \nabla \tilde{p}_T(\eta^{(k)}, \phi^{(k)}), \tag{3.47}$$

where $0 < c_1 < c_2 < 1$ is required for the function value tolerance c_1 and gradient tolerance c_2. The choice $c_1 = 10^{-4}$, $c_2 = 0.9$ in [80] is kept.

4. Update by advancing by the step size

$$\begin{aligned} \eta^{(k+1)} &= \eta^{(k)} + \alpha^{(k)}\Delta\eta^{(k)} \\ \phi^{(k+1)} &= \phi^{(k)} + \alpha^{(k)}\Delta\phi^{(k)} \end{aligned} \tag{3.48}$$

5. Update the trust region

$$\delta^{(k+1)} = \begin{cases} \max\left(\delta^{(k)}, \alpha^{(k)}\hat{\nu}\|N^{(k)}\mathbf{s}^{(k)}\|, \gamma_3\|N^{(k)}\mathbf{s}^{(k)}\|\right) & \rho^{(k)} \geq c_2 \\ \alpha^{(k)} \min\left(\delta^{(k)}, \|N^{(k)}\mathbf{s}^{(k)}\|\right) & \rho^{(k)} < c_2 \end{cases} \tag{3.49}$$

where the increase of the trust region is determined by $\gamma_3 > \nu \geq 1$. The decrease of the trial step is compensated by the parameter $\hat{\nu} \in [1, \nu]$, and in our case, since the exact line search is combined with a problem that converges rapidly, the conservative choice of $\hat{nu} = \nu = 1$ is used. For the potential trust region increase, $\gamma_3 = 2$ is used. The specific form of the case $\rho^{(k)} < c_2$ is chose to be the lower-bound within the update rule type described in [79], pp. 20.

In [79], the choice of QP subproblem with $Q^{(k)}$ or the more stringent, constrained Hessian determinant $\hat{Q}^{(k)}(\mathbf{s}) \equiv (\mathbf{g}^{(k)})^T\mathbf{s} + \min(\mathbf{0}, \mathbf{s}^T\mathbf{B}^{(k)}\mathbf{s})$ in updating the trust region radius is left somewhat ambiguous (cf. [79], section 2.2.2). Applying to practical events, $Q^{(k)}$ appears to be sufficient for our purposes. When in the $d = 2$, (η, ϕ) space, a trust region with respect to the maximum norm is used, the constrained optimization subproblem is relatively simply solved by enumerating the four $d-1 = 1$ and the four $d-2 = 0$ dimensional, constrained problems.

The targeted (η, ϕ) precision is set $\tau_F = 4\epsilon_M$, with ϵ_M being machine precision. The parameter ϵ_A specifies the achievable machine accuracy when evaluating $f(\mathbf{x})$, which is defined as the lower bound for ϵ_A, with

$$\overline{f(\overline{\mathbf{x}})} - f(\mathbf{x}) \leq \epsilon_A \tag{3.50}$$

around the proximity of $\mathbf{x}$. In the case of the Gaussian filter, a full evaluation of ϵ_A is avoided, since the target function is sufficiently smooth, and instead the simple estimate

$$\epsilon_A \approx \epsilon_M[1 + f(\mathbf{x})] \tag{3.51}$$

is used. The (logically or-chained) termination criteria are the U1–U4 in [78], section 8.2.3.2, pp. 306–307

$$f(\mathbf{x}_{k-1}) - f(\mathbf{x}_k) < \tau_F[1 + |f(\mathbf{x}_k)|] \tag{3.52}$$

$$\|\mathbf{x}_{k-1} - \mathbf{x}_k\| < \sqrt{\tau_F}(1 + \|\mathbf{x}_k\|) \tag{3.53}$$

$$\|\mathbf{g}_k\| < \sqrt[3]{\tau_F}[1 + |f(\mathbf{x}_k)|] \tag{3.54}$$

$$\|\mathbf{g}_k\| < \epsilon_A, \tag{3.55}$$

where (3.52) is the termination condition on the function value, (3.53) the condition for the argument, and (3.54) and (3.55) are the conditions on the gradient. The condition U5 in [78] on the positive definiteness of the local Hessian is not necessary, since the constrained solver will always find a non-decreasing step.

While so structured optimization guarantees descent with each step, optimization starting from stationary points will (necessarily) converge to a local maxima in proximity. This leads to multiply, close maxima as the optimization output, which is rectified by applying a "ghost jet" with $\Delta R < \epsilon_M^{2/3}$ is applied.

3.3 Collinear and Infrared Safety

To test that the fully implemented algorithm for infrared and collinear (IRC) safe, event are generated with the following characteristics

- $2 \leq N \leq 9$ lightlike particles
- flat p_T between ϵ_M and 1 TeV
- $|\eta| \leq 1.5$

IR safety is tested by adding $1 \leq n \leq 5$ particles with $p_T = \epsilon_M \approx 1\,\text{eV}$ in the same pseudorapidity range. 3×10^9 random events were generated. IR safety violating event were found at a rate of 10^{-6}. Inspection of the corresponding events show that these are jets on the phase space boundary, where jets are formed which can be either merged or split into two Gaussian peak, with a near-saddle point in between. Not only is the behavior essentially consistent with the expected phase space from the finite IR test particle magnitude, behavior at such low rate will not cause problems for even complex jet analysis such as cocktail subtraction, for the foreseeable future.

Collinear safety is tested by generating a random $(\Delta\eta, \Delta\phi)$ direction with magnitude $\epsilon_M \approx 10^{-6}$, and then every track in the event is split by a random ratio r and with the perturbed (η, ϕ), while another particle with $(1 - r)\,p_T$ and the Lorenz balancing direction is added to the event. Also here, a collinear violation was found at the rate of 10^{-6}, consistent with the phase space expectation, and again, coming from jets at the exact splitting phase space boundary.

3.4 Fake Jet Rejection

Random overlap of hadronization processes in the underlying event can give large fluctuation to the jet energy. When measuring a steeply falling spectrum such as jet production, the spectrum itself (in linear scale) is in fact nearly a delta function, and the convolution by the underlying event fluctuation in low p_T is dominated by the smearing process. This behavior only terminates when the tail of the energy smearing crosses over with the jet spectrum, which given a steep spectrum at mid-$\sqrt{s_{NN}}$ can exclude a significant portion of the statistically accessible jet p_T. Not only would labeling a, say 100 MeV "jet" that receives 10 GeV/c from pure fluctuation as a real 10 GeV jet not make any sense. It will be clear in a moment why operationally, these jets that predominantly obtain their energy from fluctuation and not actual hard scattering process, should be considered as falsely reconstructed jets, or "fake jets".

Since behavior of producing these "jets" with mostly fluctuation-based energy only terminates at high-p_T and at a low jet yield, this also demonstrate a key problem that confused many people. The problem of

heavy ion underlying event energy smearing is inherently the sampling of the statistical tail of the underlying event smearing. Another way to describe the problem is that it is insufficient to reject *per heavy ion event* enough jets from fluctuation, but you have to reject this sufficiently *per observed hard scattering*. Below the smearing–jet yield cross over, this is not possible without a strategy to remove these background "jets".

Another proposed approach, where some colleagues have staked their hope on, is to statistically unfold away the yield coming from background smearing. Essentially the hope is that the unfolding would "move" these background jets into their correct p_T, i.e. around 0 GeV. This approach will fail from two reasons

- It is plainly impossible to quantify the background interaction (without resorting to some model) with the jet reconstruction algorithm at this level of statistical tail. Any attempt to quantify this by embedding into actual minimum bias heavy ion event will encounter intrinsic jet production, and – unsurprisingly – at exactly the same range of the statistical tail you would like to quantify.

- The necessary unfolding is simply numerically infeasible. As it was discussed above, the low p_T portion of the jet spectrum – where you would want to unfold these backgrounds jets into – looks to the unfolding like a delta distribution. Compounded by the issue of Poisson counting noise, numerical inversion cannot reliably unfold a nearly Gaussian distribution against a Gaussian distribution, and obtain a near-delta distribution. Another way to look at this is that in the Fourier domain the inversion of a Gaussian smearing is the multiplication of e^{ω^2} against $e^{-\omega^2}$, which is not stable for low ω, whereas the "movement" of background jets in to a delta-function like peak require the reliable reconstruction of a function that is nearly constant in the Fourier domain.

The fake rejection discriminant we developed is based on the fact that by restricting to a small $\sigma_{\text{dis}} = 0.1 \approx \sqrt{2\pi/(dN/d\eta)}$ (here taking the $dN/d\eta$ of Au + Au), the weighted energy inside the region is unlikely to attain a high value compared to the small angular opening in jets.

We define the "simple" Gaussian fake rejection discriminant to be

$$g_{\sigma_{\text{dis}}}(\eta, \phi) = \sum_{i \in \text{fragment}} p_{T,i}^2 h_{\sigma_{\text{dis}}}(\eta_i - \eta, \phi_i - \phi). \tag{3.56}$$

Then we introduce the leading, filter weighted, off-center fragment to be

$$m \in \text{fragment with } p_{T,m}^2 h_{\sigma_{\text{fil}}}(\eta_i - \eta, \phi_i - \phi) \text{ maximized.} \tag{3.57}$$

The center adapted Gaussian fake rejection discriminant is then

$$g'_{\sigma_{\text{dis}}}(\eta_{\text{jet}}, \phi_{\text{jet}}) = \max\left[g_{\sigma_{\text{dis}}}(\eta_{\text{jet}}, \phi_{\text{jet}}), g_{\sigma_{\text{dis}}}(\eta_m, \phi_m)\right]. \tag{3.58}$$

The discriminant was studied using HIJING [81] and for Au + Au collisions at $\sqrt{s_{NN}} = 200$ GeV. An impact parameter $b = 0$ fm was used, which corresponds to $dN_{\rm ch}/d\eta = 858$. The phenomological FRITHJOF radiation scheme used by HIJING was not used. While it enhances the $dN/d\eta$ fluctuation, it causes rare but unphysical gluon jets radiated from forward rapidity and low-p_T strings. The fake rate of the Gaussian filter was determined using 10^6 HIJING events, which is necessary to quantify the residual fake rate for an algorithm that would sufficiently suppresses the fake jets across the entire p_T range, while for the non-fully fake rejected SISCone and Fast-k_T, 8×10^5 and 4×10^5 events were sufficient to determine the fake rate, respectively.

HIJING also contains intrinsic hard scattering. While [82] tried to obtain a "non-jet" sample by imposing a maximum momentum transfer Q for the individual scattering in HIJING, this approach introduces a bias towards a smooth background, which would be especially problematic for RHIC energies, where a relatively low Q has to be imposed. We were able to obtain a clean sample by tagging each string system inside HIJING. Each string system undergoes fragmentation and individual jet reconstruction. The efficient Gaussian filter algorithm makes $\approx 10^9$ event reconstruction feasible.

The jet–string system ΔR versus the jet–string system p_T ratio $p_{T,\rm jet}/p_{T,\rm ss}$ distribution exhibits two components, one being the a correlated region where the reconstructed jet aligns with a string system, and an general, combinatorial background that however subsides rapidly above $p_T^{\rm ss} > 4$ GeV/c. We there fore use a conservative polygon cut

$$p_T^{\rm ss} > 4\ {\rm GeV}/c \wedge \Delta R < \max\{0.5, 0.2 + 0.075[p_T^{\rm ss}/({\rm GeV}/c) - 4]\} \tag{3.59}$$

to mask out area where one would find itself on top of a single string system and unsurprisingly reconstruct the string system.

Two LHC motivated algorithm–fake rejection pairs were constructed as a baseline. The SISCone [83] was combined the ATLAS Σj_T fake rejection scheme [82]. Its implementation uses the same calorimeter tower based background subtraction scheme after the ATLAS collaboration. Specifically, the same $\Delta\eta \times \Delta\phi = 0.1 \times \pi/32$ tower segmentation as the intermediate ATLAS electromagnetic calorimeter layer is implemented at particle level. The same ATLAS tower energy redistribution algorithm to avoid negative tower energy after the underlying event subtraction is also applied. The Fast-k_T [84] was combined with the p_T/A background identification suggested by the same authors [85]. The performance of Gaussian filter with $g'_{0.1}$ was found to far exceed the that of the other algorithms, and in fact, only the Gaussian filter with $g'_{0.1}$ was sufficient for RHIC purposes.

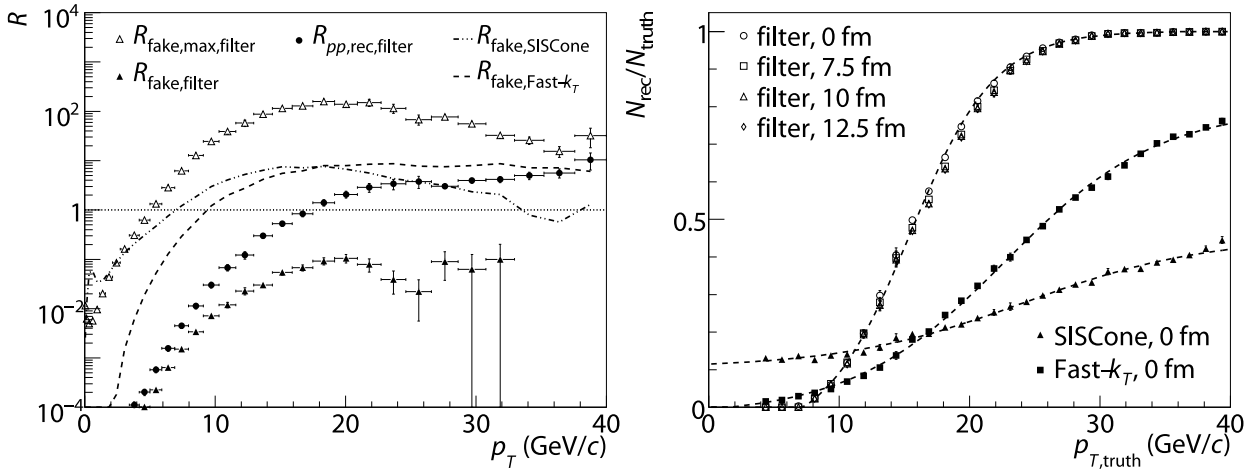

Figure 3.5: Fake rate and efficiency from HIJING's central Au + Au $\sqrt{s_{NN}} = 200$GeV collision. Shown is the performance of the Gaussian filter using $g'_{0.1}$ fake rejection, SISCone using the ATLAS Collaboration Σj_T fake rejection, and $k_\perp$ using the $p_T/A - \rho > 1.9\,\sigma/\sqrt{\langle A \rangle}$ discriminant proposed by the FastJet authors. The overall power-law behavior of the $p+p$ jet spectrum has been divided out for clarity. The rejection thresholds for SISCone and anti-$k_\perp$ were relaxed until either an efficiency of ≈ 0.3 was achieved at 20 GeV/c, or in the case of $p_T/A - \rho$, mean plus 0σ is reached.

Using the same simulation, we can also demonstrate why we need to go to p_T^2 by examining the discriminant value dependent behavior of the efficiency and fake rate. While p_T^1 results in a behavior that the fake rate only changes slowly with sacrificing the efficiency, using p_T^2 drastically changes this behavior and a large reduction of fake rate can be achieved by sacrificing little to moderate level of efficiency. It can be also shown that further increasing the power to 3 offers little gain above the quadratic weighting.

Figure 3.5 shows the fake rate and efficiency from HIJING's central Au + Au $\sqrt{s_{NN}} = 200$ GeV collision. Shown is the performance of the Gaussian filter using $g'_{0.1}$ fake rejection, SISCone using the ATLAS Collaboration Σj_T fake rejection, and $k_\perp$ using the $p_T/A - \rho > 1.9\,\sigma/\sqrt{\langle A \rangle}$ discriminant proposed by the FastJet authors.

Figure 3.6 shows the efficiency versus fake rate for $p_T > 8$GeV/c jets of central Au + Au $\sqrt{s_{NN}} = 200$GeV HIJING for g (left) and u, d, s quark jets (right) for p_T^1 weighting. Figure 3.7 shows the same for a p_T^2 weighting, and figure 3.8 shows it for a p_T^3 weighting.

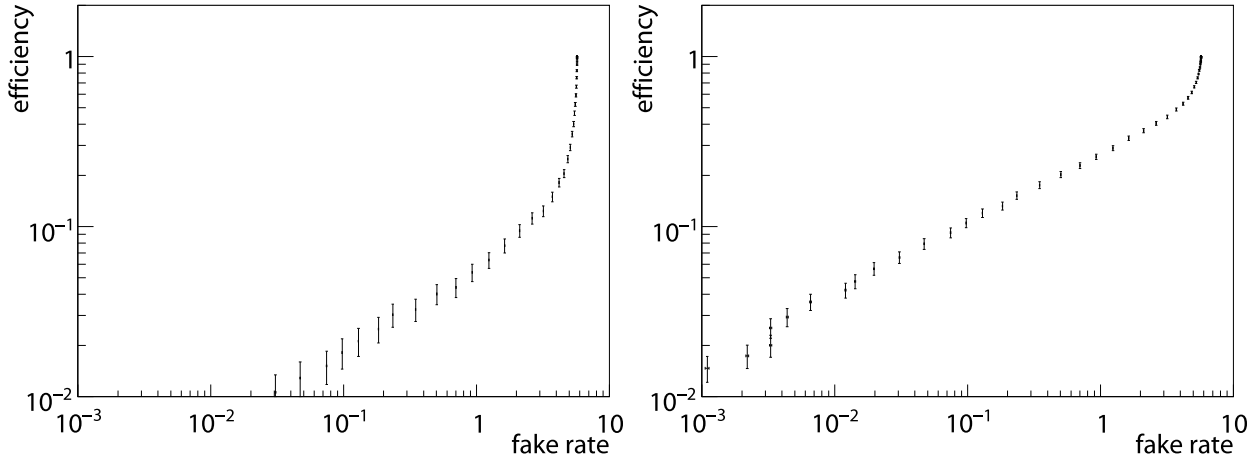

Figure 3.6: Efficiency versus fake rate for $p_T > 8$ GeV/c jets of central Au + Au $\sqrt{s_{NN}} = 200$ GeV HIJING for g (left) and u, d, s quark jets (right) for p_T^1 weighting.

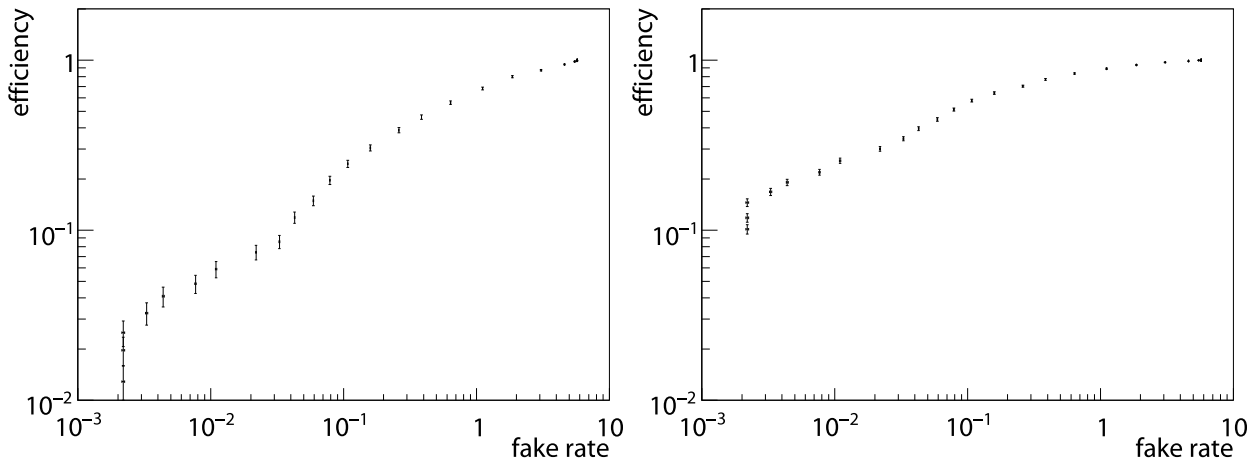

Figure 3.7: Efficiency versus fake rate for $p_T > 8$ GeV/c jets of central Au + Au $\sqrt{s_{NN}} = 200$ GeV HIJING for g (left) and u, d, s quark jets (right) for p_T^2 weighting.

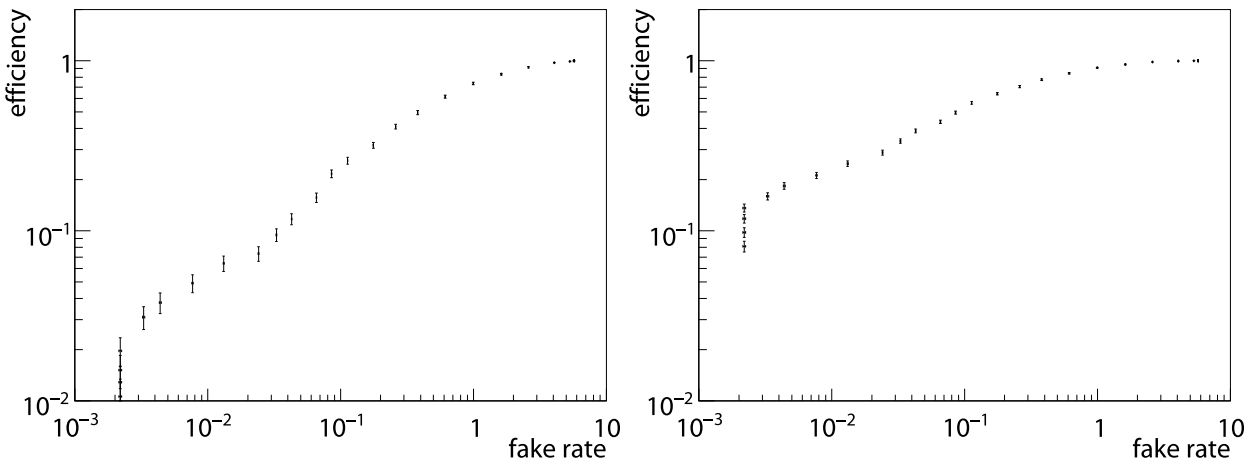

Figure 3.8: Efficiency versus fake rate for $p_T > 8$ GeV/c jets of central Au + Au $\sqrt{s_{NN}} = 200$ GeV HIJING for g (left) and u, d, s quark jets (right) for p_T^3 weighting.

Chapter 4

Experimental Setup

4.1 RHIC Accelerator Complex

The Relativistic Heavy Ion Collider (RHIC) accelerator complex is situated at the Brookhaven National Laboratory (BNL) in Upton, New York, and is the extension of the Alternating Gradient Synchrotron using the then abandoned Collider Beam Accelerator (CBA) tunnel, which serves as the injection accelerator for RHIC.

Figures 4.1 and 4.2 show the layout of the RHIC accelerator complex as a map and aerial photograph.

Depending on the beam type, the initial ionization and acceleration occurs in either the Linear Accelerator or the Tandem Van de Graaff accelerator.

4.1.1 Linear Accelerator/LINAC-to-Booster Line

The linear accelerator starts with the optically pumped polarized ion source (OPPIS), which produces a beam of spin-polarized H^-, and is pulsed 0.350 ms, corresponding to 1/4 of the AGS pulse. This is then accelerated by a 144.8 m to an energy of 200 MeV. Momentum selection is achieved using a 120° bend in the transfer line to the AGS Booster.

Figure 4.3 shows the layout of the LINAC-to-Booster and Tandem-to-Booster Line.

4.1.2 Tandem Van de Graaff/Tandem-to-Booster Line

The Tandem Van de Graaff facility consists of two model MP accelerators, manufactured by the High Voltage Engineering Corporation (HVEC, founded by R. J. Van de Graaff himself), and upgraded using the Pelletron charging system to achieve a terminal voltage of 15 MV. Generator MP7 serves as the main source for RHIC operation, which is fed using a pulsed solid state sputter source. MP6 serves as a spare for RHIC, and is also the source for the NASA Space Radiation Laboratory (NSRL) and other users.

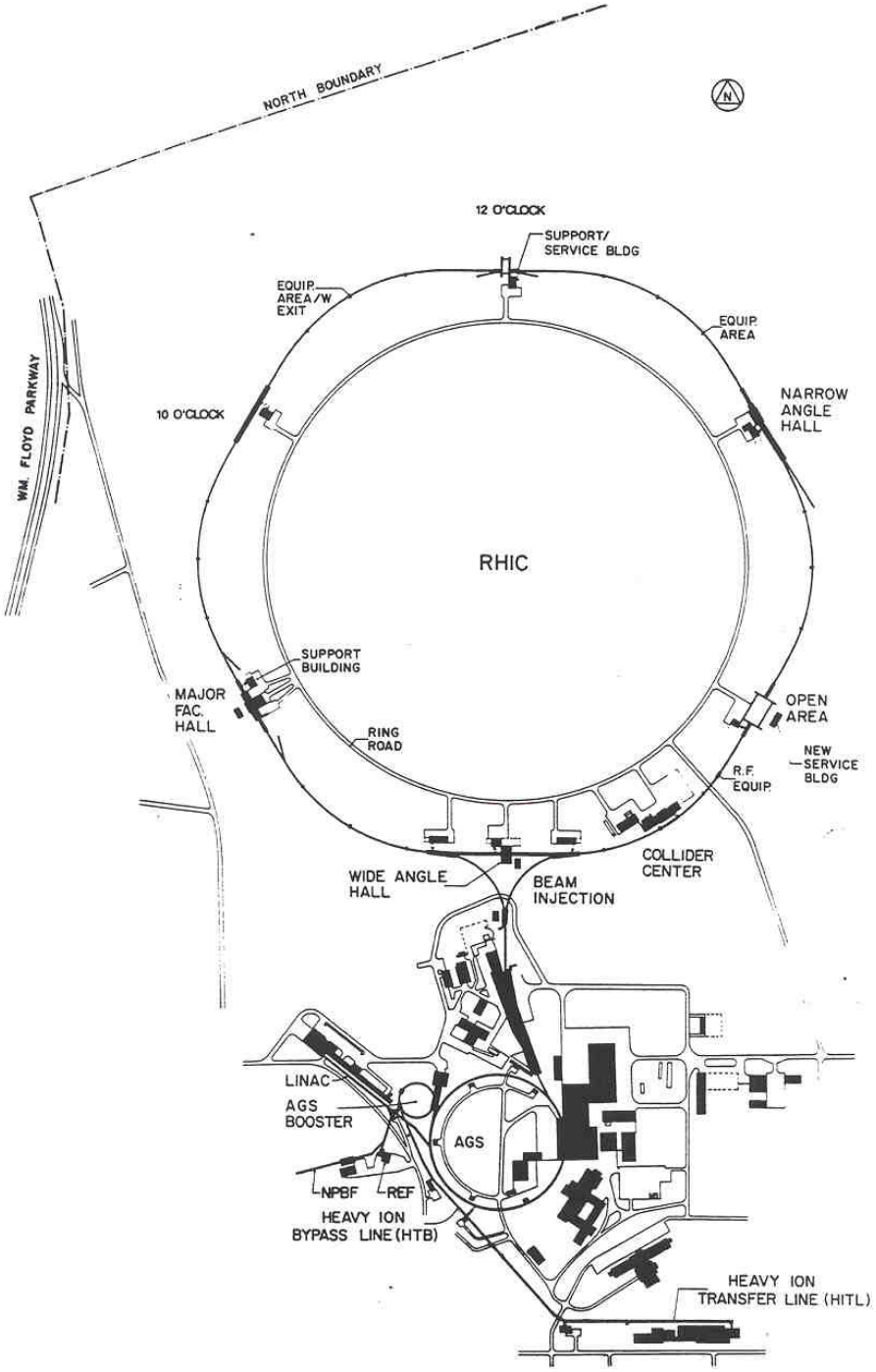

Figure 4.1: Map of the RHIC complex at BNL, from [12].

Figure 4.2: Aerial photograph of BNL superimposed with the storage rings and beam lines of the RHIC complex.

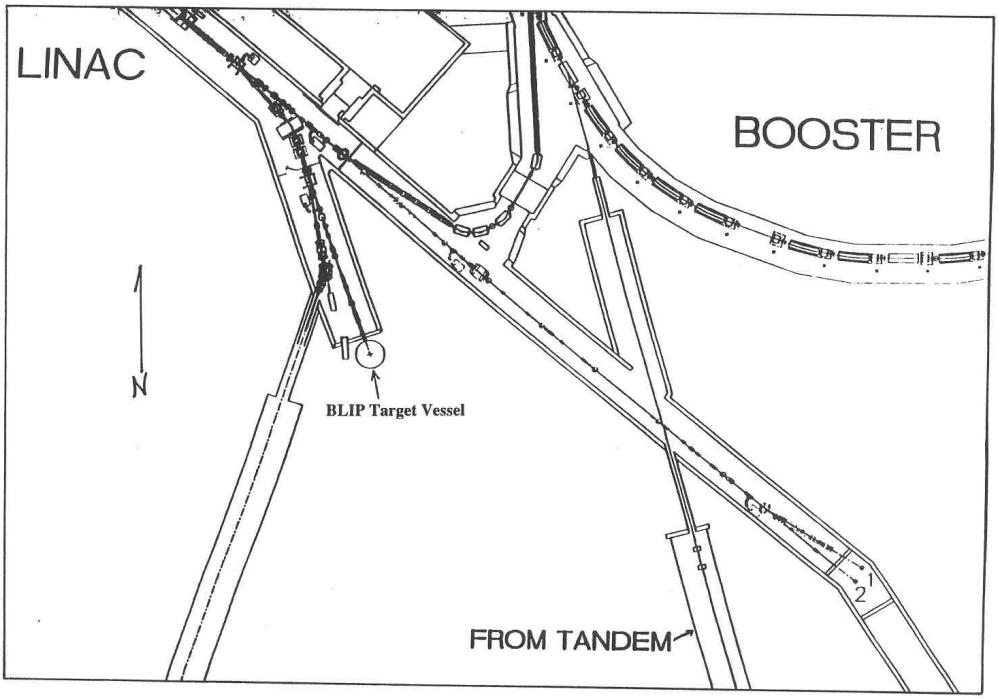

Figure 4.3: Layout of the LINAC-to-Booster and Tandem-to-Booster Line, from [12].

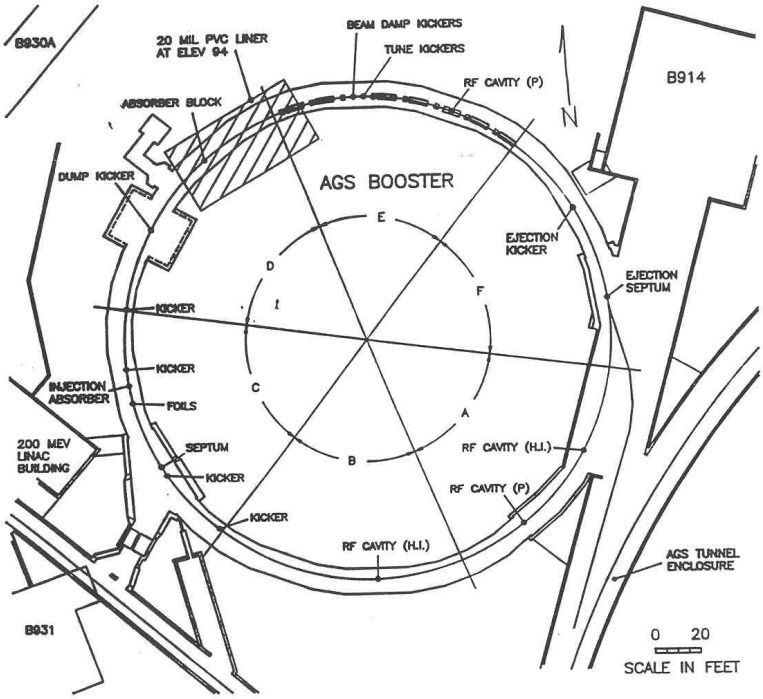

Figure 4.4: Layout of the AGS Booster and Booster-to-AGS Line, from [12].

Still in the Tandem facility, ions emerging from MP6 and MP7 makes a U-turn by two 90° bend with 1.526 83 m radius. Charge and momentum selection is accomplished by the first bend. The TTB transport line contains four additional bends, which are made acromatic using tuned quadrupole magnets.

4.1.3 Booster/Booster-to-AGS Line

As a strongly focusing synchrotron, the Booster has a alternating gradient (a principle originating from the BNL Alternating Gradient Synchrotron) lattice design, where cells are arranged to a QF OO QD OO structure, or FODO cells. QF is the quadruple focusing magnet, which (by convention) denotes one that focuses the beam horizontally and defocuses vertically, OO (as for orbit) is either drift space or a bending dipole, and QD the quadrupole defocusing magnet, which is a QF configuration rotated by $\pi/2$ with respect to the beam axis. The combination of focusing and defocusing magnet creates an overall focusing beam optics. In addition, sextupole magnets SF and SD are inserted into the FODO lattice, where the correct the chromaticity of the beam by introducing a momentum dependent focusing.

The Booster consists of six superperiods (denoted A–F) and four FODO cells per superperiod. The total circumference is $C_{\text{Booster}} = 201.78$ m, while the dipole bending radius is 13.8656 m. Booster injection from

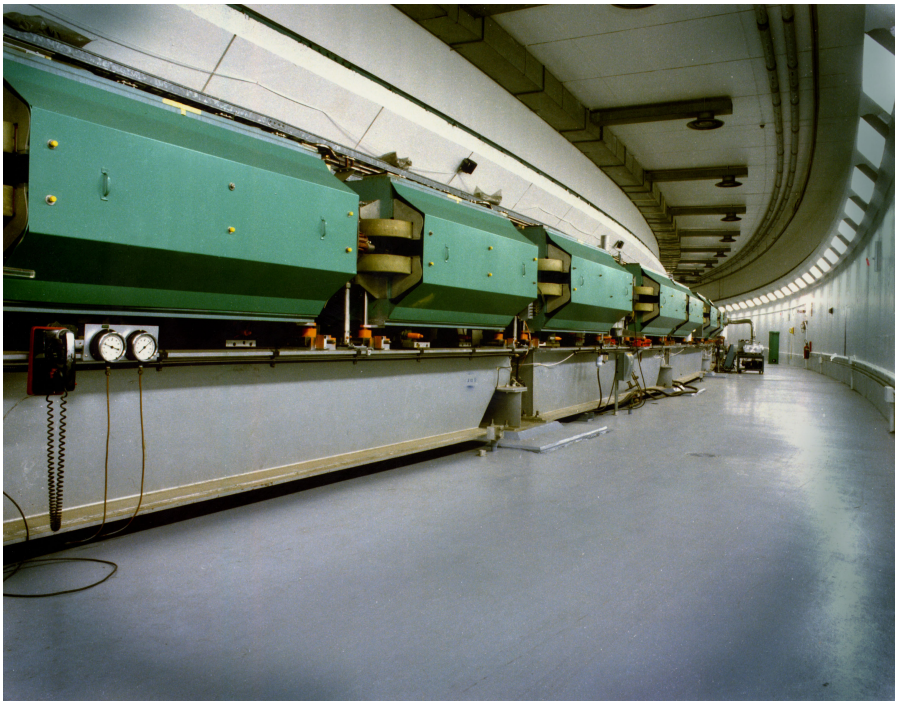

Figure 4.5: Photograph of the interior of the AGS tunnel at BNL.

the TTB occurs at the C3 straight section, and is done using a cathode and septum magnet combination, with four kicker magnets. Booster injection from the LTB uses the charge exchange method. The C5 dipole has a displaced return yoke to accommodate the injection. A 200 $\mu g/cm^2$ carbon stripping foil is inserted into the front part of the C6 straight section. And the charge exchanged protons are deflected into the orbit by the C7 dipole. Booster extraction to AGS occurs at the F6 septum, while the D6 septum magnet leads to the transport line to the NSRL target room.

Figure 4.4 shows the layout of the AGS Booster and Booster-to-AGS Line.

4.1.4 Alternating Gradient Synchrotron

The Alternating Gradient Synchrotron (AGS) is a (in fact, the first) synchrotron that controls the transverse beam dynamics, which is dominated by the betatron oscillation, using alternating focusing–defocusing cells. The nominal AGS circumference is $C_{\mathrm{AGS}} = 807.104\,75$ m, which is $4C_{\mathrm{Booster}}$. For the RHIC circumference design we will discuss below, the extraction of beam using a system of kicker magnets slightly lengthens the orbit to the extraction orbit circumference, which has been measured to $C_{\mathrm{AGS}}^{\mathrm{extr}} = 807.125\,26$ m.

The AGS lattice is divided into 12 superperiods, designated A–L, each contains 20 dipole magnets, one

horizontal plus one vertical quadrupole, and one horizontal and one vertical sextupole magnet. Injection occurs at A5, and the extraction to the AGS-To-RHIC Transfer Line G10.

Figure 4.5 shows a photograph of the interior of the AGS tunnel.

4.1.5 AGS-To-RHIC Transfer Line

The 770 m AGS-To-RHIC Transfer Line (ATR) has a more complex structure than the previous transfer lines. ATR is divided in several sections. The U-line is next to the AGS extraction, and start with the 4.25° bend, and forks with a 8° bend from the line leading to AGS E821. The W-line transports the beam to the symmetric X/Y-lines, and contains a 20° horizontal bend together with a 1.73 m level drop near the middle. A switch dipole directing the beam to either X or Y-line, each contains a horizontal 90° bend, and multiple vertical bends leading to the RHIC injection points.

4.1.6 Stripping

For proton RHIC injection, the H^- beam coming from the LINAC is fully stripped by the 200 µg/cm^2 carbon LTB foil, during Booster injection. For Cu beam, the Cu^- ions are generated from a sputter source and accelerated to +13 MV potential, where it passes through the terminal stripping (denoted S1) by a 4 µg/cm^2 carbon foil. The Cu^{11+} ions are further stripped when injected into the AGS and by a 14 mg/cm^2 carbon BTA foil (S3) to the fully stripped Cu^{29+} state. For the Au beam, the two additional object foil (S2) and ATR foil (S4) are used. The Au^- ions are stripped to Au^{12+} at S1, followed by the object foil at S2 to Au^{31+} at the entry of the TTB. S3 strips the ions further to Au^{77+} at AGS injection, and after S4 at the entrance of ATR finally reaches the fully stripped state of Au^{78+}.

4.1.7 RHIC

4.1.7.1 Basic Parameter

RHIC is a intersecting storage ring (ISR) accelerator, in which the collision of independent particle species at the center-of-mass (CM) is facilitated using two rings operated with independent magnetic and radio-frequency (RF) fields. These two rings are arbitrarily labeled using the colors “yellow” and “blue”. Looking down from the air/space, ions (or because positive ions are accelerated, equivalently $+qv$) bunches in the yellow ring travel counterclockwise, i.e. at the PHENIX interaction region, from the compass direction NNW

Figure 4.6: Photograph of the interior of the RHIC tunnel at BNL.

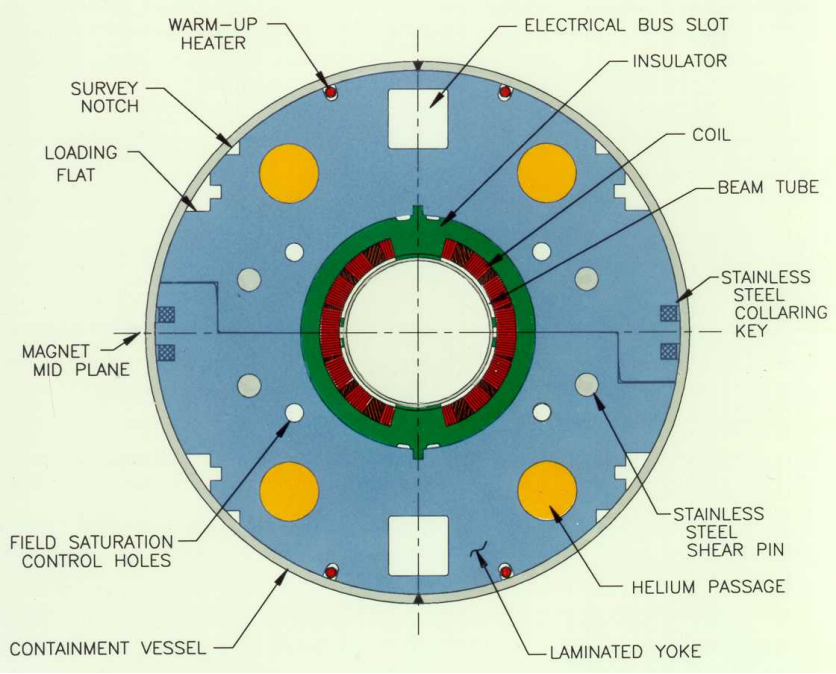

Figure 4.7: Computer-aided design drawing of the Cross section of a RHIC arc dipole magnet, color version of drawings from [13].

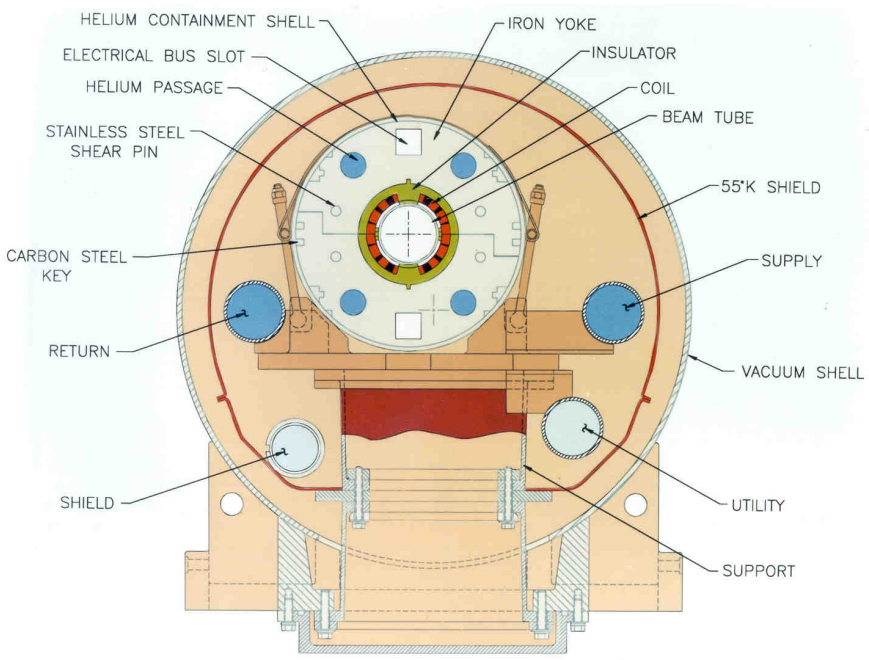

Figure 4.8: Computer-aided design drawing of the cross section of a RHIC arc dipole magnet integrated inside the cryostat, color version of drawings from [13].

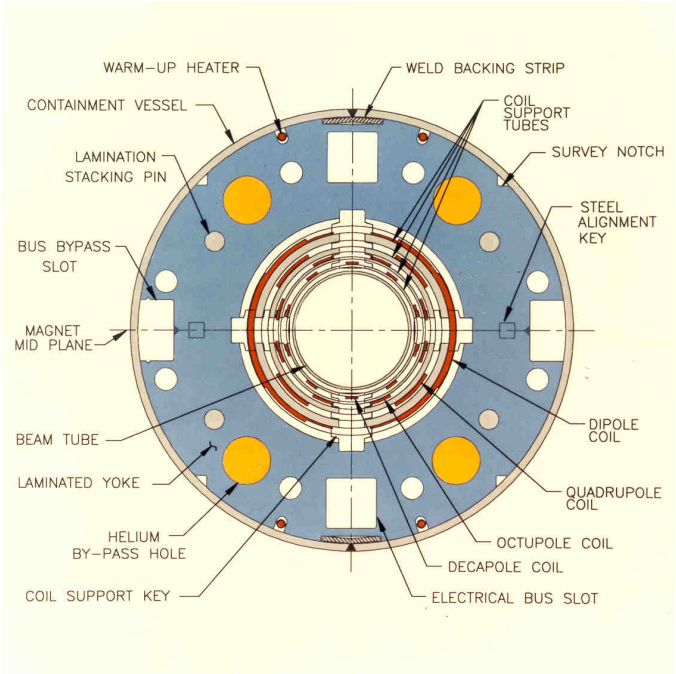

Figure 4.9: Computer-aided design drawing of the cross section of a RHIC corrector magnet, color version of drawings from [13].

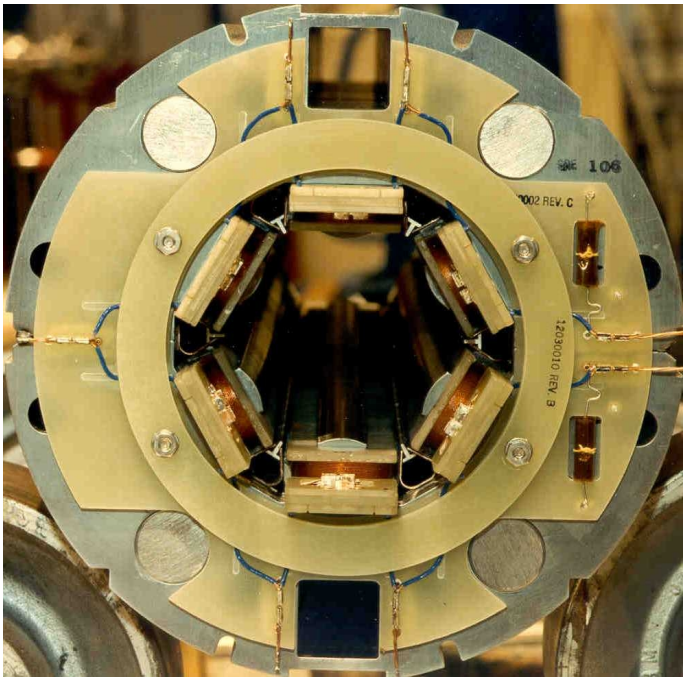

Figure 4.10: Cross section photograph of a RHIC sextupole magnet.

to SSE, and vice versa for the blue ring. When running in d + Au mode, the yellow ring is filled with Au bunches.

The difference with the blue/yellow ring as the inner/outer arc causes the RHIC to be symmetric in three superperiods, each containing 12 FODO cells each 29.622 m long, and 24 half cells with a 9.46 m long dipole, a 1.13 m long quadrupole, and a 0.75 m long sextupole. The total ring circumference is $C_{\mathrm{RHIC}} = \frac{19}{4} C_{\mathrm{AGS}}^{\mathrm{extr}} =$ 3834 m in circumference (which allows a easier injection by coupling the AGS and RHIC lattices), and has a circular–hexagonal shape, i.e. consisting of both nearly straight 313 m long and circular arc section with an average bending radius inside the arc of 380 m, the center of which sits on a hexagon with the radius 240 m.

The particles are deflected using 1740 superconducting NbTi (a type II superconductor with $T_c = 9.2$ K) dipole magnets operating 5.093kA current and 3.458T field. The arc dipole bending radius is 243m. The beam are bent into each of the six interaction regions using a pair of DX magnets. Since different species are being collided at RHIC, the final focusing magnet is place before the common dipole DX magnet, which is 18 cm wide to accommodate different species. The maximum magnetic rigidity at RHIC is $B\rho = 839.5$ T m at top energy (while $B\rho = 81.114$ T m at injection). This means that attainable beam energies are $E = 100$ GeV/u for Au beams, $E = 125$ GeV/u for light ions, and $E = 250$ GeV/u for protons.

Figure 4.4 shows a photograph of the interior of the RHIC tunnel.

Figures 4.7–4.9 shows computer-aided design (CAD) drawing of the cross section of a RHIC arc dipole, of the arc dipole integrated inside the cryostat, and of the corrector magnet. Figure 4.10 shows the cross section photograph of a RHIC sextupole magnet.

4.1.7.2 Beam Dynamics and Luminosity

Some review of the basic synchrotron beam motion is needed for the discussion RHIC luminosity. Betatron oscillation in a synchrotron is described by the Hill's equation

$$\frac{d^2x}{ds^2} + K(s)x = 0 \tag{4.1}$$

where $K(s)$ is a periodic restoring coefficient, and s parametrizes the longitudinal beam travel distance. The Hill's equation integrated is solved algebraically by Fourier transform $K(s)$, and gives three parameters from the initial condition of the beam, the transverse emittance ε, the betatron amplitude function $\beta^*(s)$, and the phase advance $\psi(s)$. The horizontal equation of motion (with the initial phase δ) takes the form

$$x = \sqrt{\varepsilon\beta^*(s)}\cos(\psi(s) + \delta) \tag{4.2}$$

The Hill's equation for the so expressed, monochromatic transverse beam motion becomes a algebraic equation of transport matrices. Since for the cross section (assuming for a moment a circular beam and note that σ_x is also the half linear size)

$$\text{cross section} = 4\pi\sigma_x^2 = 4\varepsilon\beta^*(s) \tag{4.3}$$

(avoiding multiple usage of the symbol σ for clarity), it follows that

$$\varepsilon = \frac{\pi\sigma_x^2}{\beta^*}. \tag{4.4}$$

At a storage ring with two independent beam intensities, in case of RHIC denoted as N_{blue} and N_{yellow}, the luminosity takes the slightly more elaborate form

$$\mathscr{L}_{\text{machine}} = \frac{f_{\text{rev}}}{2\pi\sigma_x^{\text{V}}\sigma_y^{\text{V}}}\sum_{\text{crossing}} N_{\text{blue}}N_{\text{yellow}} \tag{4.5}$$

Here, the f_{rev} is the revolution frequency for a given RHIC store. For identical B bunches in both rings,

$$\sum_{\text{crossing}} N_{\text{blue}}N_{\text{yellow}} = BN^2. \tag{4.6}$$

The beam profiles σ^{V} denote the convolved beam profiles, which unlike the individual "blue" and "yellow" profiles, are directly measurable using the van der Meer method, also called the vernier scan. In case of Gaussian beam profiles,

$$\begin{aligned}(\sigma_x^{\mathrm{V}})^2 &= \sigma_{x,\mathrm{blue}}^2 + \sigma_{x,\mathrm{yellow}}^2 \\ (\sigma_y^{\mathrm{V}})^2 &= \sigma_{y,\mathrm{blue}}^2 + \sigma_{y,\mathrm{yellow}}^2.\end{aligned} \tag{4.7}$$

Note that $\sigma_{x,y}^{\mathrm{V}} = 2\sigma_{x,y}$ for identical beams.

Using the result above, we obtain the machine luminosity with respect to the beam emittance as

$$\mathscr{L}_{\mathrm{machine}} = \frac{f_{\mathrm{rev}}}{4\sqrt{\varepsilon_x\beta_x^*\varepsilon_y\beta_y^*}} \sum_{\mathrm{crossing}} N_{\mathrm{blue}}N_{\mathrm{yellow}}. \tag{4.8}$$

Since adiabatic damping decreases the beam emittance as inversely proportional to the beam momentum, the BNL Collider–Accelerator Department (C–AD) frequently uses the definition of a normalized emittance that corresponds to a 95% beam contour [86]

$$\varepsilon_{\mathrm{N}} = \beta\gamma\frac{6\pi\sigma^2}{\beta^*} \tag{4.9}$$

and the machine luminosity in this form is

$$\mathscr{L}_{\mathrm{machine}} = \frac{3}{2} f_{\mathrm{rev}} \frac{\beta\gamma}{\varepsilon_{\mathrm{N}}\beta^*} \sum_{\mathrm{crossing}} N_{\mathrm{blue}}N_{\mathrm{yellow}} \tag{4.10}$$

The design luminosity for RHIC is $\mathscr{L} = 2\times10^{26}\mathrm{cm}^{-2}\mathrm{s}^{-1}$ for $E = 100\mathrm{GeV}/u$ Au beams and averaged over 10 hours. Additional, detector dependent details of the experimental luminosity measurement is deferred to section 4.2.5.

4.2 PHENIX

PHENIX combines a central rapidity spectrometer (the "Central Arms") with forward tracking and calorimetry for $\mu^{\pm}$. Unlike traditional, hermetic detector design, the central rapidity spectrometer only partially covers the midrapidity, while the magnet field is a dipole field.

In the PHENIX coordinate system, $\hat{x}$ vector points to the WSW, $\hat{y}$ skywards/away from the center of Earth, and $\hat{z}$ to the NNW, i.e. in the travel direction of ions in the blue ring. The origin $(0,0,0)$ is at the nominal collision point. PHENIX is generally measures using the CGS system of units.

Figure 4.11 shows the layout of the PHENIX detector systems.

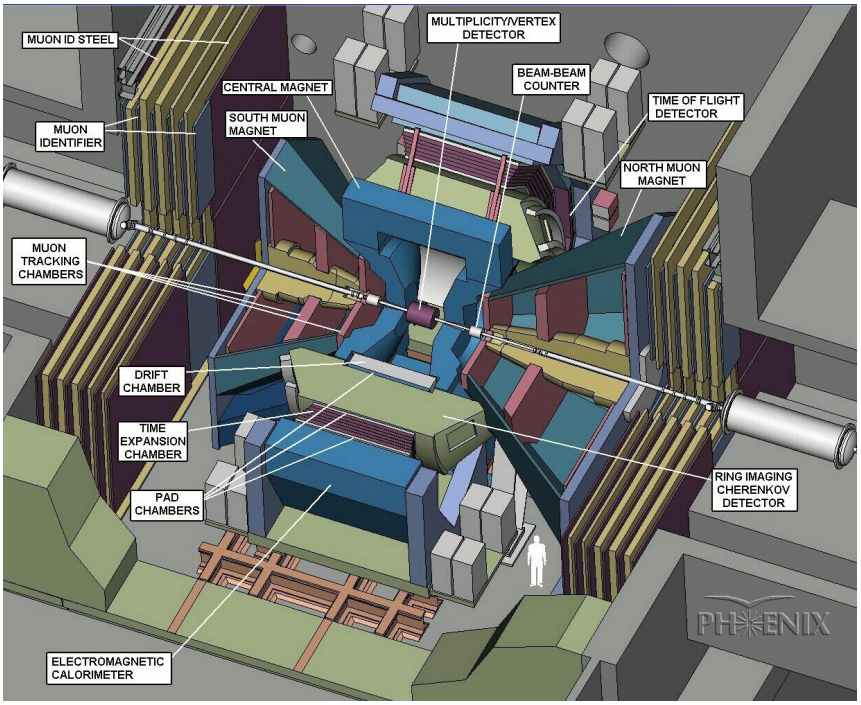

Figure 4.11: Layout of the PHENIX detector subsystems.

4.2.1 Central Arm Detectors

At midrapidity, the PHENIX detector configuration at Run-5 consists of two spectrometer arms. Because of the definition of the PHENIX coordinate system, the arm towards $+\hat{x}$ from the collision point west arm is called the West Arm, and the arm towards $-\hat{x}$ the East Arm.

4.2.1.1 Particle Identification

We will start the discussion of the PHENIX detector subsystems with a detector not directly used in this analysis, but nevertheless provides the tracking momentum scale and is crucial in determining the momentum resolution of the tracking system.

The time-of-flight detector (TOF) is a scintillation detector covering the PHENIX east arm. It consists of 10 panels with 96 scintillator slats each. The segmentation is designed for a $dN_{\mathrm{ch}}/d\eta = 1500$, for which the average occupancy per panel is kept below 0.1 to avoid large number of double hits. The scintillator material is the plastic Bicron BC404. The light is channeled through a light guide to Hamamatsu R3478S photomultiplier tubes (PMTs), which are arranged perpendicular in a residual field of $< 10^{-3}$ T strength. The TOF is placed

Variable	R_{inner} (cm)	R_{outer} (cm)
n0	3.4	8.4
n1	—	11
n2	—	8.4
n3	3.9	7.9

Table 4.1: The four PHENIX RICH phototube counting ring variables and the associated radii

5.1 m from the collision vertex, and is sandwiched between PC3 and the EMCal.

The timing resolution of the TOF is $\sigma_{\text{TOF}} \approx 100$ps and can be estimate by the observed timing distribution for π^+. A rigorous determination however requires a simultaneous fixing of the tracking momentum scale, which we defer to the next section.

The other central arm PID detector, responsible for electron identification, is the ring-imaging Cherenkov detector (RICH). Each arm contains a RICH detector, consisting of 40m^3 volume and 48 intersecting spherical Al mirror panels, which focuses the Cherenkov light onto 1280 Hamamatsu H3171S UV PMTs per sector. Since RHIC is positioned closer to the inner field, the PMTs are magnetically shielded to allow operation in field up to 10^{-2} T. Based on GEANT simulation, and due its optical transparency in UV and low radiation length, CO_2 with $n = 1.000\,410$ was chosen as radiator gas, while the better performing, but flammable ethane can be used as alternative. The radiator gas is held at an overpressure of 0.5″ water column. When filled with ethane gas, the RICH has a total radiation thickness of 2%.

The CO_2 radiator translates into a threshold $\gamma = 35$, which is $p > 0.02$ for $e^{\pm}$ and $p > 4.9$ for $\pi^{\pm}$, with the latter gives a upper momentum constraint for reliable electron identification. Electron identification is performed by observing sufficient amount of photoelectrons along the expected ring geometry of $R_0 = 5.9$ cm. Accounting for ± 2.5 cm variations, an annulus is used with the inner radius of 3.4 cm and the outer radius being 8.4 cm. Other variables have been designed for situations when misalignment is suspected or to provide a tighter cut at ± 2 cm.

Table 4.1 lists the four PHENIX RICH ring variables counting the track associated phototube and their associated radii.

Figure 4.12 shows the identification of $\pi^{\pm}$, $K^{\pm}$, and $p/\bar{p}$ using the PHENIX TOF detector in $\sqrt{s_{NN}} = 130$ GeV Au + Au collision.

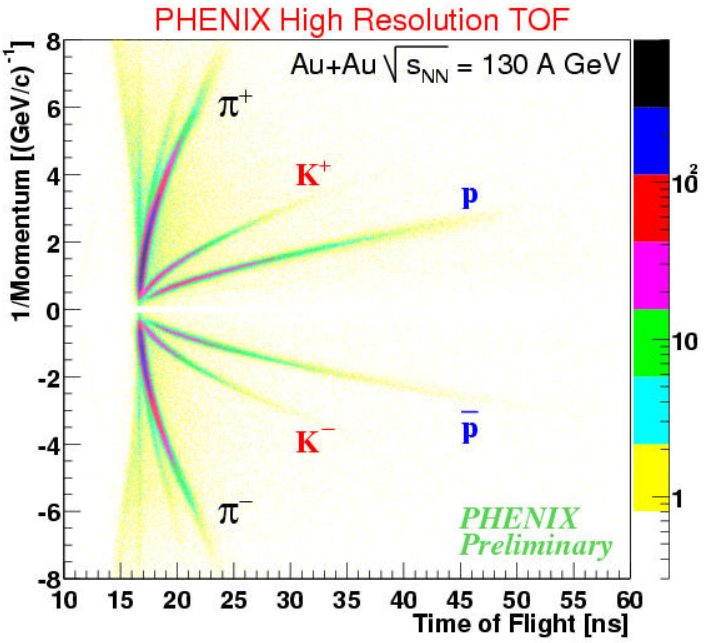

Figure 4.12: Identification of $\pi^{\pm}$, $K^{\pm}$, and $p/\bar{p}$ using the PHENIX time-of-flight detector in $\sqrt{s_{NN}} = 130$ GeV Au + Au collision.

4.2.1.2 Tracking detectors

The PHENIX central arm tracking detectors consists of a stacked sequence of drift chamber (DC) and pad chambers (PC). The DC is a specialized form of multiwire proportional counter (MWPC) with timing capability to resolve the hit position along the wire. Charged tracks causes gas in the DC to avalanche, and due to a potential gradient, electrons and ions separate and drift in a uniform field created by anode and cathode wires. The fast moving electrons causes a current pulse of $\approx$ 10 ns duration in the anode wires, which is integrated to the measured signal. The DC is characterized by two main calibration parameters, the effective ionization time t_0 and the effective drift velocity v_0. Both can be obtained by measuring the leading and tailing edge of the drift time distribution. The PHENIX DC gas mixture consists of 49% Ar, 49% C_2H_6, and $\approx$ 1.5% ethanol.

Compared to the original MWPC design, DC uses potential or field wires (P) between anode wires to improve charge collection. The PHENIX DC is additionally a DC with focused geometry, where additional field forming wires are placed to break the left/right ambiguity and narrowed sample length. Drifting electrons in the intended direction are focused towards the anode wires using gate (G) wires that localize the drift region by generating a high field near the anode wire, while electrons from the opposite drift directions are stopped

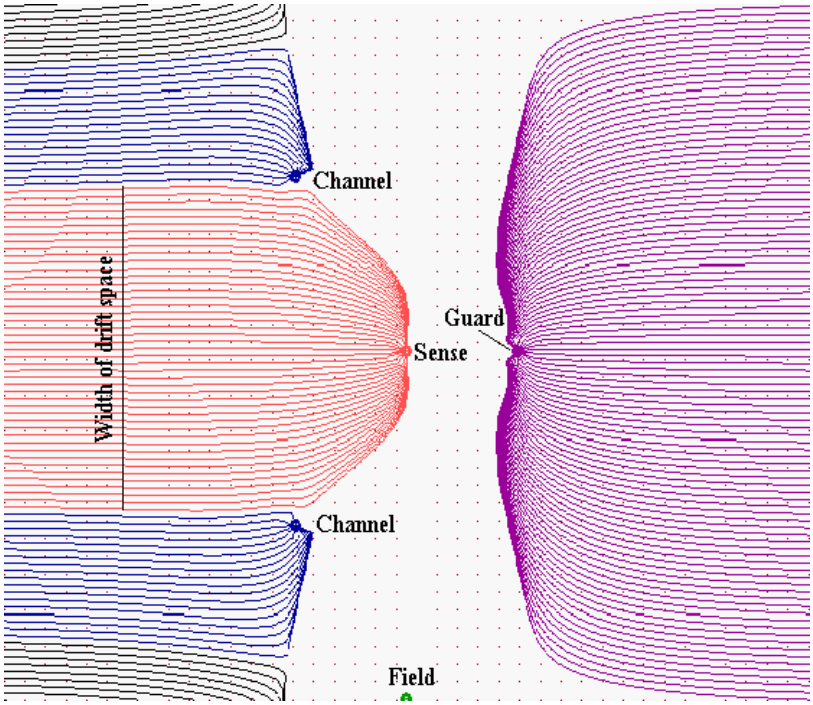

Figure 4.13: Field lines of the focused PHENIX DC geometry in a GARFIELD simulation.

by the back (B) wire. At the outer bound of the planes, the potential wires are joined by additional termination wires. The PHENIX DC single wire efficiency is $\approx$ 0.95–0.98, while the back efficiency is $<$ 7%.

The wires in the PHENIX DC is organized radially into six radial planes. The X1, X2 wires are in parallel to the z axis, and provide (r, ϕ) measurement of track hits. Each X1, X2 plane is surrounded by U1, V1, and U2, V2 stereo planes, which contain wires having a stereo angle of $\approx$ 6° to resolve the z coordinate of the track. The X planes contain 12 anode wires, and each U or V plane four. Group of four anode–cathode planes is organized into one keystone.

Figure 4.13 shows the field lines of the focused PHENIX DC geometry in a GARFIELD simulation.

The PC are the only nonprojective elements in the PHENIX central arms and therefore crucial for the pattern recognition. The PC is a MWPC with pixel-pad cathode. The pad pixel of PC1 is organized in to cells of 8.2 $\times$ 8.4 mm^2, while PC2 14.2 mm and PC3 16.7 mm. To achieve a good z resolution, the cell is subdivided into three pixels along the z direction, resulting in a z resolution of $\pm$1.7 mm. To save readout channels, three layers of three diagonal pixels are chained together into a single readout channel. Coincidence of three adjacent z pixels (which by organization of the chaining, are in three separate channels) is required to suppress electronic noise. The tracking system formed by the DC and PC1 is also called as the intermediate

DC/PC1 Hit Property	Bitmask
X1 used	000001_2
X2 used	000010_2
UV found	000100_2
UV unique	001000_2
PC1 found	010000_2
PC1 unique	100000_2

Table 4.2: DC/PC1 hit properties and associated bitmasks for the PHENIX central arm tracks.

tracker (ITR), and PC2/PC3 as the outer tracker.

Expressed in ratio to the radiation length, the DC has an thickness of $\approx$ 0.2%, the PC1 $\approx$ 1.2%, and the PC2/PC3 $\approx$ 2.4%. This still means that in the measurement of a steeply falling spectrum, momentum misconstruction due to the lack of in-field tracking can contribute significantly to the set of measured high-p_T particles. The DC and PC1 combined form the primary tracking subsystem. Each track is tagged with a track quality bitmask.

Table 4.2 lists the DC/PC1 quality bit and their properties.

The overall tracking pattern recognition and momentum reconstruction uses the combinatorial Hough transform, which calculates the track parameter for all possible combination of hits, and reconstructed tracks appear as the lining up of combinations as local maxima in the track parameter space. In a first order approximation (constant field and $\eta = 0$), the momentum scale at the DC is determined by the effective field integral

$$K = \int \mathbf{B} \times d\mathbf{l} = 87 \text{ mrad GeV}/c \tag{4.11}$$

which also enters the momentum resolution that is a combination of the intrinsic angular resolution σ_α and multiple scattering of the charged particle in the detector material σ_{MS}:

$$\left(\frac{\delta p}{p}\right)^2 = \left(\frac{\sigma_\alpha}{K} p\right)^2 + \left(\frac{\sigma_{\text{MS}}}{K\beta}\right)^2 \tag{4.12}$$

Using an additional parameter σ_{TOF}, the mass resolution of the TOF can be expressed as

$$\sigma_{m^2} = \frac{4m^4 p^2}{K^2}\sigma_\alpha^2 + \frac{4m^4}{K^2}\left(1 + \frac{m^2}{p^2}\right)\sigma_{\text{MS}}^2 + \frac{4p^2c^2}{L^2}(m^2 + p^2)\sigma_{\text{TOF}}^2 \tag{4.13}$$

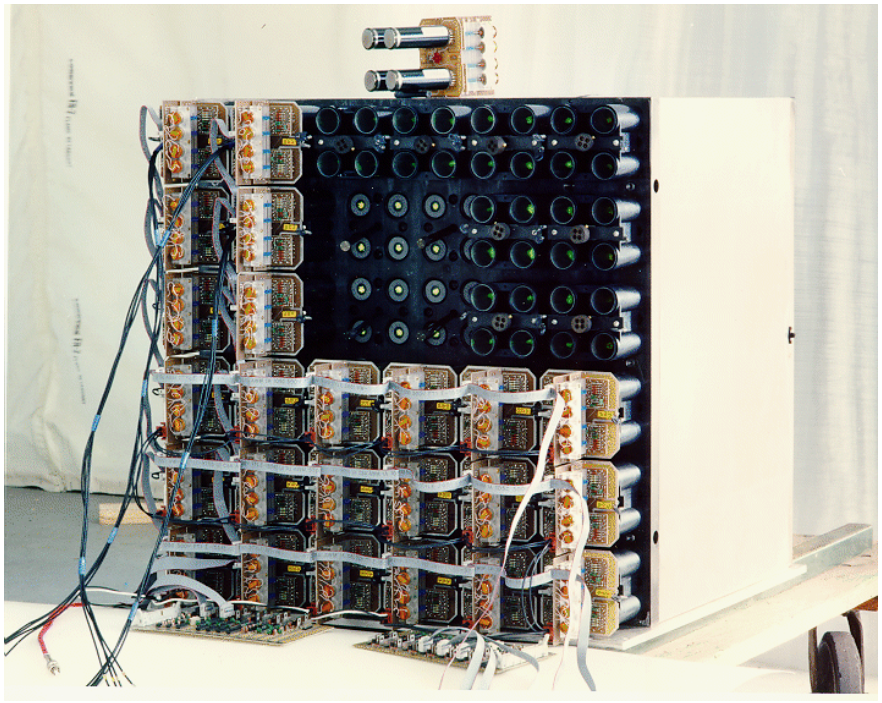

Figure 4.14: Photograph of a quarter PbGl supermodule during testing.

The angular resolution can be additionally checked using Using zero field data, the angular resolution can be additionally confirmed as $\sigma_\alpha = 0.84 \pm 0.05$ mrad $(\mathrm{GeV}/c)^{-1}$. Using the combined fit, the momentum resolution of the tracking system is determined as

$$\frac{\delta p}{p} = 0.7\% \oplus 1.0\% \frac{p}{\mathrm{GeV}/c} \tag{4.14}$$

4.2.1.3 Electromagnetic Calorimeter

EMCal measure the energy by detecting the shower of secondary particles, which is produced when the primary particle interacts with the absorber. With proper calibration, calorimeter measure the energy deposit directly, and can provide online measurement of the energy deposit in an event, as opposed to tracking, which requires pattern recognition and momentum reconstruction that are difficult to produce at the rate of the collisions. Therefore, the EMCal is also the crucial component to provide fast triggering on high-p_T events.

The PHENIX experiment contains both major types of EMCal: Six of the total eight sectors are covered by Pb–scintillator (PbSc) calorimeters. The PbSc tower is a sampling detector consisting of alternating

1.5mm Pb and 4mm scintillator layers, with the scintillator being 0.01% p-bis[2-(5-phenyloxazolyl)]-benzene (POPOP) with 1.5% additive p-terphenyl (PT). Two sectors are covered by Pb–glass (PbGl) calorimeters that were previously used at the WA98 experiment at CERN SPS. The PbGl towers are homogeneous, non-imaging Cherenkov detectors, where a Pb-glass medium with 51% Pb-oxide both generates the secondary particles and also serves as the Cherenkov radiator. In both types, the generated light is then read out using PMTs. The generated photons is proportional to the energy deposit, but leakage causes nonlinearity effects for low energy electrons and photons, which have to be corrected.

Since the longitudinal energy loss in an EMCal is given by

$$\frac{dE}{dz} = -\frac{E}{X_0} \tag{4.15}$$

the characteristic longitudinal size of the shower is exponential and decreases with the radiation length X_0. The lateral size of the shower is dominated by multiple scattering, and is described by the Moliere radius R_{M}, which is related to the radiation length via

$$R_{\mathrm{M}} = X_0 \frac{E_s}{E_c} \tag{4.16}$$

where $E_s = \sqrt{4\pi/\alpha}\, m_e c^2 \approx 21$ MeV is the scale energy, and E_c is the material dependent electron critical energy. For PbSc towers, $X_0 \approx 20$ mm, and the module length of 37.5 cm corresponds to $\approx 18X_0$. For the PbGl towers, $X_0 \approx 28$ mm and the module length of 40 cm is $14.4X_0$. For PbSc towers, $R_{\mathrm{M}} \approx 30$ mm, and for PbGl, $R_{\mathrm{M}} \approx 36.8$ mm.

While electrons and photons interact with the absorber via bremsstrahlung and pair production, hadronic interaction produce significantly different shower shapes. Rejection of hadrons are therefore done using shower shape cuts. The measured energy distribution among the towers for electrons is used to produce an analytic parametrization of tower energy distribution with respect to the impact point. The χ^2 distance of the measured distribution to the parametrization characterizes the "electromagneticness" of the shower. Distribution for electrons and pions cross over at $\chi^2 \approx 3$ dof.

Both detectors are timing capable. The PbSc has the better timing resolution of $\approx$ 120 ps for electrons and protons depositing $E \geq 0.5$ GeV, and $\approx$ 270 ps for pions. The timing resolution for electromagnetic showers in the PbGl is also $\approx$ 200 ps, but the position offset of hadronic showers causes hadronic TOF to be shifted by -800 ps.

The tower segmentation for PbSc is approximately 5.535×5.535 cm^2 or $\Delta\eta \times \Delta\phi \approx 0.01 \times 0.01$ while the PbGl segmentation is 4×4 cm^2 or $\Delta\eta \times \Delta\phi \approx 0.008 \times 0.008$ For both technologies, 12×12 towers are

grouped together to form a supermodule, while each sector contains 3×6 PbSc or 4×8 PbGl supermodules.

The resolution of both technologies has been determined using e^- test beam from the AGS between 0.5–5 GeV/c and using e^- test beam from the SPS between 10–80 GeV/c. The energy resolution was found to have a Gaussian shape. A quadratic fit to the combined AGS/SPS test beam data yields an energy resolution for the PbSc

$$\sigma_E/E = 8.1\%/\sqrt{E} \oplus 2.1\% \tag{4.17}$$

and for PbGl

$$\sigma_E/E = 5.9\%/\sqrt{E} \oplus 0.8\% \tag{4.18}$$

The EMCal energy scale can be derived from either $e^{\pm}$ E/p ratio distribution or by locating the $\pi^0 \to \gamma\gamma$ decay peak. For $\pi^0 \to \gamma\gamma$ method, the nonlinear error propagation of the finite detector resolution causes the reconstructed $m(\pi^0)$ mass peak to shift from the physical value. Given a known resolution, the energy scale, in principle, can be determined by iterative fitting of the $m(\pi^0)$ mass peak. While this method is popular in PHENIX due to the higher yield of π^0 decay photons than $e^{\pm}$, and because this "self-contained approach" does not involve another detector subsystem. However, the convergence of this method to the physical π^0 peak has not been rigorously studied or quantified. In this analysis, we therefore prefer the $e^{\pm}$ E/p method, which provides a rigorously defined energy scale that is coupled to both the TOF derived tracking momentum scale and the GEANT detector simulation.

The usage of two EMCal types has been argued to provide systematic control. While this may be true for single particle measurement, this choice significantly complicates the measurement of delocalized objects like jets. At the same time, calibration techniques such as $e^{\pm}$ E/p can easily provide an adequate determination of the EMCal energy scale.

Figure 4.14 shows the photograph of a quarter PbGl supermodule during testing.

4.2.2 Vertex, Centrality, and Reaction Plane Detectors

The Zero-Degree Calorimeter (ZDC) pair is a common detector installed at either side of all four RHIC experimental interaction regions and behind the DX dipole, covering approximately 2 mrad surrounding beam axis. In heavy ion collisions, the DX dipole deflects the colliding ions from beam pipe leading to the interaction region into either the blue or yellow ring, while spectator protons are deflected further outwards, leaving spectator neutrons hitting the ZDC undeflected. The ZDC is a sampling hadronic calorimeter with

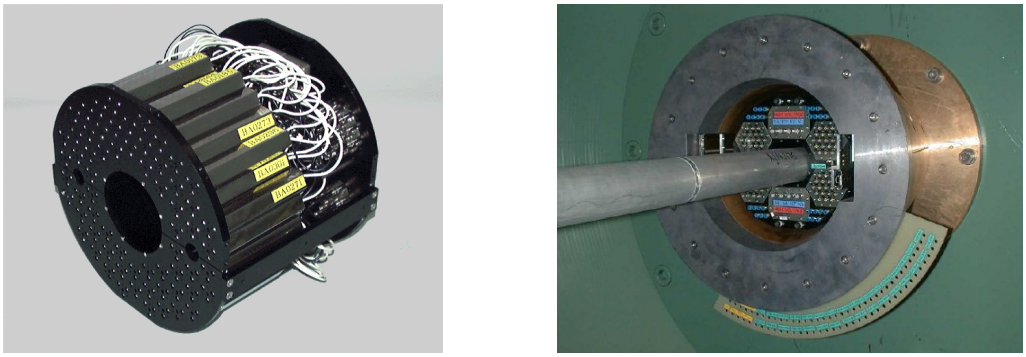

Figure 4.15: The BBC assembled (left) and inserted into the forward magnet (right).

W (tungsten) absorber and undoped optical fibers that serves as Cherenkov radiators. The optical fibers are tilted 45° toward the beam to maximize signal to noise. The timing resolution is $\approx$ 200 ps.

The Beam–Beam Counter (BBC) pair is a PHENIX-specific (although other RHIC experiments also uses a BBC, but of different design) charged Cherenkov detector consisting of 64 quartz radiation elements combined with a PMT covering $3.0|\eta| < 3.9$ and 2π in azimuth. The gain of each PMT is calibrated to provide 40 pC per minimum ionizing particle (MIP), and the dynamic range is $\approx$ 30 MIP per PMT. The single PMT timing resolution is 52 ± 4 ps, while the combined resolution is multiplicity dependent, and is at most 20 ps for high multiplicity. In contrast to the ZDC, this makes the BBC suitable to provide the collision start time for particle identification by the TOF. This also translates into a z-vertex resolution of 0.6 cm.

The BBC as a forward multiplicity detector provides information about particle production and its azimuthal modulation in heavy ion collisions. The charge sum of the BBC PMT has a monotonic correlation with the collision centrality. However, since particle production in ultraperipheral collisions is low, the ZDC as detector for the spectator neutrons provides a complementary measure for the centrality. In PHENIX, the centrality is therefore determined as a combination of the BBC charge sum Q_{BBC} and ZDC energy E_{ZDC}. Centrality bins are defined as slices orthogonal to the centroid line of the $(Q_{\mathrm{BBC}}/Q^{\mathrm{max}}_{\mathrm{BBC}}, E_{\mathrm{ZDC}}/E^{\mathrm{max}}_{\mathrm{ZDC}})$ distribution

The event plane or observed reaction plane as the dominant angle of the event eccentricity is determined by expanding the individual charge q_i in the 64 BBC PMT to the second order Fourier coefficient

$$Q_x + iQ_y = \sum_{k=1}^{64} q_i e^{2i\phi_i} \tag{4.19}$$

and obtaining the event plane or the observed reaction plane as the half phase

$$\Psi = \frac{1}{2}\arg(Q_x + iQ_y). \tag{4.20}$$

The reaction plane resolution depends on the event multiplicity and the magnitude of the event eccentricity. It is determined using the difference in the value using only the north or south BBC:

$$\Delta\Psi = \sqrt{2\langle\cos 2(\Psi_{\mathrm{BBCN}} - \Psi_{\mathrm{BBCS}})\rangle} \tag{4.21}$$

and for $\sqrt{s_{NN}} = 200$ GeV Cu + Cu collision, the resolution peaks at 10–20% centrality to $\Delta\Psi \approx 0.17$.

Figure 4.15 shows the assembled BBC outside and inserted into the forward magnet.

4.2.3 Trigger

Each trigger is associated with a Global Level-1 (GL1) bitmask. 32 of such GL1 trigger bits are assembled into a 32-bit integers and passed down to the data acquisition (DAQ). Each event record this value at three stages,

1. whether the trigger has fired, also called the raw bit,
2. whether the trigger has fired and is the $(s + 1)$-th event of a scale down value s (note the PHENIX off-by-one convention), also called the scaled bit, and
3. whether the trigger each corresponding to whether the bit fired that is recorded with the event.

From the four subsystems used in the PHENIX trigger system, the the BBC trigger and the EMCal/RICH trigger (ERT) that are used in this thesis. The BBC trigger is an and-operation of the comparison of either arm PMT firing to a threshold value, and the reconstruction of the vertex. In Run-5 (and subsequent runs), the threshold is one or more PMT in either the north or the south BBC.

The PHENIX ERT is a trigger for electromagnetic probes. The EMCal triggers are based on energy threshold comparison using disjoint 2×2 analog and staggered 4×4 analog–digital sums. Starting point of energy summing are the $2 \times 2 = 4$ tower PMT channels serviced by each analog stage application-specific integrated circuits (ASIC) chip, which produces the total current integral from the PMT of the four towers. This produces 36 2×2 energy sums per supermodule. After the analog-to-digital conversion (ADC), the quantized value of the 2×2 energy sum is relayed to three adjacent ASICs, so that 36 staggered-by-two 4×4 digital sums are formed. The ASICs are connected across supermodules – so that staggered sums can be formed across supermodule edges – but not across sectors.

The corresponding level-1 trigger is fired when the 2×2 analog and the 4×4 analog–digital sums exceed a preset threshold energy. The 2×2 sum is compared against one threshold, and the 4×4 has three thresholds, therefore giving four EMCal based triggers are available.

4.2.4 Data Acquisition

Detector signals in PHENIX are first digitized in the Front-End Modules (FEM). Optical signals from the FEM are then sent to the Data Collection Modules (DCM), which packages the data into event fragments.

Assembly of whole event package is performed by the Event Builder (EvB), which is a cluster of off-the-shelf PC, and is divided into the Sub-Event Buffers (SEB), the Assembly and Trigger Processor (ATP),

4.2.5 Luminosity Measurement

Recall that we derived the relation of the luminosity to the beam intensities N_{blue} and N_{yellow}, the betatron amplitude function β^*, and the convolved beam profiles σ_x^{V} and σ_y^{V}

$$\mathscr{L}_{\text{machine}} = \frac{f_{\text{rev}}}{2\pi\sigma_x^{\text{V}}\sigma_y^{\text{V}}} \sum_{\text{crossing}} N_{\text{blue}} N_{\text{yellow}} \tag{4.22}$$

The RHIC luminosity is therefore determined by observing the beam intensities N_{blue}, N_{yellow} using wall current monitors (WCM), and determining the beam profiles σ_x^{V} and σ_y^{V} using the van der Meer method/vernier scan.

Going back to the transverse beam motion, the focusing behavior around an interaction point $z = 0$ is described by the series expansion

$$\sigma_x^2(z) = \sigma_x^2(0)\left[1 + \frac{z^2}{(\beta^*)^2} + O(z^3)\right]. \tag{4.23}$$

When determining the luminosity using van der Meer method with a finite z vertex distribution, which is known as the Hourglass correction. The betatron amplitude function β^* can be extracted by measuring the longitudinal profile using the WCM. At injection, $\beta^* = 10$ m, but decreases during acceleration. For $\sqrt{s} = 200$ GeV and $\sqrt{s_{NN}} = 200$ GeV collisions in Run-5, $\beta^* = 1.0 \pm 0.1$ m is quoted by the C–AD.

Experimental measurement of cross section is usually directly tied to the minimum bias trigger. Using the luminosity–interaction rate definition

$$R \equiv \frac{dN}{dt} = \mathscr{L}\sigma, \tag{4.24}$$

since the BBC is the PHENIX minimum bias trigger, the BBC cross section is therefore related the machine luminosity by

$$\sigma_{\mathrm{BBC}} = \frac{R_{\mathrm{max}}}{\mathscr{L}_{\mathrm{machine}}\epsilon_{\mathrm{vertex}}}, \tag{4.25}$$

where R_{max} is the BBC trigger rate at maximum overlap, and $\epsilon_{\mathrm{vertex}}$ is the efficiency of the vertex being reconstructed by the BBC.

4.3 Detector Simulation

4.3.1 GEANT 3

The detector simulation software GEANT is a Monte Carlo simulation of the passage of elementary particles through matter, and is maintained by the CERN Application Software and Databases Group (ASD). For historical reasons, PHENIX uses the Fortran 77 based GEANT 3. The structure of GEANT 3 is roughly divided into the description of detector geometry and material, event generator interface, particle transport and interaction with material, the digitization of detector hits, and visualization.

Detector volumes are described in GEANT 3 using constructive solid geometry (CSG), which builds complex detector shapes using Boolean operation on 29 predefined shapes. The property of the volumes are described by material, which describes the atomic property and density, and tracking medium, which describes the electric and magnetic field property in that medium, and sets the parameter of the tracking algorithm. Volumes can be subdivided into cells to simulate calorimeter towers or layers of detector strips.

The basic loop processes through individual events. The four-momenta of the particles are kept in the KINE banks. Particles paths are tracked through the volumes in discretized steps, while the interaction is simulated by weighting with the the cross section of interaction processes and the energy loss of the involved particles. The motion of charged particles within a magnetic field is calculated either using the Runge–Kutta–Nyström algorithm ([74], section 25.5.20, p. 897) for generic field configuration, or for simple homogeneous fields, analytically using an helical path.

Volumes can be set as sensitive detectors, where the detector can be of a trajectory or a calorimeter type, and produces the hit information either in the form of a position or the magnitude of the energy loss. Tracking steps inside those volumes automatically cause these information to be stored into the HITS bank. It is possible to simulate detector digitization inside GEANT, but since the hits information is far more computationally expensive compared to the digitization, the digitization is typically performed outside the GEANT package.

Electromagnetic processes such as bremsstrahlung, Compton scattering, δ-ray production, and pair production are implemented in GEANT 3 by cross section evaluation and Electromagnetic processes in GEANT 3 are Hadronic processes in GEANT 3 are simulated using either the FLUKA and GEISHA package. Electromagnetic interaction are simulated internally, and validity range for electromagnetic processes extends from $E = 10$ keV–100 GeV. Muonic interaction extends to $E = 10$ TeV.

4.3.2 PISA 2000

The software package PISA 2000 is the implementation of the PHENIX detector subsystems and support structures using the GEANT 3 geometry and event particle tracking.

The beryllium–steel beam pipe is modeled as a cylinder with the materials and thickness in the (beryllium) section between the central magnets, and the (stainless steel) sections between the central magnets and the piston. The beam pipe is a major conversion source, and responsible for most of the electrons detected in the central arm. In order to improved the simulation efficiency, the thickness of the beryllium section can be increased from 1 mm in order to generate more conversions.

The drift chamber is modeled in PISA using four cells per keystone, with 20 keystones per arm. No actual wires or charge drift are simulated, but instead using eight wire groups per arm, which is in turn divided into 20 planes. As consequence, fiducial cuts has to applied to the measurement to avoid bad regions that are not properly simulated, and the GEANT efficiency has to be aligned with good DC regions, in order to obtain a realistic DC efficiency. Similarly, for the simulation of the EMCal, the hot towers are not properly simulated, and has to be cut out before comparing the GEANT simulation with the data.

Chapter 5

Data Analysis I: Raw Spectra

We now start the discussion on the measurement of jet-related quantities. Spectra here also include jet-related distribution that serves as the starting point for derived quantities (usually ratios), such as fragmentation functions, j_T distributions and related quantities.

The measurement of virtually all spectrometer quantities starts with the extraction of raw, detector energy scale spectra, which are not directly comparable to theory. In this chapter, I will describe the extraction these detector energy level spectra. Since the detector simulation are not often published, and also cumbersome to simulate for a theorist, it is generally considered not optimal to publish spectra in the detector energy scale. The detector simulation, however, provides a mean to remedy this and instead obtain results in physically universal quantities. This will be discussed in the next chapter.

5.1 Offline Analysis Software

At the time of writing, data analysis in HEP and nuclear experiments are predominantly performed using the C++ [87], an objected-oriented [88] programming language that further implements "templates" as a form of generic programming [89], together with the Standard Template Library (STL) as a standard library implemented in this technique [90].

The software package ROOT [91] is used for data input/output and plotting. Despite being an object oriented C++ framework, ROOT carried many Fortran-based design decisions and idiosyncrasies from PAW. Furthermore, the CINT "C++" interpreter is only a partial C++98 implementation (which by design as a compiled language, and difficult to implement as an interpreter), and no documentation exists regarding its deviation from the C++ standard, resulting in many examples of undefined behavior. This situation is worsening with the adoption of C++98 TR1 and C++0x. For this reason, ROOT is only used minimally, while the computational part of this analysis is implemented directly in C++0x with STL and TR1.

Two sets of C++ and Fortran 77 compilers for the Intel/AMD IA-32 and x86-64 architecture were used throughout the analysis:

- GNU Compiler Collection (GCC), versions 3.2–4.4
- Intel C++ and Fortran Compiler, versions 9.0–12.0

Using two compilers provides a check against e.g. bugs in the compiler back end and other issues that could potentially result in a nondeterministic code behavior. The usage of the Intel C++ Compiler also allowed the generation of fully vectorized and multithreaded code for this analysis, before GCC supported OpenMP and started to implement a rudimentary vectorizer. Fortran 77 sources appear in this analysis are the PISA/GEANT detector simulation code, LO event generators such as PYTHIA, HERWIG and HIJING, and the unfolding code GURU.

The compiler and generated code ran on the Linux distributions:

- Red Hat Enterprise Linux 4–6
- Fedora Core 9
- FNAL/CERN Scientific Linux 3–5

Due to legacy third-party libraries, PHENIX offline computing is unfortunately constrained to 32-bit IA-32 until the time of writing. This has the implication that any optimized single-instruction, multiple data (SIMD) code written in assembly is limited to eight registers (instead of 16 with the 64-bit x86-64), therefore limiting the performance by the achievable implementation and instruction pipelining. On the other hand, the shared implementation provides additional checks by comparing results using both architecture.

Memory debugging on the full analysis code were performed using the virtual machine Valgrind. While the instrumenting memory debugger Parasoft Insure++ was used as matter of PHENIX Collaboration policy, heavy usage of STL and also inline assembly precluded the code instrumentation in this parts (the collaboration effectively permits these parts of the code to be excluded), and the overall code coverage with Insure++ should not be considered as sufficient. Profiling of the jet reconstruction code was done using Intel VTune, which is a sampling profiler that provides a histogram of instruction code address using the x86 central processing unit (CPU) performance monitoring units (PMU).

5.1.1 Histograms

This analysis uses extensively histograms with $\approx$ 10 dimensions of binning. At the beginning of this analysis, ROOT's `THnSparse` has not been implemented, and PHENIX was using a `TTree` based, dense multidimensional histogram class `THmulf`. Therfore, a customly written, 64-bit histogram class has been implemented. While this thesis is largely histogram based, and we will not hear it further, reader from mathematical and computer science background might want to be aware of an awkward terminology. "Tree" (e.g. ROOT's `TTree`) as opposed to histograms in HEP and nuclear physics are not graph theoretic trees. It is merely data in the form of an (dense) array of 2-tuples $(\mathbf{x}, w)$, where implicitly $w = 1$ is possible as weight, that can be used to produce (or "fill") a histogram.

The underlying hash table is based on GOOGLE SPARSEHASH [92], which has been used extensively in Google's search engine. The performance characteristics of its dense hash table implementation is made possible by implementing the hash table using arrays, while one special key value is sacrificed to mark unused table entries. For the histogram operation, the maximum integer $2^{64} - 1$ is used, thus reducing the maximum number of bins by one. Since avoidance of hash collision is critical for performance, MurmurHash2 by A. Appleby has been used. Self-modifying code (although not dynamically generated) is used to maintain loop unrolling and avoid repeated branching as with ROOT's `TH1` and `THnSparse`.

Accelerating histogram filling by asynchronously filling a cache and then using multiple threads to perform the bin look-up was explored but ultimately not used, since the necessary book-keeping was found to be too large to provided a significant performance gain. However, for histogram operations such as merging, the bookkeeping of weights allows one to utilize two threads. Also, the histograms are merged using $O(N^2)$ algorithm, which is significantly more efficient (both computationally and in term of memory usage) than the incremental $O(N \log N)$ merging using binary search trees, due to the far lower complexity prefactor in the first case, and for the number of merge steps, $N_{\text{merge}} \ll N_{\text{bin}}$ holds for virtually all high energy physics applications.

Initially in this analysis, some densely binned, low dimension histograms were used e.g. for the background estimation. However, the sparse histogram implemented here is sufficiently efficient in term of speed and memory consumption, and all histogramming were therefore converted to sparse histograms.

5.1.2 Numerical Representation

For storage efficiency, normalized cut variables (which are usually of the order one and does not require high precision) are stored and processed as IEEE 754:2008 (and at that time, its draft standard) half precision numbers. The C++ implementation of half precision numbers for the OpenEXR digital image format by Industrial Light and Magic was repurposed. The main caveat for this representation is that the PHENIX "magic number" -9999 for invalid values rounds to $-10\,000$.

5.1.3 Data Production

The PHENIX DAQ system assembles the event information from the individual subsystems and stores this in the PHENIX Raw Data Format (PRDF). Starting with each collider run, track and cluster reconstruction are performed to convert hit position into physics information suitable for analyes. These information are stored in data summary tapes (DST). The full event DST type is called the nano DST (nDST). The full set of nDST is too large to held (economically) on a random accessible storage, and only resides on the Linear Tape Open (LTO) magnetic tapes in the High Performance Storage System (HPSS). Physics working groups have specific, disk resident and interactively accessible, partial event DST, in the case of the Hard/Photon Physics Working Group (H/P PWG), the Hard pico DST (pDST).

The production of a level-2 jet triggered DST is typical for collaboration with a more extensive jet physics programs. The existing PHENIX pDST are designed with traditional, non-jet analyses in mind, e.g. single particle yield, two-particle correlation, and dielectron continuum. However, the ability to process the entire Run-5 $p+p$ and Cu + Cu $\sqrt{s_{NN}} = 200$ GeV data on local disk was essential for complex analysis procedure such as $p+p$ in Cu + Cu embedding. This analysis therefore had to "reinvent" this within the PHENIX Collaboration.

To avoid the production of multiple jet DSTs and subsequent recombination, a strategy of variably scaled down DST is chosen. Each event is scaled down according to the highest jet p_T in the event, which acts as trigger. This strategy is somewhat comparable to the approach e.g. by the CDF experiment, which produces a Single Tower 05 (ST05), Jet20, Jet50, Jet70, and Jet100, with the numerical values corresponding to the different jet E_T (in GeV) thresholds [93]. And in case of heavy ion collisions, the fake jet discriminant level is also used to avoid recording large amounts background fluctuations (which are typically produced more frequently than jets) that are subsequently discarded by the fake jet rejection.

In the initial phase of this analysis, when the analysis cuts for jet reconstruction and the fake rejection

strategy has been studied, the triggering strategy is based on the total event p_T. The jet p_T based triggering was subsequently adopted once the basic analysis cuts and fake rejection discriminant are fixed.

Event are scaled down by power of two, and deterministically by the integer modulus of an sequential event counter (i.e. not the run number) with the scale down factor. The maximum scale down is $2^5 = 32$, which ensures that a subset of the minimum bias events is always recorded.

5.2 Outline of Procedure

Obtaining a jet spectrum is a surprisingly complex procedure. Before we move on to explain the individual steps, a countertop recipe to whip up the jet spectrum is described. The measurement is organized in three steps

1. Extraction of the detector level yield
2. Unfolding to the particle level yield (see next chapter)
3. Conversion to the cross section measurement

Both in order not to overload the procedure immediately, and also because detector level yields can serve a meaningful measurement for the nuclear modification factor R_{AA}, we will split off and defer the discussion to the next chapter.

5.2.1 Data Reduction

At Run-5, the following PHENIX triggers are of interest:

- The "BBCLL1(>0 tubes)" is the PHENIX minimum bias trigger, and is defined by the coincident firing of at least one phototube in the north and south BBC, which is triggered to the observation of a minimum ionizing particle inside the BBC acceptance of $3.1 < |\eta| < 3.9$.
- The "ERTLL1_4x4c" is a calorimeter-based high-p_T trigger, that fires when observing $E > 1.4$ GeV in a staggered 4×4 tower tile in the EMCal.
- The "ERTLL1_4x4b" is a calorimeter-based high-p_T trigger, that fires when observing $E > 3.5$ GeV in a staggered 4×4 tower tile in the EMCal.

To obtain yields, the following trigger selection are needed:

- BBCLL1(>0 tubes) raw (equivalent to scaled in the MB data set),
- BBCLL1(>0 tubes) $\wedge$ ERTLL1_4x4c raw (equivalent to select ERTLL1_4x4c raw only in the MB data set, or select ERTLL1_4x4c&BBCLL1 in the ERT data set),
- ERTLL1_4x4c raw (equivalent to scaled in the ERT data set).

For the cross section measure, two additional data sets are needed:

- ERTLL1_4x4c $\vee$ ERTLL1_4x4b scaled, in the ERT data set,
- (ERTLL1_4x4c $\vee$ ERTLL1_4x4b scaled) $\wedge$ BBCLL1(>0 tubes) raw, in the ERT data set.

5.2.2 Detector Level Yield

1. For each of the datasets:
   - BBCLL1(>0 tubes) raw
   - BBCLL1(>0 tubes) $\wedge$ ERTLL1_4x4c raw
   - ERTLL1_4x4c raw

   (a) Select events matching the trigger.
   (b) Apply particle level, tracking and EM cluster cuts.
   (c) Discard irregular events labeled by the particle level cuts.
   (d) Merge tracks and EM clusters.
   (e) Run jet reconstruction algorithm, record p_T^{rec} and necessary information for jet level cuts.
   (f) Apply jet level cuts.
2. Evaluate $\epsilon_{\text{ERT}}(p_T^{\text{rec}})$ using the BBCLL1(>0 tubes) and the BBCLL1(>0 tubes) $\wedge$ ERTLL1_4x4c spectra.
3. Calculate the unique event spectrum sum from the BBCLL1(>0 tubes) raw, BBCLL1(>0 tubes) $\wedge$ ERTLL1_4x4c raw, and ERTLL1_4x4c raw spectra, correct for ϵ_{ERT}.
4. Obtain the minimum bias event count N_{MB}, divide the spectrum by it.

5.2.3 Cross Section Measure

1. Evaluate the BBC efficiency $\epsilon_{\mathrm{BBC}}(p_T^{\mathrm{rec}})$ using the or-ed ERT ERTLL1_4x4c $\vee$ ERTLL1_4x4b scaled and the or-ed ERT coincidence with minimum bias trigger (ERTLL1_4x4c $\vee$ ERTLL1_4x4b scaled) $\wedge$ BBCLL1(>0 tubes) raw spectra.

2. Correct the combined spectrum for $\epsilon_{\mathrm{BBC}}(p_T^{\mathrm{rec}})$ (strictly speaking, this has to be done before unfolding the spectrum, but a constant ϵ_{BBC} makes it commutative with the unfolding).

3. Obtain σ_{BBC} by the van der Meer method/vernier scan, then divide the spectrum by $2\pi\Delta\eta p_T$, multiply by σ_{BBC} to obtain $Ed^3\sigma/dp = (2\pi)^{-1}dN/(p_T dp_T dy)$.

4. Tweak the steps to obtain systematic uncertainties.

5.3 Run Quality Assurance

The Run-5 $p+p$ data set covers 842 runs within the PHENIX run numbers 168314–179846.

The proper normalization depends on having properly matching MB and ERT file sets. Since the PHENIX Analysis Taxi/Train contains some partial file sets, this is selected by comparing the MB and ERT trigger counts against the run log. The following condition can happen:

1. Fewer events in the Run Log than on Taxi: Usually the Run Control crashed in this case.

2. Fewer events on Taxi than in the Run Log: Usually file sets are missing/removed from the Taxi, but not the entire run.

To properly detect partial runs independent of potential Run Control crashes, applying the following criterion of an ERT4x4c&BBCLL1 to BBCLL1 raw trigger count ratio appears to work best. We require

$$-0.01 < N^{\mathrm{taxi}}_{\mathrm{ERT4x4c\&BBCLL1}}/N^{\mathrm{taxi}}_{\mathrm{BBCLL1}} - N^{\mathrm{log}}_{\mathrm{ERT4x4c\&BBCLL1}}/N^{\mathrm{log}}_{\mathrm{BBCLL1}} < 0.02 \tag{5.1}$$

to remove the outliers.

There is a clear distinction between normal runs with $0.1318\ \mathrm{GeV}/c^2 < m(\pi^0) < 0.1435\ \mathrm{GeV}/c^2$ and run outliers that have a $0.1501\ \mathrm{GeV}/c^2 < m(\pi^0) < 0.1656\ \mathrm{GeV}/c^2$ for π^0 with $p_T > 2\ \mathrm{GeV}/c$. Since the corresponding runs do not have large statistics, and the egregiously wrong $m(\pi^0)$ could indicate other

calibration issues, we require the Run-5 $p+p$ runs to satisfy

$$m(\pi^0) < 0.1648 \text{ GeV}/c^2, \tag{5.2}$$

The Run-5 Cu + Cu runs have systematically lower π^0 masses, which are suspicious, as combinatorial effects should be small given the high π^0 momentum requirement, and not *decrease* the mass. For the purpose of selecting runs, however, we placed the requirement

$$0.120 \text{ GeV}/c^2 < m(\pi^0) < 0.133 \text{ GeV}/c^2, \tag{5.3}$$

to reject outlier runs showing large deviation of the energy scale.

5.4 Trigger

In term of the Run-5 $p+p$ GL1 bitmask, the triggers we use correspond to:

- BBCLL1(>0 tubes): 00000004_{16}
- ERTLL1_4x4c: 00000400_{16}
- ERTLL1_4x4c&BBCLL1: 00001000_{16}
- ERTLL1_4x4b: 08000000_{16}

In term of the Run-5 Cu + Cu GL1 bitmask, the triggers we use correspond to:

- BBCLL1(>0 tubes): 00000004_{16}
- ERTLL1_4x4b&BBCLL1: 00002000_{16}
- ERTLL1_4x4c&BBCLL1: 00004000_{16}

Note that as of Run-5, BBCLL1(>0 tubes) is synonymous with BBCLL1, since higher multiplicity thresholds proved to be unnecessary.

5.5 Electromagnetic Clusters

We require a minimum energy threshold (in term of "ecore") of $E > 500$ MeV, which is common to most PHENIX analyses with the EMCal. The rationale for this requirement is a bit artificial, the E/p based calibration for nonlinearities in the calorimeter response at PHENIX terminates at 500 MeV.

5.5.1 Energy Scale

The PHENIX momentum scale of the tracking detectors fixed by the particle identification of $\pi^{\pm}$, $K^{\pm}$, and $p/\bar{p}$, and the comparison of the particle time-of-flight measurement with their known masses. This analysis uses this momentum scale unmodified.

The energy scale of the EMCal detectors can be established by either reconstructing the decay of light and short-lived hadrons, e.g. with $\pi^0 \to \gamma\gamma$, or by determining the energy scale by comparing the energy deposit E of electrons into the calorimeter with the momentum p from the tracking detectors – commonly referred to as "E/p" calibration.

This analysis departs from the PHENIX tradition of using a purely π^0 based energy scale while using E/p to quantify the nonlinearity only. The π^0 based energy calibration requires *a priori* knowledge of the calorimeter energy resolution (a case of nonlinear error propagation, where the propagated mean, the π^0 mass, depends on the uncertainties or detector resolution). Direct measurement of the EMCal energy resolution is only accessible using test beam, which likely will not properly characterize the time-dependent change to the detector after five years of running.

The E/p calibration at PHENIX is complicated by the fact that most of the electrons observed are photon conversion in the beam pipe material. Due to the lack of in-field tracking, the momenta of these electrons are misreconstructed under the assumption that they originated from the event vertex instead of the beam pipe. The E/p calibration therefore requires the determination of the beam pipe dominated, and momenta misreconstructed E/p distribution using photon conversion in the beam pipe, which produces a momentum dependent E/p reference value ≈ 0.98 for $p > 1$ GeV/c.

5.5.1.1 Tower-by-Tower E/p Balancing

For the purpose of E/p calibration, we take all tracks with $|\mathbf{p}| > 0.75\,\mathrm{GeV}/c$ and that fires more than one RICH phototube within the nominal electron radii range 3.4–8.4 cm (refer the table 4.1), and calculate the E/p distribution for each tower (no run dependence).

For $p+p$, a Gaussian distribution is used to fit the E/p distribution in the range between $0.75 \leq E/p < 1.25$. Towers with less than 16 counts are considered to be insufficient to determine the E/p.

The rescaling of the clusters for each central tower is determined by the ratio of the E/p peak position average over all towers by the E/p peak position of each tower. The assumption is that π^0-based calibration already provides a correct global energy scale calibration. Regions within $\eta < 0.01$ are not rescaled, since

these lie within the DC dead region. If the statistics is insufficient to obtain a stable and convergent E/p fit, no rescaling is performed.

5.5.1.2 Bad Tower Mask

A spectrum binned in 0.25 GeV/c for cluster associated with each central tower is produced. width is made. This spectrum fitted with a power law. For the sets of for PbSc and PbGl towers, the overall factor and exponent are fitted to a Gaussian distribution. The peaks for both overall factor and exponent are extracted as the reference PbSc and PbGl spectrum parameter.

After the E/p based scaling, the (Pearson) χ^2 goodness-of-fit is used to select abnormal towers, requiring (not divided by degrees of freedom) $\chi^2 < 1600$ for PbSc and $\chi^2 < 350$ for PbGl. We found that cutting on the (small count corrected) Yates χ^2 has little effect on the tower map.

The tower mask is then 3×3-convoluted. No special treatments (beside that they go out of the 3×3-convolution) are made for the sector edges.

Figures 5.1 and 5.2 show the input data of the Run-5 $p+p$ and Cu + Cu tower energy balancing and the resulting tower masks.

5.5.1.3 Run-by-Run π^0 Mass Balancing

Since the π^0 mass from the reconstruction of $\gamma\gamma \to \pi^0$ is

$$m_{\pi^0} = \sqrt{2E_1E_2(1-\cos\theta)}, \tag{5.4}$$

with θ being the opening angle between the two γ, the mass is proportional to any global energy offset. To balance the run-by-run energy scale, the π^0 mass therefore offers a higher statistics than using E/p. And because there is still a final step to align the sector-by-sector energy scale to the PISA E/p, there is no need to fix the global energy scale yet.

For the rescaling, we consider π^0 with $p_T > 2$ GeV/c. Taking the good run mean value for Run-5 $p+p$

$$\langle m_{\pi^0}\rangle = 0.137\,622\,8 \pm 0.000\,007\,9 \text{ GeV}/c^2 \tag{5.5}$$

the multiplicative run-by-run energy rescaling is

$$\langle m_{\pi^0}\rangle / m_{\pi^0}^{\text{run}}. \tag{5.6}$$

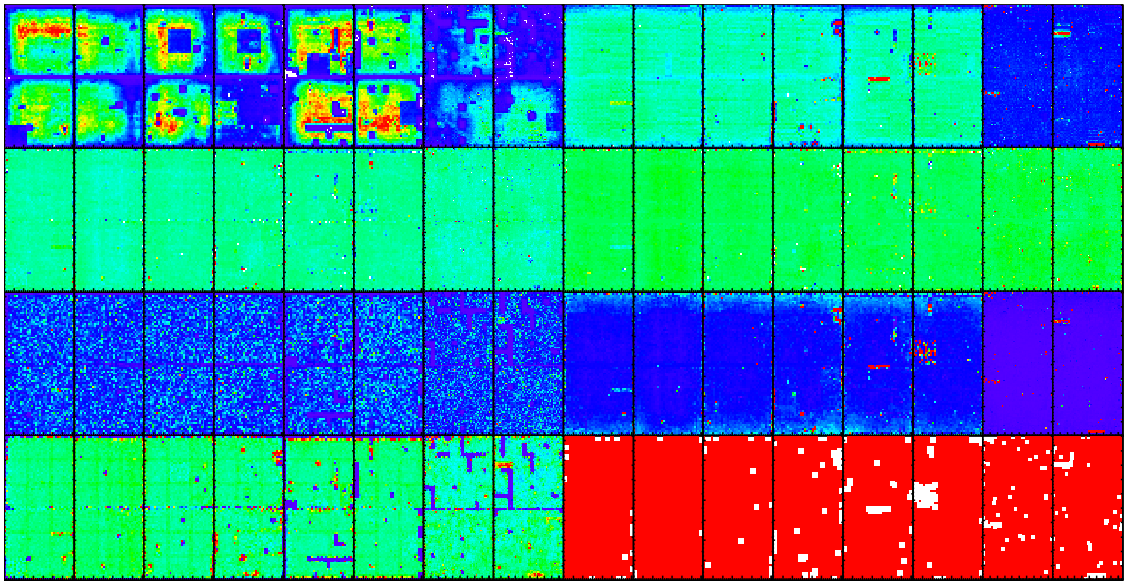

Figure 5.1: Run-5 $p+p$ tower map, split into 2×4 plots, each with W0, W1, W2, W3, E3, E2, E1, E0 rotated such that $+\hat{\phi}$ is to the right, $+\hat{\eta}$ is to the top. Left column, top to bottom: $e^{\pm}$ distribution, E/p peak position, E/p fit χ^2, E/p width. Right column, top to bottom: γ count, derived tower scaling, spectrum fit χ^2, resulting tower map (red tower not masked, white tower masked).

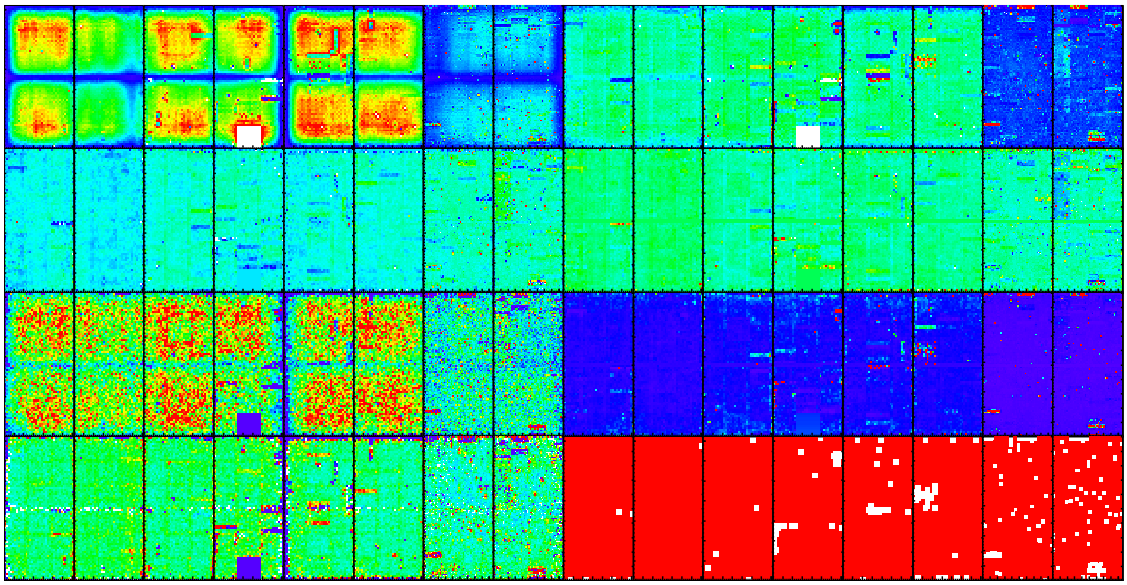

Figure 5.2: Run-5 $p+p$ tower map, split into 2×4 plots, each with W0, W1, W2, W3, E3, E2, E1, E0 rotated such that $+\hat{\phi}$ is to the right, $+\hat{\eta}$ is to the top. Left column, top to bottom: $e^{\pm}$ distribution, E/p peak position, E/p fit χ^2, E/p width. Right column, top to bottom: γ count, derived tower scaling, spectrum fit χ^2, resulting tower map (red tower not masked, white tower masked).

The rescaling to the $p+p$ value above is also applied to Cu + Cu, which given the p_T threshold used, should to the first order give a satisfactory recalibration of the EMCal energy scale due to the low combinatorial effects at such a large momentum. The real test/confirmation that this assumption is true, however, is the sector E/p calibration below, which proves that the rescaled Cu + Cu EMCal energy scale matches well to the independent momentum scale of the tracking system.

5.5.1.4 Sector E/p Calibration

The sector calibration is performed after the tower-by-tower balancing via E/p, and the run-by-run balancing via $\pi^0 \to \gamma\gamma$ mass reconstruction.

Using PISA simulation of purely γ events, we select on events where the photon converts into electrons, as identified by RICH. Since this calibration is performed on sector/arm basis, a more stringent n0 > 2 is used to select electrons. From PYTHIA Tune A, we obtain the γ spectrum

$$\frac{dN_\gamma}{dE} = \left(\frac{E}{\text{GeV}} + 1.3266\right)^{-10.074}, \quad E \geq 0.5 \text{ GeV} \tag{5.7}$$

(since also the conversion process produce an electron spectrum with a deep slope, the additional weighting has little effect, and we observe consistent E/p behavior with or without the γ spectrum weighting). Within the range of $0.5 \leq E/p \leq 1.4$, Gaussian plus a linear pedestal fitted against the E/p distribution to extract the peak position. This is done to both data and PISA simulation of beam pipe conversions.

Since the range $p < 1$ GeV/c tends to contain residual nonlinearities, the three data points for $1 \leq p < 1.5$ GeV/c, $1.5 \leq p < 2$ GeV/c, and $2 \leq p < 3$ GeV/c are used for fitting. For the PISA reference, W PbSc sectors, E PbSc sectors, and E PbGl sectors are grouped together. This is then divided by the E/p from the data to obtain the per-sector energy scale correction, which for Run-5 $p+p$ are

$$\begin{aligned}
E^{\text{W0}}/E_0^{\text{W0}} &= 1.0174 \pm 0.0041 \\
E^{\text{W1}}/E_0^{\text{W1}} &= 1.0244 \pm 0.0041 \\
E^{\text{W2}}/E_0^{\text{W2}} &= 1.0188 \pm 0.0041 \\
E^{\text{W3}}/E_0^{\text{W3}} &= 1.0203 \pm 0.0041 \\
E^{\text{E2}}/E_0^{\text{E2}} &= 1.0177 \pm 0.0068 \\
E^{\text{E3}}/E_0^{\text{E3}} &= 1.0209 \pm 0.0069
\end{aligned} \tag{5.8}$$

$$\begin{aligned} E^{\mathrm{E0}}/E_0^{\mathrm{E0}} &= 0.9565 \pm 0.0041 \\ E^{\mathrm{E1}}/E_0^{\mathrm{E1}} &= 0.9536 \pm 0.0042 \end{aligned} \tag{5.9}$$

and for Run-5 Cu + Cu are

$$\begin{aligned} E^{\mathrm{W0}}/E_0^{\mathrm{W0}} &= 1.0299 \pm 0.0058 \\ E^{\mathrm{W1}}/E_0^{\mathrm{W1}} &= 1.0349 \pm 0.0061 \\ E^{\mathrm{W2}}/E_0^{\mathrm{W2}} &= 1.0299 \pm 0.0058 \\ E^{\mathrm{W3}}/E_0^{\mathrm{W3}} &= 1.0159 \pm 0.0060 \\ E^{\mathrm{E2}}/E_0^{\mathrm{E2}} &= 1.0238 \pm 0.0069 \\ E^{\mathrm{E3}}/E_0^{\mathrm{E3}} &= 1.0190 \pm 0.0069 \\ E^{\mathrm{E0}}/E_0^{\mathrm{E0}} &= 0.9556 \pm 0.0043 \\ E^{\mathrm{E1}}/E_0^{\mathrm{E1}} &= 0.9602 \pm 0.0042 \end{aligned} \tag{5.10}$$

Except for the known poor sector W3, the p dependence within the three data points is consistent with a constant, supporting the assumption of a constant energy scale mismatch. After applying the scaling, we observe negligible impact on the π^0 distribution.

Figures 5.3 and 5.4 show the $e^{\pm}$ momentum dependent scaling values and the final values extracted using fits to the stable momentum bins.

Since we did this calibration after applying the tower-by-tower and run-by-run energy scale balancing, any residual energy offset are included in this calibration. Therefore, a self-consistent EMCal energy scale is now established that fully reproduces the PISA simulation.

The final energy scaling are therefore:

$$\frac{E(i,r)}{E_0(i,r)} = \underbrace{\frac{1}{N_{\mathrm{run}}}\sum_r \frac{E_0(i,r)}{N_{\mathrm{tower}}^{-1}\sum_j E_0(j,r)}}_{\text{relative}} \underbrace{\frac{1}{N_{\mathrm{tower}}}\sum_i \frac{E_0(i,r)}{N_{\mathrm{run}}^{-1}\sum_r E_0(i,r)}}_{\text{relative}} \underbrace{\frac{E^{\mathrm{sector}(r)}}{E_0^{\mathrm{sector}(r)}}}_{\text{absolute}} \tag{5.11}$$

5.5.2 Time-of-Flight

The requirement on TOF was first introduced when analyzing the Run-5 $p+p$ fragmentation function. The behavior of the $p+p$ fragmentation function, when evaluated without any cuts on the cluster timing, exhibits anomalous behavior around $p_T \approx 18\,\mathrm{GeV}/c$ and $z \approx 1$. Looking at the time-of-flight (TOF), it is evident that additional background were present at exceedingly high and low TOF values.

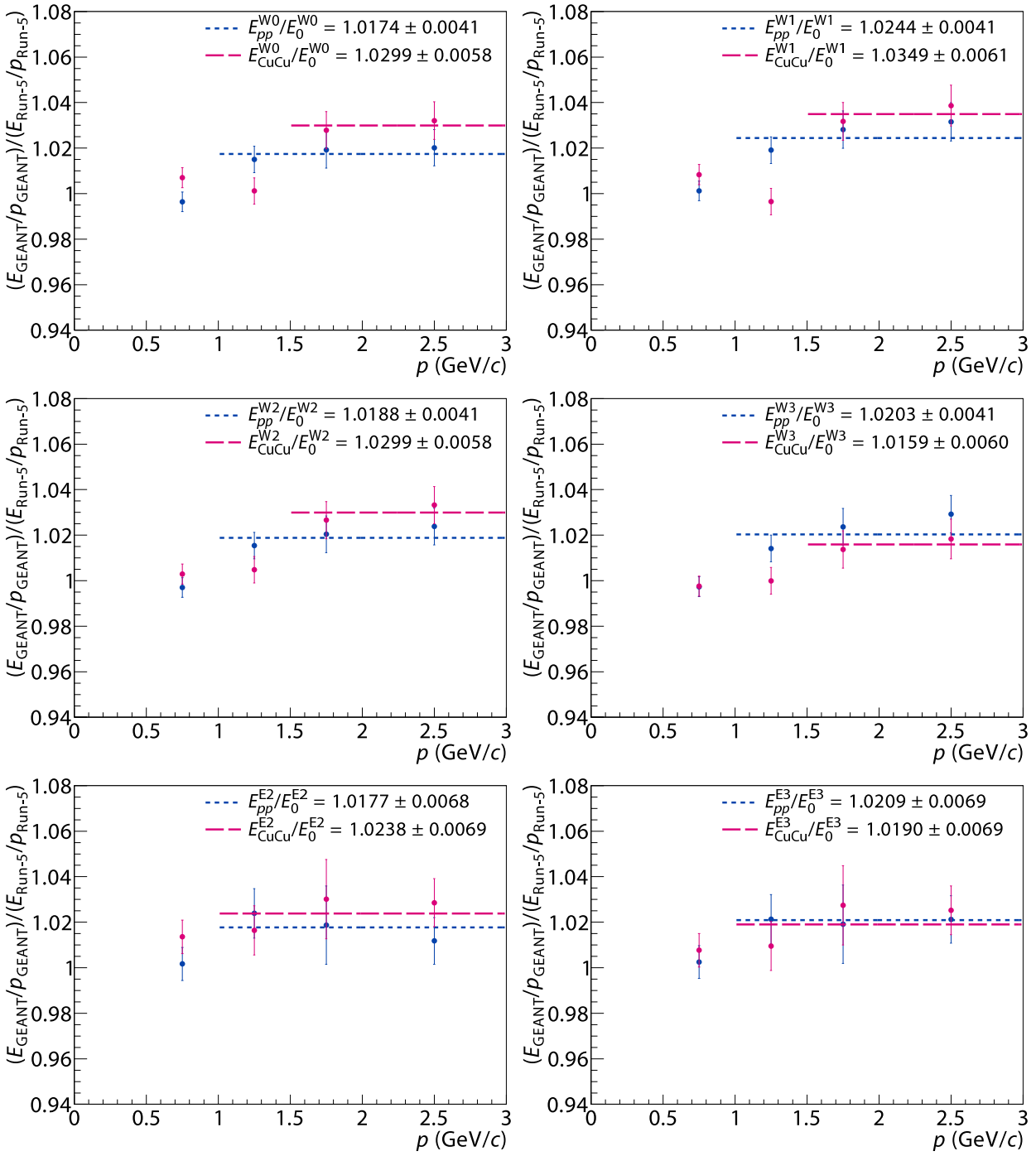

Figure 5.3: Run-5 $p+p$ and Cu + Cu sector energy scale with statistical errors, PbSc sectors. A constant scaling value is extracted by fitting the high-p_T part.

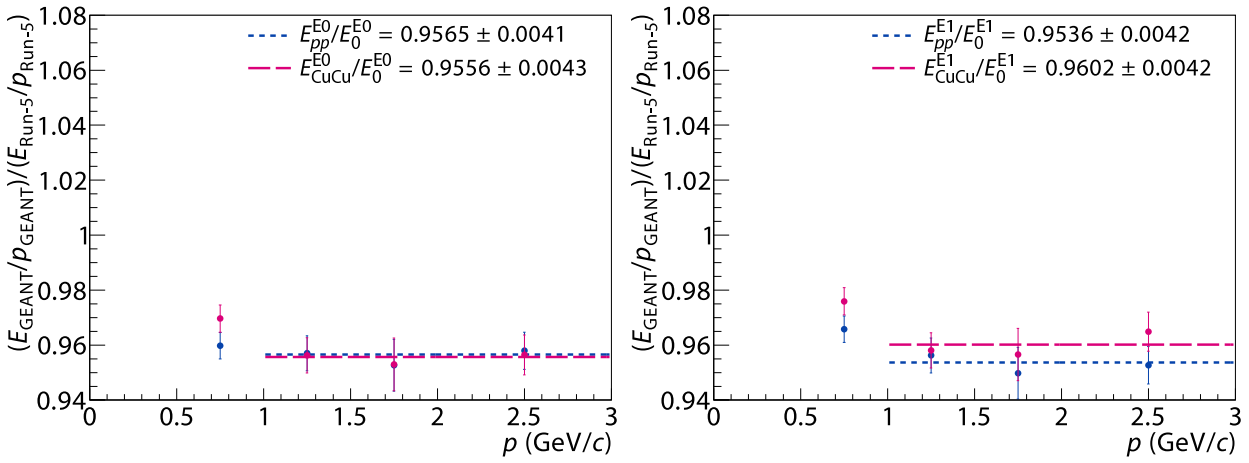

Figure 5.4: Run-5 $p+p$ and Cu + Cu sector energy scale with statistical errors, PbGl sectors. A constant scaling value is extracted by fitting the high-p_T part.

The Run-5 $p+p$ EMCal TOF appears to be poorly calibrated. There is a significant, residual tower-by-tower, and run-by-run variation in the time-of-flight. Also, while the existing Run-5 Cu + Cu calibration appear to be calibrated, it suffering from a limited resolution.

For this calibration, I assume that the TOF behavior is largely factorized into the sector–run dependence, the tower-by-tower dependence, and the energy dependent slewing. The sector–run dependence is first characterized by a histogram with 0.125 ns resolution, which is approximately twice the intrinsic TOF resolution for $\pi^{\pm}$, and covering $|\Delta t| < 64$ ns. Clusters with less than 1 GeV are removed to avoid slewing effects. The approximate position of the TOF peak is located by fitting the histogram against a Gaussian plus 4-th order polynomial distribution with the initial guess of $\langle \Delta t \rangle = -8$ ns and $\sigma(\Delta t) = 4$ ns. Because inproperly calibration introduces additional modes into the distribution and causes the Gaussian fits to be biased towards problematic runs, iterative fits are used to locate the actual peak position. The iterative fit procedure is constrained to $\pm 1\sigma$ of the initial guess, and terminates either with the Gaussian peak mean moving less than the fit uncertainty, or forcibly after the 64-th iteration.

The result of the procedures detained above in the largely uncalibrated $p+p$ TOF shows an overall drift of the timing mean with the run progression, and an approximately constant offset between the sectors.

Next, the sector–run peak position is discretized to multiples of the histogram resolution, 0.125ns, and the histogram is shifted along the timing axis to compensate for the sector–run behavior, and a tower-by-tower fit (using the same procedure) is obtained for each tower.

Quantifying the nonfactorized effect is difficult. However, since we did not encounter timing issues in the Run-5 $p+p$ using a 3σ cut, one could compare the TOF σ to see how large a cut would be appropriate for the Cu + Cu. This approach, while slightly ad-hoc, also has the benefit of producing a consistent TOF cut for the two species. Comparing the median width for the active/unmasked towers, the Run-5 $p+p$ is 0.93174 ns, while Cu + Cu has 0.571189 ns. Scaled to 3σ in $p+p$ means the TOF median adjusted cut for Cu + Cu would be 5σ.

5.6 Tracks

The structure of track pair cuts in fact the limitation factor of the the overall performance of jet reconstruction. This is also a good demonstration that seeking algorithms beyond $O(N^2)$ in fact does not make practical sense.

5.6.1 $e^{\pm}$ Tagging

This is not by itself a cut, but is needed for subsequent cuts. We noticed that the number of firing phototube within the nominal disk radius is dependent on the quality of the track reconstruction and therefore the PC3 matching. Therefore, we use a variable requirement

$$\text{is\_electron} = \text{n0} > \begin{cases} 2 & \Delta R_{\text{PC3}} < 1.5 \\ 1 & \Delta R_{\text{PC3}} \geq 1.5 \end{cases} \tag{5.12}$$

to select on $e^{\pm}$ candidate, where

$$\Delta R_{\text{PC3}} \equiv \sqrt{\left(\frac{\Delta z_{\text{PC3}}}{\sigma(\Delta z_{\text{PC3}})}\right)^2 + \left(\frac{\Delta \phi_{\text{PC3}}}{\sigma(\Delta \phi_{\text{PC3}})}\right)^2} \tag{5.13}$$

and Δz_{PC3}, $\Delta \phi_{\text{PC3}}$ are the residual displacement of the hit position in PC3 with respect to the expected PC3 intersection point from the reconstructed track trajectory. The normalization $\sigma(\Delta z_{\text{PC3}})$, $\sigma(\Delta \phi_{\text{PC3}})$ are the momentum dependent standard deviation of Δz_{PC3}, $\Delta \phi_{\text{PC3}}$.

5.6.2 Cluster-Unassociated $e^{\pm}$ Candidate

Tracks that fire the RICH as electrons, but has no associated cluster in the EMCal would indicate some type of abnormal event reconstruction, e.g. particle misidentification. We suspect the PID-based cuts would yield incorrect results applied to these events. We therefore also label these events as abnormal and discard them.

5.6.3 Quality

The DC "good quality" acceptance criterion is

$$\text{good\_quality} = (\text{quality} \,\&\, 100110_2 \neq 0) \wedge \begin{cases} \text{true} & |p| < 6\ \text{GeV}/c \\ \text{quality} \,\&\, 11_2 = 11_2 & |p| \geq 6\ \text{GeV}/c \end{cases} \tag{5.14}$$

The rationale is that we observe at high-p_T increased number of tracks with no jet association, that do not hit both X1 and X2. Restricting this requirement to high-p_T prevents incurring an inefficiency for low-p_T tracks, but will suppress conversion in the region of a significant background.

5.6.4 Maximum Track *p*

We avoid events that contains a track $p_T \geq 25$ GeV/c. This is well within the region where PHENIX Run-5 tracking is dominated by conversion and decay background. This cut does not by itself provide sufficient background rejection, but we observe that these events virtually always contain isolated tracks with no apparent jet association and therefore indicate an incorrect momentum reconstruction.

Note that cut is only applied to DC "good quality" tracks, i.e. high p_T bad quality track do not trigger the event removal.

5.6.5 PC3 matching

We observed a similar need to tighten the cuts at high p_T for the PC3 matching, where

$$\Delta R_{\text{PC3}} = \sqrt{\left(\frac{\Delta z_{\text{PC3}}}{\sigma(\Delta z_{\text{PC3}})}\right)^2 + \left(\frac{\Delta \phi_{\text{PC3}}}{\sigma(\Delta \phi_{\text{PC3}})}\right)^2} < \begin{cases} 3\sigma & p_T < 6\,\text{GeV}/c \\ 2.5\sigma & p_T \geq 6\,\text{GeV}/c \end{cases} \tag{5.15}$$

5.6.6 $e^{\pm}$ Pair

We observe that for tracks firing the RICH, usually there is a close angle conversion partner, forming a "butterfly" like shape, induced by decay kinematics plus magnetic field. While one of two electrons may be removed by a sufficiently loose ghost cut, unlike ghost cuts, we would like to remove both electrons. Note that this cut is different from the ghost cut, and cannot be achieved by using a loosened ghost cut.

We therfore apply before any ghost cuts a conversion electron cut. We found the distribution is clean and narrowly localized in η, therefore the box shape

$$\Delta\eta < 0.005 \wedge \Delta\phi < 0.2 \tag{5.16}$$

is used in lieu of a more complex geometry.

5.6.7 Ghost

For the purpose of expressing DC ghosting, which is generated by the wire structure, it is more natural to introduce a scaled azimuthal angle

$$\hat{\phi} = \frac{160\phi}{\pi} \tag{5.17}$$

such that $\Delta\hat{\phi} = 1$ correspond to the anode-to-anode or cathode-to-cathode angle in the drift chamber.

The DC ghost cut then consists of rectangular and ellipsoid cuts:

1. The same z, anode-to-anode/cathode-to-cathode structure

$$[(\Delta z < 0.01) \wedge (\Delta\hat{\phi} < 0.75)] \vee [(\Delta z < 0.02) \wedge (0.78 < \Delta\hat{\phi} < 0.88)] \tag{5.18}$$

2. The additional similar z, anode-to-cathode/cathode-to-anode structure on top of the previous

$$(\Delta z < 0.075) \wedge (\Delta\hat{\phi} < 0.35) \tag{5.19}$$

3. The same wire structure

$$(\Delta z < 0.7) \wedge (\Delta\hat{\phi} < 0.08) \tag{5.20}$$

4. The resonant anode-to-cathode/cathode-to-anode structure

$$\frac{\Delta z^2}{0.125^2} + \frac{(\Delta\hat{\phi} - 0.5)^2}{0.05^2} < 1 \tag{5.21}$$

5. The hybrid structure resulting from the anode-to-cathode/cathode-to-anode and the same wire ghosts (a octagonal shape would match the distribution better, but the elliptical expression is algebraically far simpler)

$$\frac{\Delta z^2}{0.5^2} + \frac{\Delta\hat{\phi}^2}{0.2^2} < 1 \tag{5.22}$$

The final cut is the logically or-ed combination of the above, and for all tracks within one event, tracks pairs that satisfies one of the above cut is considered as a ghosting track pair, resulting in one of the track pair to be removed from the event.

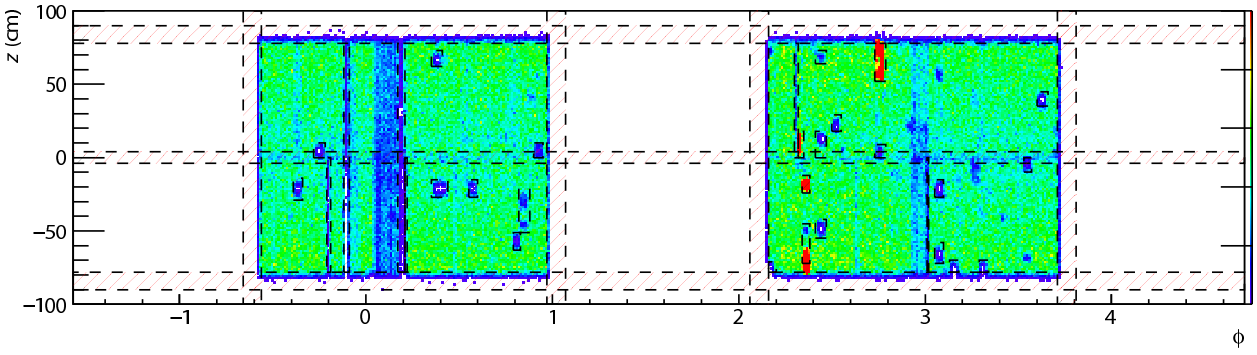

Figure 5.5: The (ϕ_{DC}, z_{DC}) distribution of tracks (with only quality > 7 applied) with box-cut for DC dead and hot regions

5.6.8 DC Dead and Hot Regions

The dead and hot regions are obtained from examining the track (z_{DC}, ϕ_{DC}) distribution at the reference radius $R_{DC} = 1.2$ m for the DC track reconstruction. Uneven acceptance are caused by broken wires and bad pixels in the pad chamber. These regions are therefore mostly rectangular (or rectangular and elongated in the case of broken wires) and are parametrized as such. The final cut is the logically or-ed (or geometrical union) of the individual rectangular regions.

Included in these irregular regions, are also the edges of the central arms, where the magnetic field can cause tracks to cross the projective detector geometry at an incident angle, and therefore result in a reconstruction efficiency that is difficult to parametrize. Unfortunately, the west arm also contains large patch of decreased efficiency, which we decided to keep, in order to avoid massive loss of acceptance.

Table 5.1 lists the parameters for the rectangular cut regions.

Figure 5.5 shows the rectangular cut regions overlaid on top of the (ϕ_{DC}, z_{DC}) distribution of tracks.

5.6.9 Electron E/p

The momentum of electron candidate with $E/p < 1/8$ is considered wrong, and the EMCal cluster energy is used instead (by calculating the momentum assuming $m^2 = 0$). No explicit restriction for the momentum scale is applied for this cut, but due to the minimum ionizing deposit in the EMCal, this cut is effective for tracks with approximately $p > 2.4$ GeV with the sectors covered by the PbSc calorimeters and $p > 4.0$ GeV for sectors with PbGl.

ϕ_0	z_0 (cm)	ϕ_1	z_1 (cm)
$-\pi/2$	-90	$3\pi/2$	-78
$-\pi/2$	-4	$3\pi/2$	4
$-\pi/2$	78	$3\pi/2$	90
-0.66	$-\infty$	-0.56	∞
0.97	$-\infty$	1.07	∞
2.06	$-\infty$	2.16	∞
3.71	$-\infty$	3.81	∞
-0.39	-29	-0.34	-14
-0.28	0	-0.22	10
-0.21	-78	-0.19	0
-0.12	-78	-0.09	78
0.17	-78	0.21	78
0.21	-78	0.22	0
0.35	-27	0.44	-15
0.35	62	0.41	73
0.55	-27	0.60	-15
0.79	-63	0.83	-51
0.82	-51	0.88	-21
0.90	0	0.95	10
2.16	-78	2.20	-71
2.30	0	2.32	78
2.32	0	2.35	18
2.34	-72	2.38	-45
2.34	-24	2.38	-12
2.41	-55	2.47	-42
2.41	0	2.47	18
2.41	64	2.47	73
2.50	18	2.55	29
2.73	0	2.79	9
2.73	52	2.79	78
3.01	-78	3.02	0
3.05	-72	3.10	-58
3.05	-27	3.10	-15
3.13	-78	3.18	-70
3.29	-78	3.34	-70
3.53	-10	3.57	0
3.60	35	3.66	45

Table 5.1: Rectangular cut parameters for DC dead and hot regions

5.7 ERT Efficiency

The PHENIX minimum bias (MB) cross section is defined relative to the BBCLL1(>0 tubes) trigger. In order to avoid exceeding the data acquisition (DAQ) capacity, both the minimum bias events and the pure ERT events are scaled down by a fixed ratio, which are denoted here as s_{MB} and s_{ERT}. The scale down are defined as the ratio between the number of events being accepted into the data stream (the scaled number of events) versus the number of events firing the trigger (the raw number of events).

Starting with the MB-coincident-with-ERT count

$$\frac{dN_{\mathrm{MBERT}}}{dp_T^{\mathrm{rec}}} = \epsilon_{\mathrm{ERT}} \frac{dN_{\mathrm{MB}}}{dp_T^{\mathrm{rec}}}, \tag{5.23}$$

and the ERT count (which is not scaled down in Run-5 $p+p$) consists of the ERT coincident with the MB trigger, plus pure ERT events, that are scaled down by the ratio s_{ERT} and for which there is no effect from the BBC efficiency ϵ_{BBC}:

$$\begin{aligned} \frac{dN_{\mathrm{ERT}}}{dp_T^{\mathrm{rec}}} &= s_{\mathrm{MB}}\epsilon_{\mathrm{ERT}} \left[1 + \frac{1}{s_{\mathrm{ERT}}} \left(\frac{1}{\epsilon_{\mathrm{BBC}}} - 1 \right) \right] \frac{dN_{\mathrm{MB}}}{dp_T^{\mathrm{rec}}} \\ &\approx s_{\mathrm{MB}}\epsilon_{\mathrm{ERT}} \frac{dN_{\mathrm{MB}}}{dp_T^{\mathrm{rec}}} \quad (\epsilon_{\mathrm{BBC}} \approx 1, s_{\mathrm{ERT}} \gg 1), \end{aligned} \tag{5.24}$$

where s_{ERT} is the scale down of the ERTLL1_4x4c trigger. The term $1 - \epsilon_{\mathrm{BBC}}$ in the denominator is due to the logical or-chaining of the triggers (we will discuss the definition and evaluation of ϵ_{BBC} in section 5.12). Note that for Run-5 $p+p$ runs, $1 \ll 1001 \leq s_{\mathrm{ERT}} \leq 12001$ (the 1 in the last digit is due to the PHENIX DAQ's off-by-one convention for triggers), and for jets, $\epsilon_{\mathrm{BBC}} \approx 1$ holds unless the p_T^{rec} is exceedingly low.

The uniquely combined event sum is therefore

$$\begin{aligned} \frac{dN_{\mathrm{UC}}}{dp_T^{\mathrm{rec}}} &\equiv \frac{dN_{\mathrm{ERT}}}{dp_T^{\mathrm{rec}}} + \frac{dN_{\mathrm{MB}}}{dp_T^{\mathrm{rec}}} - \frac{dN_{\mathrm{MBERT}}}{dp_T^{\mathrm{rec}}} \\ &= \left\{ \left[s_{\mathrm{MB}} \left(1 + \frac{1 - \epsilon_{\mathrm{BBC}}}{s_{\mathrm{ERT}}\epsilon_{\mathrm{BBC}}} \right) - 1 \right] \epsilon_{\mathrm{ERT}} + 1 \right\} \frac{dN_{\mathrm{MB}}}{dp_T^{\mathrm{rec}}} \end{aligned} \tag{5.25}$$

and the minimum bias yield is

$$\begin{aligned} \frac{1}{N_{\mathrm{evt}}} \frac{dN}{dp_T^{pp}} &= \frac{1}{N_{\mathrm{MB}}} \frac{dN_{\mathrm{MB}}}{dp_T^{\mathrm{rec}}} \\ &= \frac{1}{N_{\mathrm{MB}}} \left\{ \left[s_{\mathrm{MB}} \left(1 + \frac{1 - \epsilon_{\mathrm{BBC}}}{s_{\mathrm{ERT}}\epsilon_{\mathrm{BBC}}} \right) - 1 \right] \epsilon_{\mathrm{ERT}} + 1 \right\}^{-1} \frac{dN_{\mathrm{UC}}}{dp_T^{\mathrm{rec}}} \\ &\approx \frac{1}{N_{\mathrm{MB}}} \frac{1}{(s_{\mathrm{MB}} - 1)\epsilon_{\mathrm{ERT}} + 1} \frac{dN_{\mathrm{UC}}}{dp_T^{\mathrm{rec}}} \quad (\epsilon_{\mathrm{BBC}} \approx 1, s_{\mathrm{ERT}} \gg 1) \end{aligned} \tag{5.26}$$

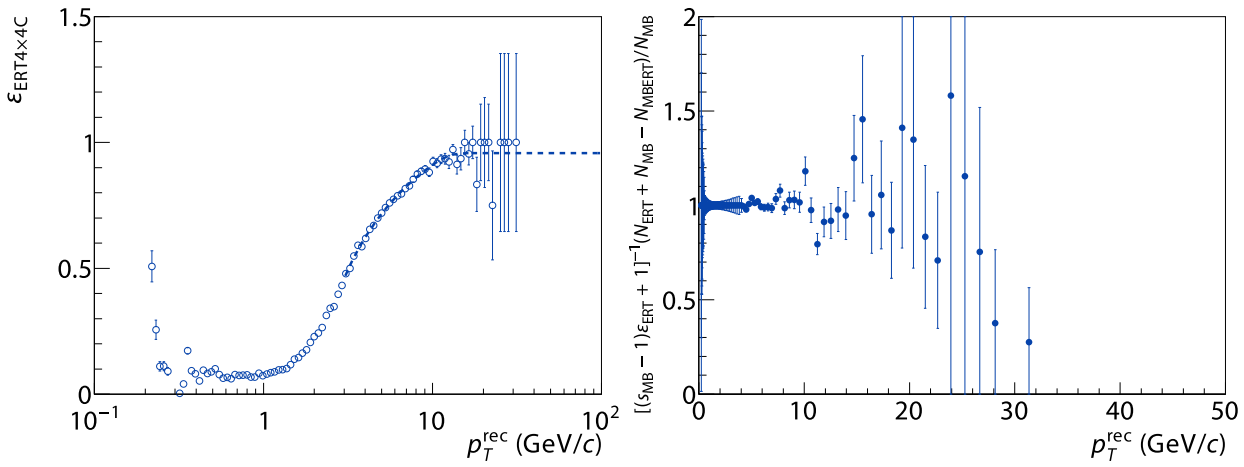

Figure 5.6: Run-5 $p+p$ ERT efficiency and fit for Gaussian filter, and the combined (corrected) spectrum to MB spectrum ratio

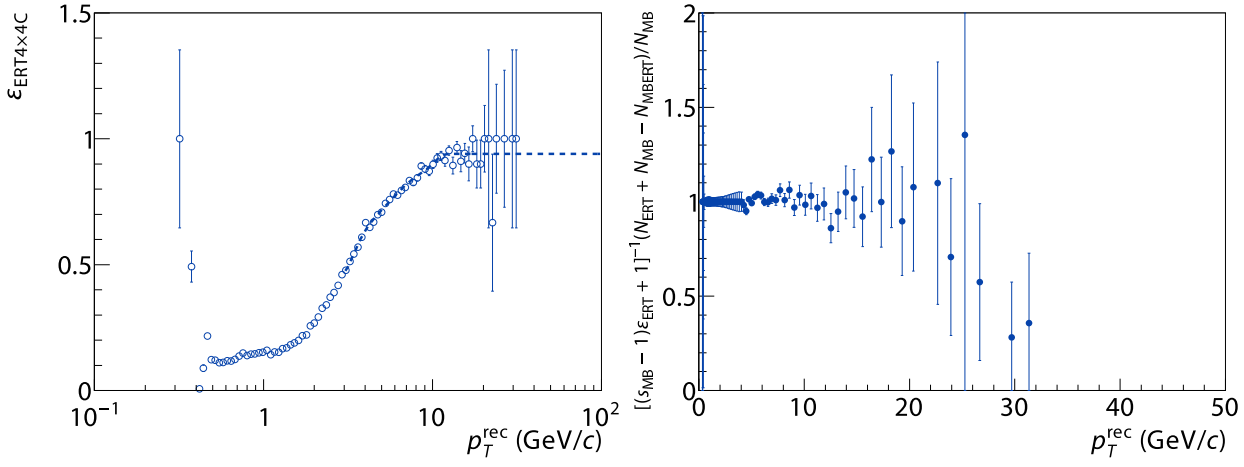

Figure 5.7: Run-5 $p+p$ ERT efficiency and fit for anti-$k_\perp$, and the combined (corrected) spectrum to MB spectrum ratio

5.7.1 Run-5 $p+p$

The ERT efficiency as function of the jet p_T^{rec} can be parametrized as

$$\epsilon_{\text{ERT}}(p_T^{\text{rec}}) = \epsilon_0 \text{erf}\left\{\sum_{k=0}^{N} a_k T_k\left[\frac{\log_{10} p_T^{\text{rec}}/(\text{GeV}/c) - 1.05078125}{0.43359375}\right]\right\} \tag{5.27}$$

where N is the order of the Chebyshev polynomial. The unusual scaling in the argument of the Chebyshev polynomials reflects the bin midpoint between approximately 4 and 30 GeV/c, but is corrected for binning (otherwise $\frac{1}{2}(\log_{10} 30 + \log_{10} 4) = 1.04$, $\frac{1}{2}(\log_{10} 30 - \log_{10} 4) = 0.44$). The logarithmic p_T scaling makes the fit more robust by preventing large numerical quantity to appear, making the bins equidistant, and deweights the statistically poor high-p_T range. The fit truncate for the largest N where the saturation is not affected by the Chebyshev polynomial starting to reproduce the bin-to-bin statistical fluctuation. For the Gaussian filter, we obtain the polynomial order $N = 6$ (since the fit is stable, coefficients consistent with zero are retained).

$$\begin{aligned}
\epsilon_0 &= 0.957 \pm 0.019 \\
a_0 &= 3.06 \pm 0.19 \\
a_1 &= 3.89 \pm 0.13 \\
a_2 &= 1.92 \pm 0.30 \\
a_3 &= 0.83 \pm 0.52 \\
a_4 &= 0.22 \pm 0.43 \\
a_5 &= 0.02 \pm 0.20 \\
a_6 &= -0.006 \pm 0.048
\end{aligned} \tag{5.28}$$

and for anti-$k_\perp$:

$$\begin{aligned}
\epsilon_0 &= 0.940 \pm 0.011 \\
a_0 &= 34 \pm 21 \\
a_1 &= 60 \pm 37 \\
a_2 &= 43 \pm 27 \\
a_3 &= 25 \pm 15 \\
a_4 &= 10.8 \pm 6.4 \\
a_5 &= 3.3 \pm 1.8 \\
a_6 &= 0.55 \pm 0.28
\end{aligned} \tag{5.29}$$

Figures 5.6 and 5.7 show the ERT 4×4C efficiency for the Gaussian filter and anti-$k_\perp$ algorithms.

5.7.2 Run-5 Cu + Cu

The Run-5 Cu + Cu is considerably harder to correct, as the rapid saturating ERT 4×4C trigger is fully masked off during the Cu + Cu running. The next higher threshold ERT trigger, 4×4A, was scaled at a higher ratio than the BBCLL1 trigger, which essentially defeated its purpose, as selecting on the scaled ERT 4×4A bit would yield less high-p_T event than in the minimum bias data. This leaves the 4×4B as the only viable trigger.

The solution used here is to perform a two staged ERT correction. The assumption is that at sufficiently high p_T, where also the 4×4B resides, the efficiency can be factorized into the Cu + Cu MB to 4×4C efficiency, and a collision system plus masked-off supermodules independent 4×4C to 4×4B efficiency, that can be estimated using the high statistics, ERT 4×4C triggered $p+p$ data

$$\epsilon^{\mathrm{CuCu}}_{4\times4\mathrm{B}}(p_T^{\mathrm{rec}}) = \epsilon^{\mathrm{CuCu}}_{4\times4\mathrm{C}}(p_T^{\mathrm{rec}})\frac{\epsilon^{pp}_{4\times4\mathrm{B}}(p_T^{\mathrm{rec}})}{\epsilon^{pp}_{4\times4\mathrm{C}}(p_T^{\mathrm{rec}})} \tag{5.30}$$

For the Cu + Cu, we use a low order version of the previous parametrization (where due to the low polynomial order, the bin correction of the Chebyshev polynomial scaling is relaxed for sake of simplicity)

$$\epsilon_{4\times4\mathrm{C}}(p_T^{\mathrm{rec}}) = \epsilon_0\mathrm{erf}\left\{\sum_{k=0}^{N} a_k T_k\left[\frac{\log_{10} p_T^{\mathrm{rec}}/(\mathrm{GeV}/c) - \frac{1}{2}(\log_{10}100 + \log_{10}4)}{\frac{1}{2}(\log_{10}100 - \log_{10}4)}\right]\right\} \tag{5.31}$$

while the remaining 4×4C to 4×4B efficiency is parametrized with a higher minimum $p_T = 8$ GeV/c.

$$\frac{\epsilon_{4\times4\mathrm{B}}(p_T^{\mathrm{rec}})}{\epsilon_{4\times4\mathrm{C}}(p_T^{\mathrm{rec}})} = \epsilon_0\mathrm{erf}\left\{\sum_{k=0}^{N} a_k T_k\left[\frac{\log_{10} p_T^{\mathrm{rec}}/(\mathrm{GeV}/c) - \frac{1}{2}(\log_{10}100 + \log_{10}8)}{\frac{1}{2}(\log_{10}100 - \log_{10}8)}\right]\right\} \tag{5.32}$$

For $\epsilon_{4\times4\mathrm{B}}(p_T^{\mathrm{rec}})/\epsilon_{4\times4\mathrm{C}}(p_T^{\mathrm{rec}})$, the fit gives

$$\begin{aligned} \epsilon_0 &= 0.907 \pm 0.015 \\ a_0 &= 1.53 \pm 0.14 \\ a_1 &= 0.84 \pm 0.16 \\ a_2 &= 0.160 \pm 0.049 \end{aligned} \tag{5.33}$$

	0–10%	10–30%	30–50%	50–70%	70–90%
ϵ_0	0.968 ± 0.047	0.918 ± 0.037	1	0.951 ± 0.093	1
a_0	1.40 ± 0.19	1.60 ± 0.29	1.44 ± 0.12	1.9 ± 1.5	1.71 ± 0.60
a_1	1.21 ± 0.24	1.30 ± 0.37	1.01 ± 0.17	1.4 ± 2.0	1.33 ± 0.88
a_2	0.231 ± 0.064	0.181 ± 0.098	0.149 ± 0.062	0.19 ± 0.56	0.32 ± 0.31

Table 5.2: Run-5 Cu + Cu minimum bias to ERT 4×4C efficiency fit without fake rejection.

	0–10%	10–30%	30–50%	50–70%	70–90%
ϵ_0	0.985 ± 0.067	0.907 ± 0.037	1	0.935 ± 0.051	1
a_0	1.28 ± 0.25	1.73 ± 0.36	1.44 ± 0.12	2.5 ± 1.4	1.58 ± 0.63
a_1	0.97 ± 0.29	1.39 ± 0.46	0.96 ± 0.18	2.2 ± 1.8	0.96 ± 0.93
a_2	0.170 ± 0.079	0.24 ± 0.13	0.162 ± 0.066	0.53 ± 0.56	0.24 ± 0.33

Table 5.3: Run-5 Cu + Cu minimum bias to ERT 4×4C efficiency fit for the $g' > 11.5$ $(\mathrm{GeV}/c)^2$ fake rejection level.

	0–10%	10–30%	30–50%	50–70%	70–90%
ϵ_0	0.959 ± 0.058	0.903 ± 0.038	1	0.921 ± 0.041	1
a_0	1.42 ± 0.31	1.83 ± 0.43	1.52 ± 0.13	3.4 ± 2.2	1.69 ± 0.67
a_1	1.09 ± 0.37	1.48 ± 0.55	1.05 ± 0.20	3.5 ± 3.1	1.05 ± 0.99
a_2	0.21 ± 0.11	0.31 ± 0.16	0.225 ± 0.076	0.97 ± 0.95	0.32 ± 0.37

Table 5.4: Run-5 Cu + Cu minimum bias to ERT 4×4C efficiency fit for the $g' > 17.8$ $(\mathrm{GeV}/c)^2$ fake rejection level.

	0–10%	10–30%	30–50%	50–70%	70–90%
ϵ_0	0.895 ± 0.027	0.867 ± 0.021	1	0.919 ± 0.029	1
a_0	2.64 ± 0.53	3.68 ± 0.85	1.84 ± 0.18	4.9 ± 2.5	2.10 ± 0.97
a_1	2.66 ± 0.72	3.9 ± 1.2	1.46 ± 0.26	5.4 ± 3.5	1.6 ± 1.4
a_2	0.86 ± 0.24	1.36 ± 0.40	0.49 ± 0.11	1.8 ± 1.2	0.64 ± 0.59

Table 5.5: Run-5 Cu + Cu minimum bias to ERT 4×4C efficiency fit for the $g' > 27.4$ $(\mathrm{GeV}/c)^2$ fake rejection level.

5.8 Jet Reconstruction in $p+p$

Using the particle and particle-pair cuts described above, a set of tracks and electromagnetic clusters are obtained. For tracks that points to an electromagnetic cluster, the PHENIX tracking algorithm will maintain a cluster association. The clusters that have been associated with a track in this fashion is removed from the list of clusters to prevent energy double counting. The momenta of the remaining clusters are obtained assuming $m = 0$, and combined with the tracks to form a set of 3-momenta.

In the case of Run-5 $p+p$, we then apply either the $\sigma = 0.3$ Gaussian filter or the $D = 0.3$ anti-$k_\perp$ jet reconstruction algorithm on the 3-momenta. For the Gaussian filter, the discrete algorithm is run using a pseudorapidity range of $|\eta| < 0.525$, which is 150% of the PHENIX acceptance, and therefore encompasses the vertex dependent "swing" of the PHENIX pseudorapidity coverage, on a $N_\eta \times N_\phi = 42 \times 256$ grid, that is approximately quadratic in the (η, ϕ) bin sizes. Since the anti-$k_\perp$ algorithm is implemented using rapidity as opposed to pseudorapidity (and internally calculates the logitudinally invariant recombination using four-momenta), $E = |\mathbf{p}|$ is set to all particles before they are inserted into the anti-$k_\perp$ algorithm to ensure a purely momentum-based recombination.

While the tracking background arising from conversions and decays will exceed the jet spectrum at high-p_T, the yield is typically still far less than one per event. Therefore, "jets" resulting from the tracking background is most severe when no multiplicity requirement is applied, and the rate rapidly decreases when the coincident detection of multiple tracks are demanded. Therefore, for all our analyses, we require a minimum multiplicity within a $\Delta\phi_J < \pi/3$ with respect to the jet axis being

$$\int d\Omega\, \theta(\pi/3 - \Delta\phi_J) \frac{dN}{d\Omega} \geq 3 \tag{5.34}$$

where fragments are either $E > 500$ GeV/c electromagnetic clusters (i.e. using the same nonlinearity cut as the overall event), or $p > 200$ GeV tracks (which is set to a sufficiently high momentum the track will reach the DC, in order to avoid residual variations).

The second cut, also with the level during introduction, was

$$\max z < 0.95 \tag{5.35}$$

which recognizes that jets containing a misreconstructed high-p_T will be longitudinally dominated by it. This is then combined with a charged fraction cut

$$f_{\text{ch}} \equiv \frac{\sum_{i \in \text{charged}} h(\eta_i - \eta_J, \phi_i - \phi_J)\theta(p_{T,i} - p_{T,\text{min}}) p_{T,i}}{\sum_{i \in \text{fragment}} h(\eta_i - \eta_J, \phi_i - \phi_J)\theta(p_{T,i} - p_{T,\text{min}}) p_{T,i}} < 0.9 \tag{5.36}$$

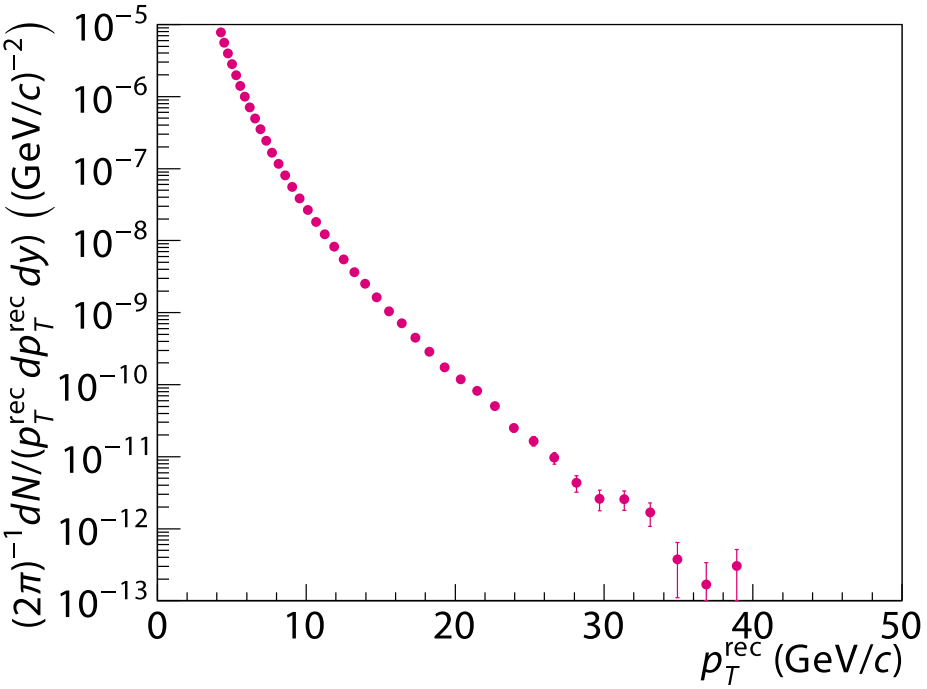

Figure 5.8: Run-5 $p+p$ $\sigma = 0.3$ Gaussian filter raw spectrum.

For $p+p$, no p_T thresholds are applied, i.e. $p_{T,\mathrm{min}} = 0$ (except for the finite momentum turn-on of the detector).

Dennis V. Perepelitsa later showed that these two cuts I proposed can be combined to improve the efficiency in preserving jet fragment phase space. For this analysis, I found that in $p+p$, a cut at

$$f_{\mathrm{ch}} < 0.95 \wedge (\max z < 0.8 \vee f_{\mathrm{ch}} < 0.8) \tag{5.37}$$

is optimal.

From the corrections specified above, we obtain a $\sigma = 0.3$ Gaussian filter and $D = 0.3$ anti-$k_\perp$ spectrum in per event yield

$$\frac{1}{N_{\mathrm{evt}}} \frac{E d^3N}{(dp^{pp})^3} = \frac{1}{N_{\mathrm{evt}}} \frac{1}{2\pi} \frac{dN}{p_T^{pp}\, dp_T^{pp}\, dy} \tag{5.38}$$

Figures 5.8 and 5.9 show the raw Run-5 $p+p$ Gaussian filter and anti-$k_\perp$ spectra.

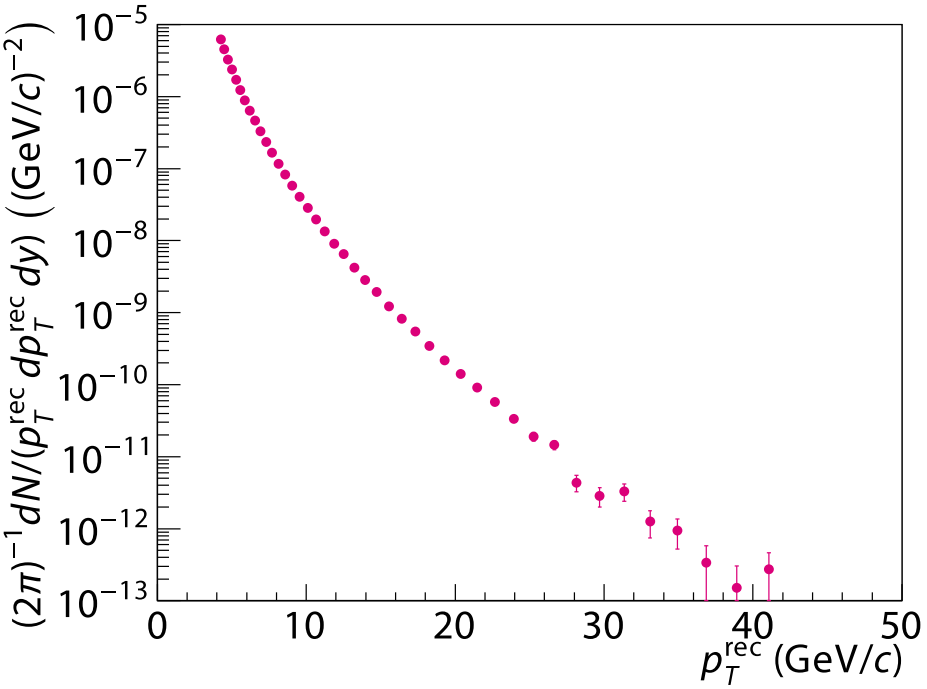

Figure 5.9: Run-5 $p+p$ $D = 0.3$ anti-$k_\perp$ raw spectrum.

5.9 Heavy Ion Background

Due to efficiency reason, the heavy ion background is obtained using the Gaussian filter applied to a (η, ϕ) binned histogram as opposed to the exact convolution using all the original particle momenta, since the latter would incur prohibitive storage and computational demand. The Run-5 Cu + Cu background being discussed here is determined using $N_\eta \times N_\phi = 84 \times 512$ bins within $|\eta| < 0.525$ (150% of the nominal PHENIX acceptance) and full 2π azimuth. This choice provides a factor of two oversampling compared to the discrete filter in the Gaussian filter algorithm, and still has sufficient occupancy per bin when integrating over the peripheral 80–95% centrality when using the Run-5 Cu + Cu statistics.

We are using a partially factorized background in the sense that the normalized (by the total event p_T) (η, ϕ) distribution is parametrized in 20% centrality bins, while the total event p_T is parametrized in 1% centrality bin. The usage of partially factorized background has both statistical and technical reasons. The parametrization of vertex and reaction plane dependence with 95 centrality bins would require about 10^8 evaluation of polynomials during initialization, which can take several minutes, and equally large amount of values to be held in memory (which was problematic due to PHENIX running computer nodes with small

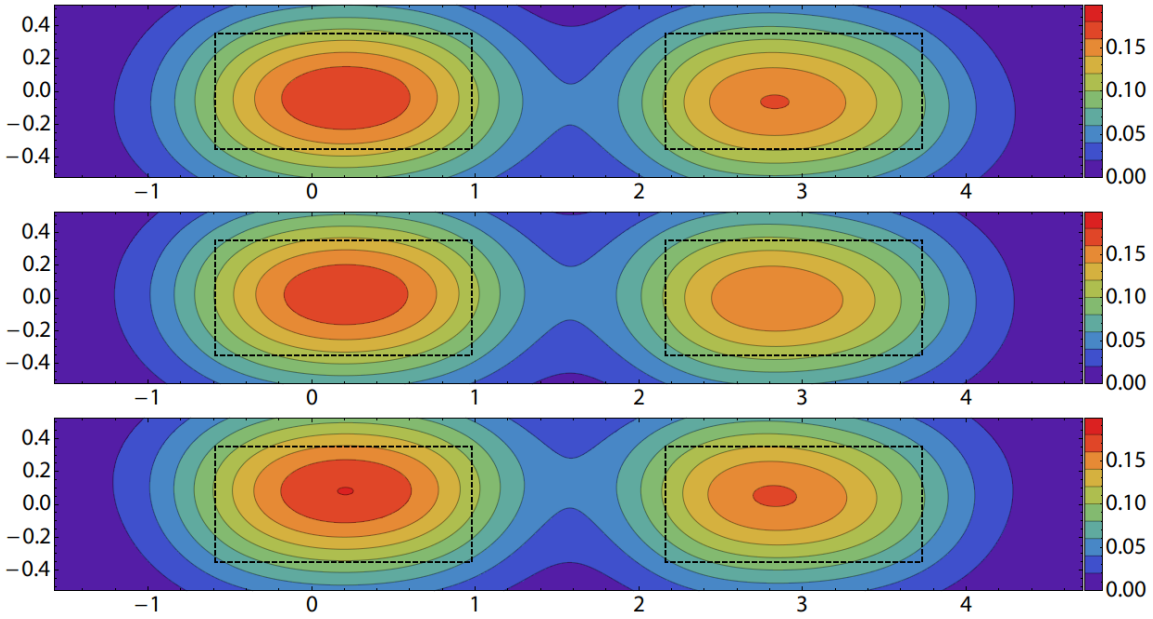

Figure 5.10: Dependence of the Gaussian filter convolved background on the vertex position.

memory sizes). And as indicated above, further subdivision the peripheral 80–95% centrality in the Run-5 Cu + Cu statistics will cause a $N_\eta \times N_\phi = 84 \times 512$ histogram to have significant portion of the histogram with no occupancy. A too fine centrality binning also bears the danger of outlier bin, where jet events are not properly averaged out against non-jet-producing events.

We used $\frac{1}{4}$ of the Run-5 Cu + Cu minimum bias events, uniformly sampled across the entire Run-5 statistics.

Figure 5.10 demonstrates dependence of the approximated on the vertex z position, using backgrounds for 0–20% centrality and $z = -25--20$ cm, $z = -5$–0 cm, and $z = 20$–25 cm bins.

Figure 5.11 demonstrates dependence of the approximated on the reaction plane, using backgrounds for 20–40% centrality and four positions from a full reaction plane rotation.

Figures 5.12 and 5.13 show the relative and absolute error of the total event p_T normalized (η, ϕ) background p_T distribution.

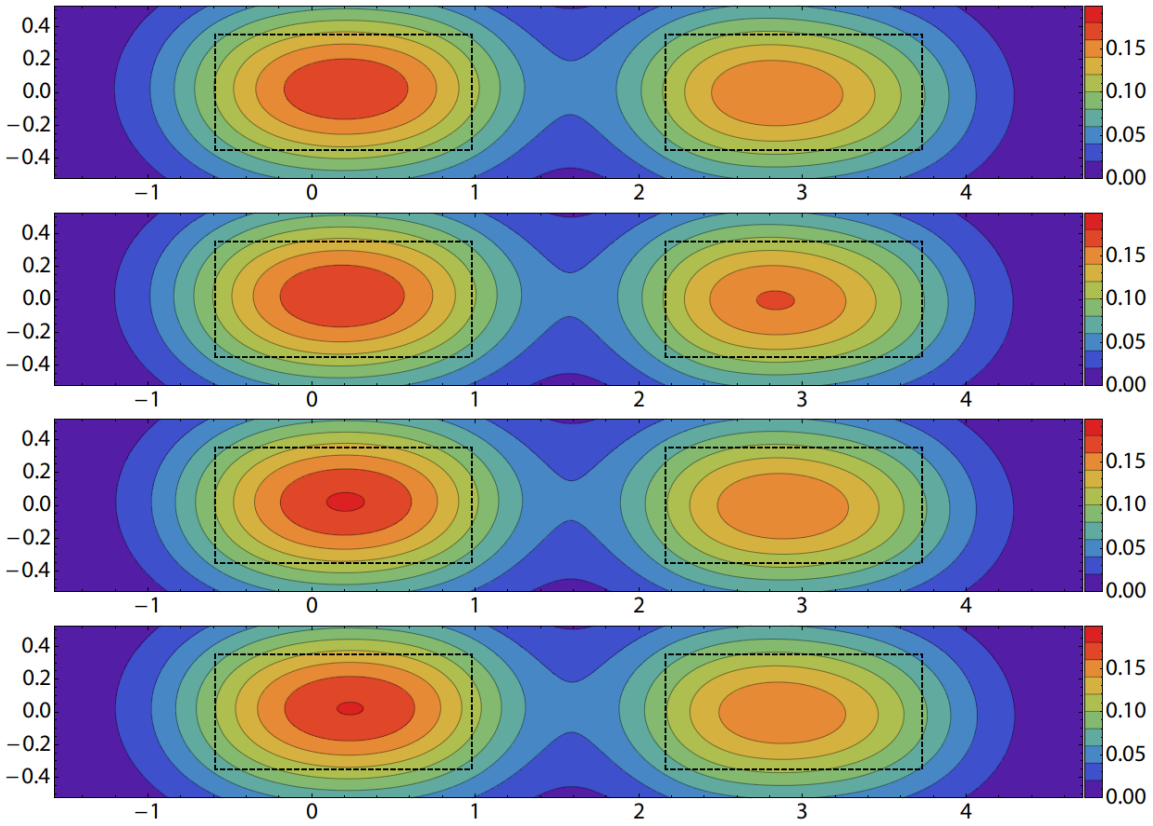

Figure 5.11: Dependence of the Gaussian filter convolved background on the reaction plane orientation.

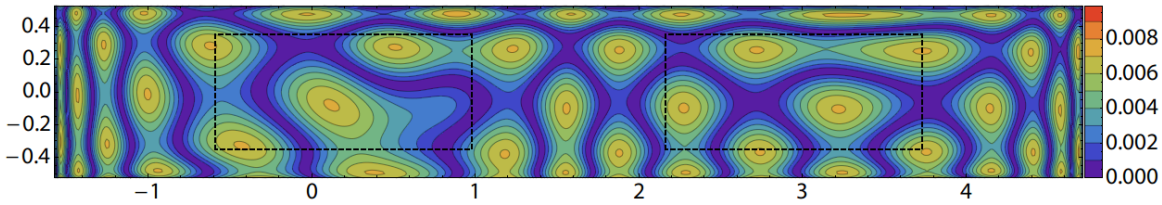

Figure 5.12: Relative approximation error using the minimax approximation and relative error metrics. Note the fully balanced out, “equiripple” structure.

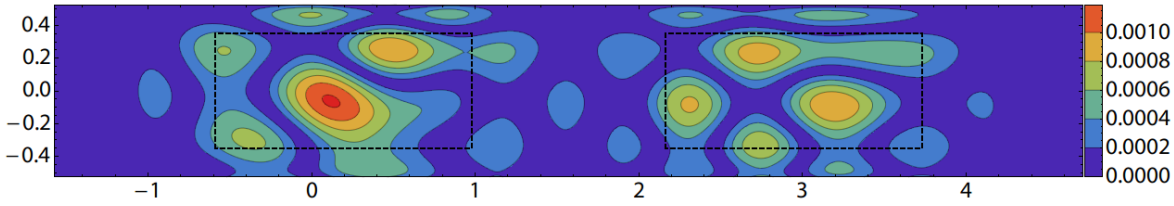

Figure 5.13: Absolute approximation error using the minimax approximation and relative error metrics.

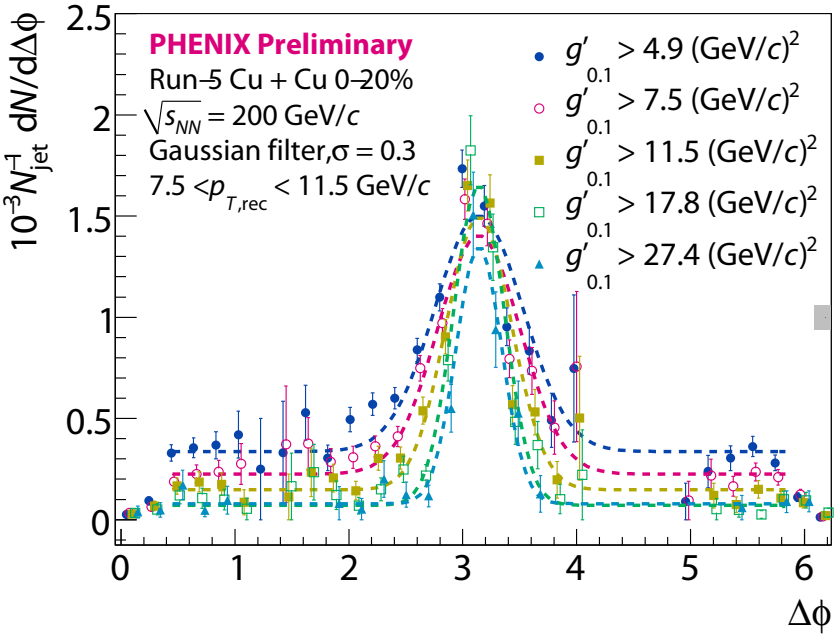

Figure 5.14: Run-5 Cu + Cu dijet azimuthal correlation for the 0–20% centrality, symmetrical dijets with 7.5 GeV/c < p_T^{CuCu} < 11.5 GeV/c, and different fake rejection level. Errors shown are statistical.

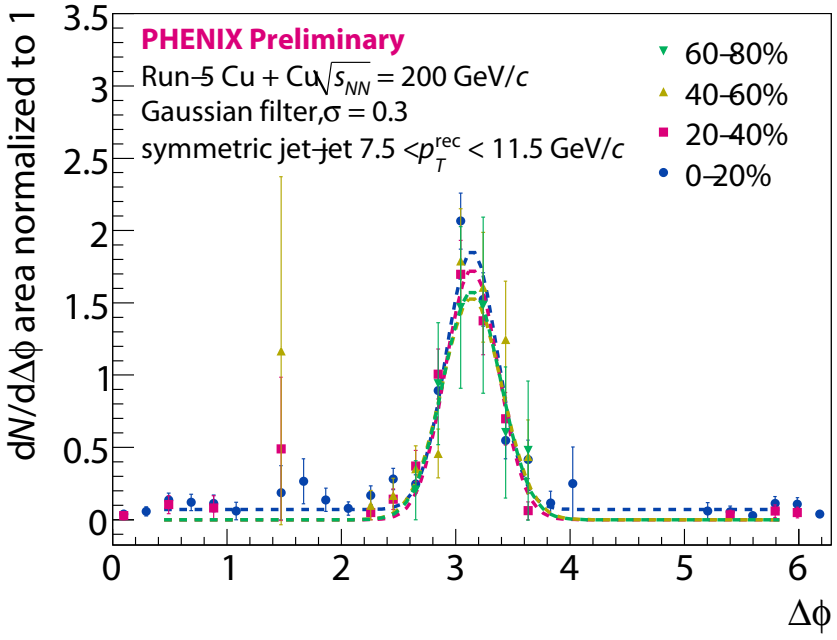

Figure 5.15: Run-5 Cu + Cu dijet azimuthal correlation for symmetrical dijets with 7.5 GeV/c < p_T^{CuCu} < 11.5 GeV/c, using the $g'_{0.1} > 17.8$ (GeV/c)^2 fake rejection level, and for different centralities. Errors shown are statistical.

Centrality	σ
0–20%	0.223 ± 0.017
20–40%	0.231 ± 0.016
40–60%	0.260 ± 0.059
60–80%	0.253 ± 0.055

Table 5.6: Widths σ of Gaussian fits to the PHENIX Run-5 Cu + Cu azimuthal angular correlation for symmetrical dijets with $7.5\,\mathrm{GeV}/c < p_T^{\mathrm{CuCu}} < 11.5\,\mathrm{GeV}/c$, using the $g'_{0.1} > 17.8\,(\mathrm{GeV}/c)^2$ fake rejection level, and for different centralities. Uncertainties listed are statistical.

5.10 Dijet Azimuthal Correlation in Cu + Cu

In order to determine the level of fake rejection discriminant sufficient to clean up the jet signal, the dijet azimuthal correlation is used to observe the level of uncorrelated signal from fake jets. The effect of the PHENIX central arm acceptance is corrected using the area normalized event mixing (e.g. [18])

$$\frac{dN(\Delta\phi)}{d\Delta\phi} = \frac{1}{A(\Delta\phi)} \frac{dN^{\mathrm{raw}}(\Delta\phi)}{d\Delta\phi} \tag{5.39}$$

where $A(\Delta\phi)$ is the detector acceptance correction. The yield of fake jets is observed to saturate at $g'_{0.1} > 17.8\,(\mathrm{GeV}/c)^2$, where the pedestal translates into an estimated fake jet contamination of 10%.

Figure 5.14 shows the Run-5 Cu + Cu dijet azimuthal correlation for the 0–20% centrality and different fake rejection level.

Using a Gaussian fit to the distribution, we also extracted the width for $7.5\,\mathrm{GeV}/c < p_T^{\mathrm{CuCu}} < 11.5\,\mathrm{GeV}/c$. The widths are consistent within the uncertainty across all centrality ranges. Assuming $L = 1\,\mathrm{fm}$, the residual statistical uncertainty of $\langle k_T \rangle < 0.5\,\mathrm{GeV}/c$ would translates into a strong constraint of $\hat{q} < 0.3\,\mathrm{GeV}^2/\mathrm{fm}$ for the BDMPS-Z type of jet energy loss.

Figure 5.15 shows the Run-5 Cu + Cu dijet azimuthal correlation for symmetrical dijets with $7.5\,\mathrm{GeV}/c < p_T^{\mathrm{CuCu}} < 11.5\,\mathrm{GeV}/c$, using the $g'_{0.1} > 17.8\,(\mathrm{GeV}/c)^2$ fake rejection level, and for different centralities.

Table 5.6 shows the widths of Gaussian fit to the PHENIX Run-5 Cu + Cu azimuthal angular correlation for symmetrical dijets with $7.5\,\mathrm{GeV}/c < p_T^{\mathrm{CuCu}} < 11.5\,\mathrm{GeV}/c$, using the $g'_{0.1} > 17.8\,(\mathrm{GeV}/c)^2$ fake rejection level, and for different centralities.

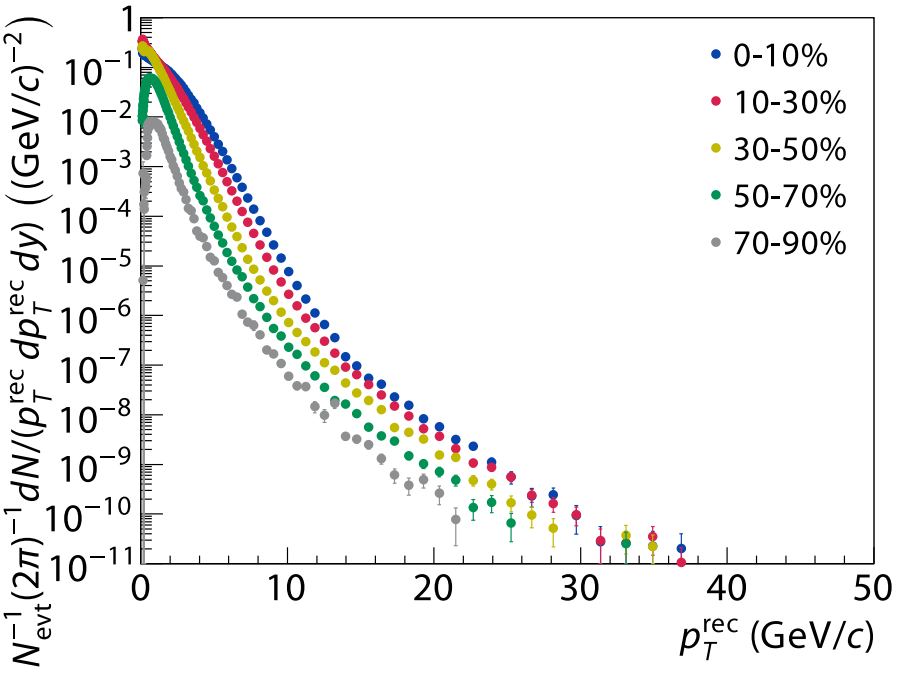

Figure 5.16: Run-5 Cu + Cu raw jet spectra without fake rejection. Error bars indicate statistical uncertainties.

5.11 Raw Spectra in Cu + Cu

For Cu + Cu, we found $p_{T,\mathrm{min}}$ below 1.5 GeV/c is insufficient to remove the large z "bump" (and since a moderate $p_{T,\mathrm{min}}$ removes the effect, it is reasonable to consider the otherwise observed "bump" not being a effect of modification). When evaluating the charged fraction of a jet, we use

$$p_{T,\mathrm{min}} = \min(0.1 p_T^{\mathrm{jet}}, 1.5\ \mathrm{GeV}/c) \tag{5.40}$$

for Cu + Cu.

for Cu + Cu, we also found that a larger max z and charged fraction cut is necessary, namely

$$f_{\mathrm{ch}} < 0.95 \wedge (\max z < 0.7 \vee f_{\mathrm{ch}} < 0.6) \tag{5.41}$$

while the aforementioned minimum p_T threshold is maintained

Figures 5.16, 5.17, 5.18, and 5.19 show the Run-5 Cu + Cu raw jet spectra with no fake rejection, and with $g' > 11.5$, 17.8, and 27.4 $(\mathrm{GeV}/c)^2$ fake rejection levels.

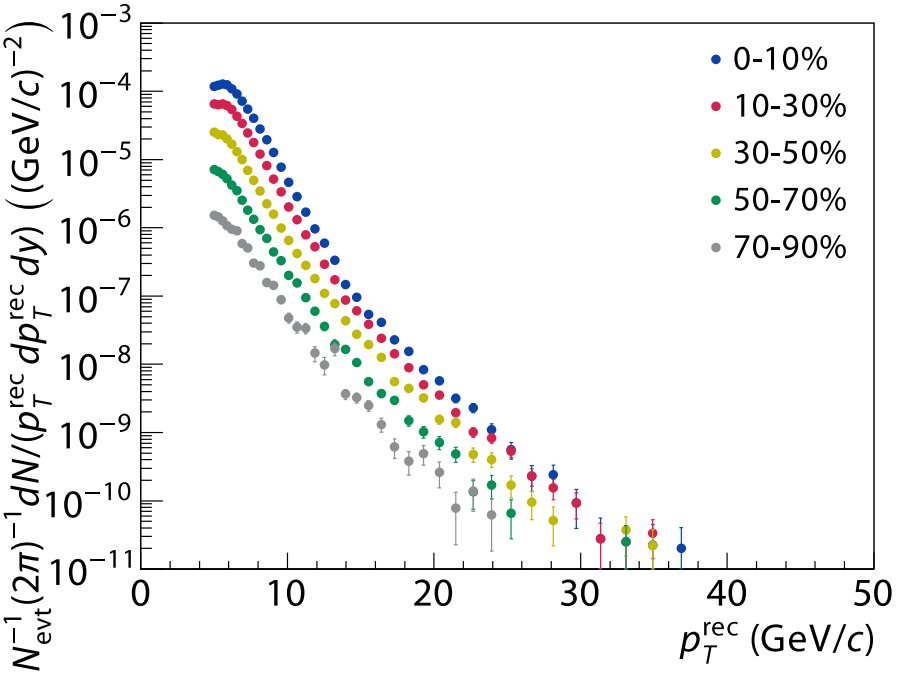

Figure 5.17: Run-5 Cu + Cu raw jet spectra at $g' > 11.5$ (GeV/c)^2 fake rejection. Error bars indicate statistical uncertainties.

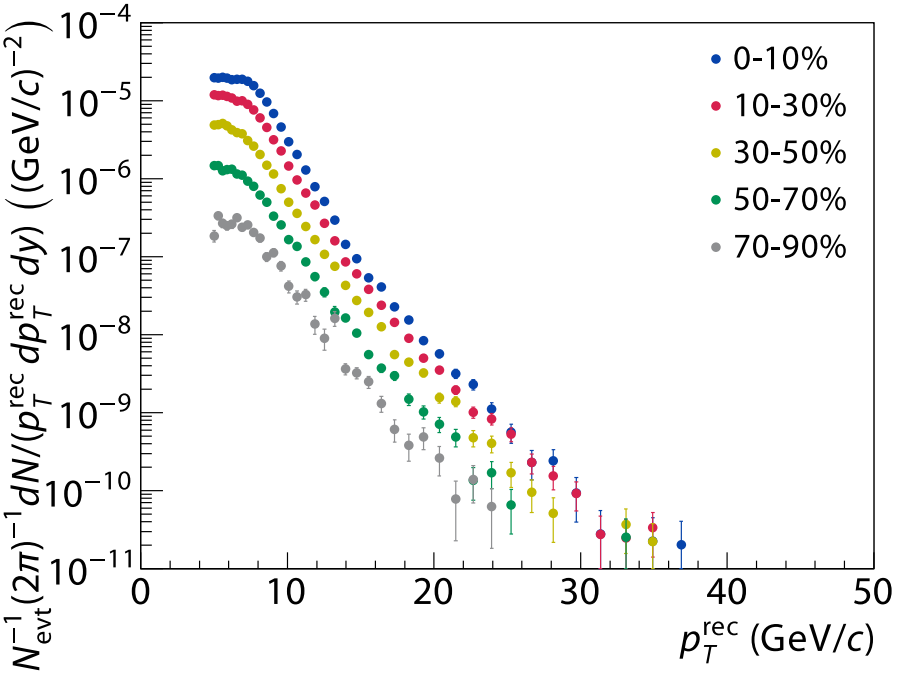

Figure 5.18: Run-5 Cu + Cu raw jet spectra at $g' > 17.8$ (GeV/c)^2 fake rejection. Error bars indicate statistical uncertainties.

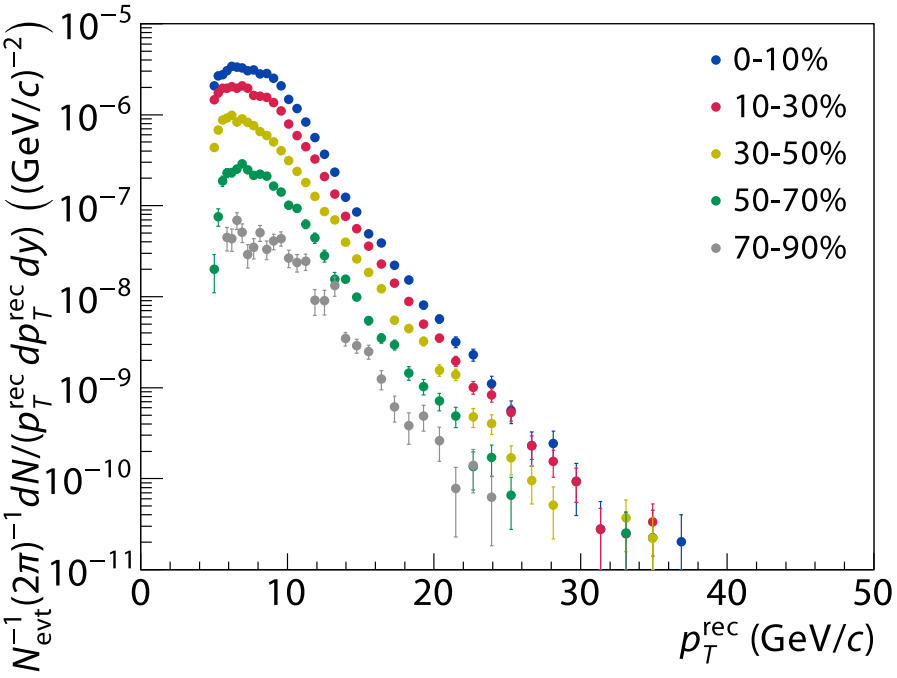

Figure 5.19: Run-5 Cu + Cu raw jet spectra at $g' > 27.4$ (GeV/c)^2 fake rejection. Error bars indicate statistical uncertainties.

5.12 BBC Efficiency

We could also include the purely multiplicative BBC cross section and BBC efficiency to obtain a cross section measure, but since the spectrum produced here is intended as input for further unfolding to the true jet energy scale, we left the previous discussion at the level of the yield.

The BBC efficiency ϵ_{BBC} is needed to convert the BBCLL1/MB trigger based cross section to the unbiased cross section. It is is the efficiency of the PHENIX MB or BBCLL1(>0 tubes) trigger firing, which at Run-5, is defined the coincident firing of at least one phototube in the north and south BBC. At the moment, evaluating the BBC efficiency using PYTHIA tune A and HERWIG in conjunction of PISA gives inconsistent result, and both event generators with detector simulation also produce a result that does not agree with the data driven method in all p_T. Therefore, the data driven method is preferred here. The fact that PYTHIA tune A and HERWIG do not agree suggest that the issue is less the detector simulation, but resides in the inability of the event generators to reproduce physical particle production across a large rapidity gap.

GL1 contains two ERT trigger that are not conincidental with the MB trigger, namely ERTLL1_4x4c and ERTLL1_4x4b. As noted above, ERTLL1_4x4c is heavily scaled down (while ERTLL1_4x4b is usually

not scaled down). The proper nonbiased event selection in a mixture of the ERT-conincidental-with-MB triggers therefore requires the test against the *scaled* bit (vs. the raw bit). A non-MB-biased selection of events therefore can be selected by triggering on ERTLL1_4x4c bit scaled logical-or ERTLL1_4x4b bit scaled:

$$\begin{aligned} P[\text{BBCLL1(>0 tubes)}] &= P[\text{BBCLL1(>0 tubes)} \mid \text{some non-MB trigger}] \\ &= \frac{N_{(\text{ERTLL1\_4x4c}\vee\text{ERTLL1\_4x4b})\wedge\text{BBCLL1(>0 tubes)}}}{N_{\text{ERTLL1\_4x4c}\vee\text{ERTLL1\_4x4b}}} \end{aligned} \tag{5.42}$$

(note that selecting solely on ERTLL1_4x4c would yield minuscule statistics in Run-5 $p+p$, that reaches single count level already at $p_T^{\text{rec}} \approx 10$ GeV/c).

Fitting the efficiency using a constant yields $\epsilon_{\text{BBC}} = 0.88694 \pm 0.00084$ The systematic uncertainty can be obtained by fitting the p_T dependence by the 3rd order Chebyshev polynomial and extract the largest component. $|a_3| = 0.013 \pm 0.010$ (15%).

The rationale to select order $N = 3$ is as follow: Fitting to order ≥ 5 starts to reproduce the statistical variation, which can be seen by significant (larger than statistical uncertainty) modification of lower order coefficients. For $N = 4$, a_4 has insignificant amplitude, but the correlation magnifies the uncertainty in a_3. Note that a_3 is consistent among $N = 3$ and $N = 4$.

We therefore obtain

$$\epsilon_{\text{BBC}} = a_0 = 0.88694 \pm 0.00084\ (\text{stat.}) \pm 1.5\%\ (\text{syst.}) \tag{5.43}$$

5.13 BBC Cross Section

The BBC Cross Section was measured in Run-5 using the van der Meer method/vernier scan to be

$$\sigma_{\text{BBC}} = 24.58\ \text{mb} \pm 5\% \tag{5.44}$$

where due to the low amount of runs that are available to perform the cross section determination, the uncertainty is a combined statistical and systematic uncertainty. However, given the low number of runs and the large hourglass correction necessary to obtain the BBC cross section, we felt that the uncertainty is likely underestimated, and assign a more conservative 10% uncertainty instead.

5.14 Summary of Systematic Uncertainties

Table 5.7 summarizes the systematic uncertainties that applies to the measurement of the raw jet spectrum.

No.	Description	Magnitude
	Global scale	
1	BBCLL1 cross section	5%
2	BBCLL1 efficiency	1.5%
3	$p+p$ ERT efficiency saturation level	2%
4	Minimum bias/ERT normalization matching	5%
5	Global energy scale	15%
	Quadrature sum	17%
	Point-to-point	
6	$e^{\pm}$ contamination for $p_T^{\mathrm{rec}} > 20\,\mathrm{GeV}/c$	10%
7	Detector boundaries/fiducial cuts sensitivity	15%

Table 5.7: Table of systematic uncertainties for the raw jet spectrum.

The accuracy to which the trigger efficiencies are known have been discussed in previous sections. The uncertainty on the energy scale is derived from the sector E/p calibration, where we observe that the π^0-only calibration produces an $E/p \approx 1 \pm 3\%$ on average. Together with the slope of the jet spectrum being approximately -5, this translates into a 15% global energy scale uncertainty.

In term of point-to-point uncertainties, from the charged fraction distribution at high p_T, we observe that residual contamination of conversion electrons is $< 10\%$, which we quote as an uncertainty above 20 GeV. The uncertainty of the cross section from the detector boundary is determined by varying the fiducial cut and observe the yield variation, which was observed to be $\approx 15\%$.

Chapter 6

Data Analysis II: Spectra Unfolding

6.1 Outline of Procedure

We continue from where we left off in the previous chapter, where we left the unfolding to the particle level yield

6.2 Unfolding

Typically, the measurement involves the

$$\frac{dN}{dp_T^{\text{det}}} = \int dp_T P(p_T^{\text{det}}|p_T) \frac{dN}{dp_T} \tag{6.1}$$

We first make a slight detour and provide an overview of unfolding techniques applied to spectra in high energy and nuclear physics. Unfolding as an inverse problem falls in the J. Hadamard's classification of ill-posed problems, which he contrasts with well-posed problem (*problèmes bien posé*), for which the solution exists and is uniquely determined [94].

A look at the current literature regarding inverse and ill-posed problems in mathematics, (optical and radio) astronomy, geophysics, and medical imaging easily reveals that a more comprehensive review of techniques suitable for spectra unfolding in high energy and nuclear physics is urgently needed. This situation also has leaded to many "rediscovery" papers, some published more than half century after the original treatise. Two methods are developed in the following, to my knowledge, has never been applied to high energy and nuclear physics: the multidimensional Phillips–Tikhonov algorihm, and the scaled Landweber algorithm.

6.2.1 Inverse Problem

Least square unfolding with linear regularization is widely known and applied in fields outside HEP (e.g. geophysics and machine lerning). Overviews to this field can be found in textbooks such as [95].

Unfolding attempts to invert the linear folding

$$\mathbf{Ax} = \mathbf{b}, \tag{6.2}$$

with $\mathbf{x}$ the truth histogram, $\mathbf{b}$ the measured histogram, and $\mathbf{A}$ the transfer matrix. Unfolding is closely related to the numerical solution of Feldholm integral equations (in fact, the solution by linear regularization is first described for integral equations).

A naïve solution to (6.2) would be

$$\mathbf{x} = \mathbf{A}^{-1}\mathbf{b}, \tag{6.3}$$

which however requires $\mathbf{A}$ being invertible, which in most cases is not true, when using Monte Carlo derived, and therefore inherently noisy $\mathbf{A}$. Furthermore, since $\mathbf{b}$ is derived by measurement, and typically contains Poisson noise, even if $\mathbf{A}^{-1}$ happens to exist, the numerically large (or near singular) eigenvalues in $\mathbf{A}^{-1}$ can drastically enhance the noise in $\mathbf{b}$ and lead a resulting $\mathbf{x}$ with unphysical bin-by-bin fluctuations (note also, that the direct inversion uses no information from the covariance of $\mathbf{b}$).

The next least square solution (i.e. the solution with $\|\mathbf{x}\| = \text{min!}$ for a rank-deficient $\mathbf{A}$) is obtained by solving

$$\|\mathbf{Ax} - \mathbf{b}\|_{\mathbf{C}} = \text{min!}, \tag{6.4}$$

Here, the right-hand side of the minimization, b is understood as the measurement that contains the folding via the linear system $\mathbf{A}$, and true vector $\mathbf{x}$ is the unknown. The rotated norm $\|\mathbf{u}\|_{\mathbf{C}} = \sqrt{\mathbf{u}^T\mathbf{C}^{-1}\mathbf{u}}$ is the Mahalanobis distance, with $\mathbf{C}$ being understood (in the Baysian interpretation) as the covariance matrix of the measurement $\mathbf{b}$. The normal equation to (6.4) is usually solved using singular value decomposition (SVD) of $\mathbf{A}$, which is given as

$$\mathbf{A} = \mathbf{U}\boldsymbol{\Sigma}\mathbf{V}^T \tag{6.5}$$

where $\mathbf{U}$, $\mathbf{V}$ are orthogonal matrices, and $\boldsymbol{\Sigma}$ is a diagonal matrix. The solution is then

$$\mathbf{x} = \mathbf{V}\boldsymbol{\Sigma}^{-1}\mathbf{U}^T\mathbf{b}. \tag{6.6}$$

where $\mathbf{A}^{\dagger}_{\text{MP}} = \mathbf{V}\boldsymbol{\Sigma}^{-1}\mathbf{U}^T$ is the Moore–Penrose pseudoinverse of $\mathbf{A}$. Expressing the problem as linear least square solves the issue with the outright singular part when inverting $\mathbf{A}$, but still does not address the problem with near zero eigenvalues in $\mathbf{A}$, that become large singular values in $\mathbf{A}^{\dagger}_{\mathbf{MP}}$.

6.2.2 Phillips–Tikhonov Regularization

However, while **x** from physical processes are smooth, near-singular components of **A** typically amplify the unavoidable fluctuation in **b**, leading to large, non-physical fluctuations in **x**. This can be solved using linear regularization, and the general solution is known as the Phillips-Tikhonov regularization.

6.2.2.1 Scaling

The need to properly scale unfolding problem is more unique to the high-energy and nuclear physics, where spectra are usually steeply falling, with the features of interest usually being multiplicatively "on top" of a power-law or exponential distribution. This is unlike unfolding of digital images or atomic and molecular spectra, where quantities encountered are typically approximately uniformly distributed on a linear quantization scale. The representation of a steeply falling and therefore (numerically and for the purpose of spectral decomposition) δ function-like distribution always require the presence of its high frequency contribution. The spectral cut-off by the direct application of traditional regularization and reblurring techniques will always result in exhaustion of the available degrees of freedom simply by the shape of the spectrum.

Among regularized unfolding, the GURU software package [96] is special in its definition of a scaled $\hat{\mathbf{x}}$ with $\hat{x}_i = x_i/x_{\mathrm{ini},i}$, where $\mathbf{x}_{\mathrm{ini}}$ is a (typically model/event generator derived) vector of the approximate scale of **x**. Since we would like to scale the unknowns by $x_i \mapsto \hat{x}_i = x_i/x_{\mathrm{ini},i}$, the linear system **A** is inversely scaled (i.e. multiplicatively), with

$$\hat{a}_{ij} = a_{ij} x_{\mathrm{ini},i} \tag{6.7}$$

(column-wise scaling). Note that we do not want to scale **L**, since the measure of undesired fluctuation is based on the scaled **x**, (i.e. fluctuation has to be small if $\mathbf{x}_{\mathrm{ini}}$ is small, and vice versa).

This step is crucial when the unfolding involves steeply falling spectra across several order of magnitudes. Without the scaling, the residual noise would be of the same scale regardless of the actual magnitude of x_i, which would be prohibitive e.g. to obtain a high p_T tail of the jet cross section, that is 10^{-10} the size of the low p_T portion of the cross section. The original Fortran 77 implementation of GURU and port to C++ have been used extensively at the Tevatron experiments. For both our 1D and multidimensional unfolding, we closely follow the approach of GURU in order to achieve comparability in the data analysis approaches.

In the context of the Phillips–Tikhonov regularization, the scaling can also be approximately considered as applying a nonuniform regularization. One should also be aware that scaling the unfolding problem has

the inherent danger of overregularization, yet yielding a physically plausible spectrum.

6.2.2.2 Solution by Singular Value Decomposition

For typical count measurements, $\mathbf{C}$ is usually a diagonal matrix, and the inversion and rotation of both sides are trivial. And this can be tought as a row-wise scaling of $\mathbf{A}$ and $\mathbf{b}$ with $c_{ii}^{-1/2}$. Otherwise, the Cholesky decomposition $\mathbf{C} = \mathbf{\Lambda}\mathbf{\Lambda}^T$ is needed, with $\mathbf{\Lambda}$ being a lower triangular matrix (which has not been implemented in either GURU, and due to the lack of necessity, neither in our unfolding code).

The scaled regularization then has the form

$$\|\hat{\mathbf{A}}\hat{\mathbf{x}} - \mathbf{b}\|_{\mathbf{C}}^2 + \tau\|\mathbf{L}^{(2)}\hat{\mathbf{x}}\|_{\mathbf{C}}^2 = \text{min!}, \tag{6.8}$$

with

$$\mathbf{L}^{(2)} = \begin{pmatrix} -1 & 1 & 0 & \cdots & 0 \\ 1 & -2 & 1 & & \vdots \\ 0 & 1 & -2 & & 0 \\ \vdots & & & \ddots & 1 \\ 0 & \cdots & 0 & 1 & -1 \end{pmatrix} \tag{6.9}$$

being the 2nd order finite difference operator. Expressed in matrix form, this is equivalent to the linear least square problem

$$\left\| \begin{pmatrix} \hat{\mathbf{A}} \\ \sqrt{\tau}\mathbf{L} \end{pmatrix} \hat{\mathbf{x}} - \begin{pmatrix} \mathbf{b} \\ 0 \end{pmatrix} \right\|_{\mathbf{C}} = \text{min!}. \tag{6.10}$$

Because (6.8) essentially trades off least square accuracy $\|\hat{\mathbf{A}}\hat{\mathbf{x}} - \mathbf{b}\|_{\mathbf{C}}$ and smoothness $\|\mathbf{L}^{(2)}\hat{\mathbf{x}}\|_{\mathbf{C}}$, a the two norms form a "L" shaped parametric curve, which is commonly referred to as the L-curve. Typically, the location of a "kink" (or rigorously, a minimum of curvature) on the curve is considered as the ideal choice of regularization. The situation becomes however more complicated when multiple "kinks" appear.

If the regularization parameter τ is known, the problem is very simple and can be solved by a SVD of the linear system on the left-hand side (expressed with the Cholesky decomposition for the generalized $\mathbf{C} = \mathbf{\Lambda}\mathbf{\Lambda}^T$):

$$\mathbf{\Lambda}^{-1} \begin{pmatrix} \hat{\mathbf{A}} \\ \sqrt{\tau}\mathbf{L} \end{pmatrix} = \mathbf{U}\mathbf{\Sigma}\mathbf{V}^T \tag{6.11}$$

(with $\mathbf{U}$, $\mathbf{V}$ being orthogonal matrices and $\mathbf{\Sigma}$ a diagonal matrix). Then the unfolded solution mean is

$$\hat{\mathbf{x}} = \mathbf{V}\mathbf{\Sigma}^{-1}\mathbf{U}^T(\mathbf{\Lambda}^{-1}\mathbf{b}). \tag{6.12}$$

To derive the covariance matrix $\operatorname{Cov}\hat{\mathbf{x}}$, note that $\operatorname{Cov}(\mathbf{\Lambda}^{-1}\mathbf{b}) = \mathbf{I}$ follows from $\mathbf{C} = \operatorname{Cov}\mathbf{b}$, and $\mathbf{U}$ is orthogonal. Therefore

$$\begin{aligned}\operatorname{Cov}\hat{\mathbf{x}} &= \mathbf{V}\mathbf{\Sigma}^{-1}\mathbf{U}\operatorname{Cov}(\mathbf{\Lambda}^{-1}\mathbf{b})\mathbf{U}^T(\mathbf{\Sigma}^{-1})^T\mathbf{V}^T \\ &= \mathbf{V}\mathbf{\Sigma}^{-1}(\mathbf{\Sigma}^{-1})^T\mathbf{V}^T.\end{aligned} \tag{6.13}$$

To simplify the discussion below, I will drop the $\mathbf{\Lambda}^{-1}$ term that can be trivially reinserted into both sides of the least square problem.

6.2.2.3 Generalized Singular Value Decomposition

The generalized singular value decomposition (GSVD) [97] of a matrix pair $\operatorname{GSVD}(\hat{\mathbf{A}}, \mathbf{L})$ simultaneously decomposes both matrices into

$$\begin{aligned}\hat{\mathbf{A}} &= \mathbf{U}\mathbf{\Sigma}_1 \begin{pmatrix} 0 & \mathbf{R} \end{pmatrix} \mathbf{Q}^T \\ \mathbf{L} &= \mathbf{V}\mathbf{\Sigma}_2 \begin{pmatrix} 0 & \mathbf{R} \end{pmatrix} \mathbf{Q}^T,\end{aligned} \tag{6.14}$$

with $\mathbf{U}$, $\mathbf{V}$, $\mathbf{Q}$ all being orthogonal matrices, and $\mathbf{R}$ a upper triangular matrix. This is the form that e.g. is used in LAPACK. An alternative form, which makes it easier to write solutions to least square problems, is

$$\begin{aligned}\hat{\mathbf{A}} &= \mathbf{U} \begin{pmatrix} 0 & \mathbf{\Sigma}_1 \end{pmatrix} \mathbf{X}^{-1} \\ \mathbf{L} &= \mathbf{V} \begin{pmatrix} 0 & \mathbf{\Sigma}_2 \end{pmatrix} \mathbf{X}^{-1}.\end{aligned} \tag{6.15}$$

Two forms are related with each other by

$$\mathbf{X} = \mathbf{Q} \begin{pmatrix} \mathbf{I} & 0 \\ 0 & \mathbf{R}^{-1} \end{pmatrix}. \tag{6.16}$$

$\operatorname{GSVD}(\hat{\mathbf{A}}, \mathbf{L})$ is closely related to $\operatorname{SVD}(\hat{\mathbf{A}}\mathbf{L}^{-1})$ (if $\mathbf{L}$ invertible), and can be immediately seen by comparing the GSVD of the quotient matrix $\hat{\mathbf{A}}\mathbf{L}^{-1} = \mathbf{U}(\mathbf{\Sigma}_1\mathbf{\Sigma}_2^{-1})\mathbf{V}^T$ with its SVD $\hat{\mathbf{A}}\mathbf{L}^{-1} = \mathbf{U}\mathbf{\Sigma}\mathbf{V}^T$. Here $\mathbf{L}^{\dagger}_{\hat{\mathbf{A}}}$ is the $(\hat{\mathbf{A}})$-weighted pseudoinverse of $\mathbf{L}$ [97]

6.2.2.4 Matrix-Pencil Solution by Inversion, GURU

GURU however solves the problem for an arbitrary τ, which is a least square problem with the matrix pencil $(\hat{\mathbf{A}} + \sqrt{\tau}\mathbf{L})$. This is solved in GURU by by transforming the least square equation into the form

$$\left\| \begin{pmatrix} \hat{\mathbf{A}}\mathbf{L}^{-1} \\ \sqrt{\tau}\mathbf{I} \end{pmatrix} \mathbf{L}\hat{\mathbf{x}} - \begin{pmatrix} \mathbf{b} \\ 0 \end{pmatrix} \right\|_{\mathbf{C}} = \min!, \tag{6.17}$$

and calculate the SVD of $\hat{\mathbf{A}}\mathbf{L}^{-1}$. $\mathbf{L}^{(2)}$ is strictly speaking singular, and GURU works around this by using $(\mathbf{L}^{(2)} + \xi\mathbf{I})$ instead, with $\xi = 10^{-3}$ (due to the numerical precision and limitation of SVD implementation it uses).

To show that one can express the solution for arbitrary τ as

$$\mathbf{L}\hat{\mathbf{x}} = \sum_i \frac{\sigma_i^2}{\sigma_i + \tau} \frac{(\mathbf{U}_{\cdot,i})^T\mathbf{b}}{\sigma_i} \mathbf{V}_{\cdot,i}, \tag{6.18}$$

take the normal equation form of the least square problem (note that in order to come as far as to write $\hat{\mathbf{A}}\mathbf{L}^{-1}$, $\mathbf{L}$ has full rank)

$$\left((\hat{\mathbf{A}}\mathbf{L}^{-1})^T \quad \sqrt{\tau}\mathbf{I}\right) \begin{pmatrix} \hat{\mathbf{A}}\mathbf{L}^{-1} \\ \sqrt{\tau}\mathbf{I} \end{pmatrix} \mathbf{L}\hat{\mathbf{x}} = \left((\hat{\mathbf{A}}\mathbf{L}^{-1})^T \quad \sqrt{\tau}\mathbf{I}\right) \begin{pmatrix} \mathbf{b} \\ 0 \end{pmatrix}, \tag{6.19}$$

and insert the aforementioned solution into the left-hand side

$$\begin{aligned} (\mathbf{V}\mathbf{\Sigma}^T\mathbf{\Sigma}\mathbf{V}^T + \tau\mathbf{I}) \sum_i \frac{\sigma_i^2}{\sigma_i^2 + \tau} \frac{(\mathbf{U}_{\cdot,i})^T\mathbf{b}}{\sigma_i} \mathbf{V}_{\cdot,i} &= \sum_i \frac{\sigma_i^2}{\sigma_i^2 + \tau} \frac{\mathbf{U}_{\cdot,i}^T\mathbf{b}}{\sigma_i} (\sigma_i^2 + \tau)\mathbf{V}_{\cdot,i} \\ &= \sum_i \sigma_i (\mathbf{U}_{\cdot,i}^T\mathbf{b})\mathbf{V}_{\cdot,i} \\ &= \mathbf{V}\mathbf{\Sigma}\mathbf{U}^T\mathbf{b} \end{aligned} \tag{6.20}$$

(note again that several orthogonality relations are being used), which is the right-hand side. The regularization is therefore a low-pass filter for the singular values, and the Tikhonov filter function

$$f_i(\tau) = \frac{\sigma_i^2}{\sigma_i^2 + \tau} \tag{6.21}$$

is clearly visible in the solution. Therefore the solution to the least square problem with a matrix pencil form can be simply obtained by filter the singular values in $\mathbf{\Sigma}^{-1}$ by

$$\mathbf{\Sigma}'^{-1} = \mathrm{diag}(f_i(\tau)\sigma_i^{-1}), \tag{6.22}$$

and then insert into the solutions (6.12) and (6.13).

Regulating the unfolding by adding a identity matrix biases the regularization towards zero in the unfolded result, and should be avoided. This approach, especially at GURU's scale of $\xi = 10^{-3}$, can have nasty, counting statistics dependent side effects. For example, it tends to produce a systematic bias towards low R_{AA} at high-p_T in peripheral collisions due to the N_{coll} scaling in heavy ion collisions.

6.2.2.5 Solution by Generalized SVD

With $\mathbf{\Sigma}_1, \mathbf{\Sigma}_2$, the GSVD obtains a pair of singular values (α_i), (β_i), and because of the aforementioned correspondence to SVD($\hat{\mathbf{A}}\mathbf{L}^{-1}$), the singular values of $\hat{\mathbf{A}}\mathbf{L}^{-1}$ are $\gamma_i = \alpha_i/\beta_i$. The Tikhonov filtered singular values for the solution with respect to $\hat{\mathbf{x}}$ (as opposed to $\mathbf{L}\hat{\mathbf{x}}$ with GURU) becomes

$$\begin{aligned} f_i(\tau) &= \frac{\gamma_i^2}{\gamma_i^2 + \tau} \\ \mathbf{\Sigma'}^{-1} &= \mathrm{diag}(f_i(\tau)\alpha_i^{-1}), \end{aligned} \tag{6.23}$$

with. A comparison with (6.12) and (6.13) and proper book keeping in (6.16) for the rank deficient cases then gives as solutions to the unfolding

$$\begin{aligned} \hat{\mathbf{x}} &= \mathbf{X}\mathbf{\Sigma'}^{-1}\mathbf{U}^T\mathbf{b} \\ \mathrm{Cov}\,\hat{\mathbf{x}} &= \mathbf{X}\mathbf{\Sigma'}^{-1}(\mathbf{\Sigma'}^{-1})^T\mathbf{X}^T. \end{aligned} \tag{6.24}$$

The key benefit of using GSVD is that now $\mathbf{L}$ can be rank deficient, which permits us to perform unfolding with regularization terms unequal the rank of $\hat{\mathbf{A}}$, while retaining GURU's feature of doing this for many τ simultaneously. This is e.g. the case when the unfolding is peformed in D dimensions, and at least D smoothness constraint corresponding to the differential operators $\partial^{(n)}/\partial x_i^n, i = 1, \ldots, D$ is applied to each point in space.

6.2.2.6 Multidimensional regularization, masking of unphysical regions

With GSVD available, generalizing the unfolding to multidimension therefore trivially becomes a matter of filling $\mathbf{L}$ with the appropriate derivatives. As with the 1D case, $\mathbf{L}$ determines the geometry of the problem. A typical multidimensional unfolding problem has the form of a tensorial histogram (like a ROOT histogram) stored in either row-major or column-major indexing. In this case, the regularization matrix is vertically stacked from derivative operators with different leading dimensions (i.e. number of flat indexing bins one has to cross to reach the next entry along that dimension), and each of the operator has also to be replicated along multiple slices of that dimension.

To illustrate for the 2D case, if $\mathbf{L}^1$ is the 1D regularization matrix (e.g. (6.9)), the 2D $\mathbf{L}^2$ is then

$$\mathbf{L}^2 = \begin{pmatrix} \mathbf{L}^1 & \mathbf{0}_{n\times n} & \mathbf{0}_{n\times n} & \mathbf{0}_{n\times n} & \cdots & \mathbf{0}_{n\times n} \\ \mathbf{0}_{n\times n} & \mathbf{L}^1 & \mathbf{0}_{n\times n} & \mathbf{0}_{n\times n} & & \mathbf{0}_{n\times n} \\ \mathbf{0}_{n\times n} & \mathbf{0}_{n\times n} & \mathbf{L}^1 & \mathbf{0}_{n\times n} & & \mathbf{0}_{n\times n} \\ \mathbf{0}_{n\times n} & \mathbf{0}_{n\times n} & \mathbf{0}_{n\times n} & \mathbf{L}^1 & & \mathbf{0}_{n\times n} \\ \vdots & & & & \ddots & \vdots \\ \mathbf{0}_{n\times n} & \mathbf{0}_{n\times n} & \mathbf{0}_{n\times n} & \mathbf{0}_{n\times n} & \cdots & \mathbf{L}^1 \\ \\ \mathbf{L}^1_{1,\cdot} & \mathbf{0}_{n\times(n-1)} & \mathbf{L}^1_{2,\cdot} & \mathbf{0}_{n\times(n-1)} & \cdots & \mathbf{0}_{n\times(n-1)} \\ \mathbf{0}_{n\times 1} & \mathbf{L}^1_{1,\cdot} & \mathbf{0}_{n\times(n-1)} & \mathbf{L}^1_{2,\cdot} & \cdots & \mathbf{0}_{n\times(n-2)} \\ \vdots & & \ddots & & \ddots & \vdots \\ \mathbf{0}_{n\times(n-1)} & \mathbf{L}^1_{1,\cdot} & \mathbf{0}_{n\times(n-1)} & \mathbf{L}^1_{2,\cdot} & \cdots & \mathbf{L}^1_{n,\cdot} \end{pmatrix}, \tag{6.25}$$

with $\mathbf{0}_{m\times n}$ being the m-by-n zero matrix. The upper half representing the derivative along the dimension that is stored memory-near (e.g. in the ROOT histogram indexing, the x-axis), and the lower half that is memory-far (in ROOT histogram indexing, the y-axis). Adding additional blocks can generalize this to higher dimensions.

6.2.2.7 Implementation using LAPACK

The subprogram library LAPACK offers the subroutine XGGSVD ("x" denotes one of the four LAPACK data types), which our implementation for the multidimensional unfolding is based on. For the 1D case, we can compare the unfolding result against GURU, and two implementations (unsurprisingly) match within expected numerical precision. The remaining scaling and matrix–vector, matrix–matrix multiplications are implemented using BLAS and OpenMP. Either one of the several BLAS and LAPACK implementation can be used. In practice, we are using the Intel Math Kernel Library 10.2.

The major drawback of a LAPACK based implementation is that $\mathbf{L}$ is highly sparse in any given dimension, and $\mathbf{A}$ typically becomes increasingly sparse with increasing number of dimensions. There is unfortunately no publicly available sparse GSVD code, and whether writing our own sparse GSVD code, or use existing sparse SVD and blindly shoot for different τ remain something that has to be explored in the future.

Currently, the unfolding of a 50×50 histogram using our dense LAPACK-based code takes approximately

1.5 hour on an Intel Xeon E5420 (2.5 GHz with no hardware simultaneous multithreading). Note that this is also close to the maximum size that can be unfolded within a 32-bit addressable memory using the double precision GSVD implementation in LAPACK.

6.2.3 Inversion-Based Algorithms

6.2.3.1 Van Cittert Algorithm

The van Cittert [98] algorithm is a direct evaluation of the Neuman series of the inverse response

$$\mathbf{A}^{-1} = \sum_{k=0}^{\infty} (\mathbf{1} - \mathbf{A})^k \tag{6.26}$$

Evaluating series for $\mathbf{x} := \mathbf{A}^{-1}\mathbf{b}$ using Horner's rule gives the iteration

$$\begin{aligned} \mathbf{x}^{(0)} &= \mathbf{b} \\ \mathbf{x}^{(k+1)} &= \mathbf{b} + (\mathbf{1} - \mathbf{A})\,\mathbf{x}^{(k)} \end{aligned} \tag{6.27}$$

The van Cittert algorithm tends to diverge quickly.

6.2.3.2 Reblurring and the Landweber Algorithm

Reblurring is a simple procedure to "regularize" the otherwise rapidly divergent van Cittert algorithm. Its principle is to limit the contribution of "unmeasurable" frequency components, which are generated in the process of inverting **A**. The reblurring achieves this by filter (and usually blurring) the intermediate steps of the unfolding.

In the Landweber algorithm considers **A** itself to describe the frequency cutoff in the process of measuring **b**. Therefore, (6.27) is modified by

$$\begin{aligned} \mathbf{b} &\mapsto \mathbf{A}^T\mathbf{b} \\ \mathbf{A} &\mapsto \mathbf{A}^T\mathbf{A} \end{aligned} \tag{6.28}$$

And the Landweber algorithm is

$$\begin{aligned} \mathbf{x}^{(0)} &= \mathbf{b} \\ \mathbf{x}^{(k+1)} &= \mathbf{A}^T\mathbf{b} + (\mathbf{1} - \mathbf{A}^T\mathbf{A})\,\mathbf{x}^{(k)} \end{aligned} \tag{6.29}$$

6.2.3.3 Scaling the Landweber Algorithm

Directly applying an additive algorithm such as the Landweber algorithm will fail on a steeply falling spectrum, such as with most spectra in high energy and nuclear physics. The reason is that the Landweber algorithm, which contains a regularization in the form of the reblurring, will inevitably favor a smooth or bandwidth limited result. For this to succeed, the problem must be well scaled, which is not the case for steeply falling spectra.

To my knowledge, no scaled version of the Landweber algorithm has ever been published. Following the same approach as implemented in the software package GURU [96] and for the Phillips–Tikhonov regularization (compare section 6.2.2.1), the numerical stability can be improved by introducing a scaling vector $\mathbf{x}_{\text{ini}}$, which is a initial or guessed unfolding result, that scales the problem closer to unity. Because each iteration of the Landweber algorithm contains two additive terms, the scaling is more complex than with the Phillips–Tikhonov regularization for the linear least square problem. After experimentation, the approach that was found to be most stable is

$$\begin{aligned} \mathbf{x}^{(0)} &= \mathbf{b} \\ \mathbf{x}^{(k+1)} &= \operatorname{diag}(\mathbf{x}_{\text{ini}}) \left[\mathbf{A}^T \operatorname{diag}^{-1}(\mathbf{x}_{\text{ini}})\, \mathbf{b} + (\mathbf{1} - \mathbf{A}^T\mathbf{A}) \operatorname{diag}^{-1}(\mathbf{x}_{\text{ini}})\, \mathbf{x}^{(k)} \right] \end{aligned} \tag{6.30}$$

where both additive variates $\mathbf{b}$ and $\mathbf{x}$ are first prescaled with $x_{\text{ini},j}^{-1}$, and rescaled with $x_{\text{ini},j}$ at the end of the step.

6.2.4 Expectation–Maximization Algorithm

The Richardson–Lucy algorithm was independently discovered in optics and optical astronomy [99]. Today, it is widely applied in optical astronomy, and implemented in standard data analysis packages such as IRAF [100] and MIDAS [101]. Likely its most prominent usage was to deconvolve images taken by the Hubble Space Telescope's incorrectly shaped primary mirror [102]. Shepp & Vardi [103] were the first to describe the Richardson–Lucy algorithm in a shift-variant form for positron emission tomography, and also noticed that it is in fact a special case of the expectation–maximization (EM) algorithm.

The Richardson–Lucy algorithm calculates a trial folding $\mathbf{A}\,\mathbf{x}_k$, and corrects its effect multiplicatively,

together with a Landweber-style reblurring

$$\begin{aligned} \mathbf{x}^{(0)} &= \mathbf{b} \\ \mathbf{x}^{(k+1)} &= \mathbf{A}^T \left[\frac{b_j}{(\mathbf{A}\,\mathbf{x}^{(k)})_j} \right] \end{aligned} \tag{6.31}$$

The Richardson–Lucy algorithm was "rediscovered" for high energy physics by D'Agostini [104], and most peculiarly, for more than a decade, nobody in HEP noticed that D'Agostini's "Bayesian" is simply the Richardson–Lucy algorithm.

6.2.5 Overview of Other Algorithms

Since most these algorithms require elaborate, iterative numerical techniques to be employed, determining and implementing the proper scaling procedure for HEP spectra is nontrivial, and the proper error propagation is usually not known. Given the time constraint, these studies unfortunately have to be left for the future.

6.3 Jet Energy Scale

The jet energy scale is defined in multiple levels leading from the (idealized) short range interaction to the detector measurement:

- **Parton level.** This is a picture of LO only, usually $2 \to 2$ QCD processes, where the final state never merge. Already in NLO calculations, this is not a well defined energy scale anymore. However, it allows some elementary hadronization correction for the jet algorithm to be calculated, which can be used to align the measured cross sections to theoretical calculations.

- **Particle level.** Event generators, which are tuned against experimental data, describe the structure of jets with hadronization, and semi-NLO initial and final state radiation. This allows the jet energy scale to be defined with respect to a perfect detector.

- **Detector level.** Detector simulation provides a description of the detector effects due to acceptance, inefficiency, and finite energy resolution. This links the measurement to the particle level.

- **Detector level, underlying event smeared.** Especially in the heavy ion case, fluctuations in the underlying event causes a shift in the observed jet energy. In some jet algorithm, the clustering can also be

strongly modified. Because RHIC luminosity (at the moment) does not produce significant pile-up, no pile-up correction is performed.

The jet energy scale of PHENIX is determined by a interplay of various particle losses:

- The detector aperture leads to a position dependent likelihood of large angle jet fragment loss.
- Long-lived neutral hadrons (n, K_L^0, ...) are irrecoverably lost due to the lack of hadronic calorimeters.
- The lack of hadronic calorimeter means that tracking must be used to collect the energy produced by charged particles. Tracking, which is used to measure the charged hadronic energy, always suffers from a background from conversions and decay particles, that is largely flat in (the mismeasured) momentum and has to be rejected by complex tracking cuts. These cuts usually becomes progressively inefficient at increasing p_T.

6.3.1 Particle level yield

1. Generate truth/particle level events using LO event generator (e.g. PYTHIA, HERWIG), possibly discard those that do not have significant energy in the PHENIX central arm η range plus sufficient margins.
2. Obtain detector simulation using PISA and some vertex distribution.
3. For heavy ion collisions, perform event embedding to determine the additional underlying event energy shift.
4. Determine a high resolution BBC vertex distribution, obtain a vertex reweighting function from the measured and integrated BBC vertex distribution and the PISA vertex distribution.
5. For the reconstructed/detector and truth/particle level events:
   (a) Reconstruct the reconstructed/detector level jets using the same procedure as for the data.
   (b) Reconstruct the truth/particle level jets without applying any cuts, i.e. with the same jet reconstruction algorithm on the "naked" generator event.
6. Match truth jets to the reconstructed jets, apply the LO cross section weights, inverse ratio of out-of-acceptance events, and the vertex weight, obtain a p_T-to-p_T^{rec} transfer matrix.

7. Obtain the jet reconstruction efficiency as the ratio between the matched reconstructed jet (with its truth counterpart η position) vs. the total truth jets that falls inside a specific $\Delta\eta$.

8. Unfold the measured jet spectrum with the p_T-to-p_T^{rec} transfer matrix.

9. Unfold the spectrum with the p_T-to-p_T^{rec} transfer matrix.

10. Correct for jet reconstruction efficiency.

6.3.2 Event Generator and PISA

For event generators, both PYTHIA and HERWIG are used. The PYTHIA event generator offers various "tunes" to experimental data on jet production and underlying event. The CDF tune A [105] is used for PYTHIA event generation, and the default setting in conjunction with QCD $2 \to 2$ process is used in term of HERWIG (which, unlike PYTHIA, triggers on one process type).

In both PYTHIA and HERWIG, the supplied pseudorandom number generators (PRNGs) are replaced with the Mersenne Twister MT2203 generator. This choice is mostly motivated by the large scale Monte Carlo fake jet rejection study with the HIJING event generator, while for detector simulation purpose, the GEANT 3 simulation dominates the computational load, and the distributed event generation is not critical. The implementation of MT2203 is discussed in section 3.4.

Unfortunately, especially in the case of HERWIG, the maintenance of the public/official version in recent years has been poor. Since PHENIX does not maintain an up-to-date set of bug fixes for event generators, and few collaborators in PHENIX in fact use HERWIG, the bug fixes from the ATLAS collaboration has been applied, resulting in a HERWIG essentially identical to that of the ATLAS Collaboration, except for the PRNG replacement discussed above. For PYTHIA, the ATLAS version only distinguishes from the official version by the implementation of R-hadrons (hypothetical, hadronic binding states that contain a gluino or squark, where the decay of the sparticle is suppressed beyond the hadronization time scale by the R-parity), and due to its irrelevance to SM RHIC physics, the stock PYTHIA is used, except for the PRNG.

6.4 $p+p$ Collision at the True Energy Scale

The $p+p$ measurement process with a detector jet energy transfer function $P(p_T^{pp}|p_T)$ is described by the Fredholm equation

$$\frac{dN}{dp_T^{pp}} = \int dp_T P(p_T^{pp}|p_T)\frac{dN}{dp_T}. \tag{6.32}$$

Its inversion is accomplished by using unfolding. Once the unfolded $\frac{dN}{dp_T^{pp}}$ is obtained, the invariant cross section is given as

$$\frac{Ed^3\sigma^{\text{jet}}}{dp^3} = \frac{1}{2\pi p_T}\frac{d^2\sigma^{\text{jet}}}{dp_T^{\text{jet}}dy} = \frac{\sigma_{\text{BBC}}}{A\,\epsilon_{\text{BBC}}}\frac{1}{p_T^{\text{jet}}}\frac{1}{N_{\text{evt}}}\frac{dN^{\text{jet}}}{dp_T^{\text{jet}}} \tag{6.33}$$

6.4.1 Transfer Matrix

We use PISA running on PYTHIA Tune A and HERWIG events to produce a truth energy-to-reconstructed energy transfer matrix, that describes the PHENIX Run-5 jet energy scale. Approximately 15 million events using 8 event generator $\sqrt{Q^2}$ triggers are used to provide a uniform sampling of the p_T range.

The lowest $\sqrt{Q^2} = 0.375\,\text{GeV}/c$ trigger is constrained by HERWIG, which is not designed to generate very low-$\sqrt{Q^2}$, near minimum bias events. Also, $\sqrt{Q^2} = 64\,\text{GeV}/c$ is the upper limit, since the kinematical phase space sampling in HERWIG becomes very in efficient at high-x_T.

Since it is not desirable to run (computationally costly) detector simulation on events that do not contain a jet in the vicinity of the PHENIX central arm acceptance, jet reconstruction is run on the generated (particle-level) event to detect the presence of a jet in the mid-rapidity range. To allow some margin, 150% of the PHENIX pseudorapidity acceptance plus the jet algorithm radius is used, i.e. $|\eta| < 0.525 + \sigma$ for the filter and $|\eta| < 0.525 + D$ for anti-$k_\perp$.

All event generator observables are merged by cross section, where we keep track of the σ_{evt}, the LO cross section assigned by the generator for the $\sqrt{Q^2}$ trigger, and the ratio of events R_{mid} where a midrapidity jet is observed.

Tables 6.1 and 6.2 show the trigger information for the PYTHIA tune A and HERWIG event generators.

Figures 6.1–6.4 show the so evaluated jet energy scale transfer matrix for the combination of the two jet algorithms, Gaussian filter and anti-k_T, and both PYTHIA tune A and HERWIG.

The Gaussian filter exhibits a more p_T independent behavior of jets loose energy during reconstruction, due to the central arm detector edges and inefficiencies. The anti-k_T jet energy scale narrows below 10 GeV, where however jets can be reconstructed with a higher p_T than the particle/generator level jet. At $p_T < 4$,

CKIN(3) (GeV/c)	σ_{evt} (b)	R_{mid}
0.375	$2.763\,731 \times 10^{-2}$	0.898 674
0.5	$2.763\,731 \times 10^{-2}$	0.830 751
0.75	$2.763\,731 \times 10^{-2}$	0.624 602
1	$2.763\,731 \times 10^{-2}$	0.415 029
2	$1.678\,698 \times 10^{-2}$	0.203 455
3	$2.604\,001 \times 10^{-3}$	0.137 097
4	$6.503\,315 \times 10^{-4}$	0.116 626
6	$8.452\,015 \times 10^{-5}$	0.116 522
8	$1.824\,940 \times 10^{-5}$	0.131 891
12	$1.783\,908 \times 10^{-6}$	0.164 617
16	$2.923\,801 \times 10^{-7}$	0.193 316
24	$1.607\,195 \times 10^{-8}$	0.231 941
32	$1.369\,009 \times 10^{-9}$	0.249 713
48	$1.350\,614 \times 10^{-11}$	0.224 487
64	$7.806\,746 \times 10^{-14}$	0.146 631

Table 6.1: Trigger information for PYTHIA Tune A

PTMIN (GeV/c)	σ_{evt} (b)	R_{mid}
0.375	$(1.148\,38 \times 10^{-1})$	
0.5	$(1.222\,398 \times 10^{-1})$	0.951 700
0.75	$(1.220\,256 \times 10^{-1})$	0.867 875
1	$(1.217\,606 \times 10^{-1})$	0.723 055
2	$1.161\,378 \times 10^{-2}$	0.249 477
3	$1.917\,653 \times 10^{-3}$	0.123 094
4	$5.028\,591 \times 10^{-4}$	0.113 145
6	$7.056\,593 \times 10^{-5}$	0.134 862
8	$1.617\,565 \times 10^{-5}$	0.161 898
12	$1.725\,714 \times 10^{-6}$	0.203 612
16	$2.973\,515 \times 10^{-7}$	0.231 211
24	$1.670\,534 \times 10^{-8}$	0.270 607
32	$1.378\,255 \times 10^{-9}$	0.290 308
48	$1.239\,910 \times 10^{-11}$	0.286 778
64	$7.214\,417 \times 10^{-14}$	0.225 576

Table 6.2: Trigger information for HERWIG. Note that HERWIG does not implement low-p_T physics, and the values with $\sigma_{\text{evt}} > \sigma_{\text{inel}} \approx 42$ mb, corresponding to QCD $2 \to 2$ processes beyond the meaningful PTMIN range are in brackets. They should be replaced by PYTHIA Tune A $\sigma_{\text{evt}} = 2.763\,731 \times 10^{-2}$ to avoid unphysical cross sections and imbalance when merging with PYTHIA Tune A. R_{mid} is not listed for PTMIN $= 0.375\,\text{GeV}/c$ due to unstable numerical integration, and $R_{\text{mid}} \approx 1$ can be used as approximation.

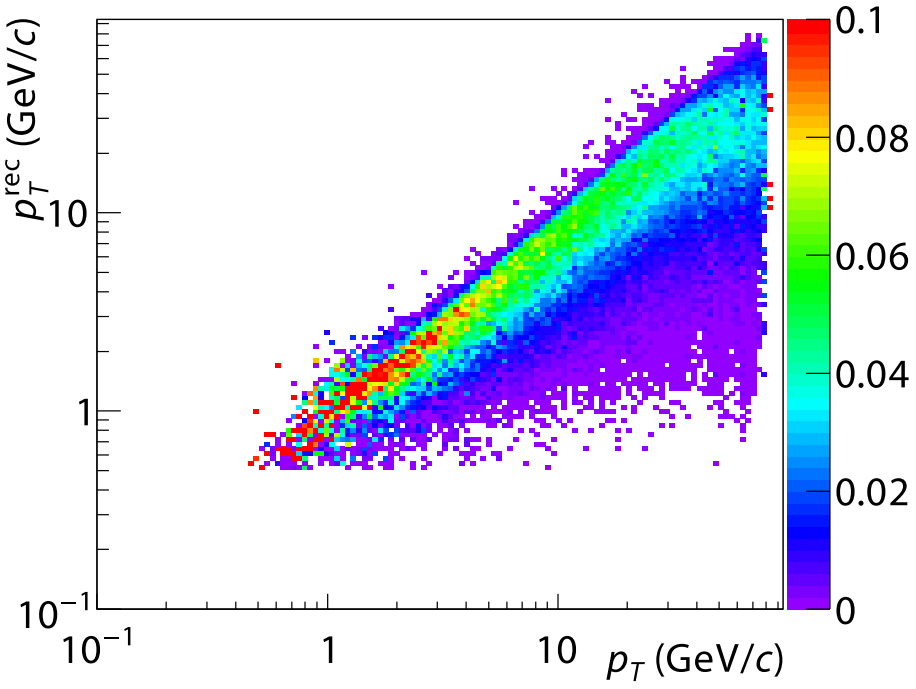

Figure 6.1: Run-5 $p+p$ Gaussian filter $P(p_T^{pp}|p_T)$ using PYTHIA tune A.

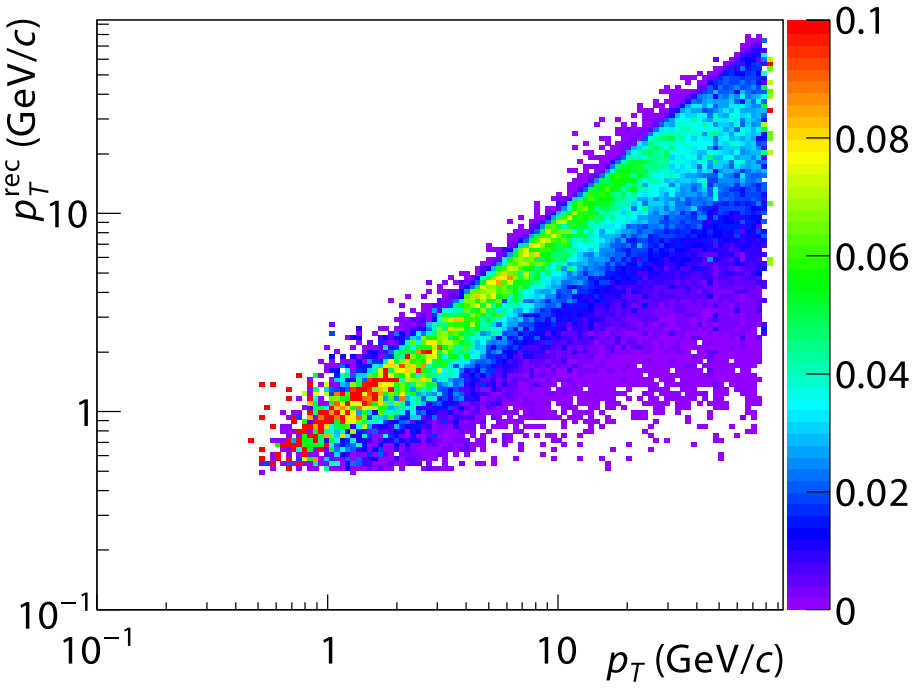

Figure 6.2: Run-5 $p+p$ Gaussian filter $P(p_T^{pp}|p_T)$ using HERWIG.

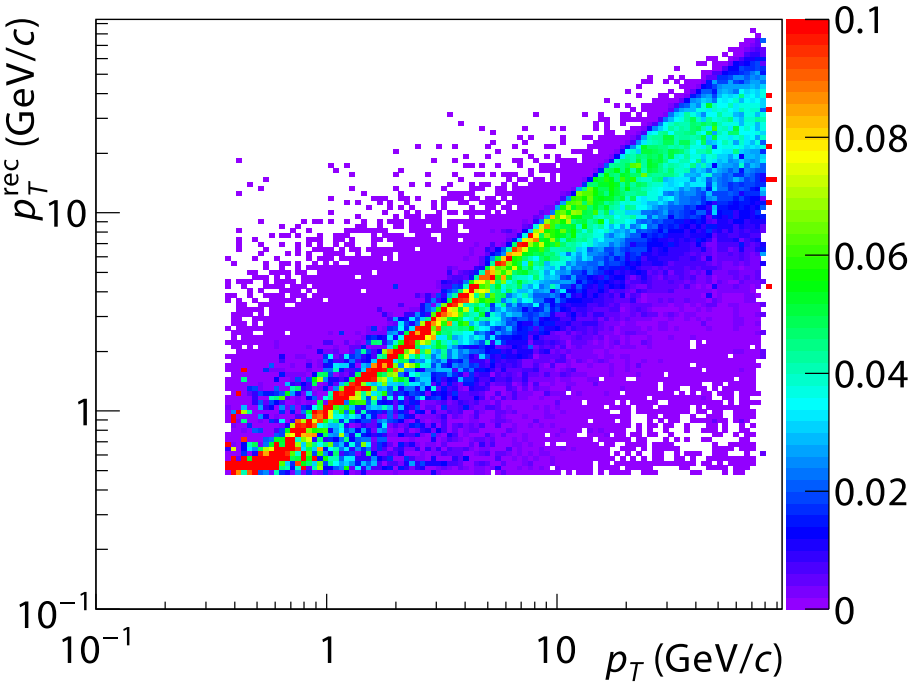

Figure 6.3: Run-5 $p+p$ anti-$k_\perp$ $P(p_T^{pp}|p_T)$ using PYTHIA tune A.

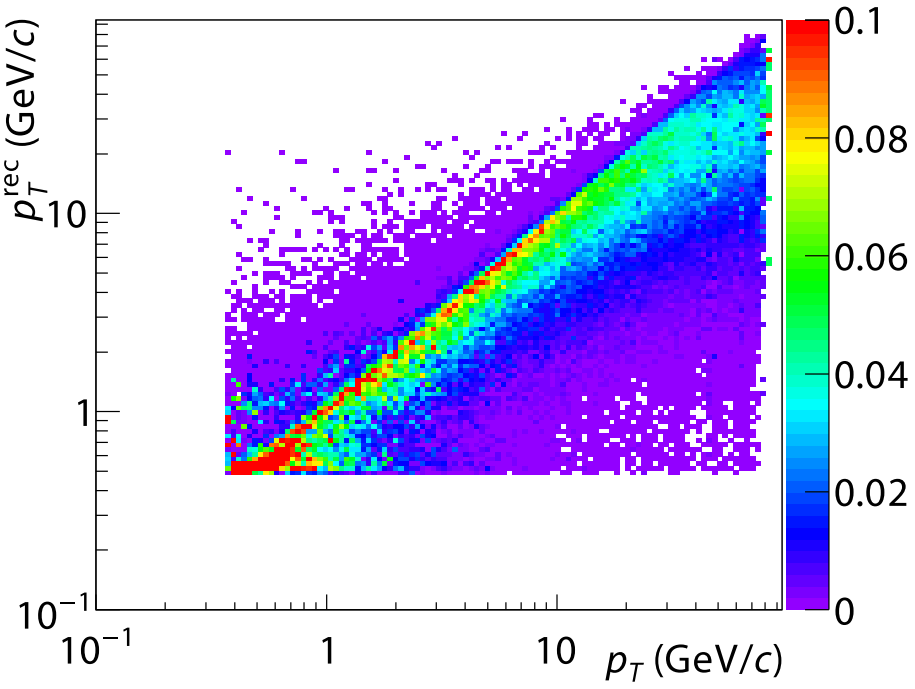

Figure 6.4: Run-5 $p+p$ anti-$k_\perp$ $P(p_T^{pp}|p_T)$ using HERWIG.

the anti-k_T transfer matrix also has a noticeable structure from low multiplicities, since a minimum 500 MeV cut is applied to clusters, while for Gaussian filter, this is smeared out by the angular weights.

6.4.2 Efficiency

The efficiency is also evaluated with the full effect of the fake rejection between $p_T^{pp} = 4$–100 GeV/c, and is parametrized by

$$\epsilon(p_T^{pp}) = \epsilon_0 \mathrm{erf}\left\{\sum_{k=0}^{N} a_k T_k \left[\frac{\log_{10} p_T^{\mathrm{rec}}/(\mathrm{GeV}/c) - \frac{1}{2}(\log_{10} 100 + \log_{10} 4)}{\frac{1}{2}(\log_{10} 100 - \log_{10} 4)}\right]\right\} \tag{6.34}$$

which is algebraically comparable in structure with the ERT 4×4C efficiency.

For Gaussian filter, we obtain for the combined PYTHIA Tune A/HERWIG:

$$\begin{aligned}
\epsilon_0 &= 0.3788 \pm 0.0014 \\
a_0 &= 2.840 \pm 0.027 \\
a_1 &= 4.115 \pm 0.045 \\
a_2 &= 2.674 \pm 0.035 \\
a_3 &= 1.865 \pm 0.035 \\
a_4 &= 1.124 \pm 0.037 \\
a_5 &= 0.553 \pm 0.035 \\
a_6 &= 0.205 \pm 0.029 \\
a_7 &= 0.047 \pm 0.021 \\
a_8 &= 0.0047 \pm 0.0093
\end{aligned} \tag{6.35}$$

For anti-$k_\perp$, combined PYTHIA Tune A/HERWIG:

$$\begin{aligned}
\epsilon_0 &= 0.3831 \pm 0.0013 \\
a_0 &= 5.849 \pm 0.030 \\
a_1 &= 9.907 \pm 0.052 \\
a_2 &= 7.557 \pm 0.039 \\
a_3 &= 5.407 \pm 0.038 \\
a_4 &= 3.366 \pm 0.041 \\
a_5 &= 1.736 \pm 0.039 \\
a_6 &= 0.701 \pm 0.030 \\
a_7 &= 0.192 \pm 0.020 \\
a_8 &= 0.0296 \pm 0.0090
\end{aligned} \tag{6.36}$$

As for the individual event generators, Gaussian filter with PYTHIA Tune A gives:

$$\begin{aligned}
\epsilon_0 &= 0.3854 \pm 0.0020 \\
a_0 &= 3.146 \pm 0.037 \\
a_1 &= 4.675 \pm 0.061 \\
a_2 &= 3.089 \pm 0.048 \\
a_3 &= 2.153 \pm 0.050 \\
a_4 &= 1.314 \pm 0.052 \\
a_5 &= 0.674 \pm 0.048 \\
a_6 &= 0.271 \pm 0.041 \\
a_7 &= 0.084 \pm 0.031 \\
a_8 &= 0.020 \pm 0.013,
\end{aligned} \tag{6.37}$$

Gaussian filter with HERWIG:

$$\begin{aligned}
\epsilon_0 &= 0.3734 \pm 0.0020 \\
a_0 &= 1.841 \pm 0.038 \\
a_1 &= 2.237 \pm 0.064 \\
a_2 &= 1.124 \pm 0.049 \\
a_3 &= 0.703 \pm 0.048 \\
a_4 &= 0.349 \pm 0.052 \\
a_5 &= 0.095 \pm 0.049 \\
a_6 &= -0.020 \pm 0.040 \\
a_7 &= -0.046 \pm 0.028 \\
a_8 &= -0.022 \pm 0.013,
\end{aligned} \tag{6.38}$$

anti-$k_\perp$ with PYTHIA Tune A:

$$\begin{aligned}
\epsilon_0 &= 0.3897 \pm 0.0018 \\
a_0 &= 9.714 \pm 0.042 \\
a_1 &= 17.168 \pm 0.072 \\
a_2 &= 13.549 \pm 0.055 \\
a_3 &= 9.754 \pm 0.054 \\
a_4 &= 6.099 \pm 0.059 \\
a_5 &= 3.180 \pm 0.054 \\
a_6 &= 1.308 \pm 0.043 \\
a_7 &= 0.373 \pm 0.029 \\
a_8 &= 0.062 \pm 0.013,
\end{aligned} \tag{6.39}$$

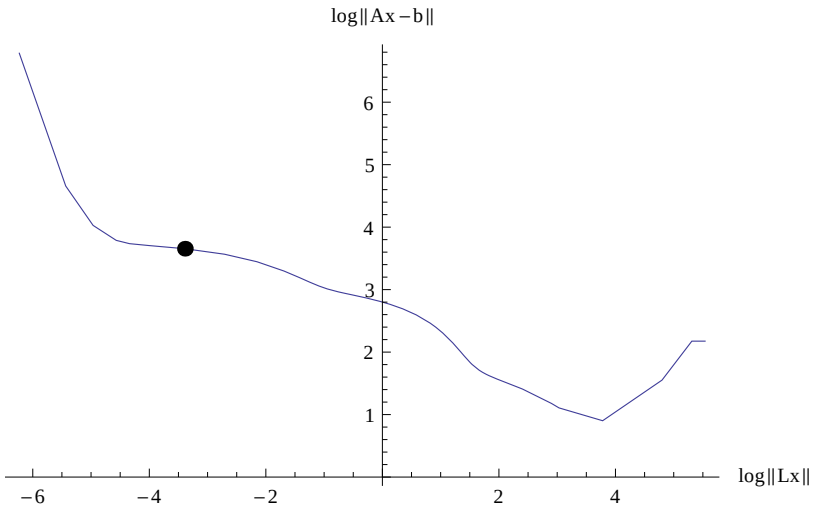

Figure 6.5: L-curve of the Run-5 $p+p$ $\sigma = 0.3$ Gaussian filter Phillips–Tikhonov regularization. The dot indicates the nominal regularization used to produce the bin center point, which is after the first "kink". The inverted kink around $\|\mathbf{Cx}\| = 0$ corresponds approximately to N_{Nyquist}, whereas the rise in $\|\mathbf{Ax} - \mathbf{b}\|$ after $\|\mathbf{Cx}\| > 3$ is due to numerical rounding error in the CERNLIB SVD routine used by GURU.

and anti-$k_\perp$, HERWIG

$$\begin{aligned}
\epsilon_0 &= 0.3789 \pm 0.0021 \\
a_0 &= 1.350 \pm 0.040 \\
a_1 &= 1.454 \pm 0.069 \\
a_2 &= 0.561 \pm 0.053 \\
a_3 &= 0.312 \pm 0.049 \\
a_4 &= 0.148 \pm 0.052 \\
a_5 &= 0.024 \pm 0.049 \\
a_6 &= -0.029 \pm 0.039 \\
a_7 &= -0.031 \pm 0.026 \\
a_8 &= -0.012 \pm 0.012.
\end{aligned} \tag{6.40}$$

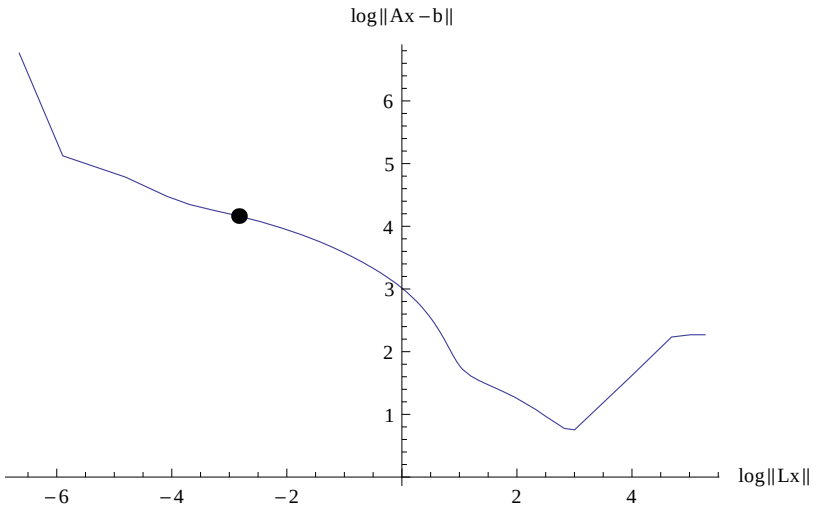

Figure 6.6: L-curve of the Run-5 $p+p$ $D = 0.3$ anti-k_T Phillips–Tikhonov regularization. The dot indicates the nominal regularization used to produce the bin center point, which is after the first "kink". The inverted kink around $\|\mathbf{Cx}\| = 0$ corresponds approximately to N_{Nyquist}, whereas the rise in $\|\mathbf{Ax} - \mathbf{b}\|$ after $\|\mathbf{Cx}\| > 4$is due to numerical rounding error in the CERNLIB SVD routine used by GURU.

6.4.3 Spectrum

A $N_{\text{dof}} \approx 7$ is used to perform the unfolding. In both Gaussian filter and anti-k_T, this location is slightly beyond the "kink", which means that the resulting distribution is weakly underregularized.

Figures 6.5 and 6.6 show the L-curve of the Phillips–Tikhonov regularization. The Cu + Cu exhibits a very short vertical section, indicating the less stable nature of the unfolding.

Figures 6.7 and 6.8 show the resulting Gaussian filter and anti-k_T spectra from unfolding. Figure 6.9 shows the two spectra overlaid on each other.

Consistent with the expectation for both jet algorithms, we observe a cross over, where the Gaussian filter has a higher cross section at low-p_T due to the larger angular range, while for well-collimated jets at high-p_T, the lack of angular weights gives anti-k_T a slightly higher cross section than the Gaussian filter. Out ability to consistently observe this type of subtle NLO jet definition difference provides an excellent test of the determination of the jet energy scale, jet reconstruction efficiencies, and unfolding.

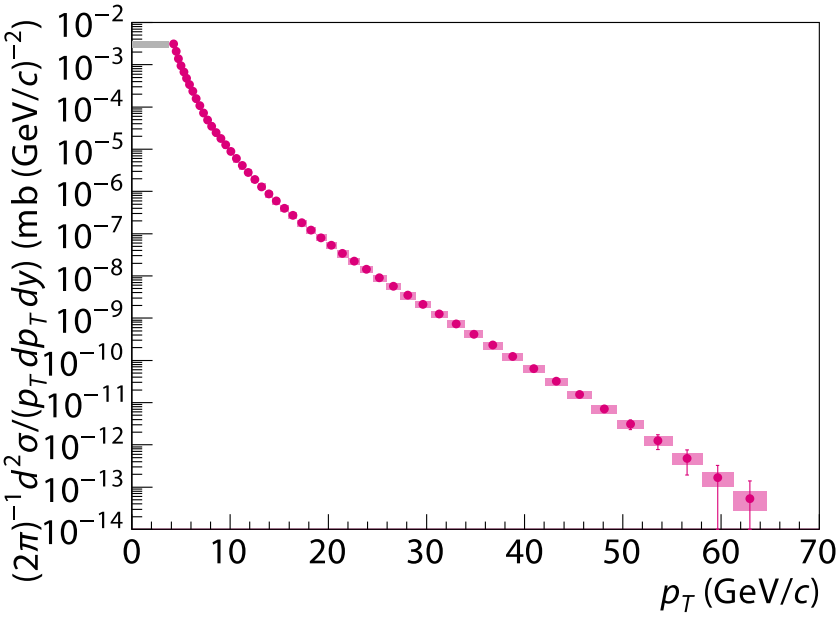

Figure 6.7: Run-5 $p+p$ $\sigma = 0.3$ Gaussian filter spectrum. Error bars indicate statistical uncertainties, shaded boxes indicate bin-by-bin systematic uncertainties. The gray box to the left indicates the correlated normalization uncertainty.

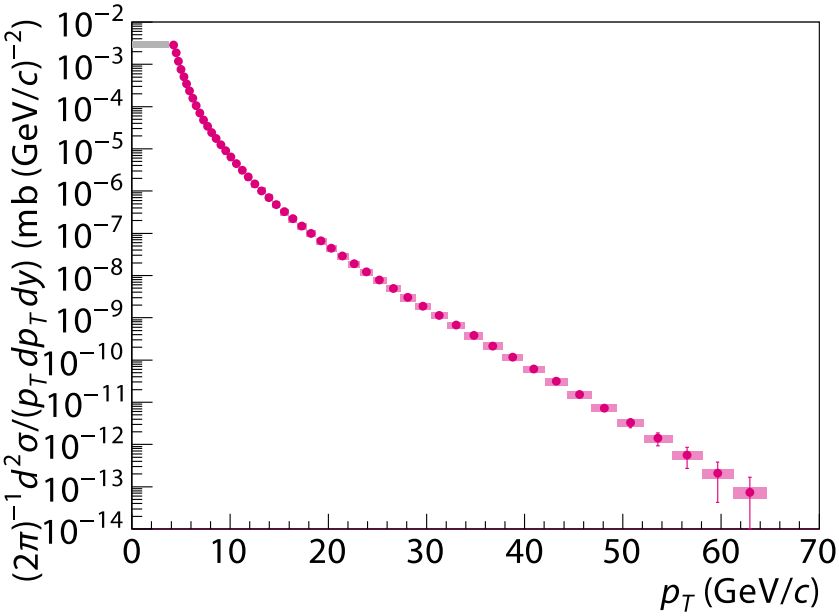

Figure 6.8: Run-5 $p+p$ $D = 0.3$ anti-$k_\perp$ spectrum. Error bars indicate statistical uncertainties, shaded boxes indicate bin-by-bin systematic uncertainties. The gray box to the left indicates the correlated normalization uncertainty.

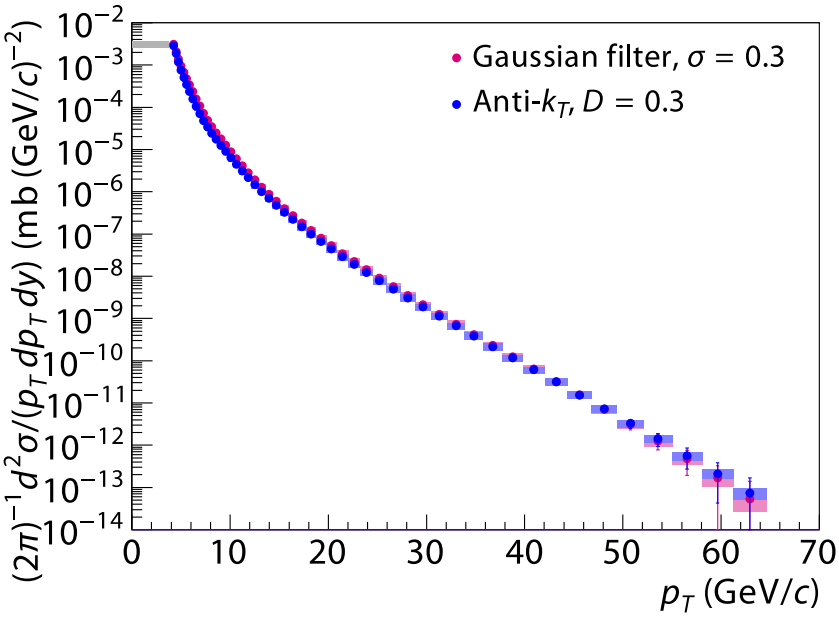

Figure 6.9: Comparison of the Run-5 $p+p$ $\sigma = 0.3$ Gaussian filter and $D = 0.3$ anti-$k_\perp$ spectrum. Error bars indicate statistical uncertainties, shaded boxes indicate bin-by-bin systematic uncertainties. The gray box to the left indicates the correlated normalization uncertainty.

No.	Description	Magnitude
	Global scale	
1	BBCLL1 cross section	10%
2	BBCLL1 efficiency	5%
3	$p+p$ ERT efficiency saturation level	3%
4	Minimum bias/ERT normalization matching	5%
5	Global energy scale	15%
	Quadrature sum	20%
	Point-to-point	
6	$e^{\pm}$ contamination for $p_T^{\mathrm{rec}} > 20\,\mathrm{GeV}/c$	10%
7	Detector boundaries/fiducial cuts sensitivity	15%
8	Unfolding systematic errors	

Table 6.3: Table of systematic uncertainties for the unfolded Run-5 $p+p$ jet spectrum

6.4.4 Summary of Systematic Uncertainties

Most of uncertainty of the raw spectrum, detailed in section 5.14, also applies to the unfolded spectrum. We evaluate the systematic uncertainty from the regularization parameter by sampling its "meaningful range". A meaningful range of the spectrum unfolding, where the low frequency component of the unfolded spectrum should behave stably, is found to be between $N_{\text{dof}} \geq 4$ and $N_{\text{dof}} \leq N_{\text{Nyquist}} = N/2$, where N is the total number of points in a 1D unfolding. Since the typical, Monte Carlo based evaluation of the transfer matrix are not properly bandwidth-limited to avoid aliasing effect of the binning, N_{Nyquist} is an information theoretical limit, to which the unfolding can be stable. $N_{\text{dof}} \geq 4$ is from experience, since lower number of degrees of freedom typically cannot properly reproduce the deviation of a real jet spectrum from the x_{ini} generated either as a perfect power-law, or using spectrum from the LO matrix elements in event generators. To evaluate the effect of regularization on the shape of the spectrum, a generalized power-law fit is performed, where the exponent is permitted to change to reproduce the kinematic phase space limiting

$$\frac{dN}{dp_T} = A p_T^{a_0 + a_1 p_T}. \tag{6.41}$$

The systematic uncertainty is then the point-by-point standard deviation of the sampled value of the fit, evaluated across the range of the regularization parameter.

Figures 6.10 and 6.10 show the point-to-point regularization dependence evaluated to obtain the unfolding systematic uncertainty.

Table 6.3 summarizes the systematic uncertainties that applies to the measurement of the unfolded jet spectrum.

6.5 $p+p$ Fragmentation Function

Unlike the spectrum measurement, the relationship between the true and measured fragmentation function is given as the Fredholm equation for the $(p_T^{\text{jet}}, p_\parallel)$ distribution

$$\frac{dN}{dp_T^{\text{jet},pp} dp_\parallel^{\text{rec}}} = \iint dp_T^{\text{jet}}\, dp_\parallel\, P(p_T^{\text{jet},pp}, p_\parallel^{\text{rec}} | p_T^{\text{jet}}, p_\parallel) \frac{dN}{dp_T^{\text{jet}} dp_\parallel}. \tag{6.42}$$

where in case of negligible single particle energy resolution, we have a 4D tensor where one dimension is diagonal

$$P(p_T^{\text{jet},pp}, p_\parallel^{\text{rec}} | p_T^{\text{jet}}, p_\parallel) = P(p_T^{\text{jet},pp} | p_T^{\text{jet}}, p_\parallel) \delta(p_\parallel^{\text{rec}} - p_\parallel) \tag{6.43}$$

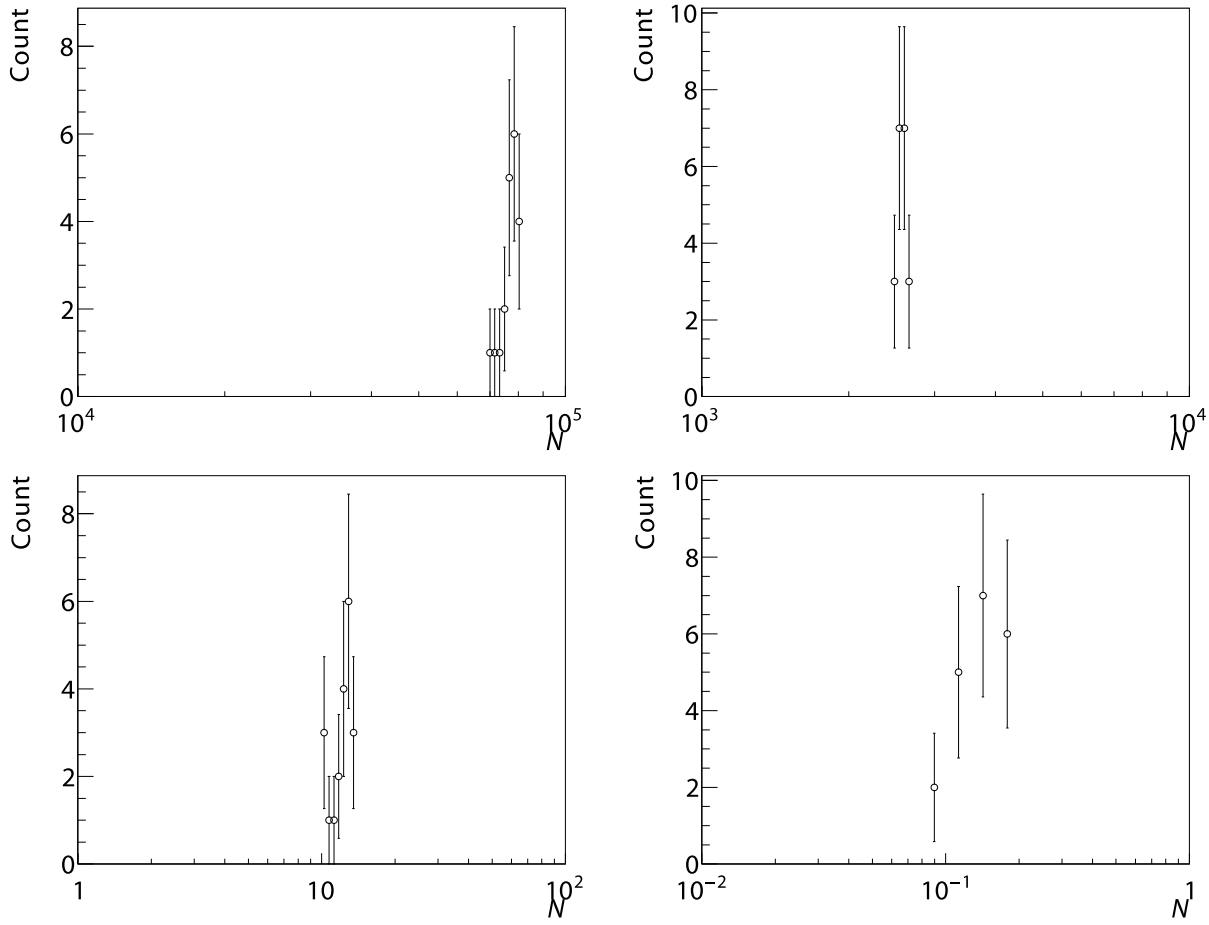

Figure 6.10: Distribution of the regularization dependence of Run-5 $p+p$ Gaussian filter raw unfolded counts at (top left) $p_T = 10.1$ GeV/c, (top right) $p_T = 20.4$ GeV/c, (bottom left) $p_T = 41.1$ GeV/c, (bottom right) $p_T = 59.9$ GeV/c, evaluated between $N_{\text{dof}} \geq 4$ and $N_{\text{dof}} \leq N_{\text{Nyquist}}$

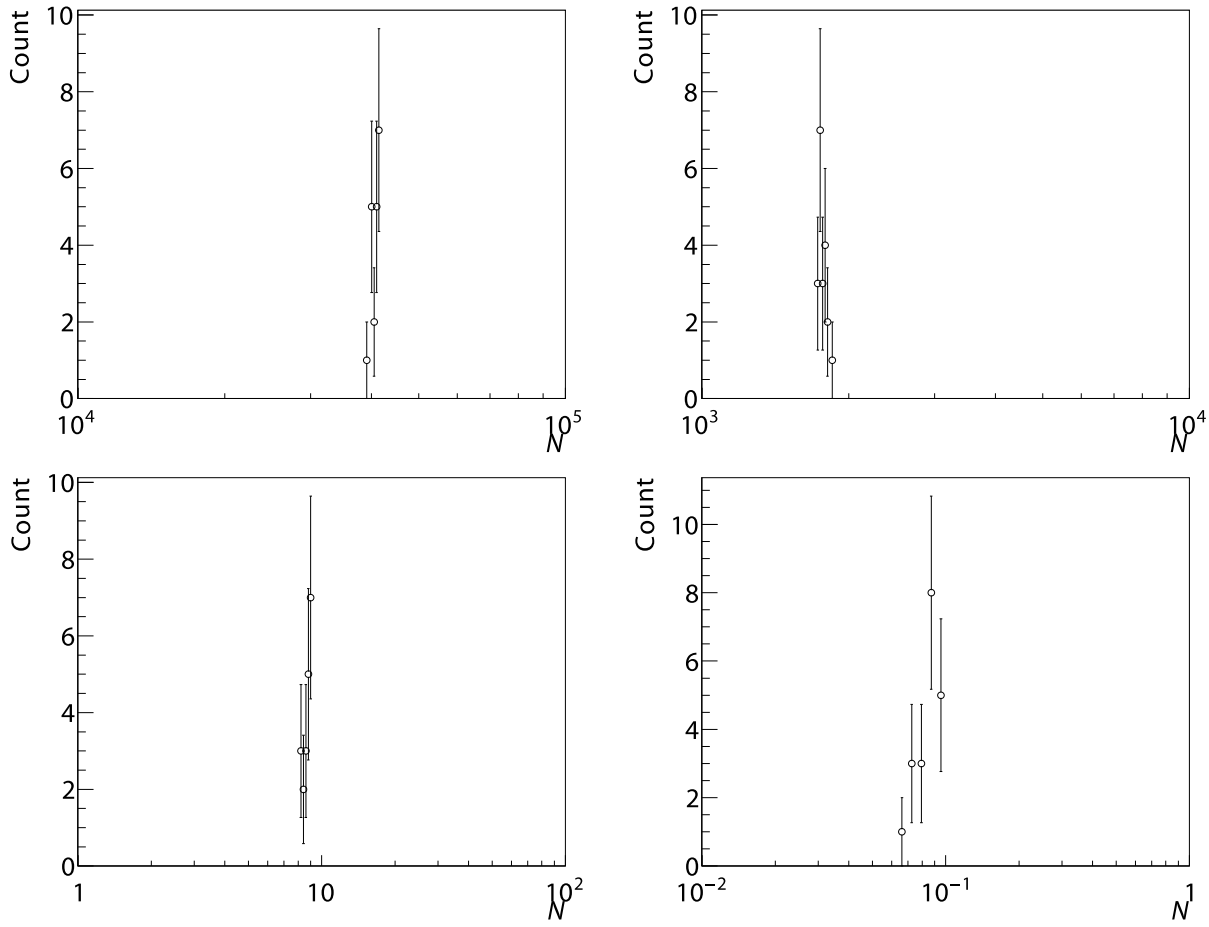

Figure 6.11: Distribution of the regularization dependence of Run-5 $p+p$ anti-k_T raw unfolded counts at (top left) $p_T = 10.1$ GeV/c, (top right) $p_T = 20.4$ GeV/c, (bottom left) $p_T = 41.1$ GeV/c, (bottom right) $p_T = 59.9$ GeV/c, evaluated between $N_{\text{dof}} \geq 4$ and $N_{\text{dof}} \leq N_{\text{Nyquist}}$

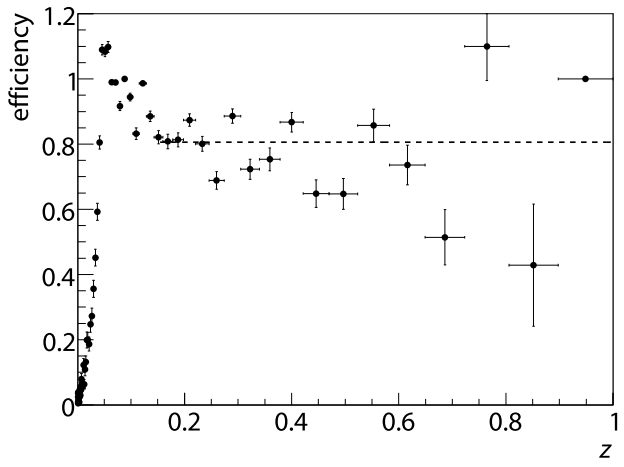

Figure 6.12: Cluster reconstruction efficiency as function of the longitudinal momentum fraction z for $p_T^{\text{jet}} = 11.1$ GeV/c.

The fragmentation function, which is normalized per reconstructed jet, is obtained by dividing the true energy scale, $(p_T^{\text{jet}}, p_\parallel)$ distribution by the true energy scale

$$D(z) = \frac{1}{\epsilon(z, p_T^{\text{jet}})} \left(\frac{dN_{\text{jet}}}{dp_T^{\text{jet}}} \right)^{-1} \frac{dN}{dp_T^{\text{jet}} dz} = \frac{1}{\epsilon(z, p_T^{\text{jet}})} \left(\frac{dN_{\text{jet}}}{dp_T^{\text{jet}}} \right)^{-1} p^{\text{jet}} \frac{dN}{dp_T^{\text{jet}} dp_\parallel} \Bigg|_{z=p_\parallel/p^{\text{jet}}} \tag{6.44}$$

with $\epsilon(z, p_T^{\text{jet}})$ being the single particle efficiencies that is evaluated using PYTHIA events and GEANT detector simulation. The cluster efficiency is largely independent of z and the jet p_T, and therefore a constant function is used. For the tracking efficiency, the magnetic field bending and electron conversion cuts result in a z dependence, and a field bending saturation plus polynomial fit are used to parametrize the tracking efficiency for different jet p_T.

Figures 6.12 and 6.13 shows the Run-5 $p+p$ tracking and cluster efficiency as function of z.

Since the DC efficiency deviates from the GEANT, due to the lack of modeling of broken wires and bad pad pixel, the DC efficiency is corrected by comparing the run dependent observation of track distributions, and aligning the efficiency using two regions in the west arm that are visually without defects. The observed DC efficiency divided by the GEANT simulation has been observed to 0.898 ± 0.023.

Figure 6.14 shows the Run-5 $p+p$ charged and neutral fragmentation function, obtained using the 2D Phillips–Tikhonov unfolding.

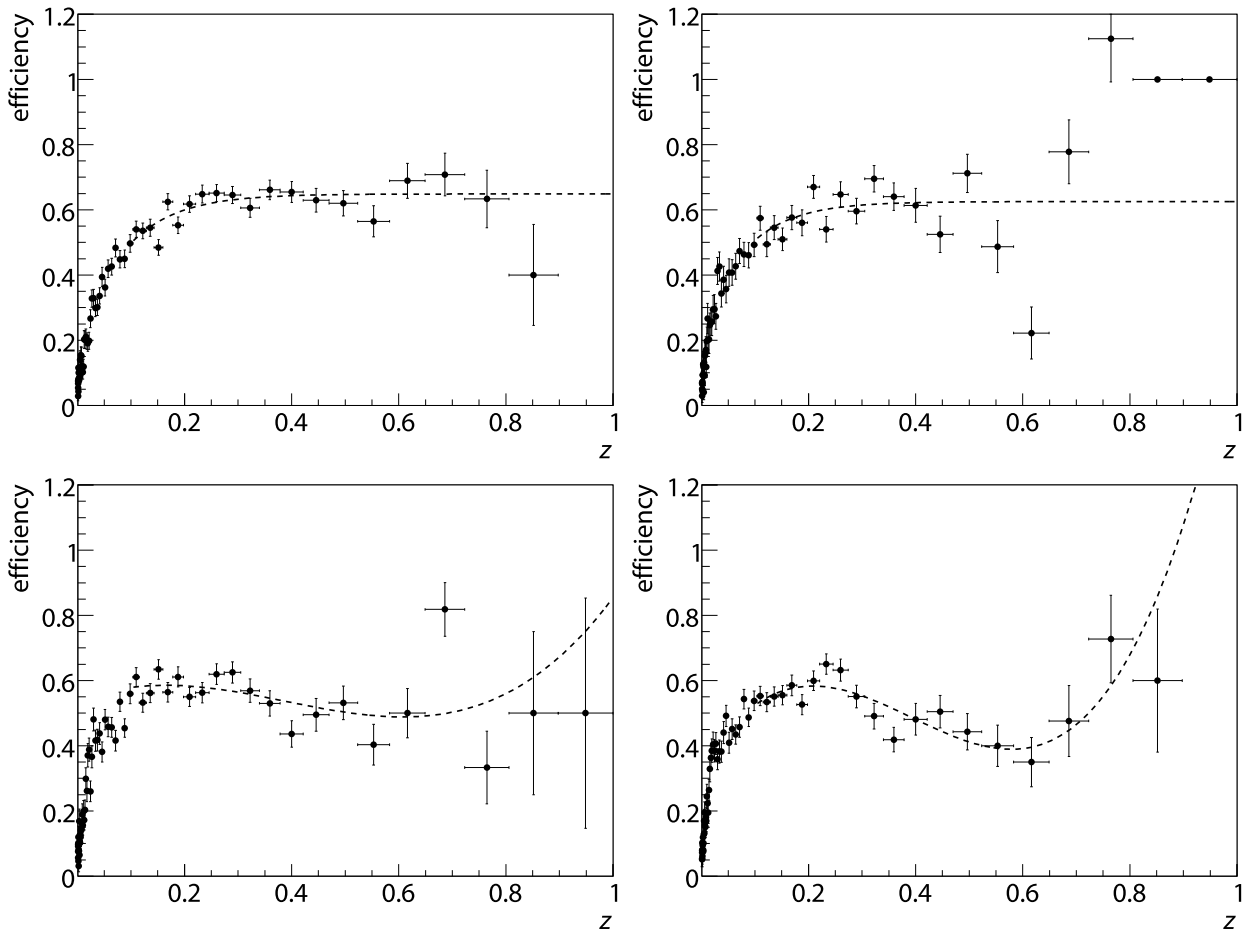

Figure 6.13: Run-5 $p+p$ tracking reconstruction efficiency as function of the longitudinal momentum fraction z, for top row, left $p_T^{\text{jet}} = 11.1$ GeV/c, right $p_T^{\text{jet}} = 13.1$ GeV/c, bottom row, left $p_T^{\text{jet}} = 15.4$ GeV/c, right $p_T^{\text{jet}} = 18.3$ GeV/c. Fit function for $p_T^{\text{jet}} = 18.3$ GeV/c will be constrained to the highest efficiency point.

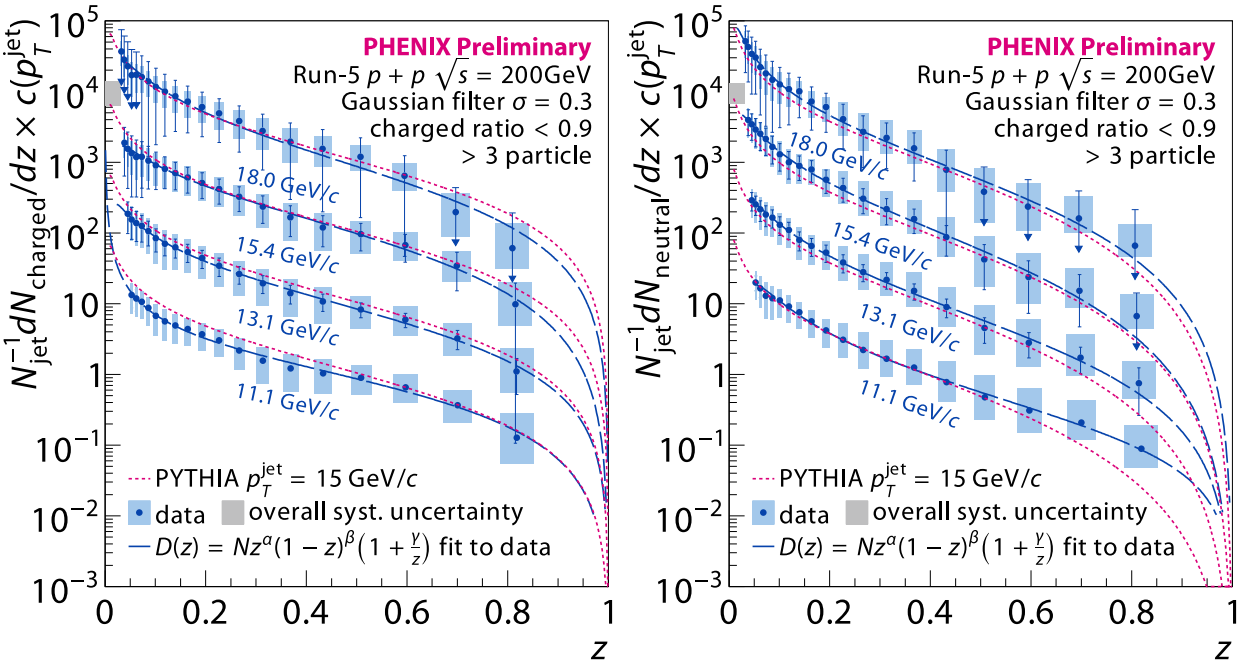

Figure 6.14: Run-5 $p+p$ charged and neutral fragmentation function, obtained using the 2D Phillips–Tikhonov unfolding. The different jet p_T bins are are vertically scaled by integer powers of ten for clarity. Error bars indicate statistical uncertainties, shaded boxes indicate bin-by-bin unfolding systematic uncertainties. The gray box to the left indicates the correlated normalization uncertainty.

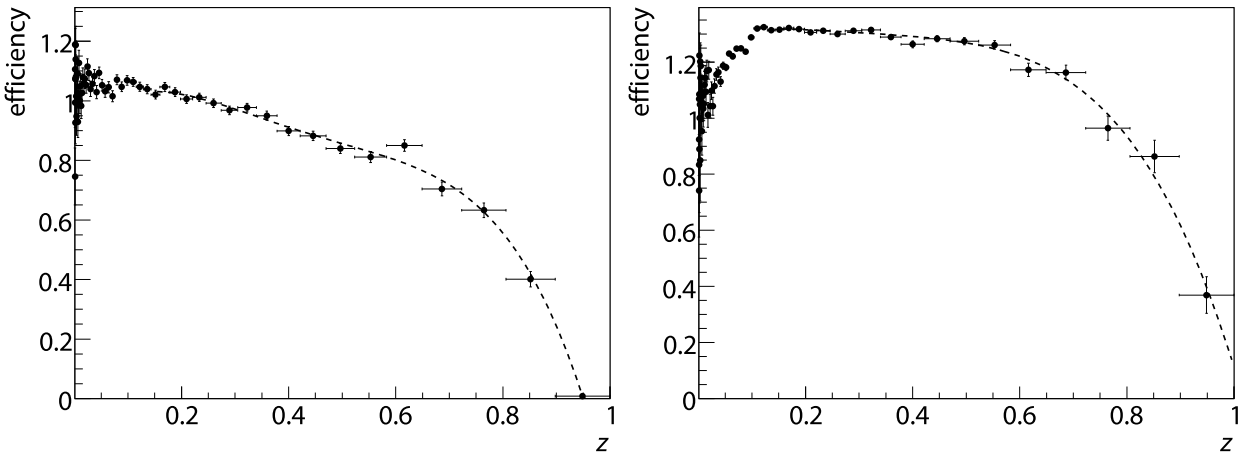

Figure 6.15: Run-5 $p+p$ three particle requirement bias as function of the longitudinal momentum fraction z, for the charged (left) fragmentation function and neutral (right) fragmentation function at $p_T^{\text{jet}} = 18.3$ GeV/c.

6.5.1 Summary of Systematic Uncertainties

From fits the z dependent efficiency using GEANT simulation, we obtain a systematic uncertainty for the overall tracking efficiency of 10% and cluster efficiency of 5%. The run dependent efficiency variation was observed to be 2.3%. The inefficiency to hard fragmenting jets due to the the three particle multiplicity requirement for the jet reconstruction is evaluated and quoted as a z dependent, upward systematic uncertainty.

Unfolding systematic uncertainty is evaluated using power law times the Review of Particle Physics $D(z)$ fits, where we vary the unfolding regularization between 4×4 until the Nyquist frequency, properly taking into account the 2D tensor nature of the unfolding.

Figure 6.15 shows the fragmentation function ratios, after divided by before applying the three particle requirement, for both the charged and neutral fragmentation function, for the most severe $p_T^{\text{jet}} = 18.3\,\text{GeV}/c$.

Table 6.4 summarizes the systematic uncertainties that applies to the measurement of the unfolded jet fragmentation function.

6.6 Cu + Cu Collisions at the Detector Energy Scale

The Cu + Cu jet event energy scale and the associated efficiency can be determined by embedding either $p+p$ events simulated by detector simulation, or using the measured $p+p$ event. The latter can be difficult if the detector configuration differs significantly between the $p+p$ and heavy ion runs. The PHENIX Run-5 with

No.	Description	Charged magnitude	Neutral magnitude
	Global scale		
1	Tracking efficiency	10%	—
2	Cluster efficiency	—	5%
3	DC efficiency	2.3%	—
	Quadrature sum	10%	5%
4	Unfolding normalization		
	Point-to-point		
5	Three particle jet requirement		
6	Unfolding systematic errors		

Table 6.4: Table of systematic uncertainties for the unfolded Run-5 $p+p$ jet fragmentation functions

both $p+p$ and Cu + Cu in the same run is a notable exception.

Embedding using actual heavy ion underlying event avoids any parametrization of the underlying event, whose interaction with jet reconstruction algorithms can be very complex and difficult to study. However, since jets are always present in the data, and the jet production is in fact enhanced by N_{coll}, it is crucial to avoid intrinsic jet production in the minimum bias Cu + Cu events to contaminate the evaluation of the energy scale. This causes a slightly paradoxical situation where the low jet yield e.g. at RHIC's $\sqrt{s_{NN}} = 200$ GeV Cu + Cu system hurts the statistics of the measurement, but benefits the evaluation of the energy scale. In my case, the intrinsic jets are removed by both fake jet rejection, and requiring an angular alignment of $\Delta R < 0.3$ for the input and embedded jet.

The problem with intrinsic jets may initially appear surprising, since you would expect some amount of intrinsic jet production to produce combinatorial overlap and contribute to the energy scale. But note that the "naïve" embedding do not preserve the correct yield ratio, and a real overlap with a high-p_T processes always is rarer in reality. Embedding with correct yield ratio is therefore a costly approach, but may be an interesting venue to explore for experiments that have higher energy, such at the LHC, and larger problem of removing intrinsic jets with the naïve embedding.

Embedding with measured $p+p$ events has the additional difficulty that the set of $p+p$ events is usually contaminated with nonreal jet events arising from the tracking background. During embedding, these jets

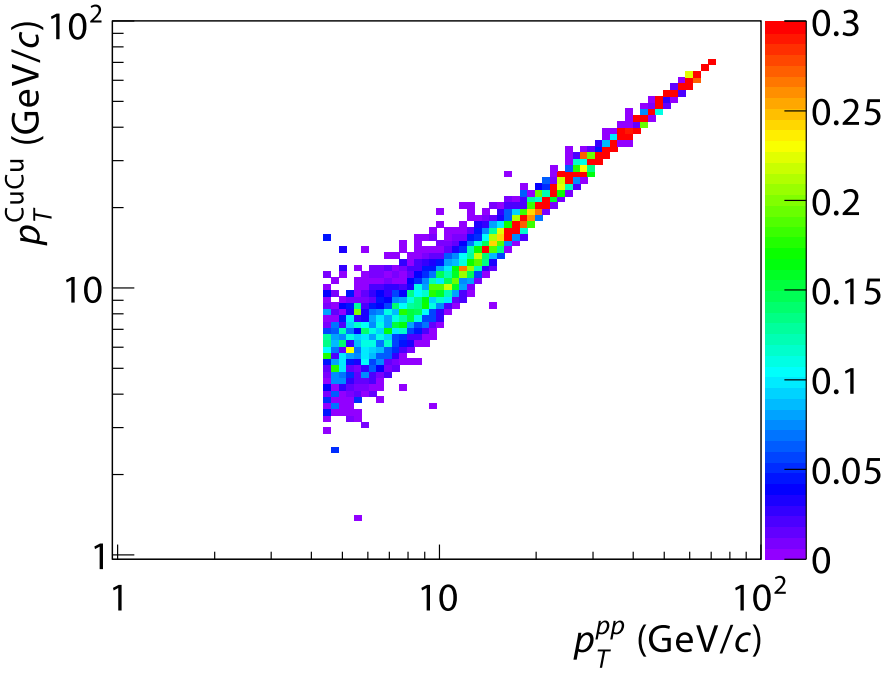

Figure 6.16: Run-5 Cu + Cu 0–10% $P(p_T^{\mathrm{CuCu}}|p_T^{pp})$ by embedding PYTHIA tune A and HERWIG jets into minimum bias heavy ion events.

have to be detected and removed.

$$\frac{dN}{dp_T^{\mathrm{CuCu}}} = \int dp_T^{pp} P(p_T^{\mathrm{CuCu}}|p_T^{pp}) \frac{dN}{dp_T^{pp}}. \tag{6.45}$$

6.6.1 Embedding Procedure

Embedding starts with a stream of $p+p$ events from PISA simulated PYTHIA and HERWIG events, and another stream of minimum bias Cu + Cu events.

Because we observe the energy scale in distinct centrality bins, the embedding reuses the $p+p$ events by replicating them in centrality bins of 20%. Since the PHENIX acceptance is vertex dependent, a $\Delta z = 5$ cm vertex bin is used, and both $p+p$ and Cu + Cu events are required to fall inside the same bin. In addition, to simulate the proper DC hit of the combined event, the DC hit position of the $p+p$ event is shifted to align at the same vertex z position as the Cu + Cu event.

Figures 6.16–6.20 show the Run-5 Cu + Cu $P(p_T^{\mathrm{CuCu}}|p_T^{pp})$ for different centralities using embedding of PYTHIA tune A and HERWIG jets into minimum bias heavy ion events.

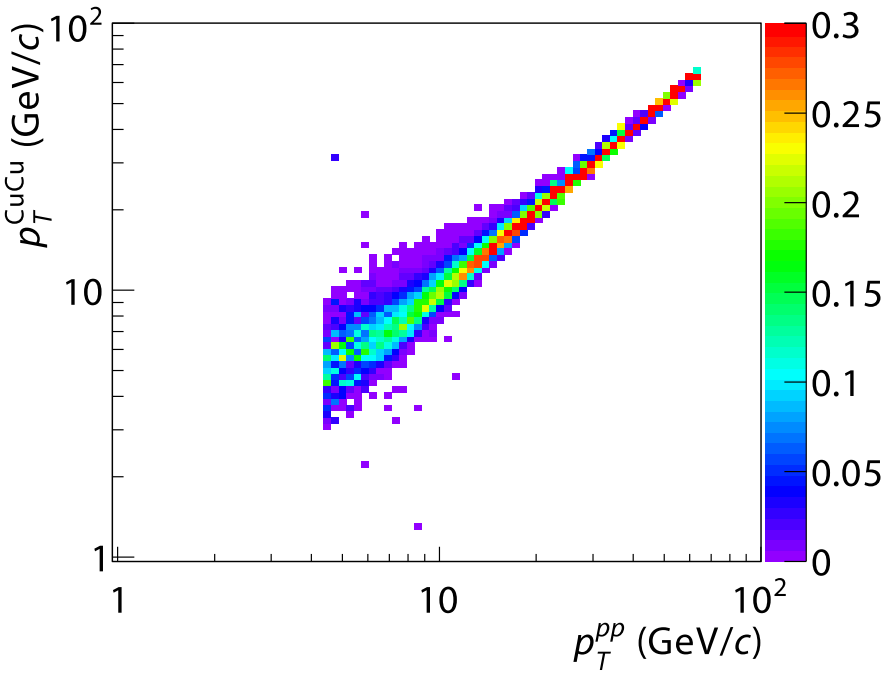

Figure 6.17: Run-5 Cu + Cu 10–30% $P(p_T^{\mathrm{CuCu}}|p_T^{pp})$ by embedding PYTHIA tune A and HERWIG jets into minimum bias heavy ion events.

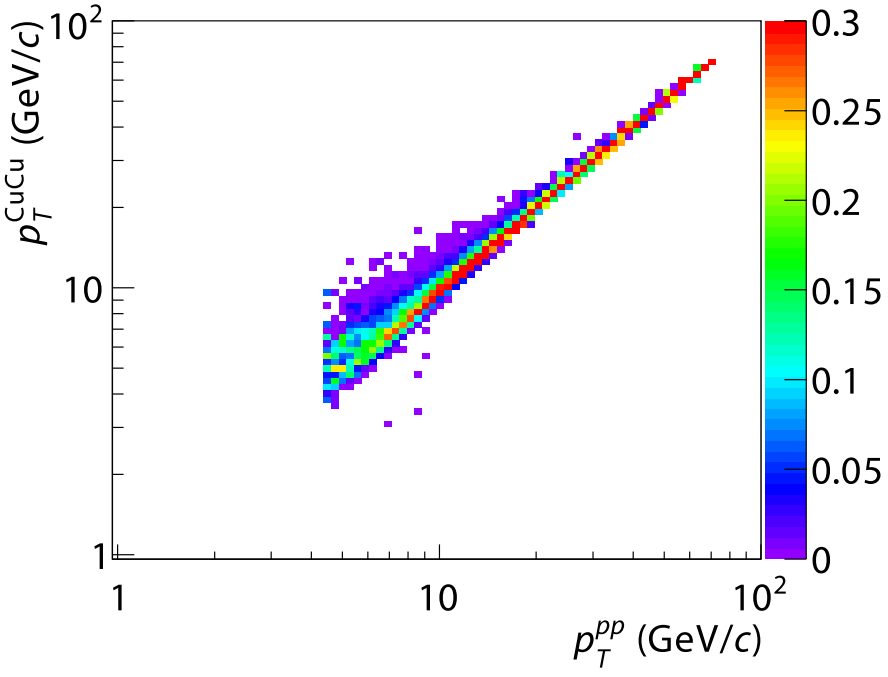

Figure 6.18: Run-5 Cu + Cu 30–50% $P(p_T^{\mathrm{CuCu}}|p_T^{pp})$ by embedding PYTHIA tune A and HERWIG jets into minimum bias heavy ion events.

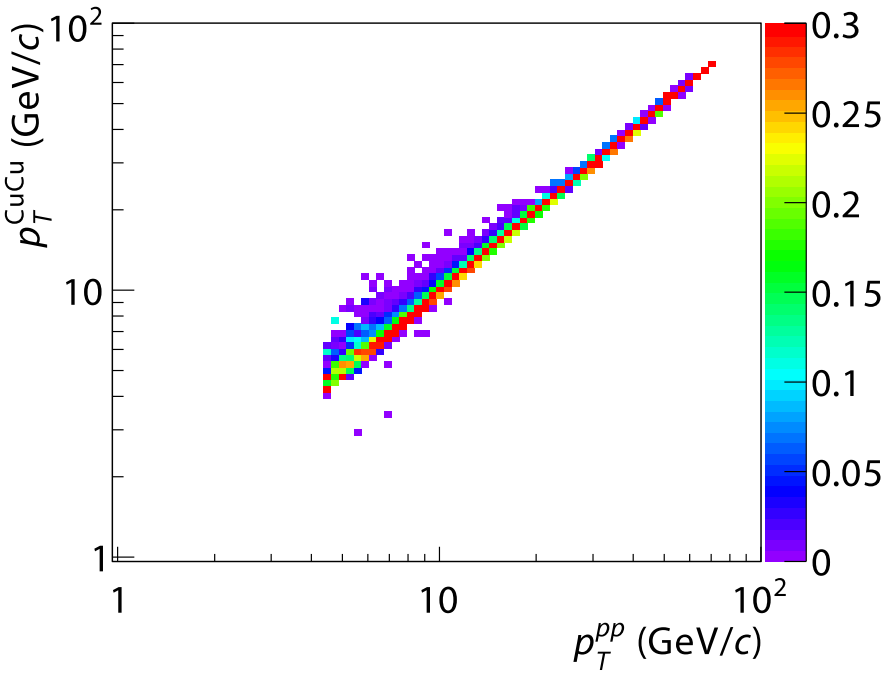

Figure 6.19: Run-5 Cu + Cu 50–70% $P(p_T^{\mathrm{CuCu}}|p_T^{pp})$ by embedding PYTHIA tune A and HERWIG jets into minimum bias heavy ion events.

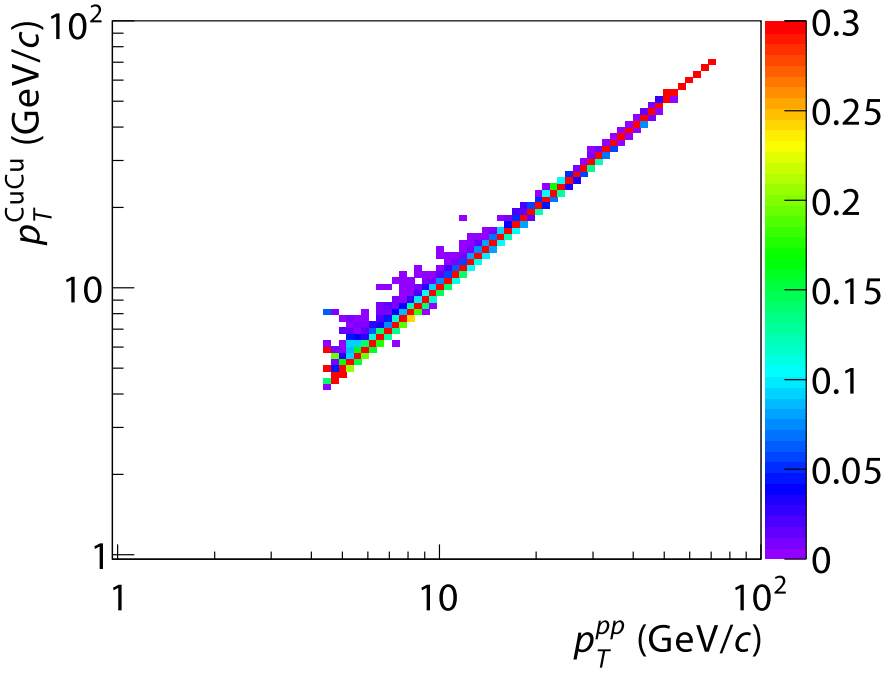

Figure 6.20: Run-5 Cu + Cu 70–90% $P(p_T^{\mathrm{CuCu}}|p_T^{pp})$ by embedding PYTHIA tune A and HERWIG jets into minimum bias heavy ion events.

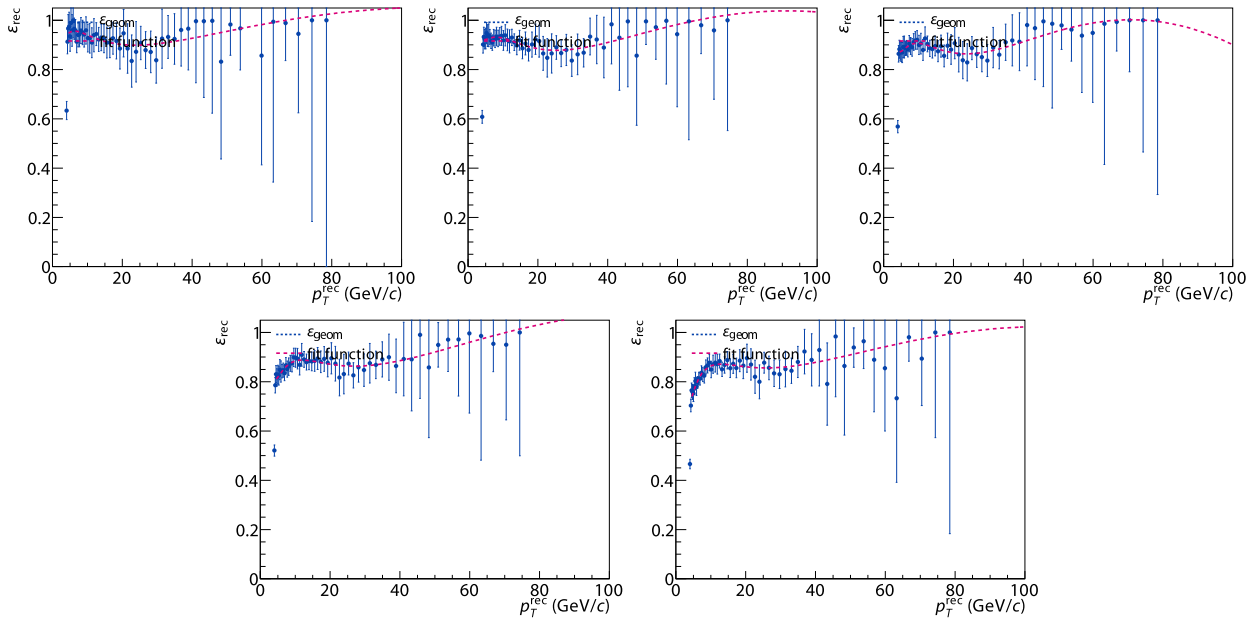

Figure 6.21: Run-5 Cu + Cu jet reconstruction efficiencies without fake rejection. Top row, left to right: 0–10%, 10–30%, 30–50%, bottom row, left to right: 50–70%, 70–90%. The p_T region where the efficiency exceeds unity are beyond the statistical reach in Cu + Cu.

6.6.2 Efficiency

The same equation as (6.34) is used here to parametrize the efficiency turn on for the fake rejection. In the case where the fake rejection is turned off, there is no saturation, and a pure Chebyshev polynomial form is used to parametrize the residual p_T dependent effect of the different charged fraction–z max cut and the centrality dependent, random benefit the jet may receive from the background

$$\epsilon(p_T^{pp}) = \sum_{k=0}^{N} a_k T_k \left[\frac{\log_{10} p_T^{\mathrm{rec}}/(\mathrm{GeV}/c) - \frac{1}{2}(\log_{10} 100 + \log_{10} 4)}{\frac{1}{2}(\log_{10} 100 - \log_{10} 4)} \right] \tag{6.46}$$

Here, a_0 roughly takes over the function of ϵ_0 as the base value of the efficiency.

Figures 6.21–6.24 show the Run-5 Cu + Cu jet reconstruction efficiencies for different centralities, and with no fake rejection, fake rejection at $g' > 11.5$ (GeV/c)^2, 17.8 (GeV/c)^2, and 27.4 (GeV/c)^2.

Tables 6.5–6.9 lists the coefficients for the parametrization of the Run-5 Cu + Cu jet reconstruction efficiencies for different centralities, and with no fake rejection, with fake rejection level at $g' > 11.5$ (GeV/c)^2, 17.8 (GeV/c)^2, and 27.4 (GeV/c)^2.

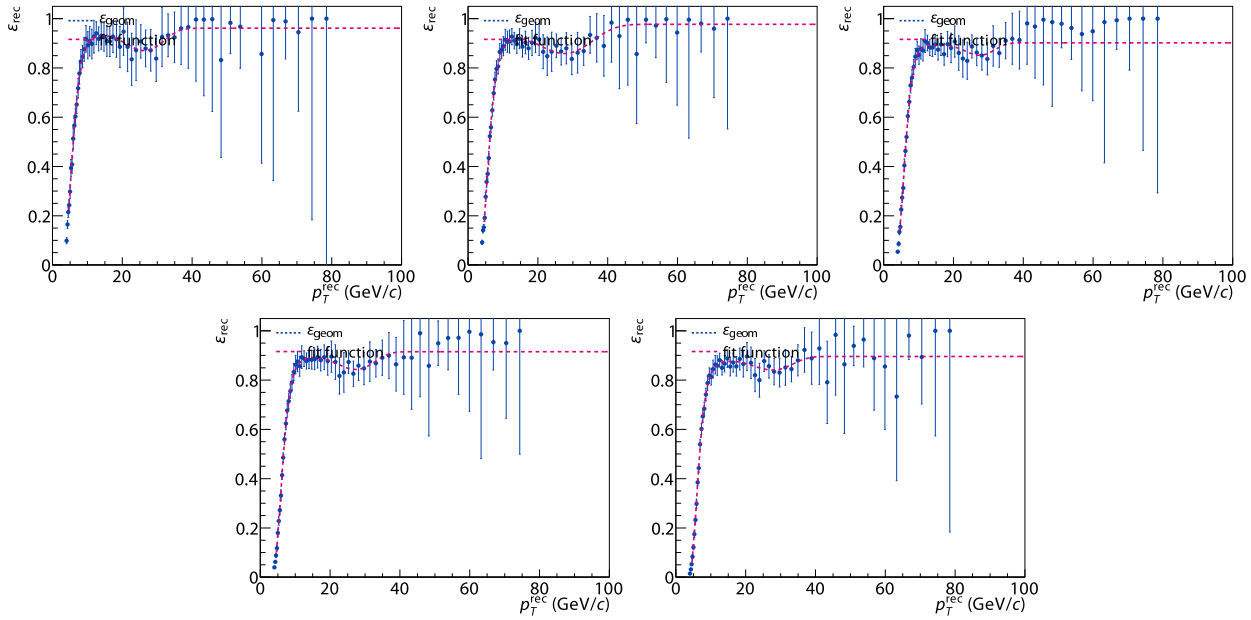

Figure 6.22: Run-5 Cu + Cu jet reconstruction efficiencies with fake rejection at $g' > 11.5$ (GeV/c)^2. Top row, left to right: 0–10%, 10–30%, 30–50%, bottom row, left to right: 50–70%, 70–90%.

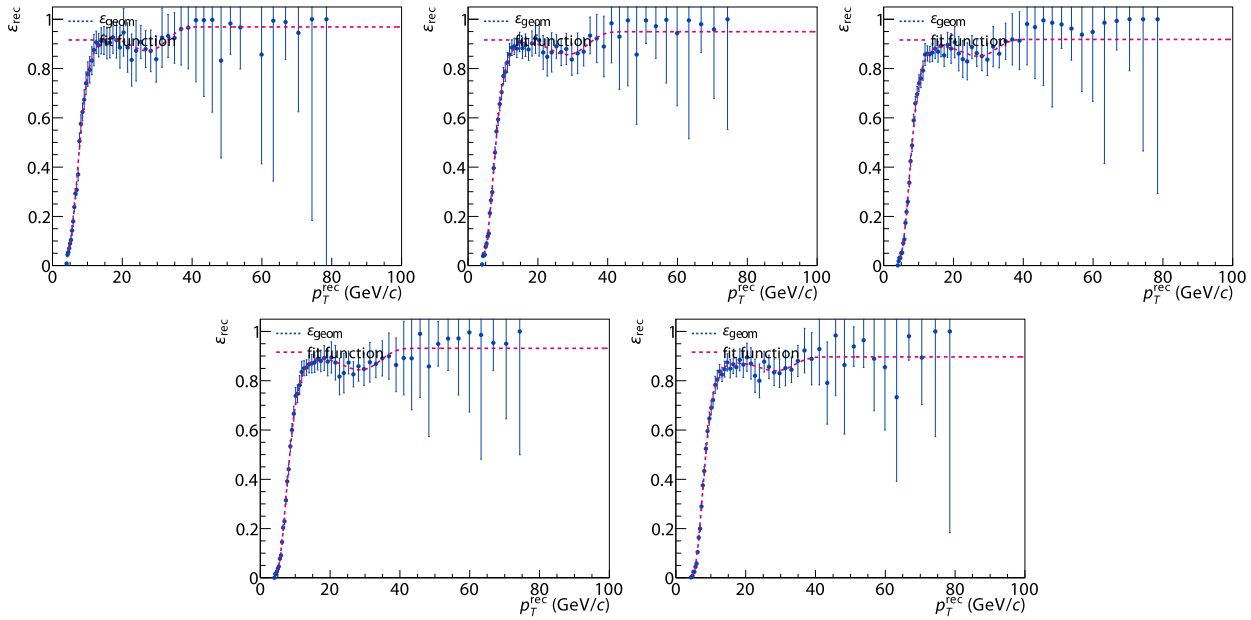

Figure 6.23: Run-5 Cu + Cu jet reconstruction efficiencies with fake rejection at $g' > 17.8$ (GeV/c)^2. Top row, left to right: 0–10%, 10–30%, 30–50%, bottom row, left to right: 50–70%, 70–90%.

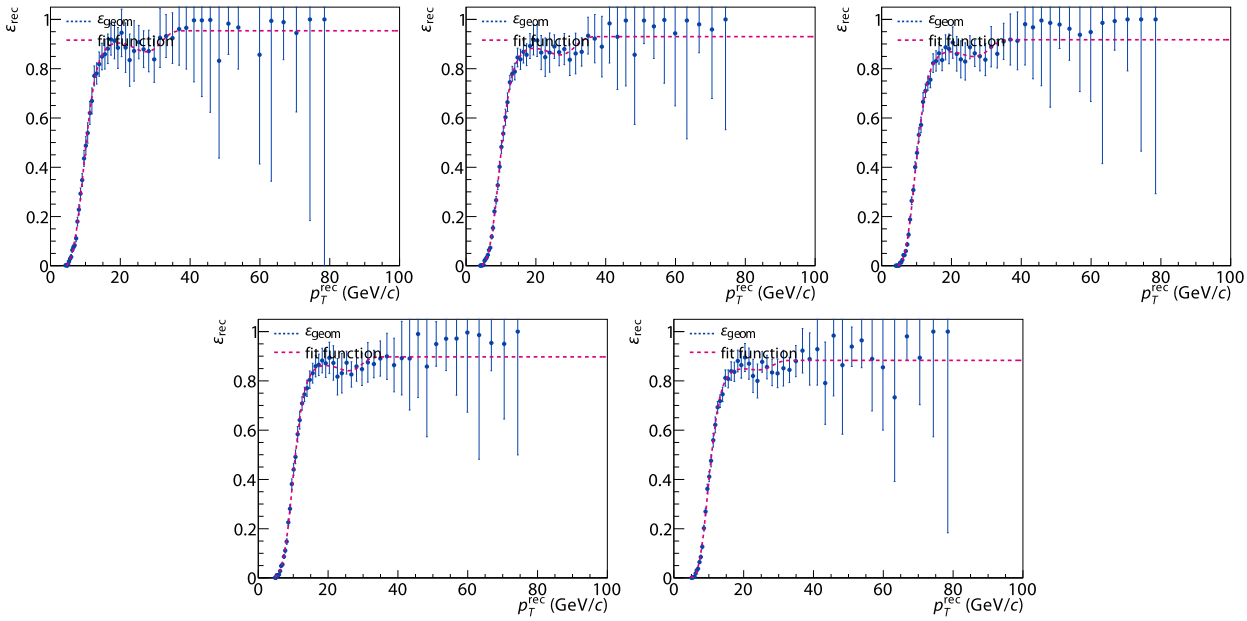

Figure 6.24: Run-5 Cu + Cu jet reconstruction efficiencies with fake rejection at $g' > 27.4$ (GeV/c)^2. Top row, left to right: 0–10%, 10–30%, 30–50%, bottom row, left to right: 50–70%, 70–90%.

	0–10%	10–30%	30–50%	50–70%	70–90%
a_0	0.954 ± 0.048	0.940 ± 0.037	0.915 ± 0.034	0.896 ± 0.037	0.865 ± 0.030
a_1	0.027 ± 0.092	0.041 ± 0.070	0.055 ± 0.066	0.092 ± 0.070	0.112 ± 0.057
a_2	0.042 ± 0.079	0.046 ± 0.060	0.028 ± 0.056	0.027 ± 0.060	0.000 ± 0.049
a_3	0.022 ± 0.066	0.026 ± 0.049	0.015 ± 0.047	0.037 ± 0.049	0.039 ± 0.040
a_4	-0.008 ± 0.045	-0.006 ± 0.033	-0.016 ± 0.031	0.004 ± 0.032	-0.002 ± 0.027
a_5	-0.003 ± 0.028	-0.010 ± 0.020	-0.019 ± 0.020	-0.010 ± 0.020	-0.009 ± 0.017

Table 6.5: Parametrization using the saturation level and Chebyshev polynomial coefficients for the level efficiency without fake rejection.

	0–10%	10–30%	30–50%	50–70%	70–90%
ϵ_0	0.961 ± 0.028	0.977 ± 0.027	0.902 ± 0.012	0.915 ± 0.015	0.896 ± 0.011
a_0	5.196 ± 0.087	2.489 ± 0.055	7.746 ± 0.052	5.053 ± 0.043	4.531 ± 0.030
a_1	8.11 ± 0.13	3.338 ± 0.076	12.703 ± 0.068	7.987 ± 0.056	7.044 ± 0.036
a_2	5.34 ± 0.12	1.829 ± 0.076	8.664 ± 0.077	5.184 ± 0.063	4.419 ± 0.044
a_3	3.56 ± 0.14	1.419 ± 0.071	5.756 ± 0.082	3.523 ± 0.065	3.075 ± 0.044
a_4	1.54 ± 0.14	0.592 ± 0.073	2.683 ± 0.089	1.625 ± 0.071	1.448 ± 0.048
a_5	0.271 ± 0.057	0.034 ± 0.031	0.567 ± 0.038	0.301 ± 0.030	0.252 ± 0.022

Table 6.6: Parametrization using the saturation level and Chebyshev polynomial coefficients for the $g' > 11.5\,(\mathrm{GeV}/c)^2$ fake rejection level efficiency.

	0–10%	10–30%	30–50%	50–70%	70–90%
ϵ_0	0.969 ± 0.027	0.949 ± 0.018	0.918 ± 0.014	0.931 ± 0.015	0.8963 ± 0.0092
a_0	5.658 ± 0.047	4.769 ± 0.031	6.531 ± 0.025	4.823 ± 0.021	5.4342 ± 0.0084
a_1	9.383 ± 0.061	7.780 ± 0.039	10.966 ± 0.031	7.946 ± 0.026	9.0198 ± 0.0097
a_2	6.320 ± 0.073	5.132 ± 0.049	7.437 ± 0.039	5.255 ± 0.033	5.984 ± 0.012
a_3	4.120 ± 0.068	3.444 ± 0.045	4.813 ± 0.037	3.512 ± 0.031	3.979 ± 0.012
a_4	2.024 ± 0.070	1.760 ± 0.047	2.386 ± 0.039	1.830 ± 0.033	2.095 ± 0.014
a_5	0.467 ± 0.031	0.402 ± 0.021	0.562 ± 0.017	0.440 ± 0.015	0.5166 ± 0.0067

Table 6.7: Parametrization using the saturation level and Chebyshev polynomial coefficients for the $g' > 17.8\,(\mathrm{GeV}/c)^2$ fake rejection level efficiency.

	0–10%	10–30%	30–50%	50–70%
ϵ_0	0.954 ± 0.014	0.930 ± 0.028	0.9175 ± 0.0095	0.8970 ± 0.0099
a_0	14.72496 ± 0.00080	14.756 ± 0.070	14.76716 ± 0.00050	23.135640 ± 0.000071
a_0	26.40629 ± 0.00088	26.434 ± 0.053	26.45024 ± 0.00054	41.793580 ± 0.000082
a_0	19.7375 ± 0.0012	19.68 ± 0.12	19.64942 ± 0.00072	31.47597 ± 0.00013
a_0	12.8510 ± 0.0025	12.74 ± 0.22	12.6540 ± 0.0012	20.1916 ± 0.0011
a_0	6.8379 ± 0.0030	6.73 ± 0.21	6.6546 ± 0.0013	10.51858 ± 0.00016
a_0	2.4877 ± 0.0015	2.42 ± 0.12	2.37848 ± 0.00087	3.809879 ± 0.000084
a_0	0.45334 ± 0.00094	0.427 ± 0.032	0.41427 ± 0.00058	0.718874 ± 0.000069

Table 6.8: Parametrization using the saturation level and Chebyshev polynomial coefficients for the $g' > 27.4\,(\mathrm{GeV}/c)^2$ fake rejection level efficiency, part one of the centralities.

	70–90%
ϵ_0	0.8835 ± 0.0090
a_0	23.2142 ± 0.0017
a_0	41.8376 ± 0.0020
a_0	31.2367 ± 0.0034
a_0	19.7559 ± 0.0048
a_0	10.1177 ± 0.0036
a_0	3.5891 ± 0.0021
a_0	0.6494 ± 0.0018

Table 6.9: Parametrization using the saturation level and Chebyshev polynomial coefficients for the $g' > 27.4\,(\mathrm{GeV}/c)^2$ fake rejection level efficiency, part two of the centralities.

6.6.3 R_{AA}

The nuclear modification factor R_{AA} is defined as the $T_{AB} = N_{\text{coll}}\sigma_{\text{inel}}$ corrected ratio between the heavy ion collision yield and the $p+p$ collision cross section

$$R_{AA} = \frac{N_{\text{evt}}^{-1} dN_{\text{CuCu}}/dp_T}{\langle T_{AB}\rangle d\sigma_{pp}/dp_T}. \tag{6.47}$$

From the Run-5 Cu + Cu spectrum unfolded to the $p+p$ energy scale, it is now possible to divide out the efficiency evaluated above, to obtain the ratio of the so corrected Cu + Cu spectrum to the $p+p$ raw spectrum. Since the $p+p$ raw spectrum does not contain any correlated uncertainty, the division is straightforward.

Superimposing the raw Cu + Cu spectrum divided by the T_{AB} times the $p+p$ raw spectrum gives a rough check on the size of the suppression of the R_{AA} simply from the input spectrum and uncorrected for the underlying event smearing, and the additional downward correction using unfolding. In central Cu + Cu collision, there is in fact already a sizable suppression without any correction.

When comparing the spectrum without fake rejection and with our nominal fake rejection level, one can see the effect of the fake jet in the central to mid-peripheral collisions. However, above a jet $p_T^{\text{CuCu}} \approx 17\,\text{GeV}$, there is little to none difference between the raw, unrejected spectrum, and the spectrum with fake rejection, but with the inefficiency obtained from embedding $p+p$ jets. This gives a strong constraint that the observed suppression is not caused by the fake rejection.

Figures 6.25–6.29 show, for different centralities, the Run-5 Cu + Cu R_{AA} raw, after fake rejection, and unfolded to the $p+p$ (detector) energy scale.

Figure 6.30 shows the Run-5 Cu + Cu R_{AA} unfolded to the $p+p$ (detector) energy scale.

6.6.4 R_{CP}

The R_{CP} is calculated by dividing the $\langle T_{AB}\rangle$ scaled unfolded spectra of different centralities by the $\langle T_{AB}\rangle$, most peripheral 70–90% centrality. When evaluating the uncertainties, the division take the full covariance matrix into account.

Figure 6.30 shows the Run-5 Cu + Cu R_{CP} unfolded to the $p+p$ (detector) energy scale.

6.6.5 Summary of Systematic Uncertainties

Like the unfolded $p+p$ spectrum, the R_{AA} systematic uncertainty is also based on the systematic uncertainty of the raw jet spectrum (section 5.14). Since we are evaluating a ratio, the finite acceptance partially cancel,

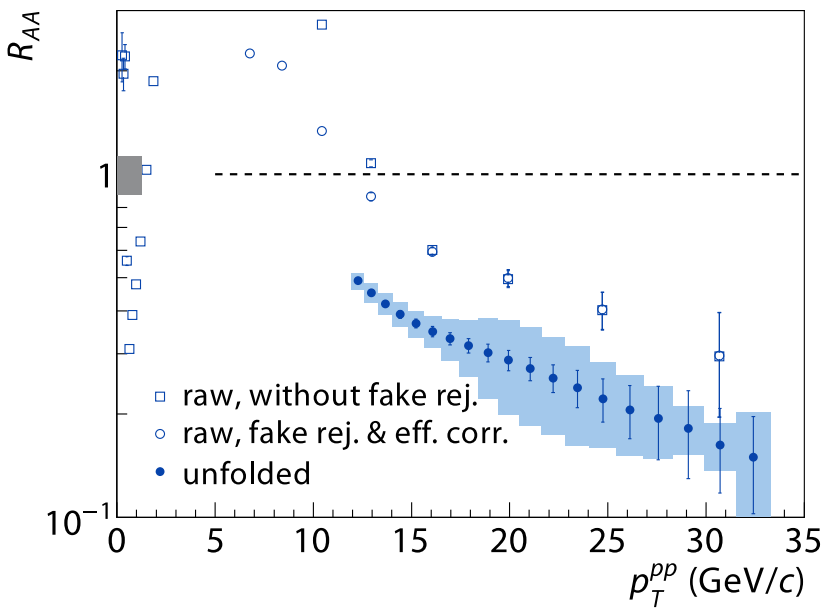

Figure 6.25: Run-5 Cu + Cu 0–10% centrality R_{AA} raw, after fake rejection, and unfolded to the $p+p$ (detector) energy scale. Error bars indicate statistical uncertainties, shaded boxes indicate bin-by-bin unfolding systematic uncertainties. The gray box to the left indicates the correlated normalization uncertainty.

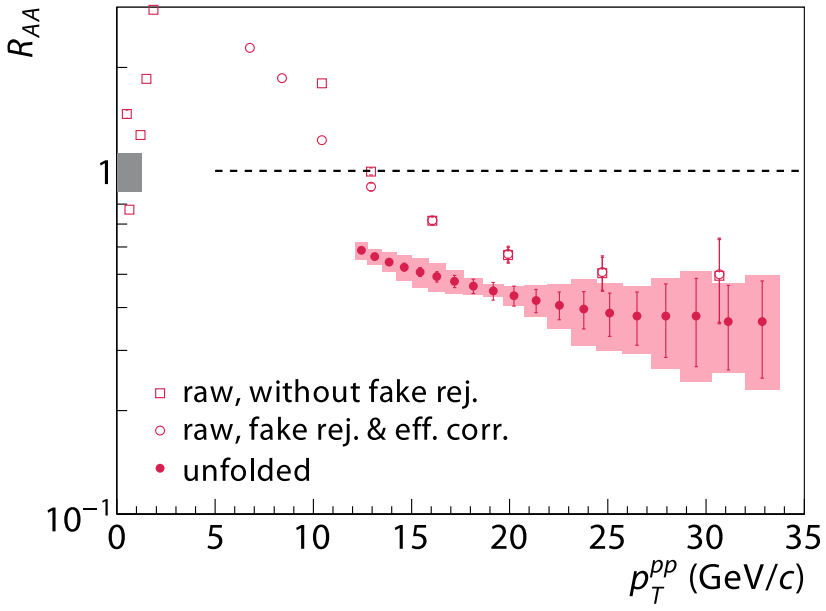

Figure 6.26: Run-5 Cu + Cu 10–30% centrality R_{AA} raw, after fake rejection, and unfolded to the $p+p$ (detector) energy scale. Error bars indicate statistical uncertainties, shaded boxes indicate bin-by-bin unfolding systematic uncertainties. The gray box to the left indicates the correlated normalization uncertainty.

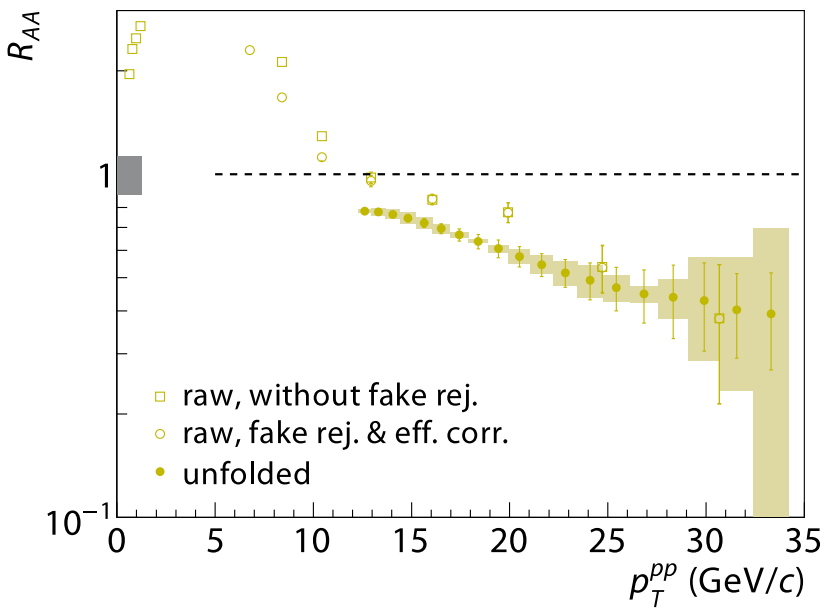

Figure 6.27: Run-5 Cu + Cu 30–50% centrality R_{AA} raw, after fake rejection, and unfolded to the $p+p$ (detector) energy scale. Error bars indicate statistical uncertainties, shaded boxes indicate bin-by-bin unfolding systematic uncertainties. The gray box to the left indicates the correlated normalization uncertainty.

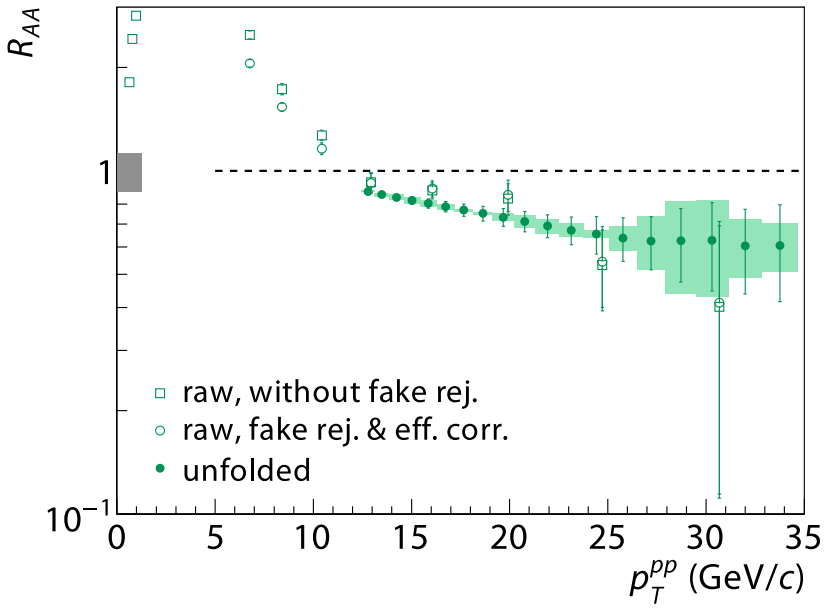

Figure 6.28: Run-5 Cu + Cu 50–70% centrality R_{AA} raw, after fake rejection, and unfolded to the $p+p$ (detector) energy scale. Error bars indicate statistical uncertainties, shaded boxes indicate bin-by-bin unfolding systematic uncertainties. The gray box to the left indicates the correlated normalization uncertainty.

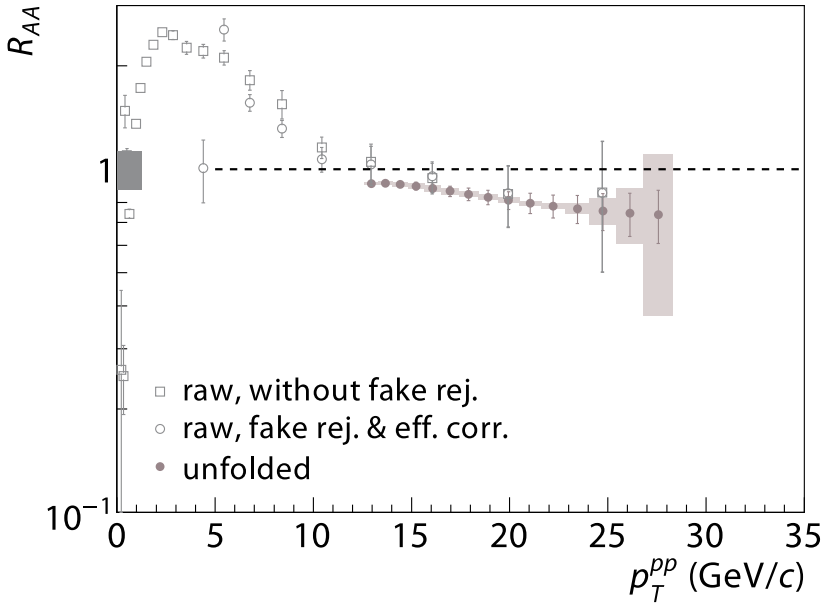

Figure 6.29: Run-5 Cu + Cu 70–90% centrality R_{AA} raw, after fake rejection, and unfolded to the $p+p$ (detector) energy scale. Error bars indicate statistical uncertainties, shaded boxes indicate bin-by-bin unfolding systematic uncertainties. The gray box to the left indicates the correlated normalization uncertainty.

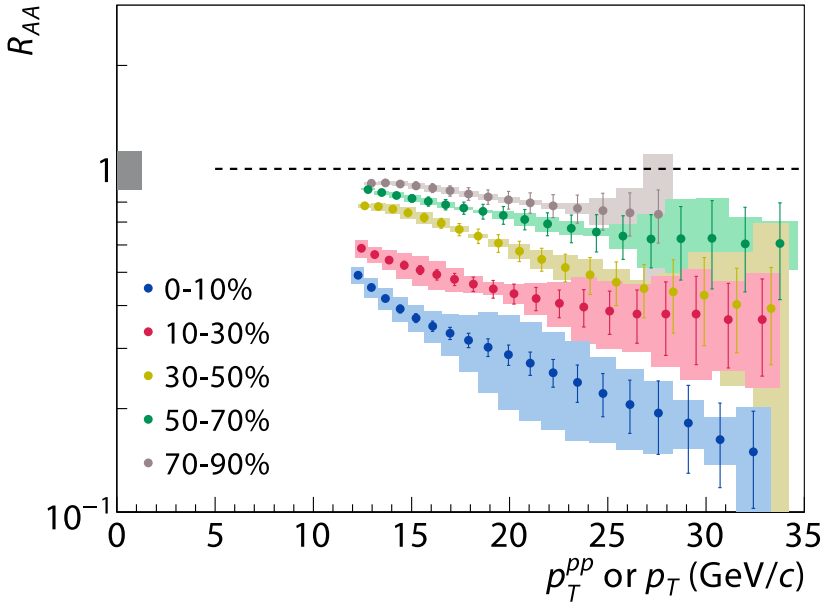

Figure 6.30: Run-5 Cu + Cu R_{AA} in the $p+p$ (detector) energy scale. Error bars indicate statistical uncertainties, shaded boxes indicate bin-by-bin unfolding systematic uncertainties. The gray box to the left indicates the correlated normalization uncertainty.

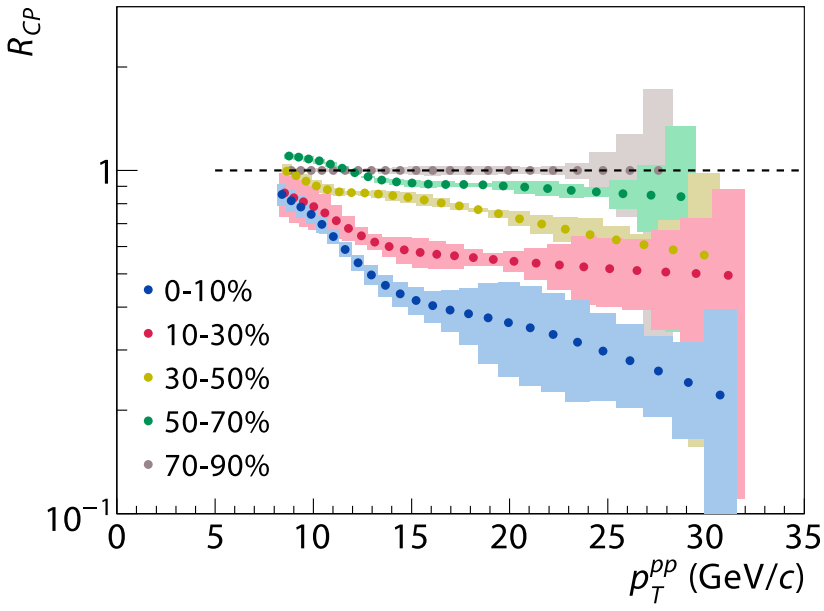

Figure 6.31: Run-5 Cu + Cu R_{CP} in the $p+p$ (detector) energy scale. Error bars indicate statistical uncertainties, shaded boxes indicate bin-by-bin unfolding systematic uncertainties.

No.	Description	Magnitude
	Global scale	
1	BBCLL1 cross section	5%
2	BBCLL1 efficiency	1.5%
3	$p+p$ ERT efficiency saturation level	2%
4	Minimum bias/ERT normalization matching	5%
5	Cu + Cu vs. $p+p$ EMCal/DC acceptance difference	5%
6	Cu + Cu vs. $p+p$ energy scale difference	10%
	Quadrature sum	13%
	Point-to-point	
7	$e^{\pm}$ contamination for $p_T^{\mathrm{rec}} > 20\,\mathrm{GeV}/c$	10%
8	Unfolding systematic errors	

Table 6.10: Table of systematic uncertainties for the raw jet spectrum.

and a 5% uncertainty is quoted based on the observation of the EMCal and DC acceptance difference between Run-5 $p+p$ and Cu + Cu. Similarly, the energy scale from sector E/p calibration between Run-5 $p+p$ and Cu + Cu are consistent within 2%, and consequently, the impact on an exponent -5 power law spectrum is about 10%.

Chapter 7

Discussion

In this thesis, we developed a Gaussian filter based jet reconstruction method, and an associated fake rejection strategy. Combining both, this approach notably can be applied to

1. $p+p$ and heavy ion collisions, where the effect of the elliptic flow can be fully parametrized
2. moderate energy jets in an high multiplicity environment
3. a detector with small aperture, where furthermore the background modulated by a nontrivial efficiency variation can be fully taken into account

I believe that it can be stated fairly that even now, three years after the development of these tools, other jet reconstruction algorithms have yet to demonstrate the features listed above at the performance shown in this thesis.

This thesis laid out much of the fundamentals how to perform jet reconstruction in $p+p$ heavy ion collision at PHENIX. I demonstrated that even with a detector consisting of two $\Delta\eta \times \Delta\phi = 0.7 \times \frac{\pi}{4}$ spectrometer arms (but efficiently triggered), it is possible to measure a fully energy corrected jet spectrum up to $x \approx 0.6$ and a jet fragmentation function up to $z \approx 0.8$. Two years after producing these results, this is still the highest x at RHIC and the only jet fragmentation function obtained at RHIC.

Strong suppression of jets in central Cu + Cu collisions was observed. The level at the central 0–10% and moderate $p_T \approx 12$ GeV/c is about $R_{AA} \approx 0.4$ and comparable to the single particle suppression level, while all centralities gain suppression with increasing p_T to a peripheral 70–90% $R_{AA} \approx 0.8$ at 25 GeV/c. This may be indicating that there is a significant initial state effect at high p_T, which was difficult to access so far at RHIC using single particle yield.

An initial attempt was undertaken to extract the dijet azimuthal correlation function. No significant $k_\perp$ broadening was observed. Assuming $L = 1$ fm, the statistical uncertainty of $\langle k_T \rangle < 0.5$ GeV/c would translates into a strong constraint of $\hat{q} < 0.3$ GeV^2/fm. This may be an initial indication that the $k_\perp$ broadening

with the BDMPS-Z type energy loss is not present. But more work is going to be needed in this area to produce an effective constraint.

Appendix A

Elementary Mathematical Tools

A.1 Floating Arithmetic

To facilitate discussion about numerical algorithms and accuracy, I will first review the IEEE 754-1985 and 754-2008 representation of floating point numbers.

The binary16, binary32, binary64 and binary128 formats are all represented by the bit tuple

$$(S, E_0, \ldots, E_{w-1}, d_1, \ldots, d_{p-1}) \tag{A.1}$$

where E_0, d_1 are the most significant bits (MSB) of the biased exponent and trailing significand (with the leading bit d_0 suppressed as being implicit) field. Taking the tailing significand field as an integer, its value is

$$T = (d_1 d_2 \ldots d_{p-1})_2 = \sum_{k=1}^{p-1} d_k 2^{p-1-k}. \tag{A.2}$$

The biased exponent is obtained by offsetting its binary value as

$$E = (E_0 E_1 \ldots E_{w-1})_2 + E_{\text{bias}} = \sum_{k=0}^{w-1} E_k 2^{w-1-k} + E_{\text{bias}}. \tag{A.3}$$

Ignoring for simplicity the representation of infinities and not-a-numbers (NaN), the three finite number representations are

- Normal numbers with $1 \leq E \leq 2^w - 2$

  $$\bar{x} = (-1)^S (1 + 2^{1-p} T) 2^{E - E_{\text{bias}}} \tag{A.4}$$

  where the addition of one corresponds to the restoration of the implicit significand bit.

- Subnormal numbers with $E = 0$, $T \neq 0$

  $$\bar{x} = (-1)^S (0 + 2^{1-p} T) 2^{E_{\min}} \tag{A.5}$$

  where $E_{\min} = 2 - 2^{w-1}$.

- Signed zero $E = 0, T = 0$

$$\bar{x} = (-1)^S(+0) \tag{A.6}$$

Most of the following discussion is intended for the binary32 format, which specifies a significand consisting of $p = 24$ implicit binary digits, an exponent width of $w = 8$. Another format used in this thesis is the storage of detector cut parameters as binary16, which has $p = 11$ and $w = 5$.

In computer arithmetics, specification of the precision of an operation is usually normalized to the expected rounding error from finite precision, denoted as the unit in the last place (ULP).

A.2 Error Propagation

It is quite peculiar to discuss error propagation in a PhD thesis, the topic usually being assumed to be familiar to every undergraduate student. However, the full-fledged form of error propagation and propagation of covariances is rarely taught at that level, and after these first classes, the matter of error propagation is quickly considered as closed. Yet one of the key derived quantity for spectra unfolding is the measurement of ratios, where we would like to obtain the full bin-to-bin covariance of the ratio with correlated, unfolded spectra. Therefore, we have the misfortune here to dig out this topic again.

Using the Taylor expansion of statistical moments and keeping terms up to the second moment, the expectation value is

$$\begin{aligned}
\mathrm{E}[f(X,Y)] = \mathrm{E}\Big\{ & f(\mu_X,\mu_Y) + f_X(\mu_X,\mu_Y)(X-\mu_X) + f_Y(\mu_X,\mu_Y)(Y-\mu_Y) \\
& + \frac{1}{2} f_{XX}(\mu_X,\mu_Y)(X-\mu_X)^2 + \frac{1}{2} f_{YY}(\mu_X,\mu_Y)(Y-\mu_Y)^2 \\
& + f_{XY}(\mu_X,\mu_Y)(X-\mu_X)(Y-\mu_Y) + O[(X+Y)^3] \Big\} \\
\approx\ & f(\mu_X,\mu_Y) + \frac{1}{2} f_{XX}(\mu_X,\mu_Y)\mathrm{Var}(X) + \frac{1}{2} f_{YY}(\mu_X,\mu_Y)\mathrm{Var}(Y) \\
& + f_{XY}(\mu_X,\mu_Y)\mathrm{Cov}(X,Y).
\end{aligned} \tag{A.7}$$

One notices that contribution of uncertainty to the propagated mean appears, which the commonly taught, "elementary" error analysis suppresses. Analogously, the variance

$$\mathrm{Var}[f(X,Y)] = \mathrm{E}\{[f(X,Y) - f(\mu_X,\mu_Y)]^2\} \tag{A.8}$$

evaluates to

$$\begin{aligned}\mathrm{Var}[f(X,Y)] \approx\ & f_X^2(\mu_X,\mu_Y)\mathrm{Var}(X) + f_Y^2(\mu_X,\mu_Y)\mathrm{Var}(Y) \\ & + 2f_X(\mu_X,\mu_Y)f_Y(\mu_X,\mu_Y)\mathrm{Cov}(X,Y),\end{aligned} \tag{A.9}$$

which is just the special case of the general result

$$\begin{aligned}\mathrm{Cov}[f(U,V),g(X,Y)] &= \mathrm{E}\{[f(U,V) - f(\mu_U,\mu_V)][g(X,Y) - g(\mu_X,\mu_Y)]\} \\ &= f_U(\mu_U,\mu_V)g_X(\mu_X,\mu_Y)\mathrm{Cov}(U,X) \\ &\quad + f_U(\mu_U,\mu_V)g_Y(\mu_X,\mu_Y)\mathrm{Cov}(U,Y) \\ &\quad + f_V(\mu_U,\mu_V)g_X(\mu_X,\mu_Y)\mathrm{Cov}(V,X) \\ &\quad + f_V(\mu_U,\mu_V)g_Y(\mu_X,\mu_Y)\mathrm{Cov}(V,Y).\end{aligned} \tag{A.10}$$

Two main types of error propagation are encountered when working with histograms, linear combination for histogram merging and scaling, and taking the quotient to obtain ratios. For the linear combination $f(X,Y) = aX + bY$, one can readily check that the linearity

$$\mathrm{E}(aX + bY) = a\mathrm{E}(X) + b\mathrm{E}(Y) \tag{A.11}$$

$$\mathrm{Cov}(aU + bV, cX + dY) = ac\mathrm{Cov}(U,X) + ad\mathrm{Cov}(U,Y) + bc\mathrm{Cov}(V,X) + bd\mathrm{Cov}(V,Y) \tag{A.12}$$

is fully preserved with the moment expansion. For the less trivial quotient $f(X,Y) = X/Y$,

$$f_X(X,Y) = \frac{1}{Y}, \quad f_Y(X,Y) = -\frac{X}{Y^2} \tag{A.13}$$

$$f_{XX}(X,Y) = 0, \quad f_{YY}(X,Y) = \frac{2X}{Y^3}, \quad f_{XY}(X,Y) = -\frac{1}{Y^2}, \tag{A.14}$$

and we obtain as the propagated values

$$\mathrm{E}\left(\frac{X}{Y}\right) = \frac{\mathrm{E}(X)}{\mathrm{E}(Y)} + \frac{\mathrm{E}(X)\mathrm{Var}(Y)}{\mathrm{E}^3(Y)} - \frac{\mathrm{Cov}(X,Y)}{\mathrm{E}^2(Y)} \tag{A.15}$$

$$\mathrm{Cov}\left(\frac{U}{V},\frac{X}{Y}\right) = \frac{\mathrm{Cov}(U,X)}{\mathrm{E}(V)\mathrm{E}(Y)} - \frac{\mathrm{E}(X)\mathrm{Cov}(U,Y)}{\mathrm{E}(V)\mathrm{E}^2(Y)} - \frac{\mathrm{E}(U)\mathrm{Cov}(V,X)}{\mathrm{E}^2(V)\mathrm{E}(Y)} + \frac{\mathrm{E}(U)\mathrm{E}(X)\mathrm{Cov}(V,Y)}{\mathrm{E}^2(V)\mathrm{E}^2(Y)}. \tag{A.16}$$

For the ratio of two independent measurements, no correlation exists between the numerator and the denominator, and the above expression simplifies to

$$\mathrm{Cov}\left(\frac{X_1}{Y_1},\frac{X_2}{Y_2}\right) = \frac{\mathrm{Cov}(X_1,X_2)}{\mathrm{E}(Y_1)\mathrm{E}(Y_2)} + \frac{\mathrm{E}(X_1)\mathrm{E}(X_2)\mathrm{Cov}(Y_1,Y_2)}{[\mathrm{E}(Y_1)\mathrm{E}(Y_2)]^2}, \tag{A.17}$$

which is the generalization of the familiar

$$\mathrm{Var}\left(\frac{X}{Y}\right) = \frac{\mathrm{Var}(X)}{\mathrm{E}^2(Y)} + \frac{\mathrm{E}^2(X)\mathrm{Var}(Y)}{\mathrm{E}^4(Y)} \tag{A.18}$$

for uncorrelated variates.

A.3 Kinematics

A.3.1 Rapidity and Pseudorapidity

The standard Lorentz boost along x_3 in matrix form (suppressing the invariant coordinates x_1, x_2) and for Minkowski coordinates is

$$\begin{pmatrix} ct' \\ x_3' \end{pmatrix} = \begin{pmatrix} \gamma & -\beta\gamma \\ -\beta\gamma & \gamma \end{pmatrix} \begin{pmatrix} ct \\ x_3 \end{pmatrix} \tag{A.19}$$

This transform is diagonalized by going into the light cone coordinate $x^{\pm} \equiv ct \pm x^3$, and the boost is then

$$ct' \pm x_3' = (\gamma ct - \beta\gamma x_3) \pm (\gamma x_3 - \beta\gamma ct) = (\gamma \mp \gamma\beta)(ct \pm x_3), \tag{A.20}$$

and therefore

$$x^{\pm\prime} = (\gamma \mp \gamma\beta)x^{\pm} = \sqrt{\frac{1 \mp \beta}{1 \pm \beta}}\, x^{\pm}. \tag{A.21}$$

This is in turn similar to the homomorphism between the Lorentz group and the Möbius group, where the Lorentz vector is a 2×2 Hermitian matrix in $\mathrm{SL}(2, \mathbb{C})$

$$\mathbf{X} = \begin{pmatrix} ct + x_3 & x_1 - ix_2 \\ x_1 + ix_2 & ct - x_3 \end{pmatrix}. \tag{A.22}$$

Using the Lie algebra structure of the Lorentz group, one can observe that the finite Lorentz boost evolves linearly (and therefore more "naturally") with a rapidity variable y, i.e. by setting

$$e^y = \sqrt{\frac{1 + \beta}{1 - \beta}}, \tag{A.23}$$

and the light cone coordinate now transforms as

$$\begin{pmatrix} x^{+\prime} \\ x^{-\prime} \end{pmatrix} = \begin{pmatrix} e^{-y} & 0 \\ 0 & e^{y} \end{pmatrix} \begin{pmatrix} x^{+} \\ x^{-} \end{pmatrix}. \tag{A.24}$$

or expressed as the hyperbolic transformation in $\mathrm{SL}(2, \mathbb{C})$

$$\mathbf{B} \equiv \begin{pmatrix} e^{y/2} & 0 \\ 0 & e^{-y/2} \end{pmatrix}, \quad \mathbf{X}' = \mathbf{B}\,\mathbf{X}\,\mathbf{B}^{\dagger}. \tag{A.25}$$

Symmetrization and antisymmetrization of either form gives back the boost according to the Minkowski coordinates as

$$\begin{pmatrix} ct' \\ x_3' \end{pmatrix} = \begin{pmatrix} \cosh y & -\sinh y \\ -\sinh y & \cosh y \end{pmatrix} \begin{pmatrix} ct \\ x_3 \end{pmatrix}. \tag{A.26}$$

For a four vector p in the momentum space, the rapidity (and accounting for the sign) is therefore

$$y = \frac{\operatorname{sgn} p_3}{2} \ln \frac{E + p_3 c}{E - p_3 c} \tag{A.27}$$

and a convenient, boost invariant quantity for high momentum particle can be defined by setting zero mass, which gives the purely Cartesian defined pseudorapidity

$$\eta = \frac{\operatorname{sgn} p_3}{2} \ln \frac{|\mathbf{p}| + p_3}{|\mathbf{p}| - p_3} = \tanh^{-1} \frac{p_3}{|\mathbf{p}|}, \tag{A.28}$$

with the last step being the hyperbolic Weierstrass substitution.

A common mistake made by most high-energy physics frameworks such as CLHEP and ROOT is to use numerically unstable "textbook" formula to calculate rapidity. In midrapidity,

$$\cos\theta = \frac{p_3}{|\mathbf{p}|} \ll 1 \tag{A.29}$$

and is suitable to represent the angle accurately as a floating point number, while in the forward direction $\cos\theta \approx 1$ and becomes a fixed point number, where the kinematics is stored purely in the mantissa. Two methods can be used to also cover the forward kinematics. Examining the sine gives immediately

$$\sin\theta = \sqrt{1 - \tanh^2 \eta} = \frac{1}{\cosh \eta} \tag{A.30}$$

and the pseudorapidity evaluates to

$$\eta = \cosh^{-1} \frac{|\mathbf{p}|}{p_T}. \tag{A.31}$$

Another, potentially more efficient method (since standard C library typically implements $\cosh^{-1}(\cdot)$ using two logarithms) is to note that

$$\frac{1 + \sqrt{1 - x^2}}{1 - \sqrt{1 - x^2}} = \left(\frac{1 + \sqrt{1 - x^2}}{x} \right)^2, \tag{A.32}$$

which gives

$$\eta = \operatorname{sgn} p_3 \ln \frac{1 + \sqrt{1 - \sin^2\theta}}{\sin\theta}. \tag{A.33}$$

Applying the tangent half-angle formula to (A.33) in fact gives another strangely popular, yet given that a transcendent function is needed to access half angles in the first place, a numerically undesirable relation for the pseudorapidity

$$\eta = -\ln \left[\tan \left(\frac{\theta}{2} \right) \right]. \tag{A.34}$$

A.3.2 Angular Range Reduction

Range reduction is a well-known problem in computer arithmetics, when trigonometric functions has to be implemented without loss of precision for large arguments. The Cody and Waite range reduction [106] is a standard approach to increase the effective mantissa length in order to avoid the subtractive loss of precision when obtaining ϕ^*. In the following implementation, a three coefficient Cody and Waite range reduction

$$\phi^* = [(\phi - kC_1) - kC_2] - kC_3. \tag{A.35}$$

is used for the azimuth, where $k \in \mathbb{Z}$ and $-\pi < \phi^* \leq \pi$. Eight bits are reserved for an exact multiplication, which gives a range reduction sufficient for $|\phi| < 512\pi \approx 1608.5$, which is completely sufficient (except for unintended, numerically unstable situations with run away arguments). The coefficients for IEEE 754 single precision are

$$\begin{aligned} C_1 &= \frac{3217}{512} \\ C_2 &= -\frac{38\,263}{2\,147\,483\,648} \\ C_3 &= 2\pi - \frac{13\,493\,037\,705}{2\,147\,483\,648} \\ &\approx -2.225\,772\,67 \times 10^{-10} \end{aligned} \tag{A.36}$$

and for double precision

$$\begin{aligned} C_1 &= \frac{27\,633\,741\,218\,861}{4\,398\,046\,511\,104} \\ C_2 &= -\frac{26\,691\,486\,927\,953}{1\,237\,940\,039\,285\,380\,274\,899\,124\,224} \\ C_3 &= 2\pi - \frac{7\,778\,206\,666\,007\,221\,413\,453\,810\,769}{1\,237\,940\,039\,285\,380\,274\,899\,124\,224} \\ &\approx 3.537\,488\,226\,454\,280\,448\,1 \times 10^{-28} \end{aligned} \tag{A.37}$$

Range reduction over the entire range of machine floating point numbers can be implement using the Payne and Hanek range reduction. Here, typically $2^k/\pi$ is expanded into 16-bit integer digits (to facilitate multiplication on 32-bit architectures).

A.4 Pseudorandom Number Generation

In the classification of pseudorandom number generators (PRNG), the Mersenne Twister (MT) is a twisted generalized feedback shift register (TGFSR), where the twist matrix is in the rational normal form, and with

added state bit reflection and tempering. The period length of MT is given by $l = 2^{nw-r} - 1$, n being the degree of recurrence, w the word size in bits, and r is the separation point of one word (defined as the number of bits of the lower bitmask). Choosing the period length to be a Mersenne prime simplifies the primitivity test necessary for the twist matrix search.

Unlike the popular MT19937 and the SFMT – a later MT version that is more adapted for the single instruction, multiple data (SIMD) architectures –, a reduced degree of recurrence allows a computationally feasible search of different twist matrices and tempering bitmasks using the "dynamic creator" [107], and therefore provides a parallel stream PRNG for distributed event generation with guaranteed no stream overlap. Each stream is characterized by **a**, being the coefficients of the rational normal form twist matrix, and (**b**, **c**) which is a pair of tempering bitmasks. Among the commercially available SIMD PRNG libraries, the Intel Math Kernel Library [108] provides 2^{10} MT2203 generators, the ClearSpeed Random Number Generator Library [109] 960 MT2203, while the IBM Cell Broadband Engine SDK [110] 2^{10} MT1279 and MT2281 each. Note that even for MT1279, $l \approx 1.041 \times 10^{385}$ is more than 300 orders of magnitude larger than the number of baryons in the observable universe.

A Streaming SIMD Extension 2 (SSE2) assembly based implementation of MT2203 was written for HIJING and HIJING's JETSET (and later also used for PYTHIA and HERWIG). The generated streams is identical to Intel Math Kernel Library 9.x. The typical performance on an Intel Core 2 processor is measured to be 9.1 cycle/element, slightly faster than Intel Math Kernel Library (10.2 cycle/element), and significantly outperforming other popular MT19937 implementations found in high energy physics libraries, like CLHEP (22 cycle/element, used e.g. by the ATLAS Collaboration). Similar to the revised reference code by Nishimura & Matsumoto (the initial reference code had a bad seeding procedure), scalar seeding of the FSR is done using two multiplicative congruential generators (MCG), both have been reviewed in the table of MCG by Knuth [111]. These are the Lavaux & Janssens multiplier (1 664 525, line 16 in aforementioned table), and the Waterman multiplier (1 566 083 941, line 14 in the table).

Since I initially was preparing for simulation on the order of 10^4–10^5 parallel processes, a large scale search for MT2203 parameters was performed, which covers 1/16 of the total parameter space, and resulted in 344,682 possible combinations of MT2203. But ultimately, 1024 HIJING processes using the MT2203 parameters from the Intel Math Kernel Library proved to be sufficient.

Appendix B

Implementing Gaussian Filter Algorithm

B.1 IIR Approximation

Unlike I. T. Young and L. J. van Vliet [70], who used a traditional, L_p norm optimization (with increasing p) to approximate the minimax optimization, an initial guess is found here by brute force (randomized) sampling of the phase space. This gives

$$\begin{aligned} d_1 &\approx 1.047 + 1.277\,i \\ d_3 &\approx 1.664 + 0.472\,i \end{aligned} \tag{B.1}$$

which is about $\Delta \operatorname{Re} d \approx \Delta \operatorname{Im} d \approx 10^{-3}$ away from the true minimum. This initial guess already contains alternating extrema, and is therefore sufficiently close to express the problem directly in a Remez form. The solution can be found by solving the problem for an equiripple design, where the alternating extrema are of equal magnitude.

Implementing the equiripple design algorithm requires an 1-dimensional minimizer and a nonlinear solver for systems of equations. In our case, it is implemented (for simplicity) using MATHEMATICA [112]. The solution (to 20 decimal digits) is

$$\begin{aligned} d_1 &= 1.047\,190\,104\,512\,483\,612\,5 + 1.276\,949\,802\,260\,221\,097\,3\,i \\ d_3 &= 1.664\,976\,595\,012\,524\,238\,0 + 0.472\,723\,701\,118\,885\,756\,46\,i \end{aligned} \tag{B.2}$$

while the norm of the approximation residual is $L_\infty = 3.578 \times 10^{-3}$, which is a 20.7% improvement over the poles published by Young and van Vliet.

Note that modulo the $\pm\omega$ symmetry and the trivial minimum $H_{1,4}(\omega = 0) = 1$, the minimax design here has five nontrivial extrema, giving four minimax constraints, which is the same four degrees of freedom in d_1, d_3. Because of the pole structure, there is also no other possible solution with the extrema inverted. By

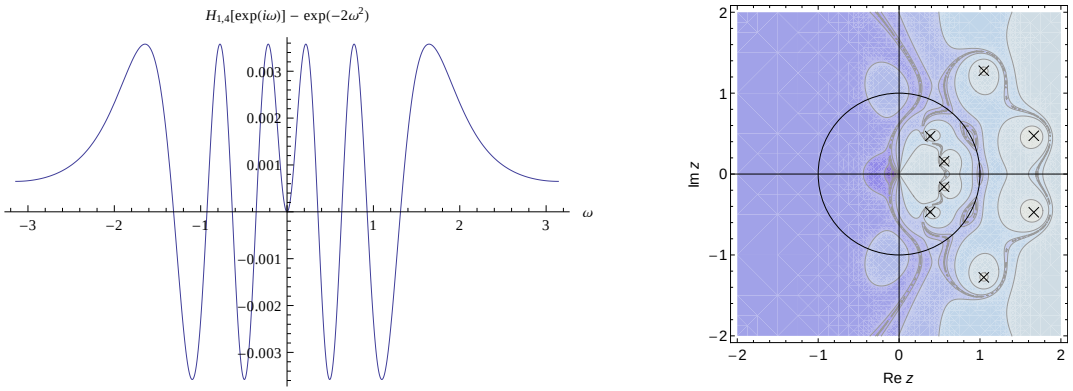

Figure B.1: The residual approximation error $H_{1,4}[\exp(i\omega)] - \exp(-2\omega^2)$ and the complex function $|H_{1,4}(z) - \exp[-2(\arg z)^2]|$, with the poles marked by "×".

comparison, the poles by Young and van Vliet results in a double (quartic as opposed to a parabolic) minimum at $H_{1,4}(\omega = 0)$, therefore missing one remaining minimax constraint. This should serve as a cautionary tale to blindly trust a locally minimizing conjugate gradient optimization, as Young and van Vliet claiming to have used.

Figure B.1 shows the error function of the minimax design in both the frequency and the complex z domain.

B.2 SIMD Biquad Filter

The discrete, IIR realization of the Gaussian filter, as described in section 3.2.1.1, can be efficiently implemented using single instruction, multiple data (SIMD) methods, such as using the Streaming SIMD Extension (SSE) in Intel and AMD processors.

For this section and below, I will use an assembly "semi-pseudocode", where I show the algorithm using IA-32/x86-64 opcode mnemonic defined in [113], and the AT&T operand syntax, for which a modern reference can be found in [114]. For clarity and brevity, load/store operations are provided symbolically, and constants are provided as immediates (vs. explicitly loading them and pass by register/address). C99 [115] and POSIX [116] constants are used. Compare also D. E. Knuth [117] for some of these notations.

Since the original SSE does perform multiply–accumulate (MAC) as a single operation, an extra register is needed every time. A biquad fits – some path planning required – tightly into eight total XMM registers on IA-32. Therefore, the implementation of a IIR biquad on IA-32 SSE assembly is quite instructive. The ability

of instruction pipelining is sacrificed to achieve the register usage.

Four XMM registers are occupied by the biquad coefficients. In the direct form 1 (DF1) realization [118], the direct and recursive delay lines each occupy two registers, completely occupying all registers, but the registers can be successively freed for MAC. While the direct form 2 (DF2) is usually considered simpler, this however not necessarily true for small number of registers, where the duplication of the combined delay line and coding the MAC around the register containing w_{i-1} becomes the dominant issue, and therefore, the DF2 is missing one register to even gain a clear advantage in term of pipelining.

For an eight register DF1 realization, we start with the initialization

`%xmm0` $\leftarrow x_{i-1}$

`%xmm1` $\leftarrow x_{i-2}$

`%xmm2` $\leftarrow y_{i-1}$

`%xmm3` $\leftarrow y_{i-2}$

The loop is dynamically unrolled, i.e. the delay line is mapped on to a ring buffer of length $N = 2$, where the indexing is explicitly hard-coded, and is repeated N times until the loop cycle is completed. Note how `%xmm1` and `%xmm3` are strategically freed for further multiply–accumulation, and one `%xmm1` $\leftrightarrow$ `%xmm0` is embedded to complete the loop unrolling:

```
mulps  b2, %xmm1
mulps  a2, %xmm3
subps  %xmm3, %xmm1
movaps %xmm0, %xmm3
mulps  b1, %xmm3
addps  %xmm1, %xmm3
movaps %xmm2, %xmm1
mulps  a1, %xmm1
subps  %xmm1, %xmm3
```

Now load

`%xmm1` $\leftarrow x_i$

then assemble the biquad output

```
addps %xmm1, %xmm3
```

and store

$y_i \leftarrow$ %xmm3

To complete the loop, repeat above with the register exchange %xmm1 $\leftrightarrow$ %xmm0, %xmm3 $\leftrightarrow$ %xmm2 and add loop bookkeeping.

B.3 SIMD Exponential Function

The continuous realization of the Gaussian filter, as described in section 3.2.1.4, involves the evaluation of large number of exponentially weighted distance squares, and the performance can be enhanced using SIMD, which calculates the exponential function of an array in parallel. However, the SSE instruction set (unlike the x87 FPU) on IA-32/x86-64 does not provide transcendental functions, which must be implemented in a subprogram library. This section describes the implementation of such a function.

Several comparable implementation of the (vector or scalar) exponential functions are currently available for Intel and AMD central processing units (CPUs):

1. Glibc, which evaluates the exponential function using the x87 FPU opcode `f2xm1`, is typically the most inefficient approach when multiple vector elements are exponentiated simultaneously. Since switching the FPU precision incurs a considerable latency, usually EXPF is still evaluated with either double or the Intel extended precision (64-bit mantissa). Consequently, this approach provides a 0.5 ulp implementation.

2. The Intel Short Vector Math Library (SVML) [119] provides with VMLSEXP4 a fully IEEE Std 754 [120] compliant implementation, i.e. with defined behavior with infinity, NaN, and subnormal (or denormal) [121] input and output (not "flush-to-zero") with 8 XMM register footprint. Its accuracy is significantly lower than 1 ulp.

3. The AMD Core Math Library (ACML) [122] provide with __VRS4_EXPF a non-IEEE Std 754 implementation with 8 XMM register footprint. Subnormal output triggers a "flush-to-zero" behavior. The implementation is x86-64 architecture only.

Here I will describe an implementation that has a footprint of four %xmm registers (i.e. inlineable on IA-32 while having four accumulation registers) and achieves an execution latency of < 20 cpe on Intel Core 2 architecture.

On floating point units with fast multiplication, the exponential function is typically implemented with an accurate approximation $g(x^*) \approx \exp(x^*)$ in a small interval, then with an additive range reduction in the form of $x^* = x - kC$ to generalize $g(x^*)$ into the full definition range, and the unrestricted approximation becomes

$$\exp(x^*) \approx \exp(C^k)\, g(x^*). \tag{B.3}$$

For a software implementation without any tables (in order to maintain cacheability) and on a hardware with binary arithmetic, $C = \ln 2$ is the natural choice as $\exp(C^k) = 2^k$ can be applied without any floating point operations.

Typically, $\exp(x^*)$ is implemented within an interval of width C. However, when implementing in SSE, which implements all four IEEE Std 754 binary rounding modes ([121] and [113], section 4.8.4), but is unable to revert to central rounding efficiently, extending the range to accomodate the different range reduction results from all rounding modes is usually more efficient than enforcing the rounding mode.

The argument x of an exponential function has a range in which there is no overflow and underflow limited by $x \in [-(\ln 2)^{-1}2^{e-1}, (\ln 2)^{-1}2^{e-1}) \subset [-2^e, 2^e]$, therefore a Cody and Waite range reduction is completely sufficient. Section A.3.2 already described the Cody and Waite range reduction with three coefficients for the azimuth angle. Empirically, it can be shown that a two coefficient version achives the neccessary precision. In the two coefficient form of the Cody and Waite range reduction, C is expanded into as $C = C_1 + C_2$, and the range reduction becomes

$$x^* = (x - kC_1) - kC_2. \tag{B.4}$$

Since $|k| \leq \frac{1}{2}e \ln 2 < e$, iteratively rounding $C_i = n_i 2^{-(m-e)}$, $n_i \in \mathbb{Z}$ for $i = 1, 2$ gives

$$\begin{aligned} C_1 &= \frac{22\,713}{32\,768}, \\ C_2 &= \ln 2 - C_1 \approx 1.428\,606\,82 \times 10^{-8}. \end{aligned} \tag{B.5}$$

In the semi-pseudocode notation, the range reduction is:

```
%xmm0 ← x
movaps   %xmm0, %xmm2
```

Implementation	x_{worst}	$\overline{\exp}(x_{\text{worst}}) - \exp(x_{\text{worst}})$ (ulp)
EXPF_SSE2	$-\frac{14\,324\,743}{524\,288}$	$+1.05$
VMLSEXP4	$-\frac{14\,638\,661}{536\,870\,912}$	-3.22
__VRS4_EXPF	$-\frac{2\,862\,199}{32\,768}$	-8.30×10^6

Table B.1: Accuracy and the worst argument of the SIMD IEEE 754 single precision exp functions, the Gaussian filter EXPF_SSE2, the Intel SVML VMLSEXP4, and the AMD ACML __VRS4_EXPF, for the round to the nearest (even) mode. The large inaccuracy of __VRS4_EXPF is due to the flush-to-zero behavior for subnormalized results.

Rounding mode	x_{worst}	$\overline{\exp}(x_{\text{worst}}) - \exp(x_{\text{worst}})$ (ulp)
nearest (even)	$-\frac{14\,324\,743}{524\,288}$	$+1.05$
directed $+\infty$	$\frac{363\,249}{4\,096}$	$+2.32$
directed $-\infty$	$-\frac{8\,863\,745}{34\,359\,738\,368}$	-3.56
directed 0	$\frac{11\,628\,949}{524\,288}$	-2.55

Table B.2: Accuracy and worst argument of the Gaussian filter SIMD IEEE 754 single precision exp function for different rounding modes.

```
mulps    (ln 2)^-1, %xmm2
minps    FLT_MAX_EXP − 1, %xmm2
cvtps2dq %xmm2, %xmm3
cvtdq2ps %xmm3, %xmm2
movaps   %xmm2, %xmm1
mulps    C1, %xmm1
mulps    C2, %xmm2
subps    %xmm1, %xmm0
subps    %xmm2, %xmm0
```

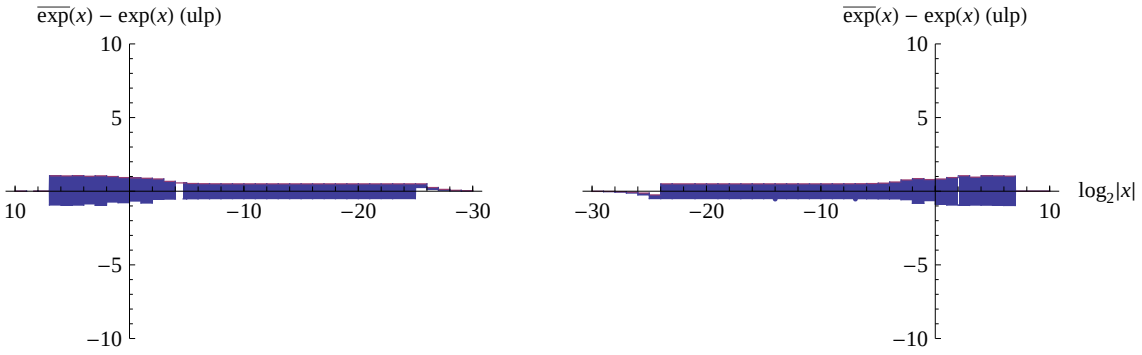

Figure B.2: The worst case accuracy as function of the exponent for the Gaussian filter EXPF_SSE2. The horizontal axis for the negative arguments is reversed for clarity.

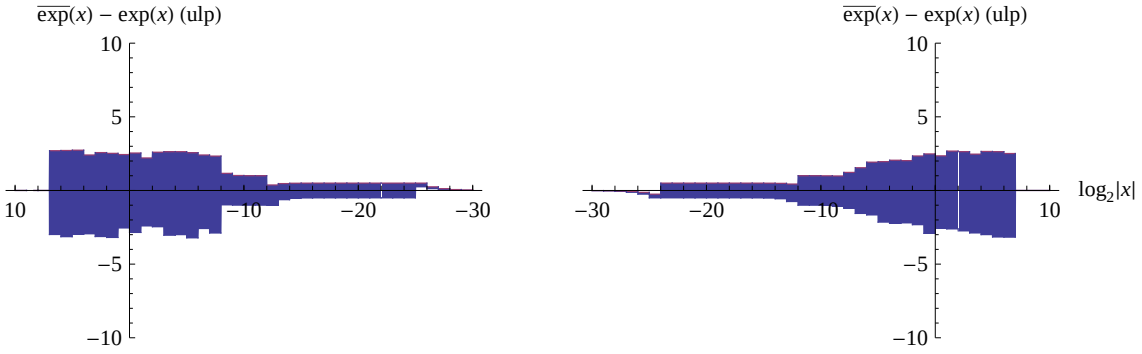

Figure B.3: The worst case accuracy as function of the exponent for the Intel Compiler 12.0.1.107 SVML VMLSEXP4. The horizontal axis for the negative arguments is reversed for clarity.

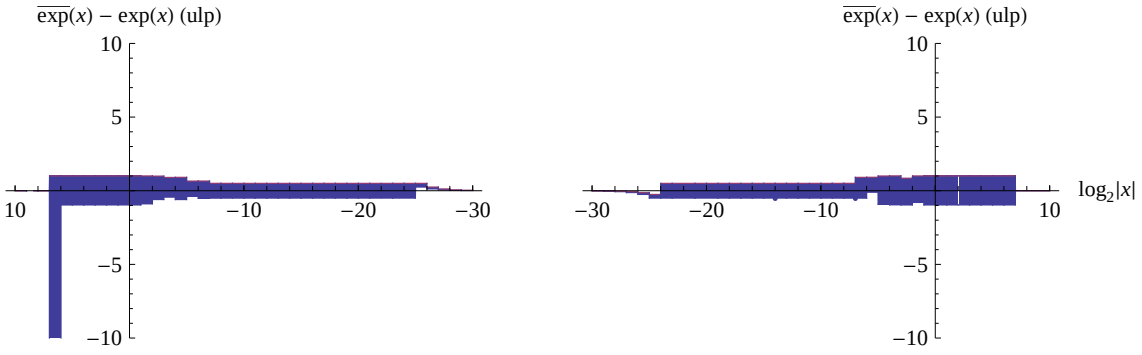

Figure B.4: The worst case accuracy as function of the exponent for the AMD Core Math Library 4.4.0 __VRS4_EXPF. The horizontal axis for the negative arguments is reversed for clarity. The large (off scale) inaccuracy of -8.3×10^6 ulp is due to the flush-to-zero behavior for subnormalized results.

For the range $x^* \in [-C, C]$, a 7th order polynomial minimax approximation to $\exp(x^*)$ is the lowest order that results in an implementation suitable for a single precision implementation with a precision < 1 ulp. The minimax approximation can be computed using the Remez algorithm [75] modified by exchanging extrema of relative approximation errors. However, rounding error in the lowest order coefficients typically degrate the approximation, which makes using the unconstrained minimax approximation, and can be approximatively minimized by evaluate the minimax approximation with the constraint of the lowest order coefficients being machine numbers (see e.g. [123], p. 51ff)

$$\bar{g}(x^*) = 1 + x^* + O(x^{*2}). \tag{B.6}$$

This gives rounded to single precision

$$\begin{aligned}\bar{g}(x^*) = 1 + x^* + \frac{1\,048\,577x^{*2}}{2\,097\,152} + \frac{11\,184\,819x^{*3}}{67\,108\,864} + \frac{11\,183\,107x^{*4}}{268\,435\,456} + \\ + \frac{8\,946\,659x^{*5}}{1\,073\,741\,824} + \frac{12\,127\,477x^{*6}}{8\,589\,934\,592} + \frac{13\,847\,623x^{*7}}{68\,719\,476\,736}.\end{aligned} \tag{B.7}$$

Machine implementation of the above using the Horner scheme should be obvious.

Handling subnormal results can be expensive and ACML omits it all together. Among several paths to implement it, the version found to exhibit the best pipelining prescales the exponent by $(m + 1)$ and rescale the result by $2^{-(m+1)}$. The prescale is generated by comparison (and therefore potentially offloads the operand to a nonarithmetic execution unit).

The exponent generation with subnormal handling is then:

```
movdqa   FLT_MIN_EXP, %xmm1
movdqa   FLT_MIN_EXP − FLT_MANT_DIG, %xmm2
pcmpgtd  %xmm3, %xmm1
pcmpgtd  %xmm3, %xmm2
pand     FLT_MANT_DIG, %xmm1
paddd    FLT_EXP_BIAS, %xmm3
psubd    %xmm1, %xmm3
paddd    FLT_EXP_BIAS, %xmm1
pslld    $23, %xmm3
pslld    $23, %xmm1
mulps    %xmm3, %xmm0
```

CPU model	Stepping	Threading	EXPF_SSE2	VMLSEXP4	__VRS4_EXPF
AMD Opteron 848	1	ST	28.43	37.31	25.15
AMD Phenom II X4 955	2	ST	21.11	37.32	25.22
Intel Core 2 Duo T7500	10	ST	16.63	17.84	20.13
Intel Xeon L5640	2	ST	15.09	16.12	18.11
Intel Xeon X5660	2	SMT	18.47	19.78	22.04

Table B.3: The speed of the SIMD IEEE 754 single precision exp functions, the Gaussian filter EXPF_SSE2, the Intel SVML VMLSEXP4, and the AMD ACML __VRS4_EXPF, measured in clocks per element (cpe) on selected x86-64 CPUs (running in 64-bit mode), either single threaded (ST) or using simultaneous multithreading (SMT), averaged over 10^{10} values uniformly distributed within the valid argument range. The systematic uncertainty is $\approx$ 0.1 cpe, the statistical measurement uncertainties are $<$ 0.02 cpe.

```
mulps    %xmm1, %xmm0
andnps   %xmm0, %xmm2
```
$\exp(x) \leftarrow$ `%xmm2`

where `FLT_EXP_BIAS` $=$ 127 is the IEEE 754 single precision exponent bias, and not defined by either C99 or POSIX.

Figures B.2–B.4, shows the worst case accuracy in the round to the nearest (even) mode of the implementation described here, Intel SVML, and AMD ACML.

Table B.1 lists the accuracy and worst argument in the the nearest (even) mode of the implementation described here, Intel SVML, and AMD ACML. Table B.2 lists the accuracy and worst argument of the implementation described here for all four IEEE 754 rounding modes.

The performance of the different implementations are measured in clocks per element (cpe), i.e. the effective number of elapsed CPU clock ticks for each of the four IEEE 754 single precision argument in the 128-bit SSE vector. The processor time stamp counter is used to measure the elapsed clock ticks, which on IA-32 and AMD64, is accessible using the `rdtsc` instruction, that moves the 64-bit unsigned integer value into the register pair `%eax` (low bits) and `%edx` (high bits). The overhead of the C++ loop is measured by repeating the loop with the `nop` instruction, while the impact of the `rdtsc` instruction overhead is minimized by measuring 10^8 vector evaluations at once.

Table B.3 compares the speed of the Gaussian filter EXPF_SSE2, the Intel SVML VMLSEXP4, and the AMD ACML __VRS4_EXPF, measured in clocks per element, on four different CPU.

Bibliography

[1] S. Bethke, Eur. Phys. J. C **64**, 689 (2009).

[2] A. Bazavov *et al.*, Phys. Rev. D **80**, 014504 (2009).

[3] S. B. Rüster, V. Werth, M. Buballa, I. A. Shovkovy, and D. H. Rischke, Phys. Rev. D **72**, 034004 (2005).

[4] Y. Watanabe and E. Komatsu, Phys. Rev. D **73**, 123515 (2006).

[5] R. K. Ellis and J. C. Sexton, Nucl. Phys. B **269**, 445 (1986).

[6] X. Artru and G. Mennessier, Nucl. Phys. B **70**, 93 (1974).

[7] B. R. Webber, Nucl. Phys. B **238**, 492 (1984).

[8] P. Bagnaia *et al.*, Phys Lett. B **138**, 430 (1984).

[9] S. Wicks, W. Horowitz, M. Djordjevic, and M. Gyulassy, Nucl. Phys. A **784**, 426 (2007).

[10] W. A. Horowitz and M. Gyulassy, Phys. Lett. B **666**, 320 (2008).

[11] D. Comaniciu and P. Meer, IEEE Trans. Pattern Anal. Mach. Intell. **24**, 603 (2002).

[12] D. E. Paquette, "Brookhaven National Laboratory Groundwater Monitoring Improvements Plan for FY 1998 and 1999," (1998).

[13] M. Anerella *et al.*, Nucl. Instrum. Meth. A **499**, 280 (2003).

[14] E. V. Shuryak, Yad. Fiz. **28**, 796 (1978); Phys. Lett. B **78**, 150 (1978).

[15] G. F. Chapline, M. H. Johnson, E. Teller, and M. S. Weiss, Phys. Rev. D **8**, 4302 (1973).

[16] S. D. Drell, D. J. Levy, and T.-m. Yan, Phys. Rev. **187**, 2159 (1969), p. 187.

[17] K. Adcox *et al.* (PHENIX), Phys. Rev. Lett. **88**, 022301 (2002).

[18] S. S. Adler *et al.* (PHENIX), Phys. Rev. Lett. **97**, 052301 (2006).

[19] Aristotelēs, *Ta Meta ta Physika* (Greece, 4th c. BCE) 1.4.985^{b}4–13; 7.13.1039^{a}9–11; *Aristotle's Metaphysics: A Revised Text with Introduction and Commentary*, edited by W. D. Ross (Clarendon Press, Oxford, 1924).

[20] Vyāsa, *Bhagavad Gītā* (India, ca. 1st c. BCE) 8.9; W. Sargeant, *The Bhagavad Gītā*, 25th ed., edited by C. K. Chappel, SUNY Series in Cultural Perspectives (State University of New York Press, Albany, NY, 2009).

[21] A. B. M. al-Bāqillānī, *Kitāb at-Tamhīd* (the Abbasid caliphate, ca. 10th c.); *Kitāb at-Tamhīd*, edited by R. J. McCarthy, Kalām Series (Librairie Orientale, Beirut, 1957); P. Gassendi, *Syntagma Philosophicum*, edited by H. L. Habert de Montmor, Petri Gassendi Opera Omnia, Vol. 1–2 (Laurent Anisson and Jean Baptiste Devenet, Lyon, 1658).

[22] A. Lavoisier, *Traité Elementaire de Chimie* (Chez Cuchet, Paris, 1789).

[23] J. Dalton, *A New System of Chemical Philosophy* (R. Bickerstaff, London, 1808).

[24] D. Mendeleev, Zh. Russ. Fiz.-Khim. Obshch. **1**, 60 (1869).

[25] J. J. Thomson, The Electrician **39**, 104 (1897).

[26] E. Rutherford, Phil. Mag. Ser. 6 **37**, 581 (1919).

[27] J. Chadwick, Nature **129**, 312 (1932).

[28] R. Hagedorn, Nuovo Cim. Suppl. **3**, 147 (1965).

[29] K. Moriyasu, Eur. J. Phys. **2**, 232 (1981).

[30] W. E. Caswell, Phys. Rev. Lett. **33**, 244 (1974); D. R. T. Jones, Nucl. Phys. B **87**, 127 (1975); É. Sh. Egoryan and O. V. Tarasov, Teor. Mat. Fiz. **41**, 26 (1979); Theor. Math. Phys. **41**, 863 (1979).

[31] O. V. Tarasov, A. A. Vladimirov, and A. Yu. Zharkov, Phys. Lett. B **93**, 429 (1980); S. A. Larin and J. A. M. Vermaseren, Phys. Lett. B **303**, 334 (1993).

[32] T. van Ritbergen, J. A. M. Vermaseren, and S. A. Larin, Phys. Lett. B **400**, 379 (1997).

[33] J. J. Drake *et al.*, Astrophys. J. **572**, 996 (2002).

[34] P. O. Slane, D. J. Helfand, and S. S. Murray, Astrophys. J. Lett. **571**, L45 (2002).

[35] C.-m. Zhang, H.-x. Yin, Y.-h. Zhao, Y.-c. Wei, and X.-d. Li, Publ. Astron. Soc. Pac. **119**, 1108 (2007).

[36] D. Larson *et al.*, Astrophys. J. Suppl. **192**, 16 (2011); E. Komatsu *et al.* (WMAP), Astrophys. J. Suppl. **192**, 18 (2011).

[37] E. Witten, Phys. Rev. D **30**, 272 (1984).

[38] V. N. Gribov and L. N. Lipatov, Yad. Fiz. **15**, 781 (1972); Sov. J. Nucl. Phys. **15**, 438 (1972); Y. L. Dokshitzer, Zh. Éksp. Teor. Fiz. **73**, 1216 (1977); Sov. Phys. JETP **46** (1977); G. Altarelli and G. Parisi, Nucl. Phys. B **126**, 298 (1977).

[39] B. L. Combridge, J. Kripfganz, and J. Ranft, Phys. Lett. B **70**, 234 (1977).

[40] T. Kinoshita, J. Math. Phys. **3**, 650 (1962); T. D. Lee and M. Nauenberg, Phys. Rev. **133**, B1549 (1964).

[41] G. Altarelli, R. K. Ellis, and G. Martinelli, Nucl. Phys. B **157**, 461 (1979).

[42] L. J. Bergmann, *Next-To-Leading-Log QCD Calculation of Symmetric Dihadron Production*, Ph.D. thesis, Florida State Univ., Tallahassee, FL (1989), AAT 8915738.

[43] S. Catani and M. H. Seymour, Nucl. Phys. B **485**, 291 (1997).

[44] Z. Kunszt and D. E. Soper, Phys. Rev. D **46**, 192 (1992).

[45] P. J. Mohr and B. N. Taylor, J. Phys. Chem. Ref. Data **28**, 1713 (1999), section 2.4.1; Rev. Mod. Phys. **72**, 351 (2000), section 2.D.1; Rev. Mod. Phys. **77**, 1 (2005), section 2.D.

[46] P. J. Mohr, B. N. Taylor, and D. B. Newell, *The 2010 CODATA Recommended Values of the Fundamental Physical Constants*, NIST Standard Reference Database 121 (NIST, Gaithersburg, MD, 2010) Web version 6.0.

[47] C. E. Detar, O. Kaczmarek, F. Karsch, and E. Laermann, Phys. Rev. D **59**, 031501 (1999).

[48] T. Åkesson *et al.* (Axial Field Spectrometer), Phys. Lett. B **118**, 185 (1982).

[49] A. L. S. Angelis *et al.* (CERN-Columbia-Oxford-Rockefeller), Phys. Lett. B **97**, 163 (1980).

[50] M. Deutschmann *et al.* (Aachen–Berlin–CERN–Cracow–London–Vienna–Warsaw), Nucl. Phys. B **155**, 307 (1979).

[51] C. De Marzo *et al.* (Bari–Krakow–Liverpool–MPI Munich–Nijmegen), Phys. Lett. B **112**, 173 (1982).

[52] M. Gyulassy and X.-n. Wang, Nucl. Phys. B **420**, 583 (1994).

[53] R. Baier, Y. L. Dokshitzer, A. H. Mueller, S. Peigné, and D. Schiff, Nucl. Phys. B **483**, 291 (1997); Nucl. Phys. B **484**, 265 (1997); R. Baier, Y. L. Dokshitzer, A. H. Mueller, and D. Schiff, Phys. Rev. C **58**, 1706 (1998); Nucl. Phys. B **531**, 403 (1998); B. G. Zakharov, Pis'ma Zh. Éksp. Teor. Fiz. **63**, 906 (1996); Pis'ma Zh. Éksp. Teor. Fiz. **65**, 585 (1997); JETP Lett. **63**, 952 (1996); JETP Lett. **65**, 615 (1997).

[54] M. Gyulassy, P. Lévai, and I. Vitev, Nucl. Phys. B **594**, 371 (2001); Phys. Lett. B **538**, 282 (2002); I. Vitev and M. Gyulassy, Phys. Rev. C **65**, 041902 (2002).

[55] M. Djordjevic and M. Gyulassy, Nucl. Phys. A **733**, 265 (2004).

[56] M. H. Thoma and M. Gyulassy, Nucl. Phys. B **351**, 491 (1991); E. Braaten and M. H. Thoma, Phys. Rev. D **44**, 1298 (1991); Phys. Rev. D **44**, R2625 (1991).

[57] H. Miyazawa, Prog. Theor. Phys. **36**, 1266 (1966).

[58] A. Neveu and J. H. Schwarz, Nucl. Phys. B **31**, 86 (1971).

[59] M. B. Green and J. H. Schwarz, Phys. Lett. B **136**, 367 (1984).

[60] N. Berkovits, J. High Energy Phys. **2000**, 018 (2000).

[61] C. P. Herzog, A. Karch, P. Kovtun, C. Kozcaz, and L. G. Yaffe, J. High Energy Phys. **2006**, 013 (2006).

[62] H. Liu, K. Rajagopal, and U. A. Wiedemann, J. High Energy Phys. **2007**, 066 (2007).

[63] S. Brandt, C. Peyrou, R. Sosnowski, and A. Wroblewski, Phys. Lett. **12**, 57 (1964); J. D. Bjorken and S. J. Brodsky, Phys. Rev. D **1**, 1416 (1970); M. J. Counihan, Phys. Lett. B **59**, 367 (1975).

[64] E. Farhi, Phys. Rev. Lett. **39**, 1587 (1977).

[65] J. E. Huth *et al.*, in *Research directions for the decade: proceedings of the 1990 Summer Study on High Energy Physics* (1990) pp. 134–136.

[66] Y.-z. Cheng, IEEE Trans. Pattern Anal. Mach. Intell. **17**, 790 (1995); M. Fashing and C. Tomasi, IEEE Trans. Pattern Anal. Mach. Intell. **27**, 471 (2005).

[67] V. A. Epanechnikov, Teor. Veroyatnost. i Primenen. **14**, 156 (1969), Theory Probab. Appl. **14**, 153–158 (1969).

[68] A. Antoniou, *Digital Filters: Analysis, Design, and Applications*, 2nd ed. (McGraw-Hill, New York, NY, 1993) pp. 43–89; *Digital Signal Processing: Signals, Systems, and Filters* (McGraw-Hill, New York, NY, 2006) pp. 79–126; A. V. Oppenheim, R. W. Schafer, and J. R. Buch, *Discrete-Time Signal Processing*, 2nd ed. (Prentice-Hall, Upper Saddle River, NJ, 1999) pp. 94–139.

[69] R. Deriche, in *Proceeding International Workshop on Machine Vision and Machine Intelligence* (1987) pp. 18–23; in *Proceedings Second International Conference on Image Processing* (1992) pp. 263–267.

[70] I. T. Young and L. J. van Vliet, Signal Processing **44**, 139 (1995); L. J. van Vliet, I. T. Young, and P. W. Verbeek, in *Proceedings of the 14th International Conference on Pattern Recognition*, Vol. 1 (IEEE Computer Society, Los Alamitos, CA, 1998) pp. 509–514; I. T. Young, L. J. van Vliet, and M. van Ginkel, IEEE Trans. Signal Processing **50**, 2798 (2002).

[71] A. Antoniou, *Digital Filters: Analysis, Design, and Applications*, 2nd ed. (McGraw-Hill, New York, NY, 1993) pp. 269–270; *Digital Signal Processing: Signals, Systems, and Filters* (McGraw-Hill, New York, NY, 2006) pp. 587–588.

[72] D. Hale, *Recursive Gaussian Filters*, Tech. Rep. 546 (Center for Wave Phenomena, Colorado School of Mines, 2006).

[73] G. Alefeld, F. A. Potra, and Y.-x. Shi, Math. Comput. **61**, 733 (1993).

[74] M. Abramowitz and I. A. Stegun, eds., "Handbook of Mathematical Functions," (U.S. Government Printing Office, Washington, DC, 1964).

[75] E. Remez, Comm. Soc. Math. Kharkov **10**, 41 (1934); Compt. Rend. Acad. Sc. **198**, 2063 (1934); **199**, 337 (1934).

[76] G. A. Watson, SIAM J. Numer. Anal. **11**, 693 (1974); SIAM J. Numer. Anal. **12**, 46 (1975); J. Comput. Appl. Math. **121**, 1 (2000).

[77] R. H. Byrd, P.-h. Lu, J. Nocedal, and C.-y. Zhu, SIAM J. Sci. Comput. **16**, 1190 (1995).

[78] P. E. Gill, W. Murray, and M. H. Wright, *Practical Optimization* (Academic Press, London, 1981).

[79] E. M. Gertz, *Combination Trust-Region Line-Search Methods for Unconstrained Optimization*, Ph.D. thesis, University of California, San Diego, La Jolla, CA (1999), AAT 9935439.

[80] J. J. Moré and D. J. Thuente, ACM Trans. Math. Softw. **20**, 286 (1994).

[81] X.-N. Wang and M. Gyulassy, Phys. Rev. D **44**, 3501 (1991).

[82] N. Grau, B. A. Cole, W. G. Holzmann, M. Spousta, and P. Steinberg (ATLAS), Eur. Phys. J. C **62**, 191 (2009).

[83] G. P. Salam and G. Soyez, J. High Energy Phys. **2007**, 086 (2007).

[84] M. Cacciari and G. P. Salam, Phys. Lett. B **641**, 57 (2006).

[85] M. Cacciari and G. P. Salam, Phys. Lett. B **659**, 119 (2008).

[86] A. G. Ruggiero, *Definition of Beam Emittances*, Tech. Rep. RHIC-PG-5 (Brookhaven National Laboratory, Upton, NY, 1983).

[87] B. Stroustrup, "A History of C++: 1979–1991," (2005).

[88] J. McCarthy, P. W. Abrahams, D. J. Edwards, T. P. Hart, and M. I. Levin, *LISP 1.5 Programmer's Manual* (MIT Press, Cambridge, MA, 1962) p. 105; I. E. Sutherland, *Sketchpad: A Man-Machine Graphical Communication System*, Tech. Rep. 296 (MIT Lincoln Laboratory, Lexington, MA, 1963).

[89] United States Department of Defense, *ANSI/MIL-STD-1815A-1983: Reference Manual for the Ada Programming Language* (Springer-Verlag, New York, NY, 1983) pp. 12-1–12-16.

[90] A. Stepanov and M. Lee, *The Standard Template Library*, Tech. Rep. 95-11(R.1) (HP Laboratories, Palo Alto, CA, 1995).

[91] R. Brun and F. Rademakers, Nucl. Instr. Meth. A **389**, 81 (1997); I. Antcheva *et al.*, Comput. Phys. Commun. **180**, 2499 (2009).

[92] Google, Inc., computer code GOOGLE SPARSEHASH 1.10 (2011).

[93] C. Collaboration, *Measurement of the Inclusive b-Jet Cross Section in $p\bar{p}$ Collisions at $\sqrt{s} = 1.96$ TeV*, Tech. Rep. CDF note 8418 (Fermilab, Batavia, IL, 2006).

[94] J. Hadamard, Princeton Univ. Bull. **13**, 49 (1902).

[95] P. C. Hansen, *Rank-Deficient and Discrete Ill-Posed Problems: Numerical Aspects of Linear Inversion* (SIAM, Philadelphia, PA, 1998); R. C. Aster, B. Borchers, and C. H. Thurber, *Parameter Estimation and Inverse Problems* (Elsevier Academic Press, Amsterdam, 2005).

[96] A. Höcker and V. Kartvelishvili, Nucl. Instrum. Methods A **372**, 469 (1996).

[97] L. Eldén, BIT Numer. Math. **22**, 487 (1982).

[98] P. H. van Cittert, Z. Phys. A **69**, 298 (1931).

[99] W. H. Richardson, J. Opt. Soc. Am. **62**, 55 (1972); L. B. Lucy, Astron. J. **79**, 745 (1974).

[100] D. Tody, in *Instrumentation in Astronomy VI*, Society of Photo-Optical Instrumentation Engineers Conference Series, Vol. 627, edited by D. L. Crawford (1986).

[101] K. Banse, D. Ponz, C. Ounnas, P. Grosbol, and R. Warmels, in *Instrumentation for Ground-Based Optical Astronomy: Present and Future*, Santa Cruz Summer Workshops in Astronomy and Astrophysics, edited by L. B. Robinson, Lick Observatory (Springer-Verlag, Berlin, 1988).

[102] R. L. White, in *The Restoration of HST Images and Spectra*, edited by R. L. White and R. J. Allen (Space Telescope Science Institute, Baltimore, MD, 1991) pp. 139–143; R. J. Hanisch, R. L. White, and R. L. Gilliland, in *Deconvolution of Images and Spectra*, edited by P. A. Jansson (Academic Press, San Diego, CA, 1996) 2nd ed.

[103] L. A. Shepp and Y. Vardi, IEEE Trans. Med. Imaging **1**, 113 (1982).

[104] G. D'Agostini, Nucl. Instrum. Meth. A **362**, 487 (1995).

[105] R. Field and R. C. Group (CDF), *PYTHIA Tune A, HERWIG, and JIMMY in Run 2 at CDF*, Tech. Rep. CDF/ANAL/CDF/PUBLIC/7822 (Fermilab, Batavia, IL, 2005) hep-ph/0510198.

[106] W. J. Cody, Jr. and W. Waite, *Software Manual for the Elementary Functions* (Prentice-Hall, Englewood Cliffs, NJ, 1980); W. J. Cody, Jr., in *Problems and Methodologies in Mathematical Software Production*, Lecture Notes in Computer Science No. 142, edited by P. C. Messina and A. Murli (Springer-Verlag, Berlin, 1982) pp. 24–47.

[107] M. Matsumoto and T. Nishimura, in *Monte Carlo and Quasi-Monte Carlo Methods 1998*, edited by H. Niederreiter and J. Spanier (Springer-Verlag, Berlin, 1999) pp. 56–59.

[108] Intel Corp., *Intel Math Kernel Library Reference Manual*, Santa Clara, CA (2010), version 10.3.

[109] ClearSpeed Technology Ltd., *C^n Standard Libraries Reference Manual*, Whitney (2008), revision 3.A.

[110] IBM Corp., *Software Development Kit for Multicore Acceleration: Monte Carlo Library Programmer's Guide and API Reference*, Montreal, QC (2008), version 3.1.

[111] D. E. Knuth, *Seminumerical Algorithms*, 3rd ed., The Art of Computer Programming, Vol. 2 (Addison-Wesley, Reading, MA, 1997) p. 106, table 1.

[112] Wolfram Research, Inc., computer code MATHEMATICA 8.0.1 (2011).

[113] Intel Corp., *Instruction Set Reference, A–Z*, Intel 64 and IA-32 Architectures Software Developer's Manual, Vol. 2A–2B (Intel Corp., Santa Clara, CA, 2011) sec. 4.8.4.

[114] Free Software Foundation, *Using as*, Boston, MA (2009), version 2.20.

[115] ISO/IEC JTC 1/SC 22/WG 14, *ISO/IEC 9899:1999/Cor.3:2007: Programming Languages – C* (ISO/IEC, Geneva, 2007).

[116] IEEE Portable Application Standards Committee, *IEEE Std 1003.1-2008: Portable Operating System Interface (POSIX) Base Specifications, Issue 7* (IEEE, Piscataway, NJ, 2008).

[117] D. E. Knuth, *MMIX – A RISC Computer for the New Millennium*, 1st ed., The Art of Computer Programming, Vol. 1, Fascicle 1 (Addison-Wesley, Reading, MA, 2005).

[118] A. V. Oppenheim, R. W. Schafer, and J. R. Buch, *Discrete-Time Signal Processing*, 2nd ed. (Prentice-Hall, Upper Saddle River, NJ, 1999) pp. 341–348.

[119] A. J. C. Bik, *The Software Vectorization Handbook: Applying Intel Multimedia Extensions for Maximum Performance* (Intel Press, Santa Clara, CA, 2004); Intel Corp., *Intel C++ Compiler XE 12.0 User and Reference Guides*, Champaign, IL (2010).

[120] IEEE Computer Society, *IEEE Std 754-2008: IEEE Standard for Floating-Point Arithmetic* (IEEE, Piscataway, NJ, 2008).

[121] IEEE Computer Society, *IEEE Std 754-1985: IEEE Standard for Binary Floating-Point Arithmetic* (IEEE, Piscataway, NJ, 1985) p. 5.

[122] AMD, Inc. and NAG Ltd., *AMD Core Math Library*, Sunnyvale, CA (2010), version 4.4.0.

[123] J.-M. Muller, *Elementary Functions: Algorithms and Implementation*, 2nd ed. (Birkhäuser, Boston, MA, 2006).